UNIVERSITAT DE VALÈNCIA

Instituto de Ciencia Molecular

Hybrid magnetic materials based on layered double hydroxides: from the chemistry towards the applications

TESIS DOCTORAL

Memoria presentada por **Gonzalo Abellán Sáez**

para aspirar al grado de Doctor en Nanociencia y Nanotecnología

(programa ref. 3045)

Dirigida por:

Prof. Eugenio Coronado Miralles

Dr. Antonio Luis Ribera Hermano

Valencia, 2014

D. EUGENIO CORONADO MIRALLES, Profesor Catedrático del Departamento de Química Inorgánica de la Universidad de Valencia, y D. ANTONIO LUIS RIBERA HERMANO, Profesor Titular del Departamento de Química Inorgánica de la Universidad de Valencia.

CERTIFICAN: Que la presente Tesis Doctoral, titulada: **"Hybrid magnetic materials based on layered double hydroxides: from the chemistry towards the applications"**, ha sido desarrollada por GONZALO ABELLÁN SÁEZ, bajo su dirección en el Instituto de Ciencia Molecular, autorizando mediante este escrito la presentación de la misma para optar al grado de Doctor.

En Paterna, a 27 de junio de 2014.

Dr. Eugenio Coronado Miralles Dr. Antonio Luis Ribera Hermano

By three methods we may approach wisdom:
First, by reflection, which is noblest;
second, by imitation, which is the easiest;
and third, by experience, which is the bitterest.
CONFUCIUS

A la memoria de mi padre
A mi madre
A Edurne

Agradecimientos

En el inicio de mi juventud me planteé un reto que ahora puedo decir que es una realidad. En mi continua búsqueda de la felicidad, decidí que realizar una tesis doctoral era uno de los objetivos primordiales. Al margen de agoreros, conseguí superarme a mí mismo y alcanzar la energía necesaria para recorrer este arduo camino. Me gustaría expresar mi profunda gratitud hacia todas aquellas personas que se han cruzado en mis encrucijadas y me han ayudado a alcanzar este objetivo. Afortunadamente me he encontrado con muchas y variadas personas a las que es imposible citarlas "*nominatim*". Aún así, ellas vienen conmigo y forman parte de mi bagaje. Para ellas de entrada va mi sincero gracias.

Hay personas que con todas las letras quiero dar las gracias: en primer lugar quería agradecer a Eugenio Coronado la confianza que ha depositado en mi. Me siento muy afortunado por formar parte de su grupo de investigación y de haber contado con su experiencia, dedicación y generosidad durante el transcurso de esta tesis. Sin duda ha sido una pieza clave para mí todos estos años. Del mismo modo quiero mostrar mi gratitud hacia Antonio Ribera, que me ha obsequiado con su tiempo y serenidad desde el primer momento en que recalé en el ICMol. El honor de poder trabajar con unos directores de tesis de este calibre no tiene precio.

Con toda seguridad, esta investigación no habría sido la misma sin la inestimable ayuda de Carlos Martí. Todo un ejemplo de pasión por el trabajo en general y por la química en particular.

Mas allá de los muros de la Universidad de Valencia he podido contar con la acogida, la amistad y la sabiduría de muchas personas:

A Hermenegildo García, que me ha permitido trabajar de forma ininterrumpida en el Instituto de Tecnología Química de la Universidad Politécnica de Valencia, enseñándome gran parte de los conocimientos que hoy poseo. Allí he tenido el placer de trabajar y conocer, entre otros, a Miguel Ángel Miranda, Avelino Corma, Vicente Fornés, Jose Luis Jordá, Marcos Latorre, Pedro Atienzar y Maykel de Miguel… Gracias por hacer del ITQ mi segunda casa.

A Toribio Fernández Otero: me abrió las puertas del Centro de Electroquímica y Materiales Inteligentes en la Universidad Politécnica de Cartagena, me enseñó con entusiasmo lo maravillosa que puede llegar a ser la electroquímica y algunos rincones de Cartagena que sin duda volveré a recorrer. A José Gabriel: ha sido un lujo poder trabajar con él. Muchas gracias por hacer de mis estancias un auténtico placer.

A Félix Zamora, por compartir su tiempo conmigo en la Universidad Autónoma de Madrid, transmitirme una ingente cantidad de entusiasmo e ideas, y obsequiarme con su amistad. A Pilar Amo, Rubén Mas, Julio Gómez, Isadora Berlanga y Miriam Jaafar por la buena acogida que me dieron.

Quisiera agradecer encarecidamente su profesionalidad y dedicación a: Carlos Gómez, Helena Prima, Juan Pablo Prieto, Elena Pinilla, Cristina Almansa, Ion Such, Enrique Navarro, María Varela, João Waerenborgh y Juan Francisco Sánchez.

Un lugar privilegiado merecen mis compañeros de la Universidad de Valencia, que me han hecho sentirme afortunado durante todo este tiempo. Gracias a Alex Gaita por ayudarme tanto y deleitarme con sus reflexiones. A Guillermo Mínguez y Mónica Giménez por su amistad y buen ánimo. A Michele Sessolo, por tantos momentos de jazz y gastronomía. A mis compañeros de fútbol, comida y música: Salvador Cardona, José Jaime Baldoví, Toni Pertegás, Daniel Tordera y Alex Recuenco, por hacer tan agradable el día a día y ser mucho más que compañeros de trabajo. Y qué decir de Jose Alberto Carrasco, Jorge Romero y Basilio Gómez, poder trabajar codo a codo con vosotros es uno de los mayores regalos que he tenido en esta tesis.

Desde la administración y los técnicos hasta el laboratorio, sin olvidarme de mis compañeros/as de pecera, he tenido la suerte de contar con unas personas excepcionales, muchas gracias a todos.

No quisiera terminar sin dedicar un merecido espacio a todas las personas que conforman el MUDIC-VBS-CV. Me he sentido honrado al poder trabajar por la divulgación científica junto a Jesús Carnicer, Juan Roldán, Fulgencio Bermejo, Manuel Nieves, Jerónimo Hurtado, Francisco Reyes, y todo el resto de miembros de la Asociación de Profesores de Ciencias Hypatia de Alejandría. Muchas gracias por haceros continuamente eco de mi investigación y mantener viva mi vinculación a Orihuela a pesar de la distancia. Soy oriolano de

nacimiento y agradecimiento.

En el plano personal, no puedo olvidar el continuo apoyo de Txema y Mª Luisa, y mis familiares en Cartagena y Madrid.

A mi hermano Pedro que me ha fortalecido con su cariño en todo momento.

A Edurne, por compartir cada día conmigo, llenarme de esperanza, renovar mis fuerzas cada mañana y no menos mi esperanza cada noche. Sin duda, el mejor regalo que me ha dado la vida.

A mi padre, por inculcarme desde la infancia el amor por la química y servir de referente en mi carrera.

A mi madre, por haber creído siempre en mi y ser el pilar sobre el que me he apoyado tantos años. Esta tesis está impregnada de tu determinación. Gracias.

Gonzalo

Possunt quia posse videntur
PUBLIUS VERGILIUS MARO
Aeneis, 5, 231

Contents

Abbreviations

AC	Alternate Current
AEC	Anion-Exchange Capacity
AF	Antiferromagnetic
AFM	Atomic Force Microscopy
AMR	Anisotropic Magnetoresistance
ARR	Ammonia-Releasing Reagent
BDDT	Brunauer-Deming-Deming-Teller
BE	Binding Energy
BET	Brunauer-Emmett-Teller
BLCNT	Bamboo-like Carbon Nanotube
BS	Basal Spacing
ca.	circa (approximately)
CMR	Colossal Magnetoresistance
CNF	Carbon Nanoforms
CNO	Carbon Nano-Onions
CNT	Carbon Nanotubes
CV	Cyclic Voltammetry
DC	Direct Current
DLS	Dynamic Light Scattering
DR	Dubinin-Radushkevich
DTA	Differential Thermal Analysis
EA	Elemental Analysis
ED	Electron Diffraction
EDAX	Energy Dispersive X-ray Analysis

EDLC	Electric Double-Layer Capacitor
EELS	Electron Energy Loss Spectroscopy
EPMA	Electron Probe Microanalysis
ESR	Electron Spin Resonance
ES-VRH	Efros-Shklovskii Variable Range Hopping
et al.	et alii (and the others)
EtOH	Ethanol
EXAFS	Extended X-Ray Absorption Fine Structure
F	Ferromagnetic
FC	Field Cool
FCC	Face-Centered Cubic / Fluid Catalytic Cracking
FESEM	Field Emission Scanning Electron Microscopy
FT-IR	Fourier Transform Infrared
G	Graphene
GO	Graphene Oxide
GMR	Giant Magnetoresistance
HAADF	High Angle Annular Dark Field
HMT	Hexamethylenetetramine
HRTEM	High Resolution Transmission Electron Microscopy
HT	Hydrothermal
i.e.	id est (that is)
IS	Isomer Shift (Mössbauer)
IUPAC	International Union of Pure and Applied Chemistry
JCPDS	Joint Committee on Powder Diffraction Standards

LB	Langmuir-Blodgett
LbL	Layer-by-Layer
LDH	Layered Double Hydroxide
LDO	Layered Double Oxide
LFMR	Low-Field Magnetoresistance
M	Magnetism
MOF	Metal Organic Framework
MR	Magnetoresistance
MW	Microwave
MWCNT	Multi-Wall Carbon Nanotube
NP	Nanoparticle
OER	Oxygen Evolution Reaction
OMR	Ordinary Magnetoresistance
Pc	Phthalocyanine
PMMA	Poly(methyl methacrylate)
PPMS	Physical Properties Measurement System
PSS	Poly(styrene sulfonate)
PVDF	Poly(vinylidene fluoride)
PVS	Polyvinylsulfonate
PXRD	Powder X-ray Diffraction
QD	Quantum Dot
QS	Quadrupole Splitting (Mössbauer)
rGO	Reduced Graphene Oxide
RHE	Reversible Hydrogen Electrode

RMS	Root Mean Squared (roughness)
rpm	revolutions per minute
SAED	Selected Area Electron Diffraction
SDS	Sodium Dodecyl Sulphate
SEM	Scanning Electron Microscopy
SQUID	Superconducting Quantum Interference Device
STEM	Scanning Transmission Electron Microscopy
SWCNT	Single-Wall Carbon Nanotube
TEA	Triethanolamine
TGA	Thermogravimetric Analysis
TIP	Temperature Independent Parameter
TMDC	Transition Metal Dichalcogenide
TMR	Tunneling Magnetoresistance
TPPS	5,10,15,20-tetrakis(4-sulfonatophenyl)porphyrin
UHV	Ultra High Vacuum
UV	Ultraviolet
WOC	Water Oxidation Catalysis
WS	Water Splitting
XPS	X-ray Photoelectron Spectroscopy
XRD	X-ray Diffraction
ZFC	Zero Field Cool

Preface

Layered double hydroxides (LDHs) are the *leitmotiv* of this dissertation. Contradicting the assertion that "any past was better", LDHs have been continuously revisited from the middle of the twentieth century, and represent an excellent example of the never-ending beauty of Chemistry. New synthetic perspectives are giving a new impetus to LDH chemistry, which among hybrid materials, are finding their heyday. This is resulting in novel materials and also paving the way for new fundamental and practical insights. This dissertation is focused on magnetic LDHs, and for the sake of clarity it is organized in three main parts: we will move from basic synthetic and physical aspects of LDHs, through the preparation of multifunctional hybrids that respond to external stimuli, and towards some of the most innovative applications in energy storage and spintronics. Due to the wide number of techniques employed, and to facilitate the reading, we have included the experimental procedures and the specific instrumentation at the end of each Chapter.

The **first part** deals with the chemical design, synthesis, exfoliation and physical characterization of new magnetic layered double hydroxides. Chapter 2 provides an in-depth insight into the synthesis of highly crystalline, hexagonal-shaped NiFe–LDH with tunable composition, a kind of LDH that up to now had been elusive. In addition, exfoliation of this magnetic LDH into unilamellar nanosheets has been achieved for the very first time. Chapter 3 is devoted to the physical properties of these new layered materials, unveiling their controllable magnetic behaviour, and shedding light on the cation order within the layers, elucidating the origin of the spin-glass behaviour in this sort of materials. Concluding this part, Chapter 4 addresses the profound effect exerted by extrinsic impurities in the magnetic behaviour of LDHs, highlighting the enormous possibilities offered by these magnetic materials.

The **second part** explores the preparation of new hybrid magnetic multilayers based on LDHs, with special emphasis on the control of the magnetic properties of LDHs by means of an external stimulus. In this sense, Chapter 5 and 6 focuses on the physical effect induced by the intercalation of a macrocyclic phthalocyanine and porphyrins in the interlamellar space provided by magnetic LDHs, respectively. Moreover, the synthesis and characterization of novel stimuli responsive hybrid materials has been surveyed in this section, showing the very first examples of the reversible switching of the magnetic

properties in LDH-based materials. Along this front, Chapter 7 deals with the photo-switching in a hybrid material made of azobenzene intercalated LDHs, whilst Chapter 8 examines the reversible thermo-responsive switching of a thermochromic-LDH hybrid.

Finally, the **third part** is devoted to the applications of several LDH-based materials in different fields of utmost importance, such as energy storage and conversion or spintronics. On the one hand, in Chapter 9 we have studied the intrinsic electrocatalytic properties towards water oxidation of NiFe–LDHs. We have also investigated the effect of their hybridization with graphene showing an excellent behaviour as supercapacitors and water oxidation electrocatalysts. On the other hand, in Chapter 10 we have reported the use of hybrid NiFe–LDHs as catalytic nanoreactors for the *in-situ* synthesis of novel magnetic nanocomposites formed by $FeNi_3$ nanoparticles embedded in carbon nanoforms. These hierarchical nanocomposites can be used as precursors for the low-temperature isolation of nanocarbons, ranging from carbon nanoonions to graphene. Furthermore, we have tested these nanocomposites as electrode materials for supercapacitors, obtaining high values of specific capacitance and excellent rate capabilities.

In the end, we have explored the application of the previously synthesized graphene–$FeNi_3$ nanocomposites in the field of spintronics. Concretely, Chapter 11 describes the magnetotransport properties of these hybrids, showing striking crossover behaviour from negative to positive magnetoresistance, arising from the correlation of the physical properties of its initial constituents in a synergistic way.

1. Introduction

1.1. Introduction

Hybrid multifunctional materials constitute a remarkable and growing category within the world of materials science.[1] In these classes of materials the intimate molecular interaction between components transcends the simply physical mixture, and therefore makes possible the coupling of two properties. Aside from recent works, the origins of the hybrid materials science rely on extremely ancient serendipitous discoveries that perfectly exemplify the beauty of these materials. In fact, as suggested by Weiss in 1963, the first example of intercalation dates from over two thousand years ago, and refers to the intercalation of kaolinite (an aluminosilicate clay), explaining the secret behind the finest Chinese porcelain.[2] Moreover, anthropologists have discovered that the ancient Maya Blue pigments used in Mesoamerica from about A.D. 300 to 1500, and that exhibit high chemical resistance, consists on a nanostructured material based on palygorskite (microfibrous clay mineral) and indigo dye extracted from plants.[3–6] As stated by Pérez-Romero and Sanchez, these antiquities remain a source of inspiration for novel hybrid materials designers.[1]

More recently, the development of soft inorganic chemistry processes (so called "Chimie Douce"), allowed for the exponential growth of the existing list of hybrid materials, with the subsequent development of their applications.[7] Through the last century, anionic clays, and more specifically layered double hydroxides (LDHs), have been widespread as excellent constituents for hybrid functional materials, offering an ideal scenario for blurring of distinctions between organic and inorganic chemistry, while materials science stands as the ultimate guest to this charming research field.[8]

Layered double hydroxides are a wide family of anionic clays with layered structure and interlayer spaces containing exchangeable anions. Synthetic LDHs are very promising materials for a large number of possible applications due to their low cost and high versatility, as reflected by their easily manipulated properties and wide range of composition and preparation variables, among others.[7,9–11] Thus, it is not surprising that, as such or after thermal decomposition, they find many practical applications. Over the past few years, there has been a huge increase in publications related to these applications, most of them of industrial interest.[11,12]

This dissertation deals with a rather academic approach to the synthesis, properties and, finally, applications of newest LDH-based systems. We will start from novel synthetic pathways towards magnetic LDHs, continuing with a series of multifunctional LDH hybrids, and finishing with some practical applications of interest in energy storage and conversion and spintronics.

1.2. History

Hydrotalcite ($Mg_6Al_2(OH)_{16}(CO_3)\cdot 4H_2O$), a white hydrous mineral that resembles talc, hence its name, was first discovered in Snarum (Norway), but the mineral was found in New South Wales and Tasmania (Australia).[10] This mineral is rare in nature, and is often encountered associated with other compounds such as phyllosilicates and gibbsite. LDHs have been approached in the last 100 years from two different directions, namely, mineralogy and descriptive inorganic chemistry, being focused on the non-straightforward identification of natural and synthetic materials, respectively.[7] As revised in 2004 by Brateman, Xu and Yarberry, the hydrotalcite and pyroaurite families of minerals had been known since the mid-19th century and were described by 1910 by Flink.[7,13] Later on, Freitknecht (1936-1942) mistakenly described MgAl mixed hydroxide as alternating magnesium-rich and aluminium-rich layers.[14–16] He named the structures *Doppelschichtenstruktur* —literally meaning doubly layered structure— from which the expression layered double hydroxide is probably derived. Around 1967, several groups correctly identified the structural features of the LDHs, starting a lively controversy about the cation order/disorder within the layers, which is still a topic of interest (as addressed in this dissertation).[7,17–19] Moreover, thermal transformation of LDHs into spinel was first reported in 1944 by Caillere, paving the way to an ever-expanding research area.[20] The first clinical usage of LDHs as antacids dates back at 1960, and their use as flame-retardants was patented in 1975.[21,22] Later on, Miyata published on 1973 the ground-breaking work regarding the range of formation and anion exchange in LDHs.[23] This latter work is considered as the starting point of the viral growth experimented by LDHs to date.

1.3. Structure and Composition

LDHs consist of a layered structure where each sheet is composed of edge-sharing octahedra, in the same way as found in the brucite ($Mg(OH)_2$).[8,9]

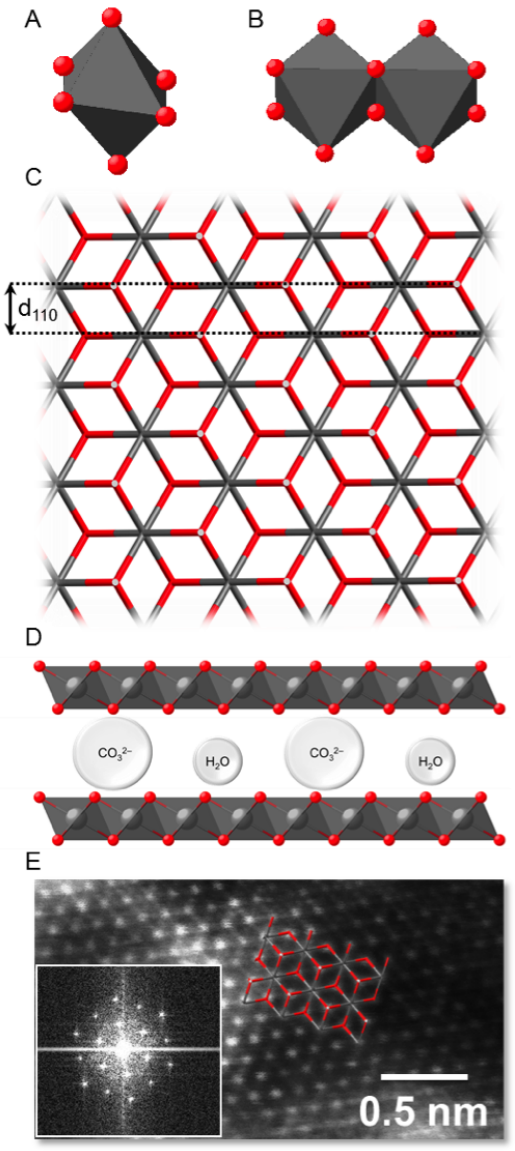

Figure 1. Structure of LDHs as found in the mineral brucite. (A) Brucite consists of Mg^{2+} cations octahedrally coordinated by hydroxils which (B) edge share, (C) to form 2D sheets, (D) which stack to form a layered structure. In LDHs, M^{III} are isomorphically substituting some of the M^{II} and the excess of positive charge is balanced by anions. (E) High magnification HAADF image showing the structure of an LDH sheet. The inset shows the image fast Fourier transform, which exhibits the hexagonal symmetry of the crystal.

Figure 1 illustrates this structure. The brucite structure is built up from Mg^{2+} cations octahedrally coordinated by hydroxyl ligands. The edge sharing octahedra form a two-dimensional sheet in the crystallographic *a* and *b* directions. Each Mg^{2+} cation shares one-third of six hydroxide ligands (μ_2-hydroxide bridges). In LDHs some of the divalent metals M^{II} are isomorphically substituted by trivalent cations M^{III}, generating an overall positive charge balanced by anions occupying the interlamellar space (*vide infra*). As can be observed in **Figure 1B** the dashed lines indicates the 110 crystallographic planes, which point out the spacing between adjacent cations in the LDH layers. Owing to the differences in the ionic radii of M^{III} and M^{II}, the inclusion of smaller trivalent metals leads to a contraction in the distance between adjacent cations and hence the 110 planes. The change in distance results in a variation in the 110 reflection in the XRD pattern towards lower spacings at lower M^{II}/M^{III} ratios. These hydroxide layers stack in the *c* crystallographic direction to form the characteristic layered structure. The crystallographic thickness of one layer of brucite is estimated to be 4.78 Å, and therefore subtracting this value to the basal space (the distance between the centers of adjacent layers) leads to the height of the gap between the inorganic sheets, commonly referred as gallery height. Ideally, for brucite, the *a* parameter —indicative of the M–M distances parallel to the plane— should have a value of 0.2973 nm, but experimental X-ray diffraction experiments revealed a larger 0.3142 nm distance. Moreover, experimental O–M–O bond angles of 96.7º and 83.3º rather than regular 90º were measured, confirming that the octahedra exhibit a significant distortion, in particular, they are compressed along the stacking axis, so that the local geometry at the metal is D_{3d}, rather than O_h.[11,24–26] The distortion of the hydroxide layers does not change the hexagonal symmetry ($a_0 = b_0 = 0.3142$ nm, $c_0 = 0.4766$ nm, $\gamma = 120º$), being the space group P3*m*1.

The main difference between brucite and LDHs is that the introduction of a M^{III} generates an excess of positive charge that must be compensated by interlamellar anions. These anions occupy the space between the layers in coexistance with water molecules (although other molecules have also been described), stabilized by weak interactions, namely hydrogen bonding and dispersion forces. It is the possibility of varying the nature and relative proportion of the M^{II} and M^{III} cations, as well as the identity of the interlayer

anions, that gives rise to a large variety of materials having the general formula $[M^{II}_{1-x}M^{III}_{x}(OH)_2]^{x+}[A^{n-}]_{x/n}\cdot yH_2O$. Here the most common divalent metals may be $M^{II} = Mg^{2+}$, Zn^{2+}, Ni^{2+}, Co^{2+}, Fe^{2+}, Cu^{2+}, Ca^{2+} or Mn^{2+}; and the trivalent metals may be $M^{III} = Al^{3+}$, Fe^{3+}, Co^{3+}, Ni^{3+}, Cr^{3+}, Mn^{3+}, Ga^{3+} or In^{3+}.[7–11,27] There is also the possibility of preparing ternary or quaternary LDHs involving mixtures of different M^{II} and/or M^{III} cations. It is even possible to extend the LDH family towards monovalent lithium ions or tetravalent titanium ions; the inclusion of lanthanide cations is still controversial.[11]

Concerning the nonframework charge compensating inorganic or organic anions, the possibilities are endless, as A^{n-} could represent halides, non-metal oxoanions (BO_3^{3-}, CO_3^{2-}, NO_3^-, $Si_2O_5^{2-}$, HPO_4^{2-}, SO_4^{2-}, ClO_4^-, AsO_4^{3-}, SeO_4^{2-}, BrO_4^-, etc.), oxometallate anions (VO_4^{3-}, CrO_4^{2-}, MnO_4^-, $V_{10}O_{28}^{6-}$, $Cr_2O_7^{2-}$, $Mo_7O_{24}^{6-}$, $PW_{12}O_{40}^{3-}$, etc.), anionic complexes of transition metals and macrocyclic ligands ($Fe(CN)_6^{2-}$, phthalocyanine and porphyrins derivatives, etc.), volatile organic anions (CH_3COO^-, $C_6H_5COO^-$, $C_{12}H_{25}COO^-$, $C_2O_4^{2-}$, $C_6H_5SO_3^-$, etc.), photoactive molecules (C_{60}/SDS, polythiophene, dyarylethenes, indolinespirobenzopyrane, etc.), anionic polymers (PSS, PVS, PMMA, etc.), biological molecules of pharmaceutical interest (including biopolysaccharides, vitamins, drugs, and DNA strands), and so on…[7–11,27–29]

The number of anions that may be intercalated per unit weight of LDH, commonly known as the anion-exchange capacity (AEC), is dependent on the charge density of the layer, *i.e.* the number of M^{III} cations within the layer. The degree of M^{III} substitution is dependent upon the method and specific conditions of synthesis. It is often said that pure LDH phases can be only formed for stoichiometries in the range $0.20 < x < 0.33$, *i.e.* M^{II}/M^{III} ratios in the range 2–4.[11] This assumption leads to avoid in theory the presence of M^{III}–O–M^{III} linkages despite the higher charge repulsion originated by the proximity of the trivalent cations (the so-called cation avoidance rule). This brings with it a number of associated controversies related with the extent of the long-range cation ordering within the layers, which has significant implications in the physical properties of LDHs, such as their catalytic or magnetic behaviour (amply discussed in the present dissertation).[7,25,30–32] Moreover, theoretical calculations have suggested that the most stable stoichiometry for LDH phases is $x = 0.25$. In point of fact, NiFe–LDHs synthesized via hydrothermal approach

gives $NiFe_2O_4$ spinel impurities for values of $x > 0.25$, a limitation not overcome till the development of this dissertation.[33] In addition, there have been several claims that LDHs can be synthesized outside from this "ideal" compositional range, but detailed studies revealed that the abnormal stoichiometry can be attributed to extrinsic phases such as $M^{II}(OH)_2$, $M^{III}(OH)_3/M^{III}OOH$, that most often are likely to be amorphous and remain undetected by XRD.[7] This fact is strengthened by the conventional preferred orientation of LDH samples during X-ray experiments, which tend to complicate the observation of weak reflections from small amounts of impurities.

Structural studies of LDHs indicate that the expected values for the M–M distances in MgAl–LDHs and ZnAl–LDHs oscillates with the stoichiometric composition in the 0.302–0.307 and 0.306–0.311 nm ranges, respectively, due to the differences in the radii of the metal cations in the layers. These differences are also reflected in the appearance of intrinsic corrugation within the layers due to differences in the M^{II}–O and M^{III}–O distances, as demonstrated by Bellotto et al. with XRD and EXAFS radial distribution function analyses.[7,26,34] Other interesting aspect of LDH layers is their relatively flexible character (interlayer rigidity parameter, p~5). In fact, they exhibit much more interlayer rigidity than graphite (p~2) and graphene, but much less rigidity than conventional phyllosylicate clays (p~7).[34–36] Interestingly, LDHs behaves similarly to metal dichalcogenides (p~3.5), and exert an uniaxial stress of about 14 GPa on the intercalated anions, which may have an important influence on their electronic properties.[37]

The interlamellar space of LDHs contains a complex network of hydrogen bonds between layer hydroxyl groups, anions and water molecules, which are substantially disordered. At room temperature the hydrogen bonds are in a continuous state of flux, and can be best exemplified by the interlayer water molecules, which behave following a Grotthuss-type mechanism, showing significant behavioural deviations from bulk water. It is worth to mention that the hydroxyl groups bonded to trivalent cations are strongly polarized and predominantly interact with the interlayer anions.[7,11]

The stacking of the LDH layers can appear in different ways, originating a variety of possible polytype structures; among them, the most common are rhombohedral polytype 3R1 and hexagonal polytype 2H1.[8,9] In synthetic

samples, stacking faults often arise from an intergrowth of these two polytypes, and the nature and degree of the observed stacking faults may vary with the method of preparation, or the sample composition.

1.4. Synthesis

LDHs crystals are traditionally prepared by means of a coprecipitation procedure where two soluble metal salts are precipitated simultaneously in the presence of a base, generally under supersaturation conditions controlled by the solution pH.[8,23,38] The materials obtained by this approach are often submitted to thermal post-treatment in order to enhance their crystallinity. On the other hand, coprecipitation under low supersaturation is also commonly used for the synthesis of LDHs. In this case, the slow addition of metal salts into a reactor containing an aqueous solution of the desired interlayer anion is required. Simultaneously, a second alkaline solution is added into the reactor to maintain pH constant. This is achieved by means of an automatic titration device.[11] In addition, inert atmosphere such as nitrogen or, even better, argon (due to its larger atomic weight) is required in order to avoid carbonate contamination (a problem inherent to the LDH synthesis). This synthetic approach leads to a better control of the in-plane composition as well as a better crystallinity than that obtained under high supersaturation conditions due to the predominance of the crystal growth over the nucleation process.

Yet, another type of coprecipitation methodology relies in separating the nucleation and aging steps by means of very rapid mixing and nucleation processes in a colloid mill followed by a separate aging process.[39] The materials obtained with this methodology present a narrower particle size distribution and good crystallinity.

Other synthetic approaches like rehydration using the structural memory effect of LDHs,[40] the so-called salt-oxide method involving salts and oxides as metal sources, the sol-gel approach using acetylacetonates and related precursors, or the nonaqueous alkoxide-intercalated synthetic path have also been developed.[11,41–44]

However, the reason to explain why interest in LDH materials has grown exponentially in recent years is precisely the development of new synthetic routes using ammonia-releasing reagents (ARR). This has opened the possibility

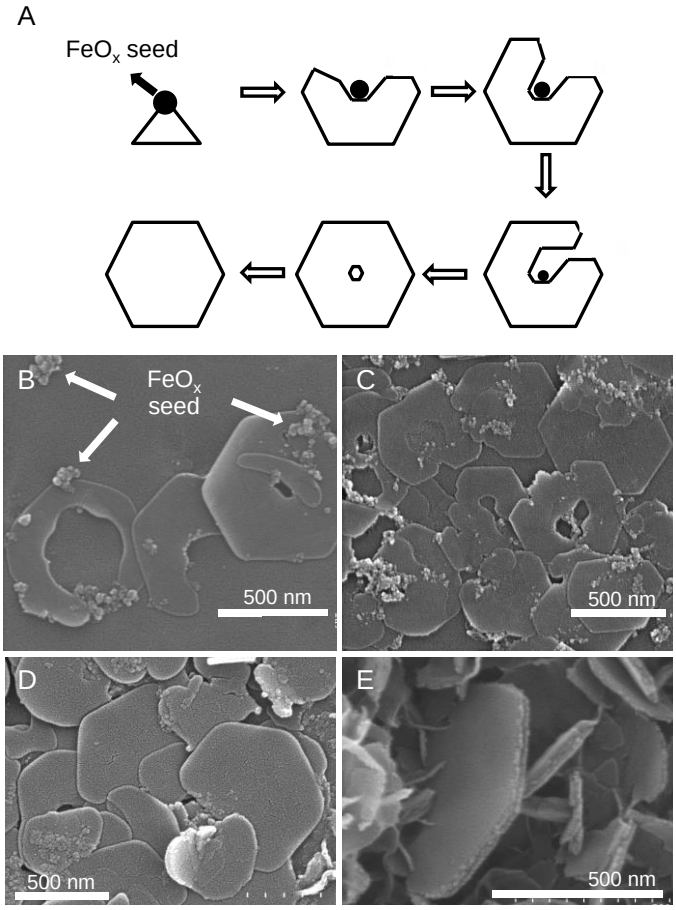

Figure 2. (A) ARR formation route of a LDH crystal, according to the circle-like growth motion mechanism proposed by Okamoto and co-workers. (B and C) FE-SEM images of a NiFe–LDH sample corresponding to the intermediate stages of the growth route. They show the imperfect morphology and the FeO_x nanoparticle seeds, in agreement with the proposed growing mechanism. (D and F) FE-SEM images showing the final formation of an LDH crystal with a normal hexagonal platelet shape.

to control not only the crystallinity but also the morphology of the samples, affording hexagonal crystals, which can be easily exfoliated into 2D nanosheets.[45–51] In these methodologies very weak Brønsted or Lewis bases, like urea or hexamethylenetetramine —which are highly soluble in water and possess a temperature-controllable hydrolysis rate— are employed. Recently, a

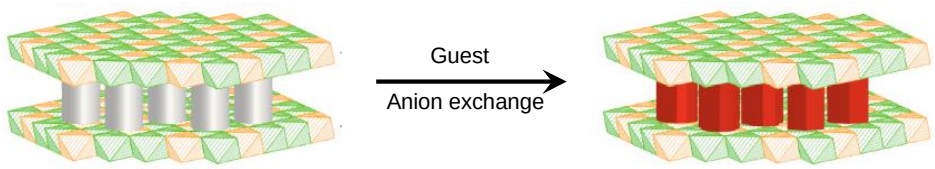

Figure 3. Schematic illustration of anion exchange process in LDHs.

growing mechanism in which the LDH crystal grow in a circle around a M^{III}–rich seed has been developed, leading to well-defined hexagonal morphologies[51] (**Figure 2**). In this sense, it is worth to mention the topochemical oxidative intercalation synthetic path developed by Sasaki, Ma and co-workers leading to superb hexagonal morphologies.[49,52–54]

1.5. Anion Exchange

One of the most characteristic properties of LDHs is their extremely high ion exchange capacity (**Figure 3**). The anionic exchange process is a bivariant thermodynamic system in isothermal and isopressure conditions. The ion-exchange isotherms described by Miyata in 1983 revealed a sigmoid shape arising from a mixed continuous composition range of the anions in the LDH.[55–57] Moreover, non-miscibility of the different anions was observed. The exchange reactions are favoured for in-going anions with a high charge density. Experimental studies revealed that nitrate- and chloride-containing LDHs are the best candidates for exchange reactions.[9] Controlling the concentration of the in-going anion (*i.e.* "infinite solution conditions") it is possible to force the equilibrium towards the desired product. This allows the synthesis of a large variety of inorganic- and organic-containing LDHs. Furthermore, when the intercalation of very big anions is prevented by a too small basal spacing of the precursor or very high interlayer electrostatic interactions, the synthesis of organic-intercalated precursor LDHs could be successfully employed.[7,58] Finally, the pH plays a crucial role in the anionic exchange processes, as carbonate-containing LDHs often requires weak acidic pHs in order to protonate the anions, reducing their charge density and expel them more easily, working under CO_2-free atmosphere. Recent studies have revealed that under hydrothermal conditions it is possible to directly exchange carbonate anions for

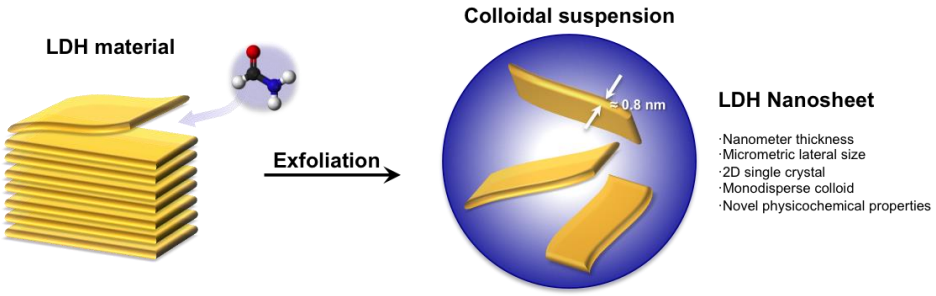

Figure 4. Schematic illustration showing the exfoliation of a layered double hydroxide with formamide into colloidal nanosheets of *ca*. 0.8 nm. Modified from Ma and Sasaki.[54]

alkylsulfonates under moderate temperatures and pHs.[59]

1.6. Exfoliation

Exfoliation of layered hydroxides, defined as the segregation of these lamellar inorganic solids into single entities through soft chemistry methods,[27,54,60–63] can be regarded as a versatile synthetic route to prepare stable suspensions of positively charged 2D sheets. 2D materials have attracted increasing interest in the last few years due to their unique morphology and properties and their use in a variety of applications, ranging from electronics to gas storage or separation, catalysis, high performance sensors or inert protective coatings, among others.[64] Beyond graphene,[65] layered chalcogenides,[66] phosphates,[67] titanates,[61] perovskites[68] and metal oxides or hydroxides[54] appear as promising alternatives, displaying complementary physical properties.[1,9,11,27,69]

Compared to cationic clays, which can be exfoliated in water, LDHs exhibit strong interlayer electrostatic interactions, which can hardly be exfoliated under mild conditions. Thus, organic solvents like formamide, butanol, acrylates, CCl_4, toluene or N,N-dimethylformamide–ethanol mixtures among others are often required to obtain nanosheets.[27]

The obtention of positively charged monolayers (experimentally *ca.* 0.8 nm in thickness due to the solvation effects) of LDHs is a topic of utmost importance, as these nanometric entities can be employed as extremely useful building blocks in the design of novel heterostructured materials (**Figure 4**).[27,54,64]

1.7. Hybrid Materials

Hybrid inorganic/organic materials such as those based on LDHs have found many applications because they allow combining the properties of inorganic solids, such as robustness, durability and mechanical strength, with those introduced by the organic component, such as functionality, tunability and convenient derivatization by synthesis.[70]

LDHs containing intercalated organic anions can be prepared by anionic exchange, direct synthesis and by the exfoliation-restacking approach (flocculation), presenting hybrid stacking of inorganic-organic layers whose structure in monolayers or double layers depends on the number of anionic anchoring groups, the aromatic rings and the hydrophilic/hydrophobic interactions.[71–74] Moreover, in-between these organic layers, neutral organic species such as alcohols or simply water molecules commonly give rise to interlayer swelling phenomena.[75–78]

The 2D interlamellar space provided by LDHs is usually in the range of 0.3–4 nm allowing for a huge variety of organic guests to be incorporated into the interlamellar space of the LDH hosts.[79] These hybrids usually show new specific physical and chemical properties if compared with their pristine counterparts. Interestingly, the LDH host matrix provides a confined stable environment, which minimizes the molecular thermal agitation (intermolecular collisions, vibrations and rotations) by supramolecular interactions.[80,81]

Last but not least, there is a relatively new kind of hybrid materials based on LDHs that is attracting considerably attention known as hybrid nanocarbon–LDH materials.[82] These hierarchical hybrid nanocomposites take advantage of the complementary properties of both constituents. Carbon nanoforms like 0D fullerenes, 1D CNTs and 2D graphene exhibit excellent mechanical properties, high electrical and thermal conductivities, and high specific surface areas.[83,84] But these nanoforms show a general lack of chemical reactivity that can be complemented by the high chemical reactivity inherent to LDHs. In turn, LDHs, suffer from a seriously hindered electrochemical performance because of their low electrical conductivity and moderate porosity that avoids the appropriate ion diffusion (20–120 $m^2 \cdot g^{-1}$). In this sense, various kinds of hierarchical LDH/carbon nanoforms —or thermally derived compounds, the so-called layered double oxides (LDO)— have been synthesized overcoming the

limitations of their initial constituents, and expanding the already extensive list of applications of these systems.[82,85–88]

1.8. Applications

Potential technological applications have been the *leitmotiv* of the research in LDHs for many years and across many disciplines. Their atomically-distributed network, the control over composition and their anion exchange properties have made LDHs (and their thermally-derived materials) interesting in a variety of areas such as catalysis, catalyst precursors, anion exchangers, CO_2 absorbents, bioactive nanocomposites, photoactive materials, energy storage and conversion, or medicine (**Figure 5**).[7,11,12,81,89–92] This is probably due to their high versatility, easily tailored properties and low cost.

Concretely, their application as catalysts of high industrial and scientific relevance covers their usage in the polymerization of olefins, the SO_x removal in fluidized cracking units, the selective catalytic reduction of NO_x, the immobilization of enzymes or the heterogeneization of noble metal nanoparticles, among others.[93] As wide spectrum catalysts in important organic reactions, LDHs have been amply and successfully used in epoxidation reactions, Knoevenagel condensations, Michael additions, Claisen-Schmidt condensations, Meerwein-Ponndorf-Verley reductions, Henry reactions or the synthesis of CNTs via catalytic chemical vapour deposition, to name a few.[7–11,91,93] Concerning "green" catalytic processes, LDHs were one of the most effective at catalysing the reduction of SO_x and NO_x emissions from fluid catalytic cracking (FCC) units in oil refineries, as demonstrated by Corma and co-workers.[94–97]

These ubiquitous materials have been also employed in the removal of pollutants, including highly contaminant anions such as Cr(VI), Ar(V), cyanides, pesticides, phenols, surfactants, dyes or radioactive wastewaters.[8,11] With respect to pharmaceutical applications, LDHs are used as antacids, hypherphosphatemia preventers, excipients and target-specific drug-delivery carriers of several formulations including ibuprofen, folate derivatives, ciprofloxacin, methotrexate, cefazolin, 5-fluorouracil, etc.[98,89,90]

Other applications encompass spinel precursors,[99] additives in functional polymer materials,[100] flame retardants,[22,101] or sensors for several processes:

potentiometric ion selective electrodes (sulphate, nitrate, chloride, calcium, iodate), oxidase detection, hydrogen peroxide detection and enzymatic amperometric biosensors for medical applications, food industry or environment quality control.[12]

Notwithstanding these extremely interesting uses of LDHs, and boosted by the rapid depletion of fossil fuels and severe environmental pollution, energy applications have become one of the most important topics concerning LDHs in the last years.[102,12,103] LDHs show great potential for several key applications in this field, and indeed significant breakthroughs have been achieved in supercapacitors, lithium ion batteries (LIBs), or photo- and electrocatalysts.[12,27,82]

Lithium ion batteries are rechargeable batteries that evolve high energy density and efficiency. They dominate the market of portable electronic devices such as laptops, mobile phones or digital cameras.[104] However, their application in electric vehicles requires increased energy densities and cyclabiblity, as well as better safety and low cost. In this sense, many metal atoms (e.g. Mn, Co, Fe, Ni) can be well arranged into the LDH layers, and the calcination of these LDHs can led to the corresponding LDOs, which are a highly active component for LIBs. CoFe– and NiMn–LDHs have been successfully employed, delivering high specific energies.[105,106]

On the other hand, electrochemical capacitors, also called supercapacitors, are complementary to LIBs as they have the potential to deliver high power density in very short periods of time, exhibiting excellent cyclability. These devices have raised enormous interest in industrial stationary applications, automotive transportation and portable electronic applications.[107,108] Supercapacitors can be classified into two types, according to the predominant mechanisms involved in energy storage: (i) superficial ion adsorption and desorption, named electrochemical double-layer capacitors, and (ii) multi-electron-transfer faradaic reaction with fast charge-discharge properties, so called pseudo-capacitors or redox capacitors. In spite of their appealing properties, SCs energy density remains much lower than that of batteries. Along this front, pseudo-capacitors with extremely high specific capacitances have been reported by using electroactive CoAl–, NiAl–, NiMn– and CoNi–LDHs, among others.[12,107,109–112] In this sense, LDHs and its derivatives represents and excellent alternative to traditional electrode materials since they have also the

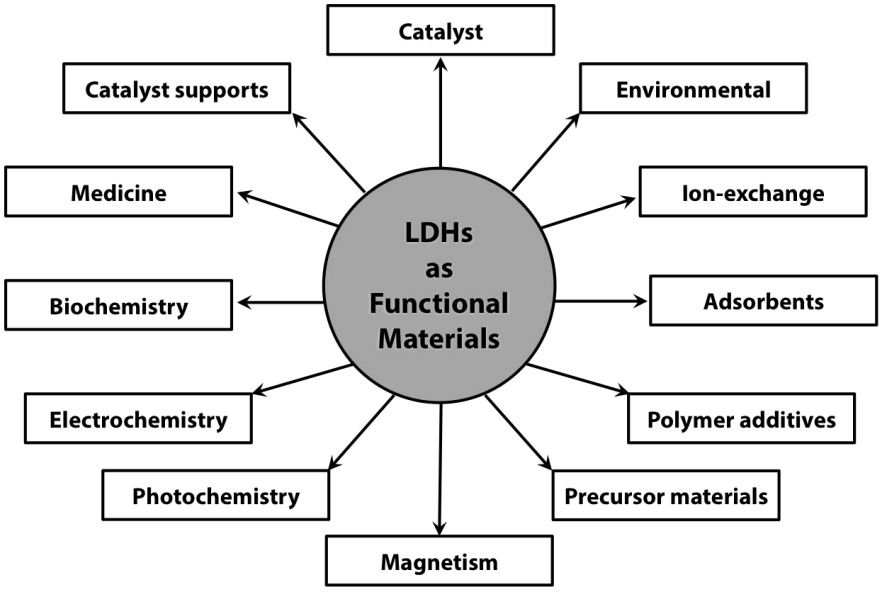

Figure 5. Diagram of the possible fields of applications of LDHs.

possibility of being hybridized with conducting nanocarbons, generating a new family of superb materials with sinning performances. In addition to SCs, one can find other electrochemical systems, such as fuel cells and water splitting devices, which constitute a hot focus of interest as they represent some of the most efficient and environmentally friendly technologies for energy conversion and storage.[113] LDHs could also contribute to these areas, judging by the latest results reported on their impressive electrocatalytic performance, surpassing that of the best precious metal catalysts.[114–117]

1.9. Magnetism

Despite the plethora of applications described, and the large number of compounds that have been synthesized containing magnetic transition metals, very few studies on magnetic properties of LDH systems have been done. In general, magnetic LDHs (*i.e.* those including paramagnetic transition metals within the layers) have been mainly studied as precursors for metal oxides, since their thermal decomposition leads to the formation of mixed metal oxides with a high metal dispersion and high surface area. On the other hand, the recent

insertion of magnetic anions into the interlayer space has usually been studied with nonmagnetic LDHs.[27,69,74] Polyoxometalates, nitronyl nitroxides, cyanide based magnets and homo- and bimetallic oxalate-based 2D magnets have been embedded into LDH frameworks.[29,118–120] However, no effects upon the magnetic properties were observed by the confinement of the molecules due to the absence of magnetic properties in the LDH layers. In our group, LDH systems have been studied for some time, providing a magnetic approach to the science of these layered materials.[121–124] In LDHs, although the metallic random distribution in the layers will affect the local magnetic environment of individual M^{II} ions, in all cases, superexchange must occur through the oxo bridges between adjacent [MO_6] octahedra-sharing edges.[122,125] The M^{II}–O–M^{II} angle in this type of structure should be close to 90° (as commented above), favouring orthogonality of the M^{II} magnetic orbitals and therefore promoting ferromagnetic exchange among d^7 and d^8 cations.[126] Concretely, the classical qualitative Goodenough–Kanamori–Anderson rules clarified by Ginsberg, allows for the prediction of the nature of the interaction between two spin carriers according to their symmetry.[125,127] The most common magnetic divalent cation in LDHs is Ni^{2+}. In octahedral symmetry this d^8 ion has a high spin $(e_g)^2$ configuration with two magnetic orbitals a_1' and b_1. In the case of a d^8–d^8 pair the exchange interaction, J, can be given according to the expression:

$$J = (1/4)(Ja_1'a_1' + Jb_1b_1 + 2Ja_1'b_1)$$

The sign of the first two terms in the right-hand side of the equation depends on the bridging angle. The third term is weakly positive, so therefore the sign of J will depend on the angle in a simple way. In fact, J is expected to be positive (ferromagnetic, F) for values close to 90º, and negative (antiferromagnetic, AF) when the angle is large enough. On the contrary, if a paramagnetic M^{III} metal, like Fe^{3+} or Cr^{3+}, is incorporated —despite the strong synthetic limitations of replacing Al^{3+}— within the layers, M^{II}–O–M^{III} and M^{III}–O–M^{III} pairs will lead to antiferromagnetic coupling due to orbital symmetry considerations (overlapping of the Ni^{II}_{eg} magnetic orbitals with the M^{III} t_{2g} magnetic orbitals and between M^{III} t_{2g}–M^{III} t_{2g} and M^{III} t_{2g}–M^{III} e_g magnetic orbitals).[122,123] These specific considerations allows to obtain tuneable magnetic behaviours in LDHs, including ferromagnetic, antiferromagnetic and ferrimagnetic behaviours, which can be hybridized to obtain hybrid magnetic multilayers with interacting

subnetworks. Still, the control of the magnetic properties of LDHs by means of a external stimulus remains unexplored.[74,126,128] The very first efforts developed in this direction can be encountered in the following Chapters.

1 2D magnetic LDHs

2. Synthesis, Exfoliation and Restacking of NiFe–LDH Nanosheets[†]

Here we report the synthesis of a crystalline micrometric-sized hexagonal-shaped $Ni^{II}Fe^{III}$–LDH family by following a modified homogeneous precipitation method. This approach permits controlling the in-plane composition of the layers in the $0.20 < x < 0.33$ interval, without altering the crystallinity and morphology of the samples. The exfoliation of these materials in formamide leads to stable suspensions of hexagonal nanometric sheets, which have been extensively characterized. Our data confirm that the intrinsic properties of the bulk material are retained by these segregated nanosheets, thus opening the door for their use in the construction of layered multifunctional materials.

[†] Abellán, G.; Coronado, E.; Martí-Gastaldo, C.; Pinilla-Cienfuegos, E.; Ribera, A. *J. Mater. Chem.* **2010**, *20*, 7451. b) Abellán, G.; Coronado, E.; Martí-Gastaldo, C.; Waerenborgh, J.; Ribera, A. *Inorg. Chem.* **2013**, *52*, 10147

2.1. Introduction

Exfoliation of layered hydroxides, defined as the segregation of these lamellar inorganic solids into single entities through soft chemistry methods,[60,61,63,129] can be regarded as a versatile synthetic route to prepare stable suspensions of sheets, typically exhibiting homogeneous micrometric lateral size and nanometric thickness. Concerning materials science, these 2D nanosheets offer very interesting features:

a) Owing to the nanometric thickness of these layers, they may exhibit new physical properties different from the bulk.

b) Compared to other low dimensional nanomaterials (0D or 1D), the 2D structure facilitates their processabilty. In fact, these layers can be reassembled into highly oriented anisotropic films by employing Langmuir-Blodgett (LB) or Layer-by-Layer (LbL) techniques.[49,130,131]

c) They can be used as starting building blocks for the design of new multifunctional materials combining sophisticated physical properties through the rational choice of these building blocks and the precise control of their arrangement in the solid state.[132,133] In this way, the exfoliation of LDHs produces steady colloidal suspensions of positively charged nanosheets,[134,135] which, in the presence of anionic components, can be further re-assembled into sandwich-like layered materials thanks to attractive Coulombic interactions.[136] In addition, LDHs offer a wide plethora of intrinsic magnetic, optical or catalytic properties,[10] which in ultimate term will be retained by the segregated layers and transferred to these layered super-structures.

Unfortunately, the synthesis of crystalline Fe^{3+}-based LDHs with hexagonal morphology has been elusive so far. More generally, the synthesis of non-Al^{3+}-based LDHs is very disfavoured mainly due to the specific amphoteric behaviour of $Al(OH)_3$. With a few exceptions[52,137,138] —namely the topotactic approach developed by Sasaki and co-workers using iodine as oxidant, or the employment of trisodium citrate as catalytic chelating reagent reported by Ooi et al.— the use of traditional coprecipitation methods, based on the direct combination of the constituting ions in a basic medium, has just led to the isolation of amorphous phases. Although these materials can indirectly enhance its crystallinity after an additional hydrothermal treatment, they

cannot be effectively exfoliated due to the intercrossing of particles in the so-called "sand-rose" structure.[33,139–142]

Here we describe a modified homogeneous precipitation method, whose novelty resides in the use of the chelating agent triethanolamine (TEA; $C_6H_{15}NO_3$) as auxiliary reagent, that permits the synthesis of highly crystalline micrometric-sized hexagonal-shaped $[Ni_{1-x}Fe_x(OH)_2](CO_3)_{x/2}$ LDHs. This methodology permits to chemically engineer the in-plane composition of the layers in the $0.20 < x < 0.33$ interval, whilst maintaining the phase purity, morphology and size of the isolated particles unchanged.

Besides, this material can be readily ion-exchanged with nitrate anions through the so-called "acid-salt treatment",[143] permitting its quantitative exfoliation in formamide. Regarding the potential magnetic functionality of these $Ni^{II}Fe^{III}$–LDH nanosheets,[122] our work constitutes the first successful attempt to the synthesis of NiFe–LDHs nanosheets, and paves the way for the use of these building blocks in the design of advanced multifunctional materials, as recently demonstrated for the $[Ni_{0.66}Fe_{0.33}(OH)_2][TaS_2]$ system.[124]

2.2. Results and Discussion

2.2.1. Synthesis of LDHs

$Ni^{II}Fe^{III}$–LDHs were synthesized from aqueous solutions of the nitrate salts of Fe^{3+} and Ni^{2+}, TEA and urea under hydrothermal conditions, according to the homogeneous precipitation method (See the experimental section).[144] In comparison with the traditional co-precipitation methods, the modified homogeneous precipitation route leads to LDH materials with better crystallinity and avoids the "sand rose" morphology. TEA has been widely employed in the synthesis of mesoporous materials according to the so called "atrane route", in view of its ability to chelate metallic ions forming complexes which remain inert towards hydrolysis.[145] This feature pushed us to employ it as an auxiliary reagent in the synthesis of LDHs, since it could prevent the formation of non-soluble metallic oxides or some amorphous phases like ferrihydrite (FeOOH), maintaining a constant ratio of the LDH constituting metals in solution. On the other hand, urea, acting as an ammonia releasing reagent (ARR), is responsible for gradually increasing the pH of the synthetic gel in a controlled manner under the reaction conditions, inducing the slow precipitation of the resulting LDH.

Figure 1 shows the X-ray diffraction patterns of **1-3** $[Ni_{1-x}Fe_x(OH)_2](CO_3)_{x/2}{\cdot}yH_2O$ [x = 0.20 (**1**), 0.25 (**2**) and 0.33 (**3**)]. They exhibit general structural features of LDH materials, with sharp intense peaks at low theta values and weaker and less defined reflection lines at higher angular values. The diffraction patterns have been indexed and refined by assuming a hexagonal lattice with *R3m* rhombohedral symmetry and the calculated cell parameters are summarized in **Table 1**. The calculated basal spacings (*BS*) are in the range 7.78–7.82 Å, in excellent agreement with those reported for other carbonate-intercalated LDHs.[45,46] These data, together with the metal analysis, FT-IR and TG/DTA studies permiting to estimate the molecular formula of the samples **1**–**3** (**Table 2**).

The morphology, thickness and lateral dimensions of the samples have been studied with field emission scanning electron microscopy. According to FESEM (**Figure 2**) measurements, our solids can be described as hexagonal-shaped platelets 20 nm thick, with lateral sizes in the range of *ca.* 900–1700 nm

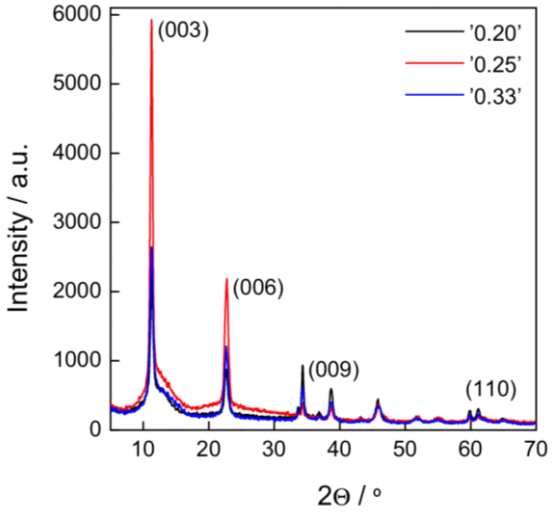

Figure 1. X-Ray powder diffraction patterns and of **1** (0.20, black), **2** (0.25, red) and **3** (0.33, blue).

Table 1. Summary of the unit cell parameters for 1–6 as extracted from the refinement of X-ray powder diffraction data.

Sample	*a* (Å)	*c* (Å)	*V* (Å^3)	*BS* (Å)
1	3.085(3)	23.48(2)	193.48	7.82(7)
2	3.083(2)	23.34(3)	193.13	7.78(1)
3	3.084(8)	23.5(1)	193.13	7.81(8)
4	3.089(3)	23.40(7)	193.40	7.80(1)
5	3.095(3)	23.44(3)	194.54	7.81(4)
6	3.092(4)	23.61(6)	195.39	7.87(1)

[a] $BS=c/3$

and a remarkable high base-to-height ratio, as highlighted in **Figure 2D**. It is worth outlining that higher concentration of Fe^{3+} centers in the layers yield bigger sheets.

To understand the role played by some of the most important synthetic variables and define the optimal synthetic conditions to isolate pure LDH phases, we have studied the effect played by the temperature and the

Table 2. Molecular formulae calculated for 1–6. Metal ratio of synthetic gels (calculated) and isolated compounds (experimental) are estimated from Electronic Probe Microanalysis (EPMA); water content is deduced from thermogravimetric analysis.

	x^a		water content		
	calcd	exptl	wt %	mol	Molecular formula
1	0.20	0.19	13.1	0.8	$[Ni_{0.81}Fe_{0.19}(OH)_2](CO_3)_{0.095}\bullet 0.8H_2O$
2	0.25	0.25	12.9	0.8	$[Ni_{0.75}Fe_{0.25}(OH)_2](CO_3)_{0.125}\bullet 0.8H_2O$
3	0.33	0.31	8.5	0.5	$[Ni_{0.69}Fe_{0.31}(OH)_2](CO_3)_{0.155}\bullet 0.5H_2O$
4	–	0.19	8.0	0.5	$[Ni_{0.81}Fe_{0.19}(OH)_2](NO_3)_{0.190}\bullet 0.5H_2O$
5	–	0.25	6.7	0.5	$[Ni_{0.75}Fe_{0.25}(OH)_2](NO_3)_{0.250}\bullet 0.5H_2O$
6	–	0.31	7.9	0.5	$[Ni_{0.69}Fe_{0.31}(OH)_2](NO_3)_{0.310}\bullet 0.5H_2O$

[a] $x=[Fe^{3+}]/([Ni^{2+}]+[Fe^{3+}])$

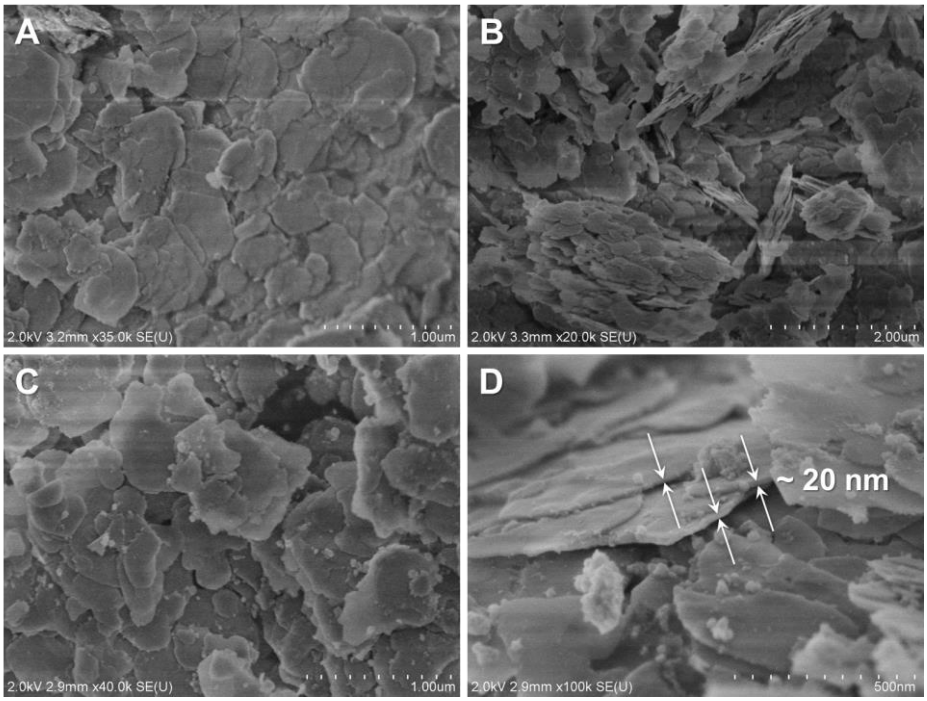

Figure 2. (A) FESEM images of compounds **1**, (B) **2**, (C) **3**, and (D) zoom showing the average thickness of the NiFe–LDH crystals.

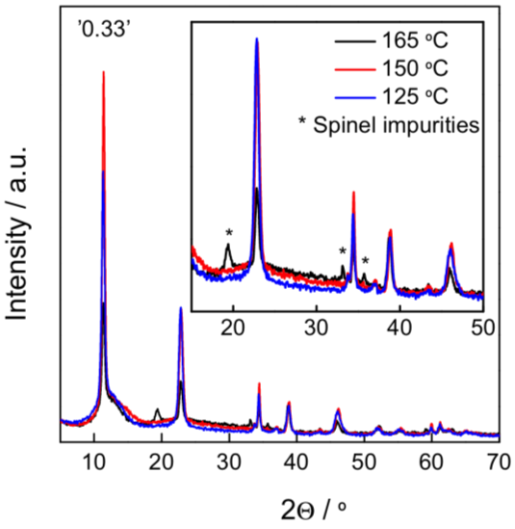

Figure 3. XRD at different temperatures keeping constant the *x* value at 0.33. The inset represents a higher magnification of the 15–50 ° region, highlighting the spinel impurities present at higher temperature.

concentration of TEA. **Figure 3** shows the PXRD patterns of several LDHs obtained from the hydrothermal reaction of a synthetic gel with a fixed metal composition (x = 0.33) at variable temperature between 125–165 °C. The highest temperature leads to the residual formation of a spinel phase together with the LDH. The identity of this contaminant phase has been additionally confirmed with magnetic measurements (*vide infra*). This is not the case for the samples prepared at lower temperatures that only indicate the formation of pure LDH phases. For the other two compositions studied (x = 0.20 and 0.25), temperature does not drive the formation of contaminant phases within the studied interval. This suggests that the reaction temperature should be fixed taking into account the metal composition in order to produce pure LDH phases with the higher crystallinity. Important attention should be paid to optimize the synthetic temperature for Fe^{3+}-containing LDHs.

Next, we studied the influence of the TEA concentration. This was varied between 0.25 and 15 mM (*i.e.* three times the iron concentration) at fixed temperature and composition values of 150 °C and x = 0.25, respectively. **Figure 4** shows how the crystallinity of the formed LDH phase increases with

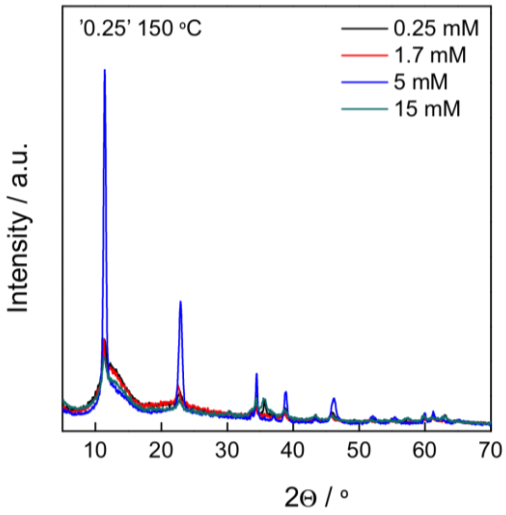

Figure 4. XRD study at different TEA concentrations. The temperature of the synthesis and the composition were fixed to 150 °C and $x = 0.25$, respectively.

[TEA] up to a maximum at 5 mM. This value corresponds to a 1:1 TEA:Fe^{3+} ratio, supporting the chelating role played by TEA in the reaction thus forming stable complexes with the Fe^{3+} ions in solution and avoiding the formation of non-soluble metallic oxides. This explains why deviations from this [TEA] value leads to poorer crystallinity and broader PXRD patterns, similar to those obtained by traditional co-precipitation methods.

2.2.2. Anion Exchange

Exfoliation of carbonate-intercalated LDHs is very unfavourable as, due to the high charge and small size of CO_3^{2-}, it promotes more intense electrostatic interactions than other monoanions like NO_3^-. For this reason, the starting carbonate LDHs (**1–3**) are transformed into nitrate-intercalated compounds (**4–6**) through an ion exchange reaction by immersing it into an aqueous salt-acid mixed solution of $NaNO_3$ and HNO_3. According to **Table 1**, the X-ray diffraction of **4–6** show a small increase in the *BS* of 0.1 Å, slightly lower than that expected for nitrate-intercalated LDHs.[8] This fact together with the presence of low intensity CO_3^{2-} vibration mode bands in the FT-IR data (**Figure 5**) seems to indicate the presence of residual non-exchanged carbonate

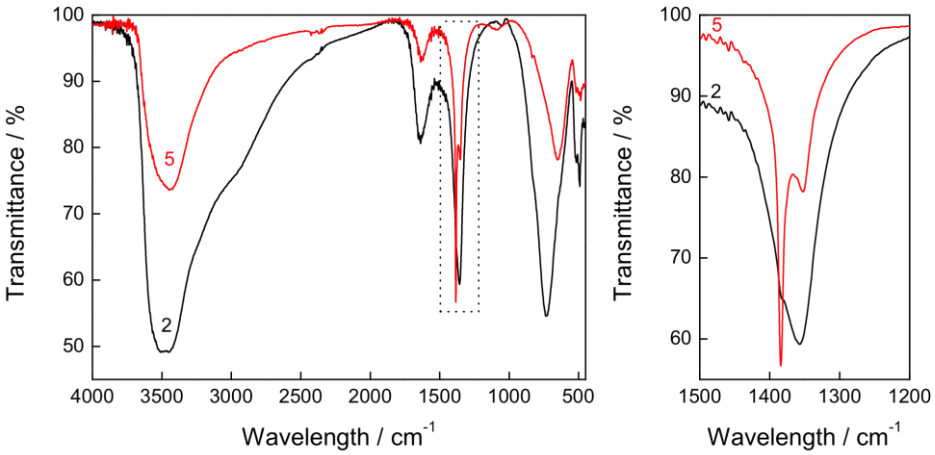

Figure 5. FT-IR of NiFe–CO_3 (**2**) and NiFe–NO_3 (**5**) LDHs. (b) Zoom-in highlighting the carbonate and nitrate anions stretching area.

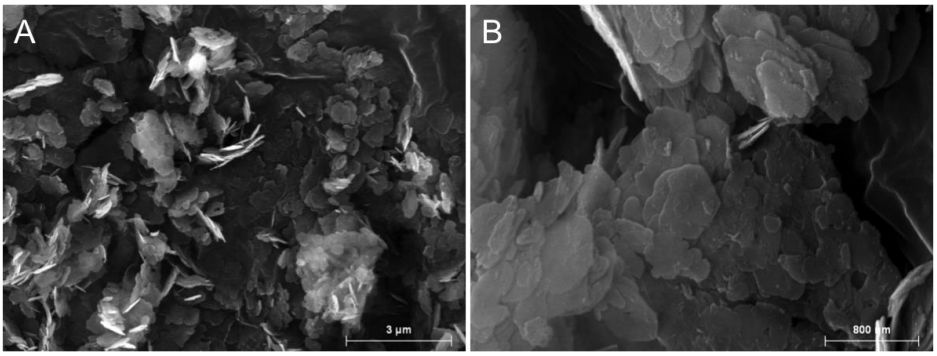

Figure 6. Selected SEM images of compound **5** at different magnifications.

anions in the interlamellar space. The PXRDs of **4–6** display sharp reflection peaks with no sign of contaminant phases, thus confirming that the exchange reaction does not affect the crystallinity of the layered hosts. This is additionally supported by the constant value of the *a* parameter that confirms that the internal symmetry of the layers is maintained (**Table 1**).

FESEM images of **4–6** confirm that the morphology, thickness and micrometric size of the nanosheets are overall maintained after the anion-exchange reaction (**Figure 6**). Electronic Probe Microanalysis (EPMA) reflects

good agreement between the metal ratios in the LDHs before and after the anion-exchange reaction, thus discarding demetalization of the metal-hydroxide slabs. The molecular formulae of the samples **4–6** are summarized in **Table 2**.

Thermal decomposition of **1–6** was studied in air in the range 25–800 °C (**Figure 7**). All the solids display analogous profile for the thermal decomposition, which undergoes through a two-step process: a) Low-temperature weight loss between 25–220 °C that can be split into two sub-processes associated to the removal of hydrated and intercalated water molecules; b) high-temperature weight loss between 220–800 °C that involves the decomposition of carbonate (**1–3**), or nitrate anions (**4–6**) and further dehydroxylation of the LDH layers. In turn, the DTA profiles show two well-defined endothermic peaks between 25 and 220 °C, associated to the two-step loss of water molecules. The water content extracted from the weight loss below 220 ºC has been used to calculate the solvent present in the as-made solids (see **Table 2**). Finally, broader endothermic peaks connected to the decomposition processes taking place at higher temperatures can be observed above 220 °C.

As expected for LDHs, higher Fe^{3+} contents lead to more charged LDH layers that require more CO_3^{2-} anions to counterbalance the charge. This promotes a shrinking of the gallery height from more intense electrostatic interaction thereby decreasing the water content allowed in the interlamellar space.

2.2.3. Structural Characterization

We used FT-IR to monitor the success of the exchange reactions and confirm the presence of water in the interlamellar space. (see **Table 3**). Compounds **4–6** show the presence of a weak band centered at 1352 cm^{-1}, that can be assigned to the ν_3 stretching mode of CO_3^{2-}. This originates from non-exchanged residual anions and supports the observed deviation in the interlayer distance when compared with the values reported for NO_3^- intercalated LDHs, as previously depicted. All compounds show a strong absorption with a broad profile in the 3490–3440 cm^{-1} interval, associated to the presence of H-bonding interactions between the interlamellar water molecules and the OH groups

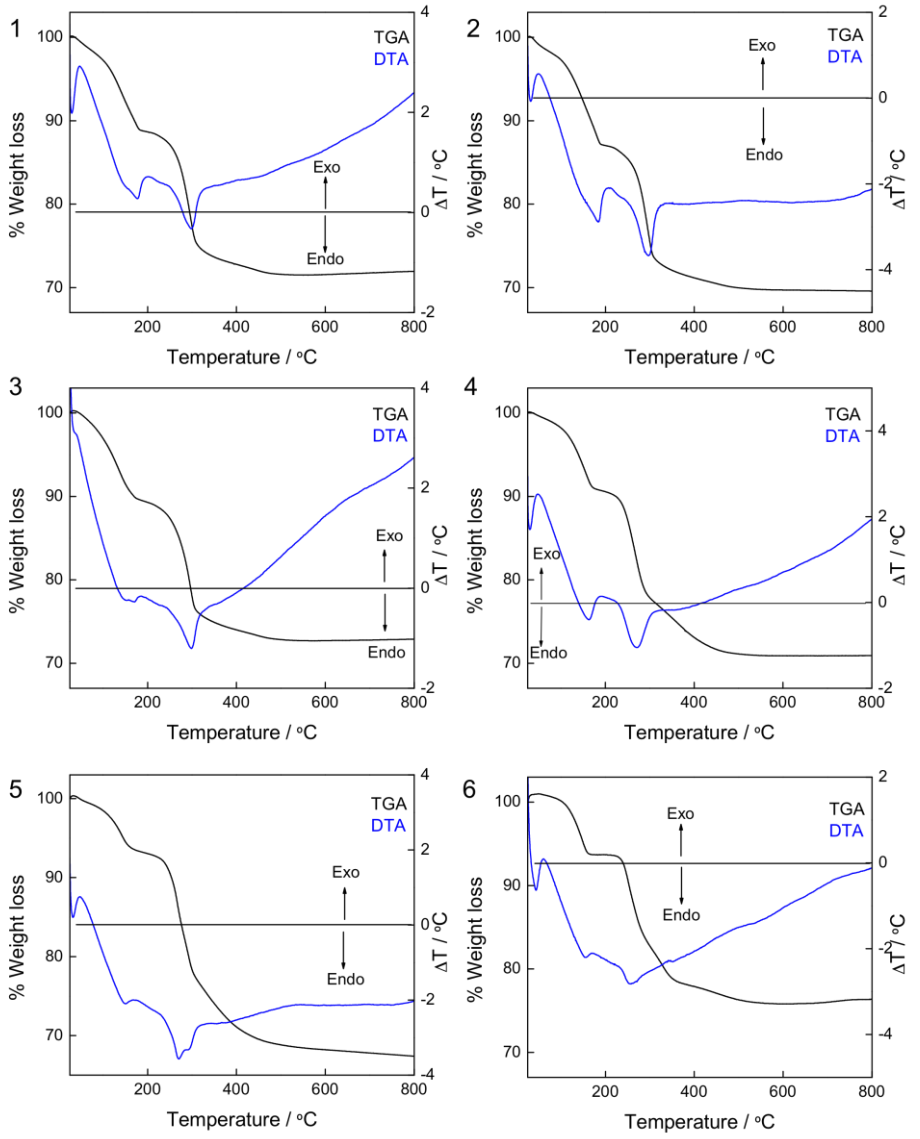

Figure 7. Thermogravimetric analysis (TGA and DTA) curves for compounds **1**–**6**.

belonging to the hydroxide-based layers. The presence of water in these materials is additionally supported by the sharp medium-intensity absorption band at 1637 cm^{-1}, related to the H_2O vibrational bending mode.

Table 3. FT-IR spectra vibration modes assignment for compounds 1–6.

Vibration modes [cm^{-1}]	1	2	3	4	5	6
υ[O–H]	3472	3446	3446	3441	3448	3450
υ[H–O–H]	1618	1637	1637	1637	1637	1624
υ[N–O]	1383	_	_	1384	1385	1384
$\upsilon[C–O]_s$	1363	1358	1357	_	1352	_
υ[M–O]	707	735	742	641	654	655
δ[O–M–O]	490	492	493	492	486	519, 491

Absorption at lower wavenumbers (between 740 and 485 cm^{-1}) must be attributed to vibrational modes associated to the $[M^{II,III}(OH)_2]^+$ complexes distributed along the LDH layers. The CO_3–intercalated LDHs (**1–3**) show a strong-intensity band at *ca.* 1360 cm^{-1}, with is typical for the carbonate anion's ν_3 stretching mode. The NO_3-exchanged LDH (**4–6**) shows a more complex doublet in the same region composed of: a) A sharp stronger band at 1385 cm^{-1}, associated to the nitrate anion's ν_3 stretching mode and b) A much weaker band centered at 1352 cm^{-1}, which is probably related to the presence of a residual amount of non-exchanged intercalated carbonate.

2.2.4. Exfoliation

Stable yellowish colloidal dispersions of $[Ni_{1-x}Fe_x(OH)_2]^{x+}$ 2D nanosheets were easily obtained by applying sequential cycles of mechanically stirring and ultrasounds to a suspension of NiFe–NO_3 in formamide [1 $g{\cdot}L^{-1}$]. The presence of exfoliated layers was firstly confirmed by the appearance of Tyndall light scattering, caused by the dispersion upon irradiation with a laser beam (**Figure 8**). Next, direct information concerning the size of the exfoliated layers was obtained by Dynamic Light Scattering (DLS), which provides the average hydrodynamic diameter, that is a complex function of both the diameter and the particle size for anisotropic materials. As illustrated in **Figure 9**, —even though the average hydrodynamic diameter of LDH dispersions is commonly biased towards the larger particles— we observe homogeneous Gaussian distributions centered close to 920, 950 and 1770 nm, for **4**, **5** and **6** respectively. Thus indicate that the size of the nanosheets increases with the

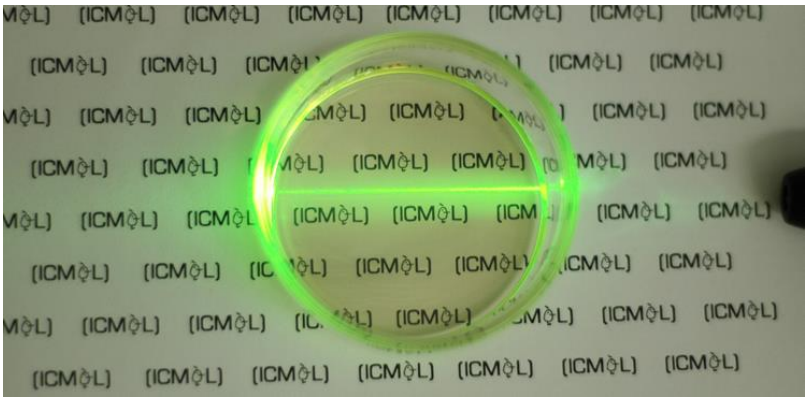

Figure 8. Picture of the colloidal emulsion obtained from the exfoliation of NiFe–NO_3 LDH in formamide. The Tyndall effect, resulting from the scattering of the irradiated beam by the particles in solution, confirms the presence of exfoliated LDH nanosheets.

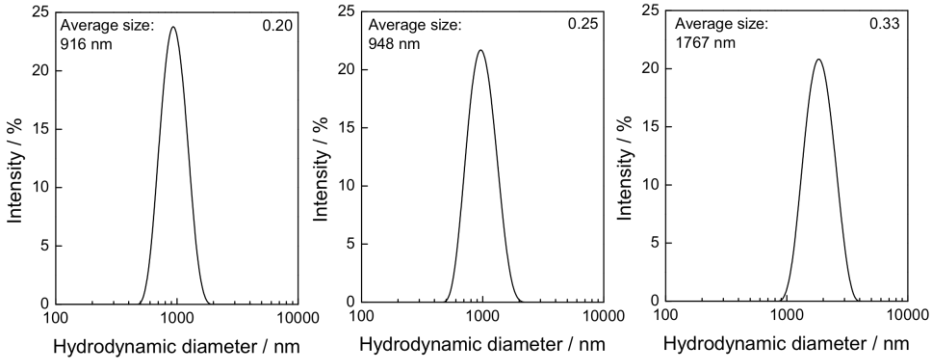

Figure 9. Distribution of sizes as extracted from DLS studies in the 0.20–0.33 composition range.

[Fe^{3+}] present in the layers. This trend is in excellent agreement with that observed for the size of the particles from the starting CO_3–LDHs (**1–3**), as confirmed by the FESEM studies performed on the bulk solids (*vide supra*).

To confirm the unilamellar nature of the exfoliated nanosheets we studied the absorption spectra for different concentrations of the as-made colloids at room temperature (**Figure 10**). The absorption spectra show an intense broad

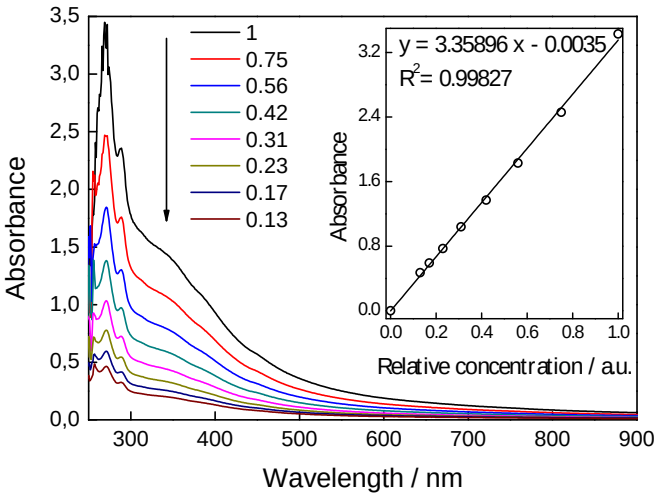

Figure 10. Optical absorption spectra of the colloidal suspension of sample **4** at various relative concentrations. Inset shows the absorbance at 270 nm as a function of the colloid content.

band centered at *ca*. 250 nm that can be ascribed to the charge transfer from the hydroxide bridge to the Fe^{3+} ions ($^6A_1 \rightarrow {}^4T_1(P)$),[146] thus confirming the presence of iron in the layers. These bands can be fitted to a linear regime according to the Beer-Lambert law (inset in **Figure 10**) confirming that the suspensions contain a monodisperse distribution of nanosheets.[62]

Figure 11 shows a selection of high-resolution transmission electron micrographs (HRTEM) of the 2D nanosheets obtained by dropping a freshly prepared dispersion of **4–6** on a carbon-coated copper grid. The exfoliated nanosheets show hexagonal morphologies with weak homogeneous contrast, as expected from their nanometric thickness, and lateral sizes coincident with those extracted from DLS studies. The selected area electron diffraction (SAED) patterns display a hexagonal arrangement of diffraction spots consistent with the in-plane symmetry intrinsic to LDH layers. Indexation of the SAED pattern under a hexagonal closed packed structure (hcp) yielded a = 2.9 Å, in good agreement with the values estimated from the indexation of the powder diffraction patterns of the bulk samples (*ca.* 3.08 Å, for **1–3**). This confirms that the nanosheets are chemically resilient and can stand the anion-

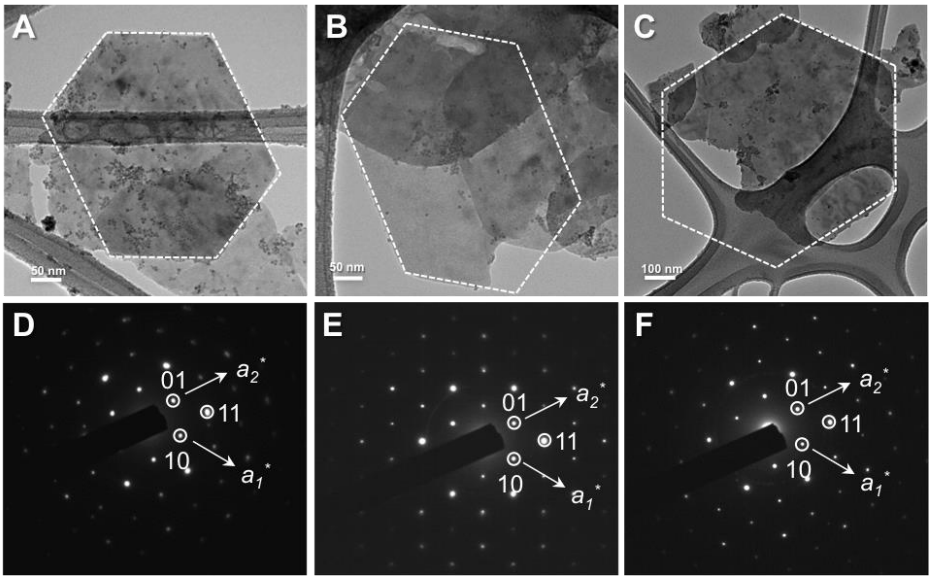

Figure 11. (A–C) HRTEM images of the exfoliated nanosheets in the 0.20–0.33 compositional range showing their hexagonal morphology. (D–F). SAED exhibiting a hexagonal arrangement of the diffraction peaks, as expected from the intrinsic symmetry of the LDH layers.

exchange/exfoliation reactions, whilst maintaining their internal atomic structure.[49,138,144]

Figure 12 displays an atomic force microscopy (AFM) image collected by dip coating a clean Si wafer in a fresh emulsion of **5.** The image covers a 6 x 6 μm area (**Figure12A**) and shows the presence of nanosheets with lateral sizes coincident once again with the DLS experiments. In some cases, the presence of regular shapes with internal angles close to 120º, reminiscent of the hexagonal morphologies of the non-exfoliated material, can be observed. The thickness of these nanosheets was studied with more detail in several areas. According to **Figure12B**, we observe the presence of an average height profile of 0.8 nm corresponding to the thickness of a single unilamellar nanosheet. The deviation with respect to the crystallographic thickness of a single brucite layer (0.48 nm), has been already observed in several AFM studies of exfoliated layered hydroxides and is generally attributed to the physical adsorption of solvent molecules and residual counterions present in the medium.[49,136,147–149]

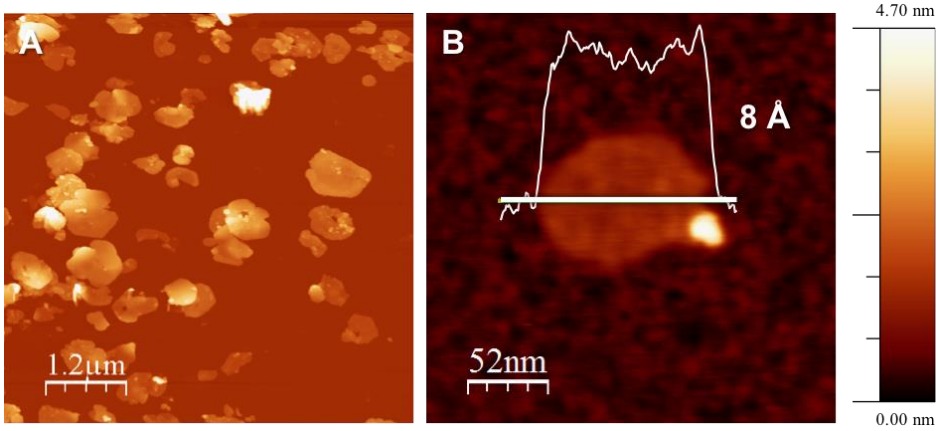

Figure 12. (A) Tapping-mode AFM image of the exfoliated NiFe–LDH nanosheets deposited on a silicon wafer substrate by drop casting. (B) Height profile concordant with that expected for a single layer.

In order to improve the deposition and measure larger atomically thin nanosheets, we have explored a different methodology. **Figure 13** shows an AFM image collected by spin coating a dispersion of **6** in formamide on a clean Si wafer. The image confirms the presence of a single nanosheet with an average height profile of 0.75 nm. This value is also in excellent agreement with previous reports.[147]

2.2.5. Restacking

Finally, to demonstrate the ability of these single layers to act as macromolecular cations, RNiFe–CO_3 (**7**; where R accounts for restacked) was obtained by adding an excess of Na_2CO_3 to the exfoliated NiFe–LDH nanosheets of ideal composition 3:1 (x = 0.25). The presence of intense electrostatic interactions between the positively charged layers and the anionic moieties mediates the re-assembling of the original layered structure having CO_3^{2-} anions in the interlamellar space as confirmed by FT-IR analysis showing the characteristic C–O stretching at around 1360 cm^{-1}. On basis of the X-ray diffraction data (**Figure 14**), the restacked material exhibits the typical pattern for LDHs, with the same unit cell parameters and *BS* exhibited by **2** (a=3.08, c=23.34 and *BS*=7.78±0.03). Besides, the barely broader profile and

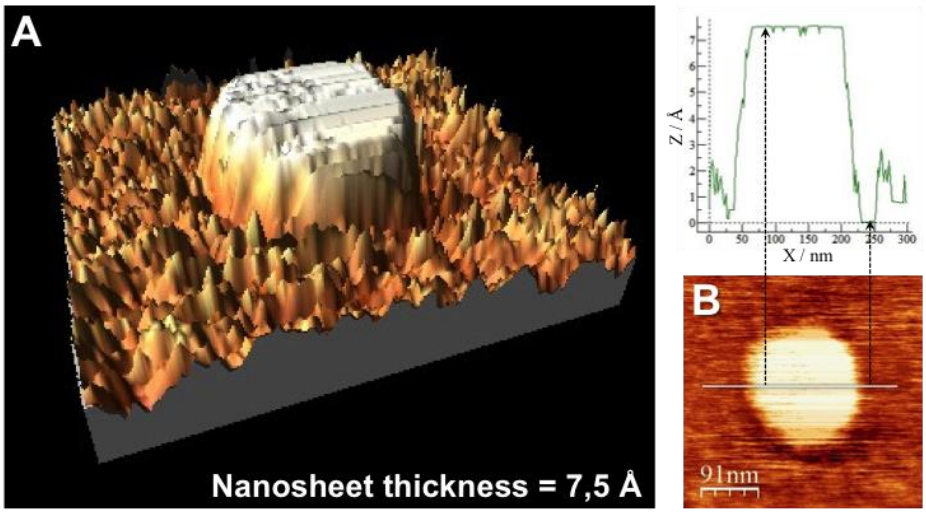

Figure 13. (A) 3D Tapping-mode AFM image (1 x 1 μm area) of an exfoliated NiFe–LDH nanosheet deposited by spin-coating on a silicon wafer. (B) Height profile, which is in agreement with that expected for a single layer, *i.e.* 0.75 nm.

less intense reflections observed denote a crystallinity quite similar to the original material (**2**). The observed decrease of the crystallinity must be probably related to the presence of a bigger amount of stacking faults and overall disorder intrinsic to the exfoliation/restacking route. Additionally, a minor impurity related to the presence of a Ni, Fe spinel-like oxide was detected. This fact is not surprising and similar features have been previously observed in the synthesis of related NiFe LDHs through co-precipitation.[150] Note that the presence of this impurity could have a significant impact on the magnetic properties as will be depicted in the following Chapters.[151] Nevertheless, the chemical nature of the LDH layers remains mainly unaffected, as confirmed by the constant metallic composition, TG/DTA and FE-SEM characterization.

2.1. Conclusions

In summary, we have successfully overcome the synthetic problems inherent to the preparation of non-Al^{3+}-containing LDHs by following an slightly-modified homogeneous precipitation method which employs TEA as auxiliary

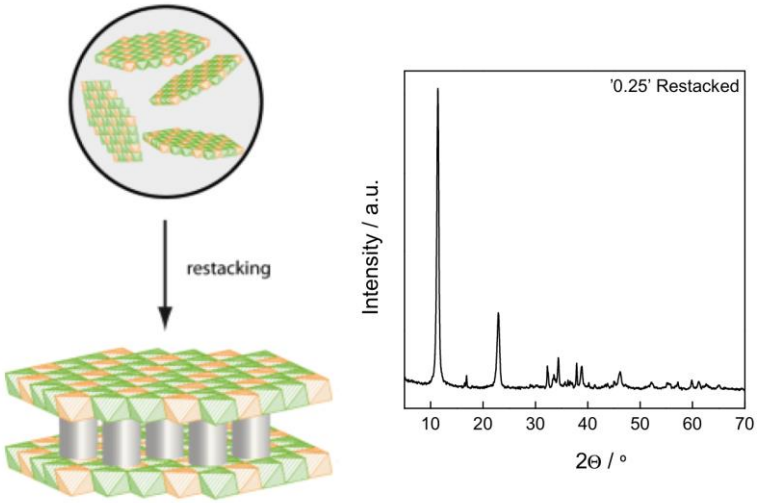

Figure 14. (left) Graphical scheme showing the structural model for the restacking process. (right) X-ray powder diffraction pattern of the restacked sample **7**.

reagent. This procedure permits obtaining a family of NiFe–LDHs with variable Ni^{2+}:Fe^{3+} in-plane composition: $[Ni_{1-x}Fe_x(OH)_2](CO_3)_{x/2}\cdot yH_2O$; x = 0.20 (**1**), 0.25 (**2**), and 0.33 (**3**). Notwithstanding the synthetic limitations inherent to replacement of Al^{3+} in the chemistry of LDHs, the use of our method enables the formation of highly crystalline, micrometric crystals with hexagonal morphologies for the compositional interval studied.

This homogeneity has been also confirmed at a nanometric scale, after exfoliation of these layered hosts into their constituting unilamellar nanosheets by sonomechanical treatment of the solids in polar solvents, by the complementary use of DLS, UV-Vis, HRTEM and AFM. Our study confirms that the exfoliated single-layers display equivalent features than their bulk counterparts and the exfoliation does not impose chemical damage or structural variations to the cationic LDH layers.

Finally, we have validated the suitability of these nanosheets as cationic macromolecular building blocks by re-assembling the carbonate-intercalated LDH in the presence of an excess of anions.

In view of the magnetic functionality exhibited by NiFe–LDHs,[122] this work must be considered as the first step in the development of advanced multifunctional materials, which will result from the combination of the physical properties intrinsic to these cationic 2D nanosheets with those introduced by electronically active anionic discrete complexes,[152] or even more complex extended layers. As a matter of fact, attention has already been drawn on these materials as illustrated by similar works recently reported.[153,154]

2.2. Experimental Section

2.2.1. Synthesis

All Chemicals $Ni(NO_3)_2{\cdot}6H_2O$, $Fe(NO_3)_3{\cdot}9H_2O$, $NaNO_3$, HNO_3, $C_6H_{15}NO_3$ (triethanolamine, TEA) and $CO(NH_2)_2$ (urea) were used as received from commercial suppliers (Sigma-Aldrich and Fluka) without further purification. LDHs were synthesized following a modified homogeneous precipitation method by using urea and TEA as ammonium releasing reagent (ARR) and chelating agent, respectively. In a typical synthesis of NiFe–CO_3 LDH, the nitrate salts of the metals were dissolved in 50 mL of Milli-Q purged water together with TEA, in order to reach a total metal cation concentration of 20 mM in the final solution, varying the stoichiometric coefficient x = Fe/(Ni + Fe) from x = 0.20 to x = 0.33. The concentration of TEA was varied in the 0.25–15 mM range. Then, 50 mL of an aqueous solution of urea (35 mM) were added. The amount of urea was fixed to be 1.75 times the total metal concentration. The resulting dark brown mixture was placed in a 125 mL stainless steel Teflon lined autoclave and heated in an oven. In order to study the effect of the temperature of the hydrothermal step in the crystallinity of the final material the temperature of the oven was ranged from 125 to 165 °C. After 48 hours, the autoclave was cooled on a bench to room temperature and the resulting yellowish fine powder was filtered, washed thoroughly with Milli-Q water and dried in a vacuum. The pH value of the remaining solution was found to be around 7.5–8.0.

2.2.2. Anion Exchange

Nitrate-exchange was carried in an excess of nitrate anions. In a typical procedure, 1 g of NiFe–CO_3 LDH was immersed in a round-bottom flask

containing 1 L of an aqueous solution of $NaNO_3$ (1.5 M) and HNO_3 (0.005 M). This mixture was mechanically stirred under inert atmosphere during 48 h. Afterwards, the resulting yellowish product was filtered, washed thoroughly with Milli-Q water and dried in vacuum at room temperature.

2.2.3. Exfoliation

NiFe–NO_3 was finely powdered and dispersed in degassed formamide at a concentration of 1 $g{\cdot}L^{-1}$ under inert atmosphere. Then, the mixture was vigorously stirred at 600 rpm for three days. To facilitate the exfoliation, the dispersion was successively sonicated in an ultrasonic water bath (Branson 5510) during three intervals of 20 min periodically during the three days, until the turbidity of the dispersion remained constant. Finally, the yellowish translucent colloidal suspension was centrifuged at 2000 rpm for 10 min to remove the remaining non-exfoliated material. The resulting emulsion clearly exhibited the Tyndall effect when irradiated with a laser beam and was also studied with UV-Vis to confirm the presence of exfoliated LDH layers.

2.2.4. Restacking

Restacked NiFe–CO_3 LDH (R-NiFe–CO_3; **7**): This sample was isolated by adding an aqueous solution of Na_2CO_3 (250 mL, 1 M) to 250 mL of a freshly prepared suspension of exfoliated layers of **5** in formamide. The mixture was mechanically stirred; with immediate appearance of the yellowish precipitate. Mechanical stirring was maintained for 5 additional minutes and finally the suspension was kept static, without stirring during 12 h, until no sign of turbidity was detected. Afterwards, the resulting finely divided powder was filtered, washed thoroughly with deionized water and dried in vacuum at room temperature.

2.2.5. Physical Characterization

Metallic atomic composition of bulk samples was determined by means of electron probe microanalysis (EPMA) performed in a Philips SEM-XL30 equipped with an EDAX microprobe. Carbon, nitrogen and hydrogen contents were determined by microanalytical procedures by using a LECO CHNS-932 in the Universidad Complutense de Madrid. X-ray powder diffraction patterns were collected with a Siemens d-500 X-ray diffractometer (Cu-Kα radiation; λ_α

= 1.5418 Å) equipped with a rotating anode D-max Rigaku operating at 80 mA and 45 kV. Samples were mounted on a flat sample plate with grease. Profiles were collected in the 2.5° < 2θ < 70° range with a step size of 0.05° over a 2.16 h period. All patterns have been indexed, unit cells searched with TREOR and refined with the routines implemented in X'Pert HighScore Plus. Particles morphologies and dimensions were studied with a Hitachi S-4800 field emission scanning electron microscope at an accelerating voltage of 20 kV and without metallization of the samples. Infrared spectra were recorded in a FT-IR Nicolet 5700 spectrometer in the 4000–400 cm^{-1} range using powdered samples diluted in KBr pellets. These pellets were prepared just before using, in order to avoid interference due to anion exchange. UV-Vis absorption spectra were recorded using an Agilent 8453 spectrometer in the range from 190 to 900 nm. Thermogravimetric analysis of all compounds were carried out with a Mettler Toledo TGA/SDTA 851 apparatus in the 25–800 °C temperature range under a 10 $°C \cdot min^{-1}$ scan rate and an air flow of 30 $mL \cdot min^{-1}$. DLS measurements were carried out at 25 °C with a Zetasizer Nano ZS instrument (Malvern Instruments Ltd.) on a freshly prepared solution of exfoliated LDH in formamide (1 $g \cdot L^{-1}$). Mean hydrodynamic diameter and correlation functions were determined by accumulative analysis. HRTEM studies of exfoliated nanosheets were carried out on a JEM-2010 microscope (JEOL, Japan) operating at 200 kV. Samples were prepared by dropping a suspension of the fresh exfoliated sample in formamide on a carbon-coated copper grid. The digital analysis of the HRTEM micrographs was done using DigitalMicrographTM 1.80.70 for GMS 1.8.0 by Gatan. AFM measurements were collected in a Multimode atomic force microscope from Veeco. Typically, a fresh diluted emulsion resulting from the exfoliation of NiFe–NO_3 samples in formamide was deposited onto a clean Si wafer by dip coating or spin coating at 5000 rpm, depending on the sample. The images were obtained with a Si tip (*fr* and *K* of ca. 300 kHz and 42 $N \cdot m^{-1}$, respectively) using tapping-mode in air at room temperature. Images were recorded with 512×512 pixel and 0.5–1.0 Hz scan rate. Processing and analysis of the images were carried out using the Nanotec WSXM software.[155]

3. Interplay Between Chemical Composition and Cation Ordering in the Magnetism of NiFe–LDHs[†]

In this chapter we have described the magnetic properties of the family of ferrimagnetic NiFe–LDHs with variable Ni^{2+}:Fe^{3+} in-plane composition: $[Ni_{1-x}Fe_x(OH)_2](CO_3)_{x/2}\cdot yH_2O$ (x = 0.20, 0.25 and 0.33) synthesized in the previous Chapter. Our magnetic study reflects that the iron content in the LDH layers controls the overall magnetism of these lamellae. Hence, the gradual replacement of Ni^{2+} with Fe^{3+} centers introduces a larger amount of antiferromagnetically coupled Fe–OH–Fe pairs across the layers, provoking that the compound with the highest Fe:Ni ratio displays spontaneous magnetization at higher temperatures (T_{irr} =15.1 K) and the hardest coercive field (3.6 kG). Mössbauer spectroscopy confirms that the cation distribution in the layers is not random and reflects the occurrence of Fe clustering due to the higher affinity of Fe^{3+} ions to accommodate other homometallic centers in their surroundings. These results clarifiy the origin of the glassy-behavior, also reported for other magnetic LDHs, and points out spin frustration as the most likely cause.

[†] Abellán, G.; Coronado, E.; Martí-Gastaldo, C.; Waerenborgh, J.; Ribera, A. *Inorg. Chem.* **2013**, *52*, 10147. This work has been carried out in collaboration with Dr. J. Waerenborgh at the IST/INT, Instituto Superior Técnico, Universidade Técnica de Lisboa, CFMC-UL, Sacavém (Portugal)

3.1. Introduction

The studies describing the magnetism of LDHs are relatively scarce.[156–160] The overall magnetism of these lamellae can be modulated by the interlayer distance and the in-plane chemical composition of the layers, as demonstrated for two families of LDHs prepared by the traditional co-precipitation method: $Ni^{II}Fe^{III}$ and $Ni^{II}Cr^{III}$, respectively.[122,123] More recently, O'Hare et al. have described the effect of the particle size and the magnetism for nanosized CoAl–LDHs synthesized by the reverse micelle method.[161] Although these works provide valuable information about the magnetism of these hosts, the true nature of the glassy-behaviour that is commonly observed at low-temperatures is yet to be properly explained. The most likely explanation for this phenomenon relies on the random distribution of metal cations across the layers. In the $Ni^{II}Fe^{III}$ case for instance, this would combine ferromagnetic Ni–OH–Fe interactions with a residual fraction of antiferromagnetically coupled Fe–OH–Fe pairs to generate spin frustration. However, the ordered or disordered nature of the specific arrangement of cations in these hydroxide-bridged layers remains still an open debate. Whereas the internal order of Mg^{2+}/Al^{3+} cations in a 2:1 ratio was initially confirmed for MgAl–LDHs with sophisticated multinuclear NMR spectroscopic studies,[30,32] Cadars et al. have recently demonstrated that the occurrence of Al–OH–Al linkages cannot be discarded in these solids as the distribution of cations slightly deviates from perfect order and displays detectable amounts of Al clustering, as confirmed with solid-state NMR and first-principle calculations.[31]

Complementary to these works centered on diamagnetic hosts, the study of magnetic LDHs by introducing Fe^{3+} ions to the layers deserves to be explored as it can provide further information on the statistical distribution of metal cations across the layers in a family of NiFe–LDHs with variable Ni:Fe ratios. Notwithstanding the synthetic limitations associated to the substitution of Al^{3+} with other trivalent metals, the use of chelating reagents described in the previous chapter has opened the way to the synthesis of NiFe–LDHs with tuneable composition. Thus, $[Ni_{1-x}Fe_x(OH)_2](CO_3)_{x/2}{\cdot}yH_2O$ with x = 0.20 (**1**), 0.25 (**2**), and 0.33 (**3**); have been isolated and magnetically studied. These solids

share carbonate as the anion occupying the interlamellar space and display equivalent separation between the magnetic NiFe layers in the layered architectures, therefore providing an ideal platform for correlating magnetic behaviour and chemical composition. By using Mössbauer spectroscopy, we have extracted direct information on the distribution of the cations across the layers.

3.2. Results and Discussion

3.2.1. Magnetic Properties

As previously pointed out, it is worthwhile introduce some general aspects of the parameters controlling the magnetism in LDHs. Their overall magnetism is controlled by two main contributions: (i) the intralayer magnetic superexchange between metal centers through the –OH bridges across the cationic sheets, and (ii) the less intense dipolar interactions operating through the space between the magnetic layers.

As the interlayer distance is constant for the samples studied (see Chapter 1), the change in the magnetic dipolar interactions in the investigated compositional range can be considered small. Hence, the differences in the magnetic behaviour can be correlated with variations in the chemical composition. If we assume that the metal cations are statistically distributed across the layers with a ratio imposed by the molecular formula (see Mössbauer data below), then for a NiFe–LDH with a 2:1 metal ratio ($x = 0.33$), each Fe^{3+} ion will be, statistically, surrounded by six Ni^{2+} ions (Ni–OH–Fe pairs), whereas each Ni^{2+} atom will be neighboured by three Fe^{3+} and three Ni^{2+} ions (Ni–OH–Ni and Ni–OH–Fe pairs).[122] Given that the nature of the magnetic superexchange mediated by the –OH bridge changes from ferromagnetic (F) for the coupling between Ni^{2+} centers to antiferromagnetic (AF) when Fe^{3+} cations are involved, variations of the Ni/Fe ratios are expected to cause a change in the relative number of F and AF pairs across the layers, therefore, modifying the overall intralayer structure. The magnetic measurements of the nanocomposite materials were performed by using *dc* and *ac* modes on the SQUID magnetometer working in the temperature range between 1.8 and 300 K to understand the magnetic behaviour of the as-synthesized samples.

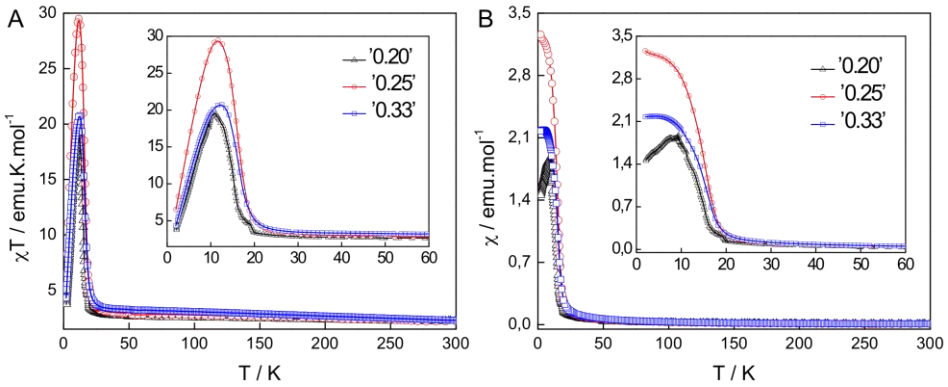

Figure 1. (A) Temperature dependence of the $\chi_M T$ product for **1** (black), **2** (red), and **3** (blue). (B) Represents the χ_M *vs* T plot. The inset shows the low-temperature regime.

The thermal variation of the product of the molar magnetic susceptibility times the temperature ($\chi_M T$ *vs.* T plot) of **1–3** shows a similar profile (**Figure 1A**). $\chi_M T$ remains almost constant upon cooling, down to 50 K, where the signal starts increasing smoothly. From 20 K, this increase becomes more abrupt and defines a maximum for each compound between 5 and 20 K. These maxima correspond to steep jumps in the χ_M signals, suggesting the appearance of a long-range magnetic correlation between the spins at low temperatures. (See **Figure 1B**)

These data were fitted to the Curie–Weiss law in the high temperature regime (150–300 K; see **Figure 2**), yielding positive Θ values (17.69, 22.57 and 29.11 K) and Curie constants (C) of 2.15, 2.20 and 2.56 emu·K·mol^{-1} for **1**, **2** and **3** respectively (see **Table 1**). Θ shows a gradual increase with the iron content, which likely reflects a higher ferromagnetic contribution to the overall magnetism of these lamellae. C values also increase with the Fe concentration, and they are consistent with those expected for a magnetically diluted combination of noninteracting Ni^{2+} and Fe^{3+} ions with the ratios fixed by the molecular formulas.

Figure 3 displays the field dependence of the initial magnetization of **1–3** at 2 K. They exhibit a sharp increase in the magnetization at very low fields followed by a continuous increase up to 5 T, reaching values of 0.90, 1.01 and

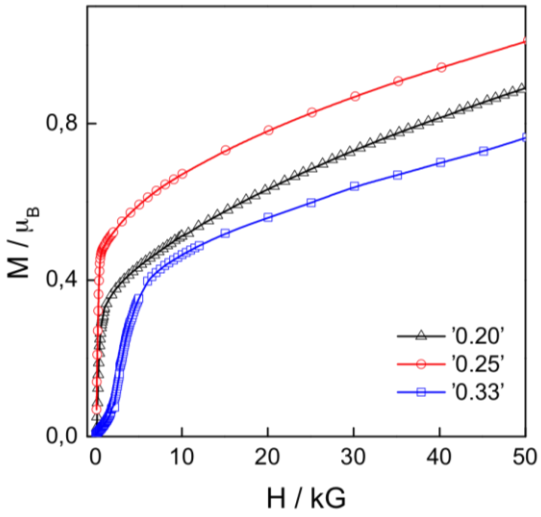

Figure 2. *M*(H) at 2 K for **1** (black), **2** (red), and **3** (blue).

Table 1. Magnetic parameters for 1–3.[a]

Sample	C_{so} (emu·K·mol^{-1})	C (emu·K·mol^{-1})	Θ (K)	M_S[b] (μ_B)	H_{Coer} (kG)	T_M (K)	T_{irr} (K)
1	1.64	2.15	17.69	0.90	<1	16.5	11.7
2	2.05	2.20	22.57	1.01	<1	16.7	15.0
3	3.81	2.56	29.11	0.76	3.6	16.8	15.1

[a] Expected spin-only value of the Curie constant [C_{so}, (emu·K·mol^{-1})], experimental Curie constant [*C*, (emu·K·mol^{-1})], Weiss constant [Θ, (K)], saturation magnetization [M_S, (μ_B)], coercive field at 2 K [H_{Coer}, (K)], temperature for the onset of spontaneous magnetization extracted from χ'' plots [T_M, (K)], and temperature of the divergence of the ZFC and FC magnetic susceptibility [T_{irr}, (K)]. $S(Fe^{3+}) = 5/2$, $S(Ni^{2+}) = 1$. [b] *Ms* measured at 50 kG.

0.76 μ_B, for **1**, **2** and **3**, respectively, that are far from saturation, as expected for ferrimagnetic systems. It is worthwhile outlining that *M*(*H*) of **3**, with the highest iron content of the series, displays a sigmoidal shape at low fields, as a result of the increasing AF interactions introduced by the replacement of Ni^{2+} with Fe^{3+}, which might be indicative of metamagnetic behaviour. For a better

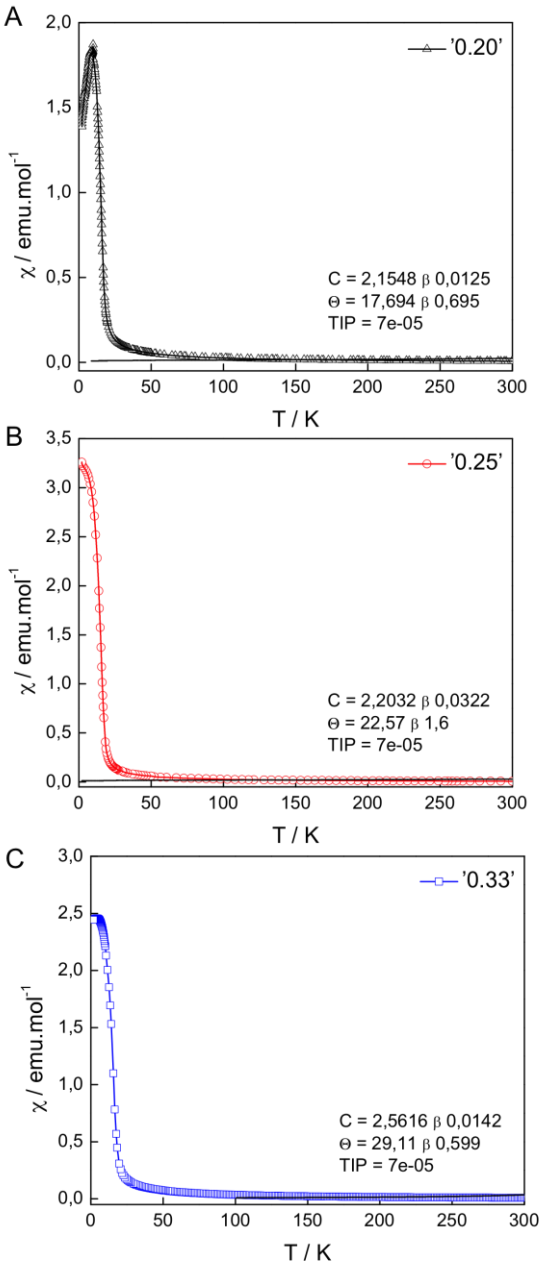

Figure 3. χ_M *vs* T plots between 2 and 300 K for **1** (black), **2** (red) and **3** (blue). The solid lines represent the best fit to the Curie-Weiss law above 150 K including a TIP.

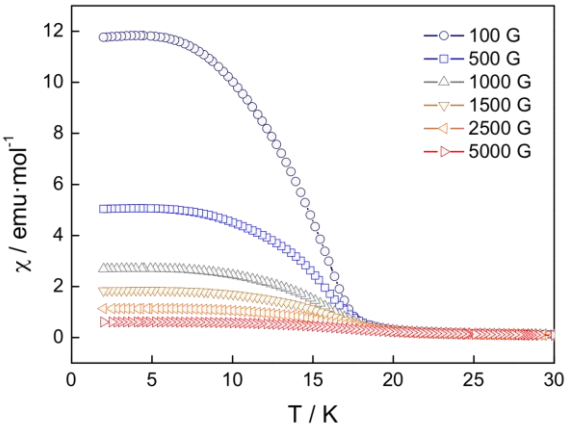

Figure 4. Thermal variation of the magnetic susceptibility of **3** for different applied magnetic fields.

understanding, we measured the field dependence of χ *vs* T between 100 and 5000 G (see **Figure 4**). Our results discard the presence of a maximum that could be correlated with a field-induced switching of the low-temperature antiferromagnetic state into ferromagnetic, thus ruling out metamagnetism.[162]

Hysteresis loops were recorded for all compounds (**Figure 5**), confirming the occurrence of spontaneous magnetization at low temperatures. The observed coercive fields (H_{Coer}) of **1** and **2** remain below 1 kG and can be, therefore, classified as soft magnets, whereas **3** is a harder magnet with a H_{Coer} of 3,6 kG (see **Table 1**).

FC/ZFC measurements permitted extracting the irreversibility temperature values (T_{irr}) for which the onset of spontaneous magnetization is observed in these systems (see **Figure 6**).[161] As expected from the increasing number of stronger AF interactions, higher iron content triggers an increase of the T_{irr} values from 11.7 K for **1** to 15.1 K for **2** and **3**. Notice that in **1**, the divergence between the FC and the ZFC curves is rather small, preventing an accurate estimation of T_{irr}.

Spontaneous magnetization at low temperatures was further confirmed with *ac* dynamic susceptibility measurements in the presence of an external field of 3.95 G, oscillating at different frequencies in the 1–10000 Hz interval.

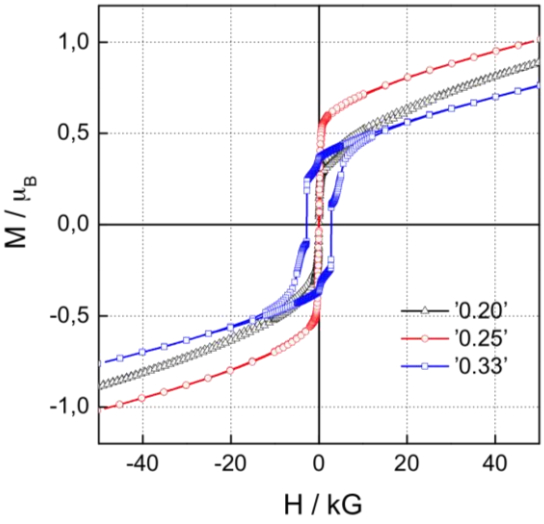

Figure 5. Hysteresis loops at 2 K for **1** (red line), **2** (black line) and **3** (blue line).

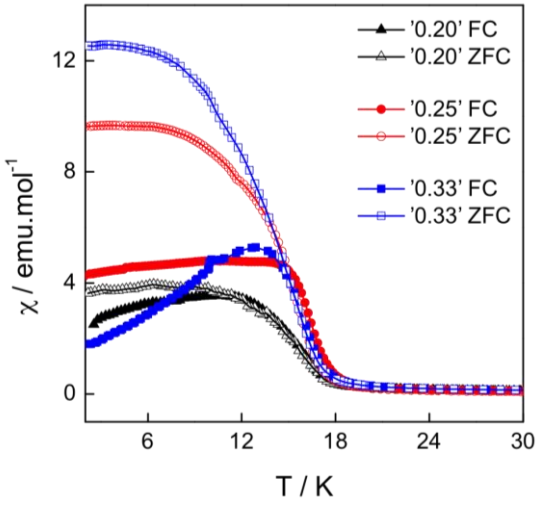

Figure 6. FC/ZFC measurements for **1** (red), **2** (black) and **3** (blue).

Both the in-phase, χ'_M (dispersive) and the out-of-phase, χ''_M (adsorptive) signals define a peak at low temperatures. The temperature for the onset of spontaneous magnetization (T_M), defined as the temperature where χ''_M

becomes nonzero, falls in the 16–17 K interval for all the solids. Note that the strong frequency dependence exhibited by the *ac* susceptibility signals hampered an accurate estimate of the T_M values (**Figure 7**). Below T_M, the χ''_M signals increase very rapidly upon cooling with a negative slope, which is frequency-independent, until reaching a maximum, whose position exhibits a small frequency-dependence.

Equivalent frequency dependence has already been observed in other families of magnetic LDH materials and generally attributed to the presence of spin-glass behaviour[122,123,161,164–166] (*i.e.* a frozen glass of spins due to competing magnetic interactions and some disorder in the moments distribution and the interactions between them[163]). Calculation of the frequency shift parameters (ϕ), defined by Mydosh as:

$$\Phi = \Delta T_{max} / [T_{max} \Delta(\log \nu)] \qquad \text{eq. [1]}$$

where T_{max} is the freezing temperature and υ is the angular frequency, gives 0.025, 0.024, and 0.021 for **1**, **2**, and **3**, respectively. These values are close to those typically observed for canonical spin glasses (0.005–0.018)[163] and in good agreement with previous LDH studies.[122,123,161,164,166]

Two relevant characteristics of the spin-glass dynamics are:
(i) a continuous closely logarithmic time relaxation and (ii) the appearance of aging phenomena at low temperature. Glassiness in these magnetic systems could arise from different origins. On the one hand, their low dimensionality can introduce some structural disorder. On the other hand, the random distribution of spins in the network causes magnetic disorder and also promotes competing interactions. Although the proposed spin-glass behaviour is corroborated by the experimental values of the Mydosh parameter for all samples, for the sake of the argument we have also validated this by fitting the magnetic relaxation of **3** (the sample with the highest Fe content) to an Arrhenius law and a 3D critical scaling law.

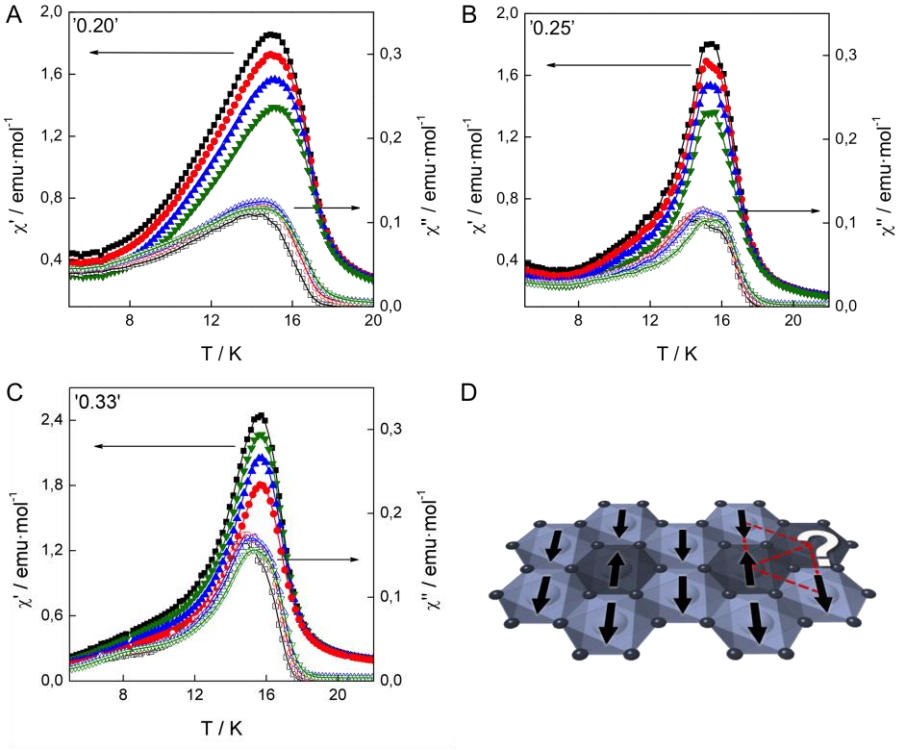

Figure 7. Measurements of ac susceptibility. Solid lines represent in-phase signals, and open symbols represent out-of-phase signals at 10, 100, 1000, and 10000 Hz (black, red, blue, and green data points, respectively, (A–C correspond to samples **1**, **2**, and **3**, respectively). (D) Schematic representation of the occurrence of spin frustration in the studied compounds.

The fitting of χ''_M frequency dependence to a thermally activated process, described by the Arrhenius law:

$$\nu = \nu_0 \cdot \exp(-E_a/kT) \qquad \text{eq. [2]}$$

yields a meaningless physical value for the energy barrier (Δ/k_B = 1381 K), as can be observed in **Figure 8A**.

We have also fitted the frequency dependence to the conventional critical scaling law that accounts for spin dynamics.

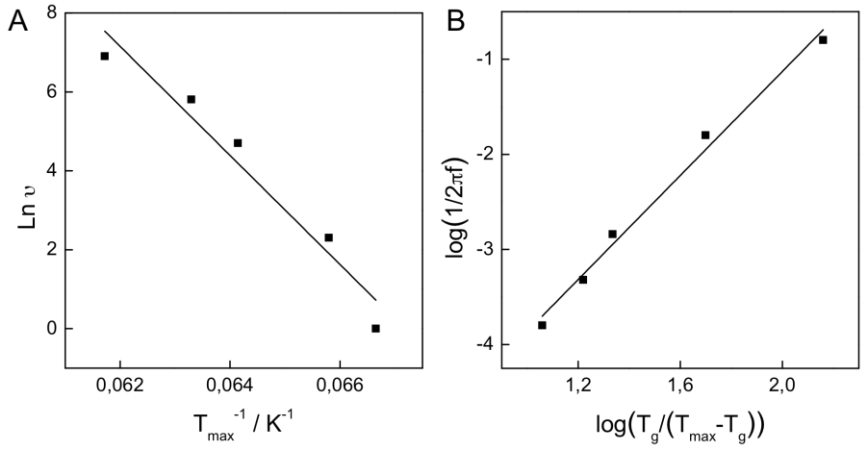

Figure 8. (A) Arrhenius plot of the peak in the χ''_M signal for sample **3**. (B) Frequency dependence of χ''_M fitted with the critical scaling law model of the spin dynamics as described by $\tau = \tau_0[T_g/(T_g/T_{max} - T_g)]^{zv}$ for sample **3**.

This is described by equation 3:

$$\tau = \tau_0[T_g/(T_g/T_{max} - T_g)]^{zv} \qquad \text{eq. [3]}$$

where T_g is the critical temperature for a spin glass phase and zv is a critical exponent (**Figure 8B**). In 3D spin glasses the relaxation time diverges at finite temperature ($T_g \neq 0$K). The best fit gives T_g = 14.9 K, τ_0 = 2.55 x 10^{-7} s, and zv = 2.7, the obtained zv value is out of the range (from 4 to 12) for canonical spin glasses, while the τ_0 value falls in the expected range of 10^{-7}–10^{-12} s, thus confirming the proposed spin glass-like behaviour for these LDHs. Our results corroborates spin glass-like behaviour as previously confirmed by Layrac et al. for magnetic LDHs intercalated with cyano-bridged coordination polymers.[166] This shows that the observed magnetic behaviour for NiFe–LDHs have to be attributed to a glasslike transition more than to the long-range magnetic ordering, or to the sum of independent single particle blocking-unblocking processes perturbed by interparticle interactions.

The origin of glassiness in this sort of compound is generally ascribed to the coexistence of competing magnetic interactions in the solid. This scenario

would result from significant disorder in the distribution of the cations in the layers, thus introducing partial substitution in some of the positions occupied by Ni^{2+} with Fe^{3+} to generate Ni–OH–Fe pairs. This would be more likely for LDHs with increasing iron content. By assuming that only the nearest-neighbour magnetic interactions are significant, this substitution would introduce spin frustration to the magnetic layers because of the concurrence of F and AF interactions. This is illustrated in the **Figure 7D**, which shows how this substitution generates spin frustration because the electronic spin of Ni^{2+} atom is required to be at the same time F and AF to satisfy the coupling with the adjacent Ni^{2+} and Fe^{3+} spins. To confirm the occurrence of Fe clustering as the origin of the glassy behaviour in our materials, we next carried out ^{57}Fe Mössbauer spectroscopy studies to provide definitive information on the local environment of the iron centers.

3.2.2. Mössbauer Spectroscopy

The Mössbauer spectra of **1**–**3** show paramagnetic behaviour at room temperature. At 4 K, the spectra reflect a slowing down of the relaxation of the Fe magnetic moments direction, below the corresponding Larmor precession rate of the ^{57}Fe nuclei, indicating the presence of strong magnetic correlations in the solids, in agreement with magnetization data.

The spectra of **1** and **2** at 4 K are similar (**Figure 9A**). They can be fitted with three magnetic sextets, and the estimated parameters are the same within experimental error for both samples (**Table 2**). Isomer shifts (IS) relative to metallic α-Fe at 295 K and magnetic hyperfine fields (B_{hf}) are typical of high-spin Fe^{III} (S=5/2) octahedrally coordinated by oxygen anions. The spectrum of **3** at 4 K (**Figure 9A**) may also be fitted with three sextets with IS and B_{hf} similar to those estimated for **1** and **2**, but with quite distinct quadrupole shifts, ε.

This constitutes an initial indication that different nearest-neighbour cation shells are present. In fact, three scenarios are possible: (i) all the Fe^{3+} cations are only surrounded by Ni^{2+} atoms; (ii) there is a random distribution of Ni^{2+} and Fe^{3+}; (iii) the distribution of Ni^{2+} and Fe^{3+} is not ordered, but there is a tendency for Fe^{3+} clustering. In the case of (i), only one sextet should be observed in the Mössbauer spectra because all the Fe^{3+} would have identical environments. Differences in the B_{hf} of Fe^{3+} cations located on the same

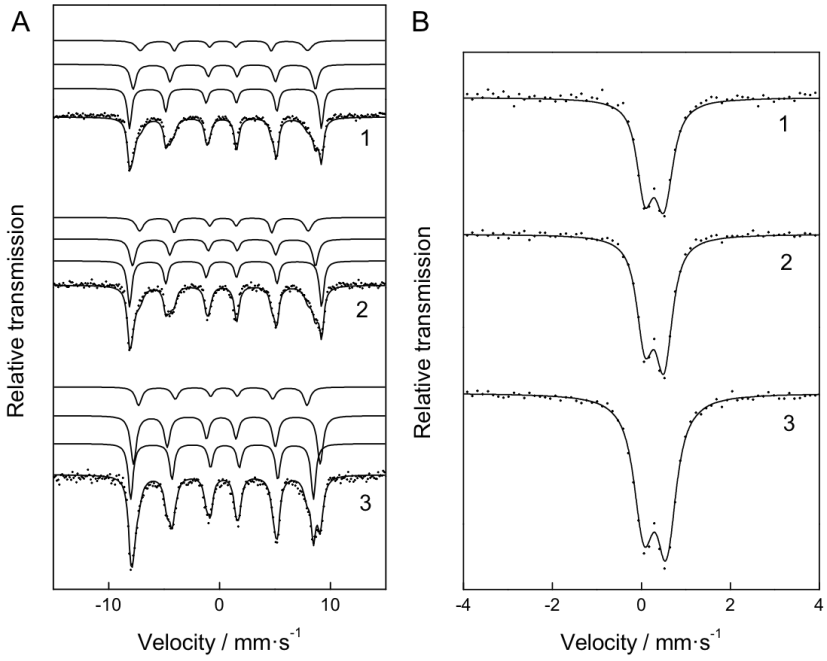

Figure 9. (A) Mössbauer spectra of **1**, **2** and **3**, collected at 4 K. Lines plotted over the experimental points are the sum of two or three magnetic sextets or magnetic hyperfine field distributions. Subspectra are shown shifted for clarity. (B) Room-temperature Mössbauer spectra.

crystallographic site are frequently observed when more than one kind of cation occupies the same nearest-neighbour positions, leading to different local environments for the Fe^{3+} center.[167,168] This seems to be the case for samples **1**, **2** and **3**. Since the AF superexchange interactions mediated by the –OH bridge in the resulting Fe–OH–Fe and Fe–OH–Ni pairs are not identical, different B_{hf} values are expected for Fe^{3+} with a different number of Ni^{2+} nearest-neighbours.

The presence of more than one sextet, thus, neglects scenario (i). Still, it remains to be established whether the distribution of the metal cations in the LDH layers is random according to scenario (ii) or is evidence of a tendency for Fe clustering (scenario (iii)). Assuming a completely random occupation by Ni^{2+} and Fe^{3+} of the cation sites in the hydroxide layers, the probability of

Table 2. Estimated parameters from the Mössbauer spectra of 1, 2, and 3 collected at different temperatures, *T*.[a]

$[Ni^{II}_{0.67}Fe^{III}_{0.33}(OH)_2](CO_3)_{0.165}$ (**3**)					
Compound	***T***	**IS**	**QS, *ε***	***B*$_{hf}$**	***I***
3	295 K	0.36	0.52	–	100%
	4K	0.51	0.50	52.3	42%
		0.46	–0.26	51.1	40%
		0.45	–0.11	47.1	18%
$[Ni^{II}_{0.75}Fe^{III}_{0.25}(OH)_2](CO_3)_{0.125}$ (**2**)					
Compound	***T***	**IS**	**QS, *ε***	***B*$_{hf}$**	***I***
2	295 K	0.36	0.46	–	100%
	4 K	0.46	0.38	53.7	43%
		0.45	0.11	51.2	33%
		0.46	0.09	47.2	24%
$[Ni^{II}_{0.80}Fe^{III}_{0.20}(OH)_2](CO_3)_{0.10}$ (**1**)					
Compound	***T***	**IS**	**QS, *ε***	***B*$_{hf}$**	***I***
1	295 K	0.35	0.45	–	100%
	4 K	0.45	0.38	53.7	42%
		0.46	0.14	51.0	36%
		0.45	0.10	46.8	22%

[a] IS (mm/s) isomer shift relative to metallic α-Fe at 295 K, QS (mm/s) quadrupole splitting, and ε (mm/s) quadrupole shift estimated for quadrupole doublets and magnetic sextets, respectively. B_{hf} (tesla) magnetic hyperfine field and, *I*, relative area. Estimated errors ≤0.02 mm/s for IS and QS, < 0.2 *T* for B_{hf}, and <2% for *I*.

finding *m* Ni^{2+} cations in a shell of six nearest-neighbour sites around Fe^{3+} is given by the binomial distribution function:

$$P(m) = \frac{6!}{m!(6-m)!} y^m (1-y)^{6-m} \qquad \text{eq.[4]}$$

where *y* stands for the fraction of the Ni^{2+} (y = 0.80, 0.75, 0.67 for **1**, **2** and **3**, respectively). Considering all the Fe^{3+} occupy similar sites (octahedrally coordinated by OH^-), there is no reason to expect that they have significantly different recoil-free fractions. In this case, the relative areas (*I*) that are estimated from the analyses of the spectra collected at 4 K should be approximately equal to the fraction of Fe^{3+} cations contributing to the

Table 2. Probability *P*(*m*) of finding Fe^{3+} surrounded by *m* Ni^{2+} nearest-neighbors according to the binomial distribution (eq 4).

Compound	*P*(6)	*P*(5)	*P*(4)	*P*(3)	*P*(2)	*P*(1)	*P*(0)
1	0.262144	0.393216	0.24576	0.08192	0.01536	0.001536	0.000064
2	0.177979	0.355957	0.296631	0.131836	0.032959	0.004395	0.000244
3	0.090458	0.267325	0.329169	0.21617	0.079854	0.015732	0.001291

Table 3. Sextet relative areas expected for a completely random cation distribution. *I*(m) correspond to the sextets arising from Fe^{3+} cations surrounded by *m* Ni^{2+}.

Compound	I(6)	I(5)	I(4)	I(m≤3)	-
1	26%	39%	25%	10%	-
2	18%	36%	30%	16%	-
	I(6)	*I*(5)	*I*(4)	*I*(3)	*I*(*m*≤2)
3	9%	27%	33%	22%	9%

corresponding sextets. Therefore, if the metal cations are randomly distributed, the estimated *I* values should be close to the calculated probabilities *P*(*m*) (**Table 3**). For instance, for compound **1**: *P*(6)=0.262144 implies that the sextet arising from Fe^{3+} surrounded by six Ni^{2+} would have a relative area of *I*(6)~26%, *P*(5)=0.393216 implies *I*(5)~39%, *P*(4)=0.24576 implies *I*(4)~25%, and finally, since sextets with $I < 5\%$ with only slightly different *IS* and B_{hf} are difficult to resolve from the main ones, we might expect that only one more sextet would be clearly observed with an estimated *I*(*m*≤3) approximately equal to the sum of the probabilities for $m = 3, 2, 1$ and 0 (~10%). As commented above, the observed differences in B_{hf} values are likely associated to local differences in the Fe^{3+} surroundings due to nonequivalent Fe–OH–Fe and Fe–OH–Ni superexchange interactions. Hence, B_{hf} values are expected to vary monotonically with the progressive substitution of Ni^{2+} with Fe^{3+} cations, thus explaining why the contribution from the unresolved sextets with $I < 5\%$ can be added to those with higher *I* values and the closest number of Fe^{3+} nearest-neighbours.[167,168] The sets of calculated *I* values for **1–3** that can be correlated with the *P(m)* values described above for **1** are summarized in **Table 4**.

The sets of experimental *I* values (**Table 1**) do not match those calculated for a random distribution of Ni^{2+} and Fe^{3+} (**Table 3**). Furthermore, whilst the

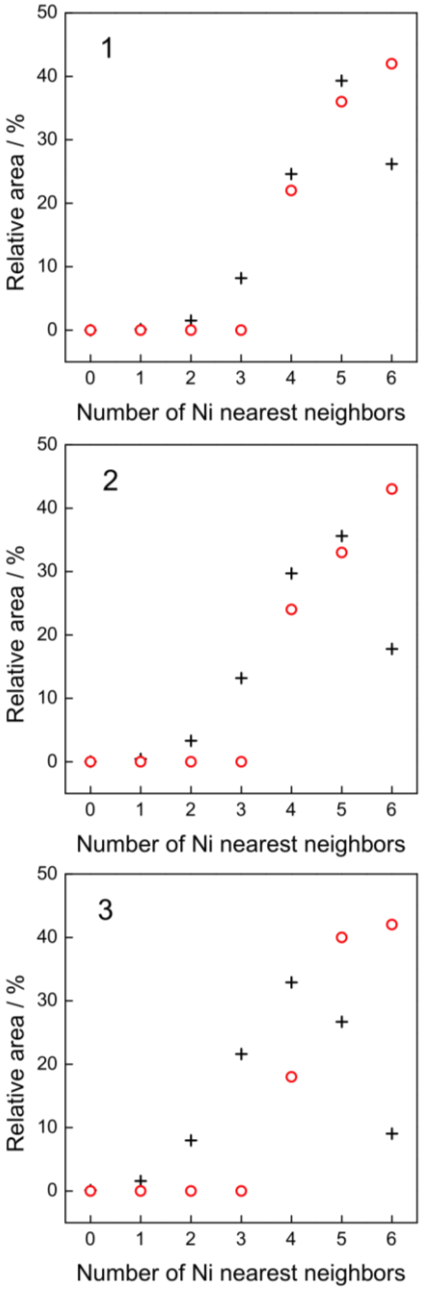

Figure 10. Sextet relative areas expected for a random distribution of Ni^{2+} and Fe^{3+} cations (+) and estimated from the Mössbauer spectra of **1**, **2** and **3** (o).

experimental I values decrease monotonically with B_{hf}, the calculated relative areas for a random distribution of cations display higher I values for intermediate B_{hf} values (**Figure 10**). These differences exclude scenario (ii) indicating that, although not perfectly ordered, the distribution of the metal cations is not completely random either. As referred above, a perfectly ordered structure would give rise to only one sextet in the spectra. Even if a residual partial substitution of Ni^{2+} by Fe^{3+} occurred, the additional sextets introduced to the overall Mössbauer spectra would have very low relative areas, as compared to the main sextet. This is clearly not the case for the present samples. By assuming that the antiferromagnetic Fe–OH–Fe exchange interactions are stronger and will lead to higher B_{hf} values than the Fe–OH–Ni interactions, B_{hf} is expected to increase with the increasing number of Fe^{3+} nearest-neighbours. The fact that the higher B_{hf} values correspond to experimental I values higher than those calculated by the binomial distribution for the completely random cation distribution, suggests that Fe^{3+} has a higher relative preference for Fe^{3+} nearest-neighbours than for Ni^{2+} nearest-neighbours, in line with the experimental results that confirm the occurrence of Al^{3+} clustering in MgAl–LDHs recently reported by Cadars et al.[38] This supports the formation of Fe clusters with the corresponding concurrence of competing F and AF magnetic interactions in the layers, therefore, confirming our previous hypothesis and outlining spin frustration as the most likely cause for the spin-glass behaviour observed in magnetic LDHs at low temperatures.

3.3. Conclusions

By using highly crystalline, micrometric sized and hexagonal NiFe–LDHs with a controlled compositional interval, it is possible to avoid the potential magnetic variations associated to variable particle size or heterogeneous morphologies. Thus, the reported lamellae provide an ideal scenario for correlating the magnetic behaviour of LDHs with chemical composition and cation distribution across the layers, as they share carbonate as the anion occupying the interlamellar space, and they display constant separation between the magnetic NiFe layers in the layered architectures. Magnetic data reflect that **1**–**3** behave as ferrimagnets, as a result of the combined action of F Ni–OH–Ni and AF Ni–OH–Fe and Fe–OH–Fe pairs across the layers and

ferromagnetic dipolar interactions operating between layers. The gradual increase of iron content, by replacement of Ni^{2+} with Fe^{3+} centers, enables the appearance of spontaneous magnetization at higher temperatures as a result of the increasing number of stronger AF interactions across the layers. The introduction of iron also translates into harder magnets with **3**, displaying the highest coercive field of the series.

As previously reported for magnetic LDHs, *ac* dynamic measurements display frequency-dependence that can be associated with spin-glass behaviour. By making use of Mössbauer spectroscopy, we demonstrate that the cations are not randomly distributed across the LDH layers and display increasing Fe clustering, that is, the probability for the appearance of AF Fe–OH–Fe pairs, for higher iron contents. This enables the appearance of spin frustration in the layers and confirms this as the origin for glassines in magnetic LDHs that displays a combination of F and AF pairs.

3.4. Experimental Section

3.4.1. Physical Characterization

Magnetic susceptibility measurements were performed on polycrystalline samples with a Quantum Design (SQUID) magnetometer MPMS-XL-5. The susceptibility data were corrected by removing the diamagnetic contributions as deduced by using Pascal's constant tables. The *dc* data were collected in the range of 2–300 K upon decreasing temperatures with an applied field in the range 100–5000 G, and hysteresis loops were collected between –5 and +5 T at 2 K. Field-cooled (FC) and zero-field-cooled (ZFC) magnetization measurements were performed under 100 Oe applied magnetic field. The *ac* data were collected in the range of 2–25 K with an applied alternating field of 3.95 G at different frequencies in the range 10–10000 Hz with Quantum Design PPMS-9 equipment.

Mössbauer experiments were performed in collaboration with Dr. Joao Waerenborgh at the IST/ITN in Sacavém (Portugal). Mössbauer spectra were collected in transmission mode using a conventional constant-acceleration spectrometer and a 25 mCi ^{57}Co source in a Rh matrix. The velocity scale was calibrated using α-Fe foil. The absorbers were obtained by packing the powdered samples into perspex holders. Isomer shifts are given relative to metallic α-Fe at room temperature. The spectra at 4.1 K were collected using a bath cryostat with the sample immersed in liquid He. The spectra were fitted to Lorentzian lines using a nonlinear least-squares method.[169]

4. Magnetism to Assess Purity in Layered Double Hydroxides: Unveiling the Origin of Magnetic Properties[†]

Some recent reports claiming room temperature spontaneous magnetization in LDHs have been published; however, the reported materials cause serious concern as to whether this cooperative magnetic behaviour comes from extrinsic sources, such as spinel iron oxide nanoparticles. The syntheses of crystalline Fe^{3+}-based LDHs with and without impurities have been developed, highlighting the care that must be taken during the synthetic process in order to avoid the misidentification of magnetic LDHs. Moreover, a general overview about the magnetic behaviour of LDHs has been tackled, paving the way for the final unveiling of their intrinsic magnetism.

[†] a) Abellán, G.; Carrasco, J. A.; Coronado, E. *Inorg. Chem.* **2013**, *52*, 7828. b) Abellán, G.; Carrasco, J. A.; Coronado, E.; Romero, J.; Varela, M. *J. Mater. Chem. C* **2014**, *2*, 3723

4.1. Introduction

Numerous reports claiming ferromagnetic behaviour exceeding room temperature in organic and metal-organic molecular magnets exist. However, for the most part, the source of magnetism is of extrinsic origin. A typical case is that of pure organic materials in which magnetism is often caused by the presence of metals, like iron, or metal oxide impurities.[170–173] The issue of intrinsic *vs.* extrinsic sources of magnetism has also been pointed out more recently in some claims about room-temperature magnetism in metal-organic Ni-TCNE charge transfer salts.[174,175]

In the case of pure inorganic materials, this issue can also be present, although the intrinsic cooperative magnetism arising from the interacting metals often overcomes the extrinsic magnetism coming from impurities. Still, when the intrinsic cooperative magnetism occurs at low temperatures, the presence of magnetic impurities can be dominant at high temperatures, thus leading to wrong claims. An illustrative example in this context is provided by the magnetic LDHs, as we will show in this Chapter.

The seminal works regarding the magnetism of LDHs were reported by Porta and co-workers in 1996.[176,177] In these works —focused on Co-containing LDHs— the magnetic characterization aimed to reveal the coordination environment and the oxidation state of the metallic ions. Prior studies on the magnetism of LDHs were developed by Leroux et al., that loosely investigated the magnetic properties of a $Co_2Fe_yAl_{(1-y)}(OH)_6Cl{\cdot}nH_2O$ family with interlayer spacings between 7.6 and 25 Å.[157] In this work, it was reported that the low-temperature regime and the apparent magnetic ordering were affected by the interlayer separation, without any detailed conclusions. Moreover, Rives et al. have reported short-range antiferromagnetic interactions for CuAl–LDHs at low temperature, leading to a certain magnetic order.[156] Apart from these works, the first thoroughly study about the magnetic properties of LDHs was published in 2002 by our group,[121] paving the way for future research in this field, highlighting the magnetic properties of this sort of materials.

These magnetic properties are inherently designed to be manifested at low temperatures because of the low intensity of the involved exchange interactions. In fact, as a result of the structural features of these layers (MO_6

octahedra sharing edges), the M–O–M superexchange path is always close to orthogonality, leading to weak exchange interactions.[74,125,178] The **Table 1** summarizes the synthesis procedure, main structural characteristics and magnetic behaviours of transition metal LDHs as found from the literature for various interlamellar anions including the materials studied in the present dissertation. In this sense, an exhaustive revision of the reported magnetic LDHs to date reveals that there are no magnetic LDHs with critical temperatures (T_M) exceeding 21 K (see **Table 1**).

Table 1. Summary of the most relevant structural and magnetic parameters of the magnetic LDHs published to date.

Composition	Anion	Synthetic Methodology	Basal Space	Particle Size (nm)	T_M (K)	Ms	Hc	Mydosh	FC/ZFC (K)	Ref.
Co_2Al	Cl^-	co-precipitation	7.6	/	<10(dc)	/	/	/	/	157
$Co_2Al_{0.75}Fe_{0.25}$	Cl^-	co-precipitation	7.7	/	<10(dc)	/	/	/	/	
$Co_2Al_{0.50}Fe_{0.50}$	Cl^-	co-precipitation	7.7	/	<10(dc)	/	/	/	/	
$Co_2Al_{0.25}Fe_{0.75}$	Cl^-	co-precipitation	7.8	/	<10(dc)	/	/	/	/	
Co_2Fe	Cl^-	co-precipitation	7.9	/	<10(dc)	/	/	/	/	
Co_2Al	$C_{12}H_{25}SO_4^-$	co-precipitation	25	/	<10(dc)	/	/	/	/	
$Co_2Al_{0.50}Fe_{0.50}$	$C_{12}H_{25}SO_4^-$	co-precipitation	25	/	<10(dc)	/	/	/	/	
Co_2Fe	$C_{12}H_{25}SO_4^-$	co-precipitation	25	/	<10(dc)	/	/	/	/	
Ni_3Al	CO_3^{2-}	co-precipitation	7.51	*ca.* 15	6	9.5 μ_B	4.2 mT	/	6.0	121
Co_3Al	CO_3^{2-}	co-precipitation	7.59	*ca.* 15	6	9.3 μ_B	5.5 mT	/	5.7	
$Ni_{0.80}Fe_{0.20}$	CO_3^{2-}	hydrothermal (urea+TEA)	7.82	*ca.* 916	16.5	0.90 μ_B	< 1 kG	0.025	11.7	179
$Ni_{0.75}Fe_{0.25}$	CO_3^{2-}	hydrothermal (urea+TEA)	7.78	*ca.* 948	16.7	1.01 μ_B	< 1 kG	0.024	15.0	
$Ni_{0.67}Fe_{0.33}$	CO_3^{2-}	hydrothermal (urea+TEA)	7.81	*ca.* 1767	16.8	0.76 μ_B	3.6 kG	0.021	15.1	
$Ni_{2.43}Cr_{0.57}$	CO_3^{2-}	hydrothermal (HMT)	7.7	*ca.* 20000	19.5	2.52 μ_B	5.4 kG	0.042	/	123
$Ni_{2.30}Cr_{0.69}$	CO_3^{2-}	hydrothermal (HMT)	7.68	*ca.* 20000	19.4	2.09 μ_B	6.6 kG	0.049	/	
$Ni_{2.19}Cr_{0.81}$	CO_3^{2-}	hydrothermal (HMT)	7.68	*ca.* 20000	20.6	1.87 μ_B	11.3 kG	0.010	/	
$Ni_{2.07}Cr_{0.93}$	CO_3^{2-}	hydrothermal (HMT)	7.59	*ca.* 20000	21	1.57 μ_B	2.8 kG	0.006	/	
$Ni_{0.66}Al_{0.34}$	NO_3^-	co-precipitation	8.80	/	*ca.* 6	6681 emu·mol^{-1}	75 Oe	/	*ca.* 5	166
$Ni_{0.65}Al_{0.35}$	$NiFe(CN)_6^-$	co-precipitation	10.8	/	*ca.* 11	7618 emu·mol^{-1}	131 Oe	/	10	

Table 1. (cont.) Summary of the most relevant structural and magnetic parameters of the magnetic LDHs published to date.

Composition	Anion	Synthetic Methodology	Basal Space	Particle Size (nm)	T_M (K)	Ms	Hc	Mydosh	FC/ZFC (K)	Ref.
$Co_{1.80}Al_{1.12}$	$C_{12}H_{25}SO_4^-$	reverse micelle	26	*ca.* 59	5.5	2.21 μ_B	< 100 kG	0.068	2.7	161
$Co_{1.83}Al_{1.05}$	$C_{12}H_{25}SO_4^-$	reverse micelle	26	*ca.* 77	5.5	2.23 μ_B	< 100 kG	0.070	2.8	
$Co_{1.83}Al_{1.02}$	$C_{12}H_{25}SO_4^-$	reverse micelle	26	*ca.* 157	5.5	2.10 μ_B	< 100 kG	0.070	3.5	
$Co_{1.89}Al_{1.00}$	$C_{12}H_{25}SO_4^-$	reverse micelle	26	2000-3000	5.5	/	/	/	/	
$Zn_{0.5}Co^{2+}_{0.28}Co^{3+}_{0.22}$	NO_3^-	co-precipitation	8.87	<1000	13(dc)	/	/	/	/	180
Ni_4Mn	CO_3^{2-}	co-precipitation	7.87	*ca.* 20	34.7(dc)	/	/	/	/	160
Ni_3Mn	CO_3^{2-}	co-precipitation	7.78	*ca.* 20	30.8(dc)	/	/	/	/	
Ni_2Mn	CO_3^{2-}	co-precipitation	7.66	*ca.* 20	26.0(dc)	/	/	/	/	
$Ni_{0.66}Al_{0.34}$	$CuPcTs^{4-}$	hydrothermal (HMT)	18.30	/	4	1.5 μ_B	80 G	/	/	165
$Ni_{0.67}Fe_{0.33}$	$CoTPPS^{4-}$	co-precipitation	22.4	/	12.5	2.12 μ_B	28 mT	0.053–0.063	/	164
$Ni_{1.86}Al_{1.14}$	NO_3^-	co-precipitation	8.60	/	3.8	2.63 μ_B	0.13 kG	/	/	122
Ni_2Fe	NO_3^-	co-precipitation	7.94	/	14.5	3.05 μ_B	3.96 kG	0.020	/	
$Ni_{1.98}Fe_{1.02}$	$C_6H_8O_4^{2-}$	co-precipitation	13.08	/	12.5	3.77 μ_B	<0.1 kG	0.031	/	
$Ni_{2.06}Fe_{0.94}$	$C_{10}H_{18}O_4^{2-}$	co-precipitation	15.39	/	11	3.34 μ_B	0.2 kG	0.058	/	
$Co_{0.75}Fe_{0.25}$	OMe/Cl^-	non-aqueous co-precipitation	9.21	*ca.* 18	7	0.98 μ_B	402 G	0.063	4.8	154
$Co_{0.67}Fe_{0.33}$	CO_3^{2-}	co-precipitation	7.59	<1000	11	/	/	/	/	
$Co_{0.65}Al_{0.35}$	$C_{14}H_{10}N_2O_4^{2-}$	reflux (urea)	20.00	ca. 2000	4.5	1.27 μ_B	<0.1 kG	/	—	181
$Co_{0.65}Al_{0.35}$	$C_{18}H_{14}N_3SO_3^-$	reflux (urea)	25.91	ca. 4000	4	1.5 emu·mol^{-1}	27 G	/	—	—

Surprisingly, Wei, Han and co-workers recently claimed in several works that Fe-containing LDHs behave as magnets at room temperature.[182–184] In fact, they found that highly crystalline colloidal LDH suspensions obtained after the co-precipitation of nickel, cobalt and iron nitrate or chloride salts, followed by a hydrothermal treatment at moderate temperatures, led to the synthesis of NiFe– or CoFe–LDHs, which were attracted by a conventional laboratory magnet. Although their applications as sensors are very appealing, this room temperature spontaneous magnetization is due to magnetic impurities, as we will demonstrate in this Chapter.

4.2. Results and Discussion

Generally, the synthesis of highly crystalline non-Al^{3+}-based LDHs via a homogeneous precipitation is very disfavoured route mainly because of the absence of a specific amphoteric behaviour in transition-metal cations like Fe^{3+}. Recent work has developed novel synthetic strategies to address these problems, including the use of additional chelating reagents, as previously depicted in Chapter 2,[138,144] or the smart topochemical approach developed by Sasaki and co-workers.[53,137] More concretely, the synthesis of iron-based LDHs has usually led to the presence of some amorphous phases like ferrihydrite (FeOOH), or even iron oxide nanoparticles (Fe_2O_3 or Fe_3O_4 maghemite and magnetite, respectively), that exhibit room temperature magnetism (See **Figure 1**).[53,185] These impurities sometimes are not detectable through powder X-ray diffraction (PXRD), as demonstrated very recently by Sommerdijk and co-workers for amorphous magnetite nanoparticles formed under basic pH.[186]

The *in-situ* cryogenic HRTEM observation of the growth mechanism of these nanoparticles has corroborated the rapid agglomeration of nanometric primary particles leading to magnetite nanocrystals. Thus, it is possible to obtain LDHs maintaining their chemical properties despite being decorated with spinel "nano impurities". As can be observed in **Figure 1**, highly crystalline NiFe–LDH phases with the highest iron content (*i.e.* Ni:Fe ratio equal to 2:1) can be prepared following a modified homogeneous precipitation method reported by our group using triethanolamine and urea as chelating

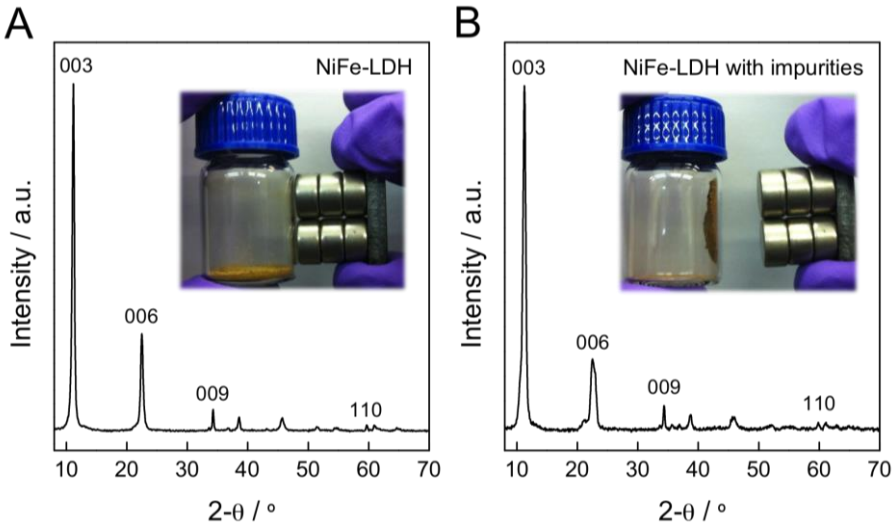

Figure 1. (A) PXRD of a NiFe–LDH (2:1 ratio) without room temperature magnetic impurities. (B) PXRD of a NiFe–LDH exhibiting a similar profile but decorated with nondetectable spinel impurities. The insets show digital photographs of the samples under an external magnetic field.

and hydrolysis reagents, respectively, at 125 °C over 48h (see the experimental section).[144,179] The PXRD pattern shows the typical profile expected for a LDH. It presents sharp intense peaks at low θ values and less intense peaks at higher angular values, with no signature of contaminant phases. Despite the crystallinity exhibited by the apparently pure bulk sample, it is attracted by a conventional laboratory magnet. Sometimes these spinel peaks are seen as very weak signals of small intensity in the PXRD experiments. This can be observed in **Figure 2A** for samples of NiFe and CoFe prepared by the widely used hydrothermal approach as detailed in the experimental section. In this case, the broad peak at around a 2θ value ranging from 17 to 19° can be detected and is related with the presence of Co and Fe spinel impurities. In addition, a detailed inspection of the crystals through HRTEM shows the presence of very small nanoparticles of *ca.* 4 nm on the surface of the NiFe–LDH crystals (**Figure 2B,C**). Moreover, Rives et al.[187] reported that when CoFe–LDH is synthesized through a traditional coprecipitation method, Co^{II} can become partially oxidized to Co^{III}, being a possible source of spinel impurities

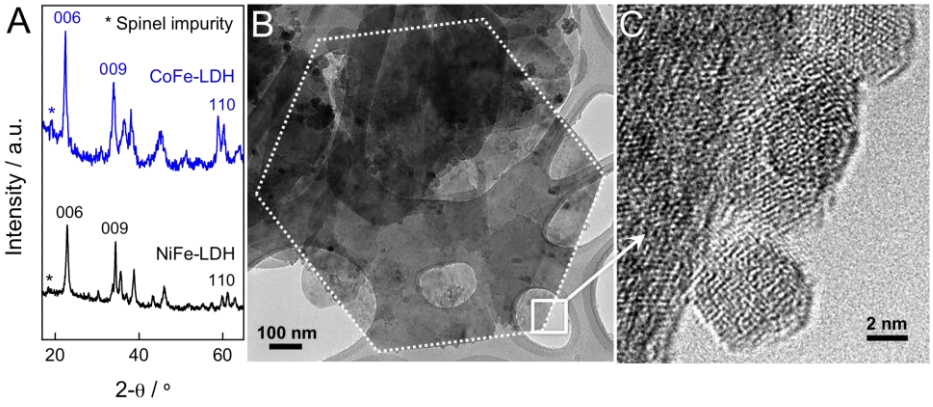

Figure 2. (A) PXRD patterns and peaks indexation of NiFe–LDH and CoFe–LDH at high angles highlighting the spinel impurities. (B) HRTEM image of a hexagonal crystal of the impure NiFe–LDH. (C) Magnified image showing some nanoparticles decorating the LDH surface.

(probably $Co^{II}Co^{III}_2O_4$, $Co^{II}Fe^{III}_2O_4$ or $Co^{II}Co^{III}Fe^{III}O_4$), which also exhibits room temperature magnetic properties.

In contrast, the non-aqueous method reported by Gardner et al.[44,151,154,188] leads to pure CoFe–LDHs (**Figure 3**). These impure LDHs are immediately attracted to a magnet (as previously observed in the inset of **Figure 1B**). Moreover, the temperature-dependent magnetic susceptibility, χ_M, of NiFe and CoFe decorated with impurities reported as $\chi_M T$ *vs.* T shows an almost linear increase above *ca.* 25 K suggesting a partial temperature-independent component that could be ferromagnetic or superparamagnetic in origin (**Figure 4**).[175] The drop observed in both the pure and "decorated" LDH phases in the $\chi_M T$ plot below 20 K defining a maximum corresponds to the intrinsic cooperative magnetism in the LDH layers and is accompanied by steep jumps in the χ_M signals. This intrinsic spontaneous magnetization at low temperature is confirmed by alternating-current (ac) dynamic susceptibility measurements (see **Figure 5**), which show the presence of defined peaks in both the in-phase (χ'_M) and the out-of-phase (χ''_M) signals (see the insets in **Figure 5**). From the position of the χ''_M signal, one can extract the critical temperature below which the spontaneous magnetization of the LDH material appears. In the case of NiFe, this temperature is about 16 K, while for CoFe, it is *ca.* 7 K.[154]

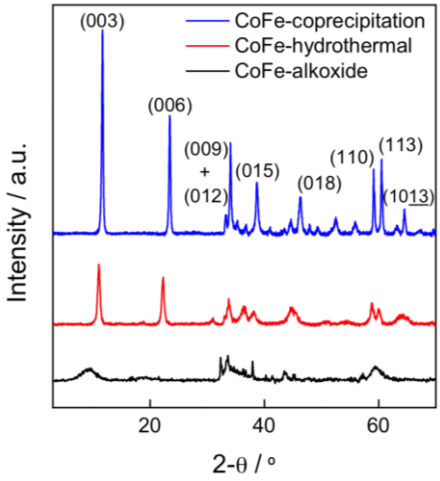

Figure 3. PXRD patterns of different CoFe–LDHs synthesized by the traditional coprecipitation route (a), the hydrothermal approach (b), or *via* the non-aqueous methanolic route (c).

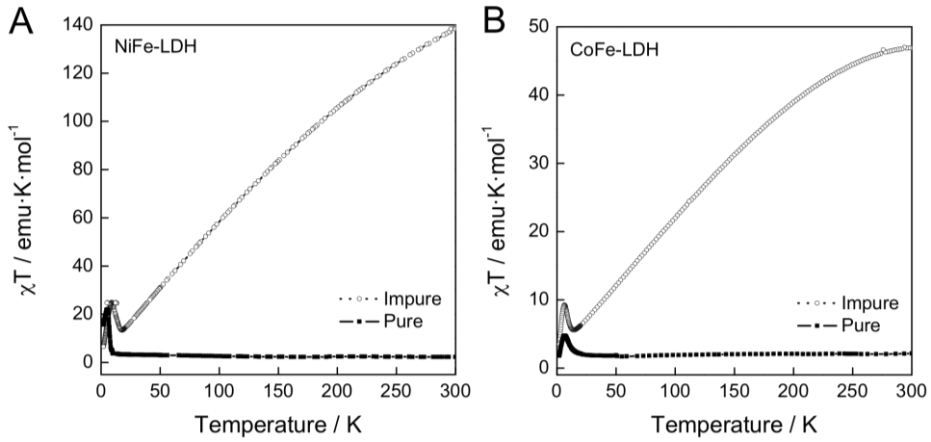

Figure 4. Temperature dependence of the $\chi_M T$ product for (A) impure NiFe–LDH (open symbols) and (B) impure CoFe–LDH. $\chi_M T$ values for pure NiFe– and CoFe–LDHs are shown for comparison (closed symbols).

These dynamic experiments are strongly sensitive to the presence of magnetic impurities in the samples. In fact, in both NiFe and CoFe, these measurements show a peak at very low temperatures that is frequency-dependent and whose

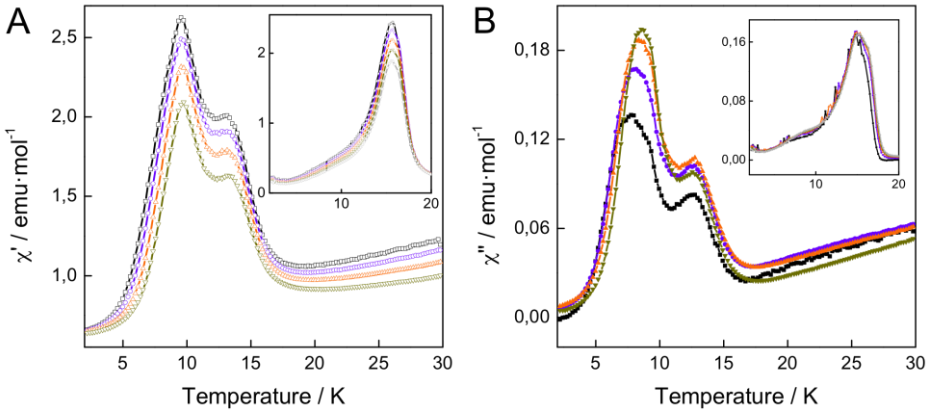

Figure 5. Measurements of ac susceptibility for the NiFe–LDH isolated compounds. (A) in-phase and (B) out-of-phase signals at 10, 100, 1000 and 10000 Hz (black, purple, orange and green data points, respectively). The inset represents the signals of a pure LDH phase.

intensity increases with the amount of impurity. This peak is probably due to the presence of very small superparamagnetic nanoparticles anchored to the LDH surface, which undergo a superparamagnetic blocking at these low temperatures. In fact, the blocking temperature for Fe_3O_4 nanoparticles of 4 nm in size is close to 8K.[189] In the examples reported in the present chapter (NiFe– and CoFe–LDHs with small intercalate anions as CO_3^{2-} or NO_3^-), one can notice that this low-*T* signal only appears when impurities are present. Still, we should remark that, in other pure LDH materials presenting a higher interlamellar space due to the intercalation of bulky anions, a similar frequency-dependent signal has also been observed at this temperature. In these cases, this signal is intrinsic and has been attributed to the movement of the domain walls in the ordered state,[122,123,161,164,179] or even to the presence of metallic disorder within the layers, which can give rise to spin-glass-like behaviour or to superparamagnetism coming from metal clustering within the layers.[161,179] The conclusion is that not always this low-*T* and frequency-dependent χ''_M signal can be taken as a proof of the presence of magnetic impurities. In fact, the application of dc magnetic fields during the ac susceptibilities measurements in homometallic Ni-hydroxides with *BS* of *ca.* 8 Å, leads to the appearance of several frequency-dependent peaks. These new

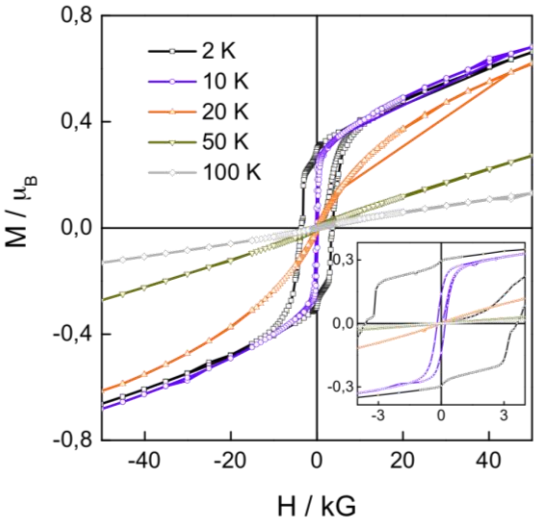

Figure 6. Field-dependent magnetization of pure NiFe–LDH at different temperatures ranging from 2 to 100 K. The insert shows the enlarged partial hysteresis curves.

signals are ascribed to nano-sized related blocking temperatures and spin-glass-like ordering of the surface spins.[190]

Other experiments, such as, for example, the presence of a hysteretic behaviour in the magnetization *vs.* field plot, can be more conclusive. In this context, we have plotted the *M* versus *H* curves at various temperatures for a pure NiFe–LDH (**Figure 6**). For the hysteresis cycle measured at 20 K, just above the critical temperature for the onset of the spontaneous magnetization, neither significant coercive field nor remnant magnetization can be measured. In addition, the *M* versus *H* curve for T > 50 K does not show any hysteresis, as expected. In turn, the impure sample exhibits a hysteretic behaviour, even at room temperature, as has already been observed.[182–184]

4.2.1. Dipolar Interactions

As depicted in the previous section, the role of dipolar interactions in this sort of materials remains challenging. According to the reported studies Al-containing–, NiMn– and NiCr–LDHs exhibited AF dipolar interactions, whereas the as-synthesized NiFe–LDHs revealed dipolar interactions of

ferromagnetic character. This is in clear contrast to that reported for homometallic-layered hydroxides, in which the hydroxide layers are covalently connected to the interlamellar anions.[72,126] This strong bond seems to exert an important role in their interlayer magnetic interactions. In fact, for shorter interlayer distances of less than 1 nm, through-bond AF interactions appeared, promoting metamagnetic behaviour. On the other hand, for higher interlayer distances (> 1 nm) dipolar F through-space interactions predominate, with a significant distance-dependence between individual spins, likely proportional to BS^{-3}.[72,74,126] Concerning LDHs, only dipolar interactions should appear, due to the non-covalent connection between the layers and the anions. In this sense, there is only one example reporting the influence of *BS* on the overall magnetism of a family of hybrid co-precipitated NiFe–LDHs, suggesting F dipolar interactions (previously reported by our group), in which the T_M values and the coercivity decrease proportionally to BS^{-3}.[122] Still, the nature of the interlamellar anion could promote some divergences to this tendency, as observed for mononuclear macrocyclic-intercalated LDHs studied in this dissertation (see **Table 1**).[164,165] From the T_M values reported to date, one can extract that ferromagnetic Al-containing LDHs, like NiAl– or CoAl–LDHs exhibit AF dipolar interactions, whereas ferrimagnetic NiFe–LDHs seems to promote F dipolar interactions, at least in the range of interlamellar anions we have reviewed.

Concerning the influence of the particle dimensions on the dipolar interactions —apart from the recently reported work of O'Hare and co-workers on the size-dependent magnetism in CoAl–LDHs synthesized through the reverse-micelle technique[161]— no works regarding the effect of crystal size on the magnetism have been reported. In this work, the authors pointed out the physical complexity of these systems, as their overall magnetism depends on the correlation between spin-glass like, cluster-spin-like magnetism or superparamagnetic behaviour.

Moreover, the study of the properties of LDHs in the 2D limit remains largely unexplored due to the lack of suitable examples, and remains a challenging task. Further work is still needed in order to elucidate the physical insights of the dipolar interactions in the magnetism of LDHs.

4.3. Conclusions

In conclusion, attention should be paid to the synthesis and characterization of iron-containing LDHs because of the possibility of having magnetic impurities that can induce wrong claims such as room temperature magnetism in LDHs. To date, there are no examples of spontaneous magnetization in LDHs exceeding *ca.* 21 K. Moreover, the physical insights underlying the role of dipolar interactions on the magnetic properties of LDHs remains an open question. Having said that, it is worth to mention that the presence of ferromagnetic or superparamagnetic spinel nanoparticles in these kinds of layered materials could be of interest in the preparation of new hybrids combining the intrinsic properties of LDHs with the room temperature magnetic properties of metal oxide nanoparticles. This possibility opens the door for the use of LDHs as building blocks of new multifunctional materials, taking advantage of the flexibility and chemical versatility of these hosts.

4.4. Experimental Section

4.4.1. Synthesis of NiFe–LDHs

All Chemicals $Ni(NO_3)_2{\cdot}6H_2O$, $Fe(NO_3)_3{\cdot}9H_2O$, $NaNO_3$, HNO_3, $C_6H_{15}NO_3$ (triethanolamine, TEA) and $CO(NH_2)_2$ (urea) were used as received without further purification. LDHs were synthesized following the modified homogeneous precipitation method described in previous chapters, by using urea and TEA as ammonium releasing reagent (ARR) and chelating agent, respectively.[151]

In a typical procedure, the nitrate salts of the metals were dissolved in 50 mL of Milli-Q purged water together with TEA, in order to reach a total metal cation concentration of 20 mM in the final solution, adjusting the stoichiometric coefficient x = Fe/(Ni + Fe) to x = 0.33. The concentration of TEA was equimolar with iron concentration. Then, 50 mL of an aqueous solution of urea (35 mM) were added. The amount of urea was fixed to be 1.75 times the total metal concentration. The resulting dark brown mixture was placed in a 125 mL stainless steel Teflon lined autoclave and heated in an oven. In order to study the effect of the temperature of the hydrothermal step in the purity of the final material, the temperature of the oven was ranged from 125 (pure) to 150 °C (impure). After 48 hours, the autoclave was cooled on a bench to room temperature and the resulting yellowish fine powder was filtered, washed thoroughly with Milli-Q water and dried in a vacuum. The pH value of the remaining solution was found to be around 7.5–8.0.

4.4.2. Synthesis of CoFe–LDHs

All chemicals $Co(NO_3)_2{\cdot}6H_2O$, $CoCl_2{\cdot}6H_2O$, $Fe(NO_3)_3{\cdot}9H_2O$, $FeCl_3{\cdot}6H_2O$, NaOH, Na_2CO_3 and MeOH were used as received without further purification.
CoFe–hydrothermal. Synthesized following the method described by Wei et al.[183]

In a typical procedure, the salts of the metals $CoCl_2{\cdot}6H_2O$ (0.16 M) and $Fe(NO_3)_3{\cdot}9H_2O$ (0.055 M) were dissolved in 150 mL double-distilled water and the pH was adjusted to 8.0 by using a NaOH solution (1.5 M). The resulting mixture was placed in a 125 mL stainless steel Teflon lined autoclave and heated in an oven and was aged at 130 °C for 24 h. After 24 h, the autoclave was cooled on a bench to room temperature and the resulting dark brown fine

powder was filtered, washed thoroughly with Milli-Q water and dried in a vacuum. The pH value of the remaining solution was found to be around 8.

$[Co_{0.74}Fe_{0.26}(OH)_2](CO_3)_{0.25}{\cdot}0.1H_2O$; Co:Fe = 3:1; (C,H,N, calc: 1.95, 2.10, 0; found: 3.35, 1.6, 0.17).

CoFe–coprecipitation. A CoFe–LDH-coprecipitate was synthesized following the method described by Rives et al.[187]

In a typical procedure, the nitrate salts of the metals, 0.012 mol of $Co(NO_3)_2{\cdot}6H_2O$ and 0.006 mol of $Fe(NO_3)_3{\cdot}9H_2O$, were dissolved in 25 mL of Milli-Q water (previously boiled in a microwave (MW) and stored under an argon atmosphere for 1 hour) and then the solution was added dropwise (*ca.* 30 drops per min) to a solution containing 0.031 mol Na_2CO_3 in 50 mL of Milli-Q water (previously boiled in a MW and stored under an argon atmosphere for 1 hour). The resulting mixture was stirred at 70 °C for 30 h under an argon atmosphere (with the system sealed hermetically). After that, the light brown fine powder was filtered, washed thoroughly with Milli-Q water and EtOH and dried in a vacuum.

$[Co_{0.67}Fe_{0.33}(OH)_2](CO_3)_{0.16}{\cdot}0.2H_2O$; Co:Fe = 2:1; (C,H,N, calc: 1.90, 2.30, 0; found: 1.56, 2.44, 0.14).

CoFe–alkoxide. CoFe–LDH-alkoxide was synthesized following a modified method described by Gardner et al.[44,154,188]

In a typical procedure, chloride salts of the metals with a stoichiometry ratio of 3:1, $CoCl_2{\cdot}6H_2O$ (30 mM, 714 mg) and $FeCl_3{\cdot}6H_2O$ (10 mM, 270 mg) were added into a three-neck flask and then dissolved with 100 mL of methanol, reaching a total metal cation concentration of 40 mM. The solution was then stirred and heated at 65 °C for 1 h. Afterwards, a solution containing 3.8 g of NaOH in 100 mL of MeOH was slowly added to the previous solution (the addition should last for around 2–3 minutes) and the mixture was left for 72 h under stirring at 65 °C. A constant pressure of an Ar atmosphere was employed to avoid the carbonate contamination and the evaporation of the MeOH. Finally, the resultant brown fine powder product was filtered, washed with MeOH and dried in a vacuum.

$[Co_{0.75}Fe_{0.25}(OH)_{1.3}(OMe)_{0.7}](Cl)_{0.25}{\cdot}0.6H_2O$; (C, H, N, calc.: 7.10, 2.10, 0; found: 7.12, 2.34, 0.16).

4.4.3. Physical Characterization

Metallic atomic composition of bulk samples was determined by means of electron probe microanalysis (EPMA) performed in a Philips SEM-XL30 equipped with an EDAX microprobe. NiFe–LDH X-ray powder diffraction patterns were collected with a Siemens d-500 X-ray diffractometer (Cu-K_α radiation; λ_α = 1.5418 Å) equipped with a rotating anode D-max Rigaku operating at 80 mA and 45 kV. Samples were mounted on a flat sample plate. Profiles were collected in the $2.5° < 2\theta < 70°$ range with a step size of 0.05°. CoFe–LDH X-ray powder diffraction patterns were obtained using a Phillips X'Pert-MPD diffractometer provided with a graphite monochromator, operating at 40 kV and 20 mÅ and employing nickel-filtered Cu-K_α radiation (λ = 0.1542 nm). Profiles were collected in the $5° < 2\theta < 70°$ range. Carbon, hydrogen and nitrogen contents were determined by microanalytical procedures using an EA 1110 CHNS-O elemental analyzer from CE Instruments. HRTEM studies of the selected samples were carried out on a JEM-2010 microscope (JEOL, Japan) operating at 200 kV. Samples were prepared by dropping a suspension of the sample in ethanol on a carbon-coated copper grid. The digital analysis of the HRTEM micrographs was done using DigitalMicrographTM 1.80.70 for GMS 1.8.0 by Gatan.

Magnetic susceptibility measurements were performed on polycrystalline samples with a Quantum Design (SQUID) Magnetometer MPMS-XL-5. The susceptibility data were corrected by removing the diamagnetic contributions as deduced by using Pascal's constant tables. The dc data were collected in the range 2–300 K upon decreasing temperatures with an applied field in the range 100–5000 G, and hysteresis loops were collected between –5 and +5 T at 2, 10, 20, 50 and 100 K. The ac data were collected in the range 2–30 K with an applied alternating field of 3.95 G at different frequencies in the range 10–10000 Hz with a Quantum Design PPMS-9 equipment.

2 Hybrid Magnetic Multilayers

5. Hybrid Magnetic Multilayers by Intercalation of Cu(II) Phthalocyanine in LDH Hosts[†]

The intrinsic flexibility of LDHs has been here exploited to design hybrid multilayered materials by intercalation of the copper phthalocyaninetetrasulfonate (CuPcTs) complex in the interlamellar space offered by these layered hosts through simple anion-exchange procedure. Taking advantage of their chemical versatility, two different LDHs, the diamagnetic ZnAl and the ferromagnetic NiAl, have been synthesized and characterized to explore the differences in the magnetic properties of the hybrids introduced by the intercalation of the paramagnetic complex.

[†] Abellán, G.; Busolo, F.; Coronado, E.; Martí-Gastaldo, C.; Ribera, A. *J. Phys. Chem. C* **2012**, *116*, 15756.

5.1. Introduction

LDHs can be described as layered hydrated materials in which the typically encountered interlamelar anions consist on carbonate, nitrate or chloride as described in the previous section.

From the materials point of view, LDHs exhibit high surface area, remarkable AEC, and variable gallery height to accommodate a wide range of anionic species with different sizes. In fact, this former feature has been fruitfully exploited to design a plethora of hybrid materials with interesting applications[28] as sorbents,[191,192] anion exchangers,[58,193] catalysts,[8,194–198] 2D nanoreactors,[120,152,199–201] or host materials for drug delivery amongst others.[98,202,203]

In the past years, the design of novel LDH-based hybrid materials has attracted important attention probably boosted by the discovery of new synthetic procedures based on ARR,[45–49,144] which enable the synthesis of highly crystalline LDH materials with variable metal compositions and well-defined particle's size and hexagonal morphology. These hybrids are generally prepared via anion-exchange procedures, in which the anionic functional entities of interest are intercalated within the interlamellar space offered by the LDH hosts. In this way, the LDH acts as a solid-state nanocontainer, not only controlling the organization of these functional species at the nanoscale but also increasing their chemical, photochemical, and thermal stability or even controlling their release[203,204] —of utmost importance in drug delivery applications— as result of the constrained geometry and the presence of host–guest noncovalent interactions.[73]

In this context, the use of magnetically active LDHs represents a step forward as it enables the design of next-generation multifunctional hybrids in which the LDH not only acts as a container but also combines its intrinsic magnetism with the physical properties provided by the intercalated species. This combination leads to a superstructure in which both properties coexist and can even interact. In this direction, the intercalation of mononuclear macromolecules like phthalocyanines (Pc) or porphyrins (Por), with optical or magnetic properties of interest, into the interlayer space offered by magnetic LDHs, represents an

avenue worth being explored as it can provides a way to obtain hybrid magnetic materials.[69,118,152]

On the basis of their promising catalytic properties, Por-intercalated LDH materials have been extensively considered,[71,196,205] while only a few examples have been described so far regarding Pc. Among them, we consider worth highlighting those from Carrado[206] and Ukrainczyk et al.[207] where the seminal synthesis of LDH–Pc materials (MgAl–CoPcTs and MgAl–CuPcTs, respectively) via ion-exchange and direct synthesis is described, and the perpendicular arrangement of the sandwiched macrocycles with respect to the LDH layers is postulated. Later on, Barbosa et al.[208] described the synthesis and physical study of CuPcTs intercalated MgAl–LDH and the related materials resulting from the direct attachment of the Pc to the LDH surface. Interestingly, they discovered that the catalytic activity of the anionic complex was reduced when sandwiched between the LDH layers, and associated this effect to the modifications induced by the 2D confinement in the copper coordination sphere and accordingly to its electronic behaviour. Although this experimental evidence points out the dramatic effects triggered by the confinement in the electronic properties of the intercalated complexes, studies reporting on the magnetic properties of LDH–Pc hybrid materials remain very scarce. This lack of information has not permitted us to compare the magnetic response of the previously reported Pc-intercalated hybrids with the properties exhibited by the materials here described.

To fill this gap, we have explored the anion-exchange intercalation of copper(II) phthalocyaninetetrasulfonate (CuPcTs) into the interlamellar space offered by a diamagnetic (ZnAl) and a ferromagnetic (NiAl) LDH host. After describing the chemical and structural nature of the intercalated hybrids, the complementary use of standard magnetometry and electron spin resonance (ESR) has permitted us to characterize the physical properties of the resulting sandwiched materials.

5.2. Results and Discussion

5.2.1. Synthesis and Chemical Composition

In a first step, the diamagnetic ($ZnAl–NO_3$, **1**) and ferromagnetic ($NiAl–NO_3$, **2**) LDH hosts were prepared by following the classical[8] and more recent homogeneous coprecipitation[45–49,144] methods, respectively. The classical methodology was discarded for **2** as it yielded materials with poor morphologies that would have severely limited the success of subsequent anion-exchange reactions. The use of hexamethylenetetramine (HMT) as ammonia releasing reagent instead permitted isolating in excellent yields a high-quality carbonate-LDH phase which was afterward transformed into the nitrate derivative according to the so-called "acid–salt treatment".[48] It is worthwhile mentioning that the substitution of carbonate with other monovalent anions more weekly attached to the LDH sheets is mandatory for the synthesis of more complex hybrid systems through mild anion-exchange reactions in a further stage.

One of the most common problems in the preparation of layered hybrids incorporating metal-containing macrocycles as interlamellar guest is to avoid the presence of non-intercalated moieties, which can be directly attached to the host surface via noncovalent interactions, or the coprecipitation of residual phases stabilized from the presence of strong intermolecular π–π interactions. In view of this and although the intercalation of related guests in a single step by direct synthesis has been illustrated in previous works,[206–208] we decided to explore the milder conditions associated to anion-exchange reactions from the nitrate LDH precursors. This approach benefits from the capability of LDHs to reversibly adapt its layered structure to accommodate a broad range of anions whose sizes can even reach *ca.* 26 Å.[209] Hence, to avoid the presence of nonintercalated moieties in the final hybrid, we made use of a Soxhlet extractor that continuously recirculates water through the as-prepared hybrids to remove adsorbed nonintercalated paramagnetic complexes. Moreover, a thorough washing of the materials has been made, until the washings were completely transparent. The as-obtained compounds were denoted as **3** and **4**, namely ZnAl–CuPcTs and NiAl–CuPcTs, respectively.

FT-IR spectroscopy was first used to monitor the progress of the intercalation process. **Figure 1** shows how the characteristic vibration modes

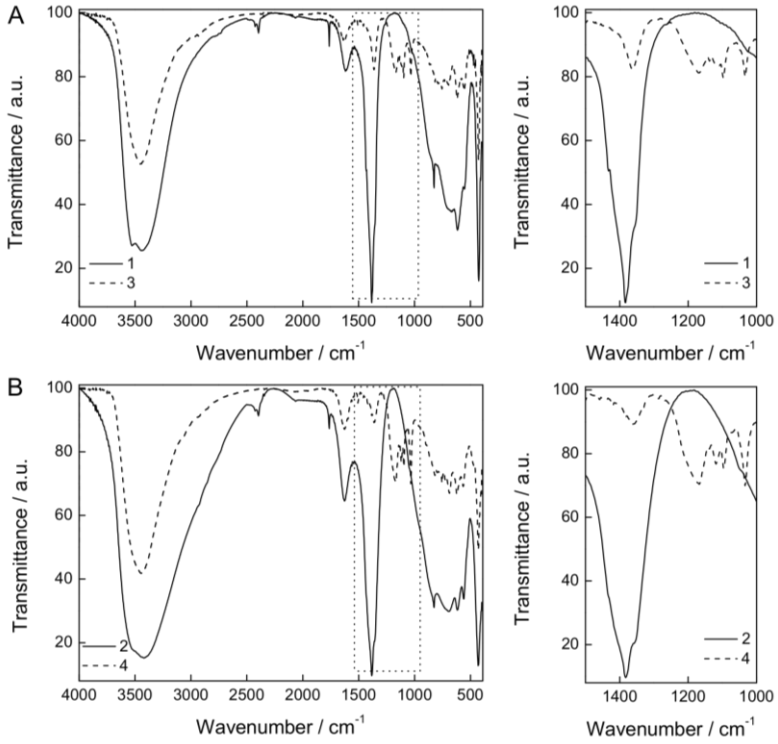

Figure 1. FT-IR spectra of compounds **1** and **3** (A) and **2** and **4** (B). The inset in the right panel represents a zoom-in of the 1500–1000 cm^{-1} region.

associated to the copper phthalocyanine[210] between 1500 and 1000 cm^{-1} are present in **3** and **4**, while the sharp stronger band at 1384 cm^{-1}, corresponding to the nitrate anion ν_3 stretching mode, disappears in both cases thus supporting complete nitrate exchange (see **Table 1** for further information). The metal compositions, as estimated from energy-dispersive analysis of X-rays (EPMA, see **Table 2**), show an excellent agreement between the M^{II}/M^{III} ratios encountered in the hybrid materials (**3**, **4**) and the corresponding LDH host precursor. The slight differences are likely due to the residual precipitation of amorphous aluminum phases under the reaction conditions. The Cu/Zn ratios indicate that the exchange process has proceeded efficiently with anion exchange capacity (AEC) values of 71 % and 94 % for **3** and **4**, respectively. Deviation with respect to complete exchange must be ascribed to the co-

Table 1. Assignment of the IR main vibration modes (cm^{-1}) of compounds 1–4.

Sample	ν_{O-H}	δ_{H-O-H}	δ_{C-N}	ν_{N-O}	ν_{C-O}	ν_{S-O3}	ν_{M-O}	δ_{O-M-O}
1	3416	1632	—	1383	1361	—	738	522, 403
2	3422	1635	—	1384	1358	—	775	523, 403
3	3453	1637	1507	—	1363	1169, 1033	755	555, 427
4	3443	1628	1507	—	1363	1167, 1033	754	566, 431

Table 2. Elemental chemical analysis data for the materials used in this study.

		x^a		water		
	Molecular formula	**exp[b]**	**theor**	**[%][c]**	**molec**	**AEC [%]**
1	$[Zn_{0.64}Al_{0.36}(OH)_2](NO_3)_{0.36}\bullet 0.4H_2O$	0.36	0.33	6.59	0.42	—
2	$[Ni_{0.65}Al_{0.35}(OH)_2](NO_3)_{0.35}\bullet 0.2H_2O$	0.35	0.33	4.01	0.24	—
3	$[Zn_{0.65}Al_{0.35}(OH)_2](CO_3)_{0.05}(CuPcTs)_{0.06}\bullet 0.7H_2O$	0.35	0.33	8.38	0.73	70.8
4	$[Ni_{0.66}Al_{0.34}(OH)_2](CO_3)_{0.01}(CuPcTs)_{0.08}\bullet 0.7H_2O$	0.34	0.33	6.66	0.61	94.1

[a] $x=[M^{III}]/([M^{II}]+[M^{III}])$. [b] Obtained with EPMA. [c] Water content derived from thermogravimetric analysis.

intercalation of a residual amount of carbonate ions as confirmed by the presence of a weak intensity band centered at 1363 cm^{-1} in the FT-IR spectra of both hybrids.

5.2.2. Structural Analysis

Powder X-ray diffraction (PXRD) patterns show the typical features of LDH materials (**Figure 2**). By assuming a rhombohedral 3R symmetry,[11] all compounds show a first set of well-defined sharp and symmetric reflections for the basal (003), (006), and (009) planes at low angular values, while a second set of less intense broader asymmetric reflections for the nonbasal planes at higher angular values can be observed. This indicates that the crystallinity of the pristine hosts is maintained after the intercalation process with no indication of the presence of contaminant phases. This fact discards the presence of nonintercalated Pc molecules anchored to the outer surface of the hybrids, as this would imply the presence of additional diffraction lines characteristic of solid-state Pc aggregates.[205] In addition, the samples display very narrow (00*l*)

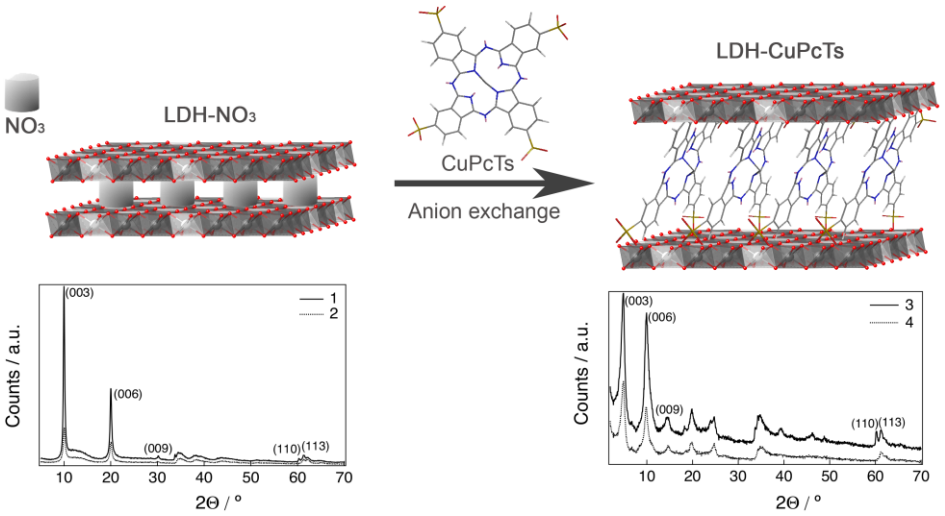

Figure 2. (top) Schematic representation of the synthesis of the CuPcTs intercalated LDHs. (bottom) From left to right: powder X-ray diffraction patterns of ZnAl–NO_3 (**1**) and NiAl–NO_3 (**2**) and ZnAl–CuPcTs (**3**) and NiAl–CuPcTs (**4**).

Table 3. X-Ray diffraction data and unit cell parameters for 1–4.

	2Θ [°] (*hkl*)					Calc param[a] [Å]		
Sample	**(003)**	**(006)**	**(009)**	**(110)**	$d_{(110)}$	***a***	***c***	***BS***
1	10.00	20.00	29.70	60.10	1.54	3.08	26.73	8.91
2	10.05	20.05	29.90	61.25	1.51	3.03	26.63	8.88
3	4.80	9.95	14.15	60.15	1.54	3.08	54.97	18.32
4	4.75	9.80	14.55	61.10	1.51	3.03	54.91	18.30

[a] $a = 2d_{110}$; $c = d_{003} + 2d_{006} + 3d_{009}$; $BS = c/3$.

diffraction lines in contrast to what is observed for other LDH-based hybrid materials which generally exhibit poorer crystallinity associated with anisotropic size effects, stacking faults or microstrains.[211] After the anion-exchange reactions, the basal spacing (*BS*) increases from 8.9 Å in **1** and **2** to 18.3 Å in **3** and **4** (see **Table 3**). This can be unambiguously attributed to the substitution of the nitrate anions with the comparatively bigger CuPcTs complex. Moreover, the difference between the estimated *BS* and the average width associated to a brucite layer, *ca.* 4.7 Å (4.777 Å; JCPDS card nº 44-1482), permits estimating a

gallery height of 13.6 Å. Taking into account that the size of the complex is estimated to be *ca.* 13.85 Å, —the size of the CuPcTs has been calculated by optimizing the phthalocyanine structure with molecular dynamics (ChemBio 3D Ultra software, CambridgeSoft) and by estimating the perpendicular distance between the two most distant oxygens— this value suggests that the Pc rings are almost perpendicular with respect to the LDH host in the interlamellar space.

5.2.3. Thermogravimetric Study

Figure 3 show the thermogravimetric/differential thermal analysis (TG/DTA) curves for **1**–**4** under an air atmosphere in the 25–800 °C range. They exhibit the classical LDH thermal decomposition with the mass loss taking place via a two-step process. In a first step, the removal of surface and intercalated water occurs between 90 and 200 °C and comes accompanied by a broad, poorly defined endothermic peak in the DTA curve. This first weight loss process has been used to estimate the water content in each case (see **Table 2**). A second weight loss, associated with the decomposition of the intercalated anions and further dehydroxylation of the hydroxide-bridged brucite layers, is observed in the 150–400 °C temperature range. In addition to this standard behaviour, the hybrids **3** and **4** exhibit a third weight loss between 450 and 550 °C that must be ascribed to the decomposition of the intercalated CuPcTs complexes. A look at the thermal behaviour of the CuPcTs tetrasodium salt (**Figure 3**), which decomposes in a broad interval of temperatures between 467 and 517 °C accompanied by a broad exothermic peak in the DTA plot, confirms the presence of the complex in the hybrids.

5.2.4. Electron Microscopy

Scanning electron microscopy (SEM) studies of the nitrate-intercalated LDH precursors (not shown) present a homogeneous distribution of well-defined hexagonal-shaped particles, with lateral sizes of *ca.* 1 and 0.1 μm for **1** and **2**, respectively. According to **Figure 4**, SEM images of **3** and **4**, reveal homogeneous materials consisting on aggregates of much smaller particles with poorer morphologies. Again, the effect of the mechanical stirring, intrinsic to the exchange procedure, used in the preparation of these hybrids is reflected by

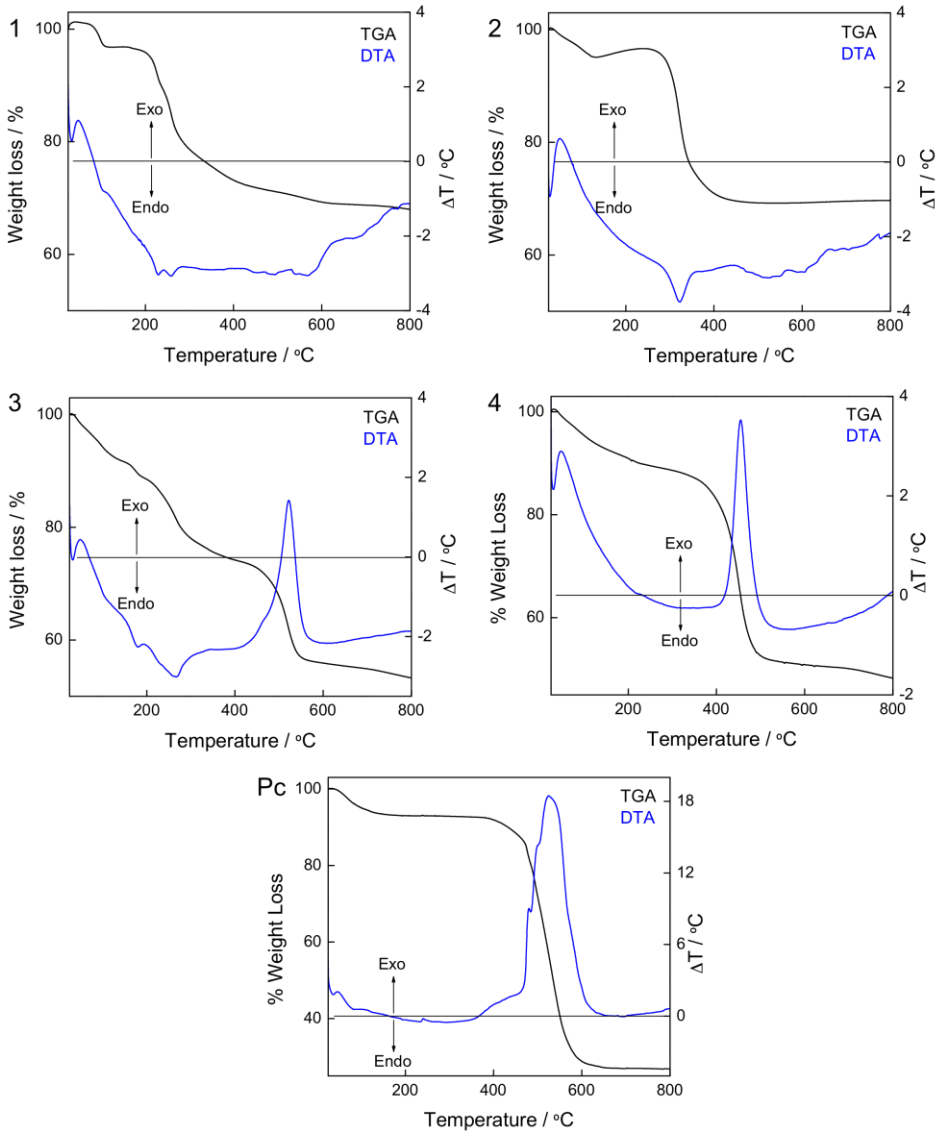

Figure 3. TGA/DTA measurements for ZnAl–NO_3 (**1**), NiAl–NO_3 (**2**), ZnAl–CuPcTs (**3**), NiAl–CuPcTs (**4**) and the CuPcTs complex.

the drastic reduction of the size of their particles. In addition, HRTEM was used to acquire digital micrographs of the LDH–CuPcTs hybrids and provide further insights on their sandwich-like morphology. **Figure 5** shows the appearance of

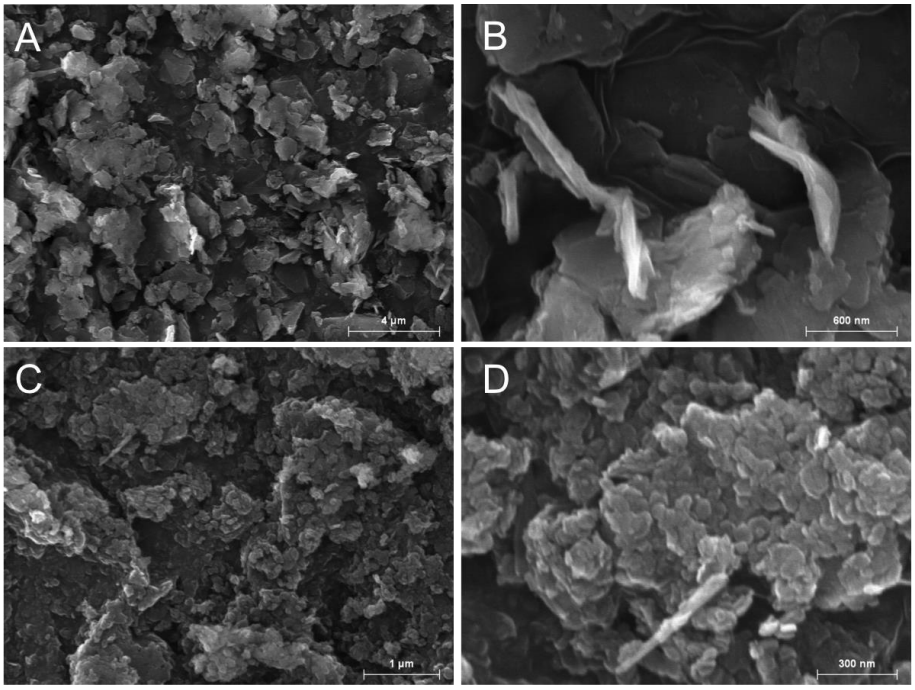

Figure 4. SEM images showing the particle's size and morphology of ZnAl–CuPcTs (**3**; *top*) and NiAl–CuPcTs (**4**; *bottom*).

homogeneous parallel high-contrast fringes, representative of the layered structure of the phthalocyanine-intercalated hybrid.

5.2.5. Magnetic Properties

The diamagnetic nature of the ZnAl–LDH host permitted studying the isolated magnetic response of the intercalated CuPcTs units. The *dc* susceptibility measurements of **3** were performed with an applied field of 1000 G in the 2–300 K range (**Figure 6**). As expected for a paramagnetic complex, χ_M follows an exponential regime in the whole temperature range with an estimated value for the Curie constant of C = 0.030 emu·mol^{-1}, in good agreement with the value calculated for the Cu (II) content derived from the metal analysis, 0.027 emu·mol^{-1}.

The magnetism of the NiAl–CuPcTs is more complex as it results from the combination of (i) the overall ferromagnetism of the NiAl–LDH host,[122] sum of

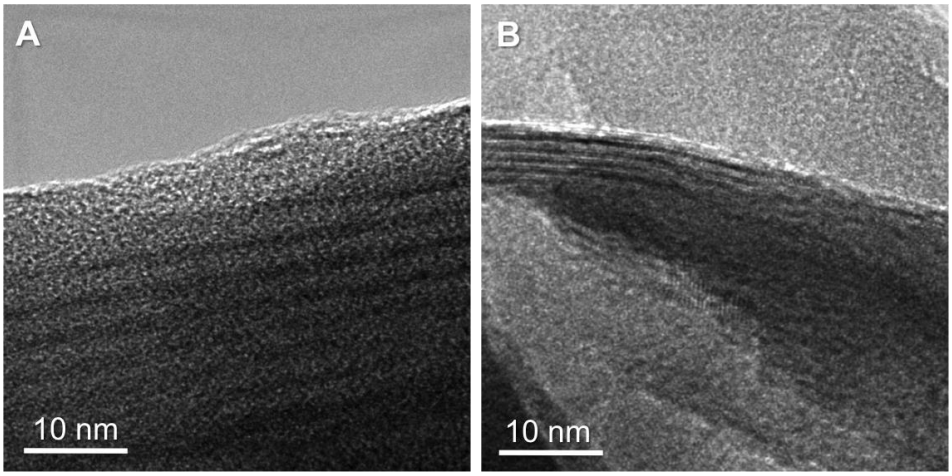

Figure 5. HRTEM image of ZnAl–CuPcTs (**3**; A) and NiAl–CuPcTs (**4**; B) showing the alternance of homogeneous parallel fringes, associated with the higher electron density of the intercalated CuPcTs complex, consistent with the sandwich-like structure fixed by the LDH hosts.

the magnetic superexchange across the layers involving the metal centers bridged by the oxo ligands and the dipolar interactions operating between the layers, and (ii) the paramagnetic response of the intercalated CuPcTs complexes. **Figure 6** displays the thermal dependence of the $\chi_M T$ product of **4**. It exhibits a room temperature value of 1.18 emu·K·mol^{-1}, in good agreement with the sum of the expected spin-only values of Ni (II) and Cu (II) ions as calculated on the basis of the metal composition as estimated with EPMA ($\chi_M T_{rt}$ = 1.1 emu·K·mol^{-1}), and increases continuously upon cooling. Below 100 K, $\chi_M T$ presents a sharp increase in the signal, which is accompanied by a sudden jump in the χ_M susceptibility, suggesting the presence of cooperative ferromagnetic interactions between the Ni (II) ions. This is additionally supported by the fitting of the high-temperature data to a Curie–Weiss law, giving C = 1.14 emu·K·mol^{-1} and a positive Weiss constant θ = 7.1 K (**Figure 7**). Despite the overall magnetism of **4** is mainly controlled by the strongest response of the ferromagnetic host, the intercalated paramagnetic CuPcTs units are likely to be responsible for the non-saturated value of χ_M at 2 K (see **Figure 8**).

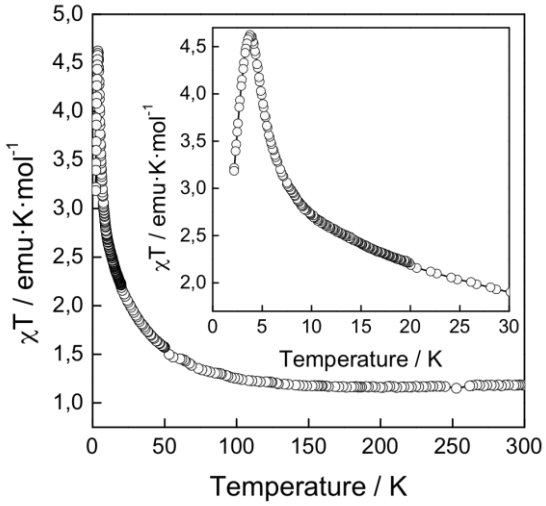

Figure 6. Temperature dependence of the $\chi_M T$ product of NiAl–CuPcTs (**4**). The inset shows a zoom-in of the 2–30 K region. Solid line is only a visual guide.

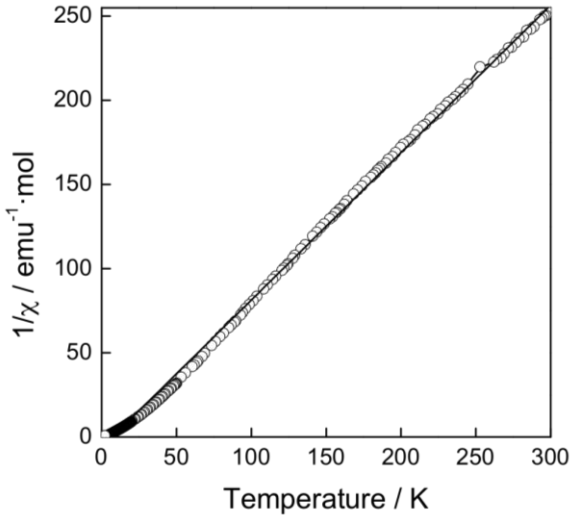

Figure 7. Best fitting (black solid line) of the magnetic susceptibility data to a Curie–Weiss law.

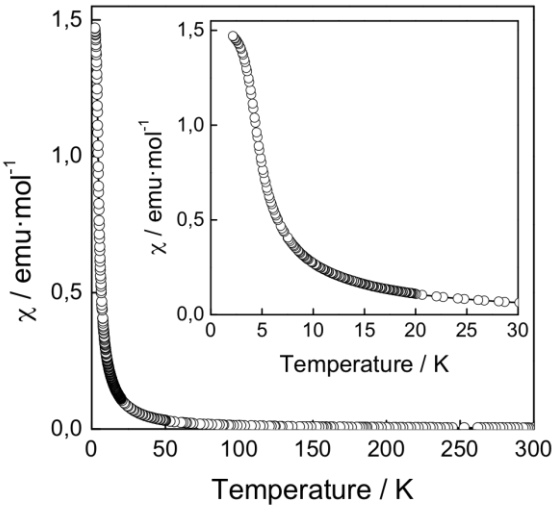

Figure 8. Temperature dependence of χ_M for NiAl–CuPcTs (**4**). The inset shows a zoom-in of the 2–30 K region

The presence of long-range magnetic correlations was next confirmed with dynamic magnetic measurements using an external applied field of 3.95 G oscillating between 10–10000 Hz. Both the in-phase (χ'_M) and out-of-phase (χ''_M) components of the ac susceptibility show a peak below 4 K (**Figure 9**), defining the temperature for the onset of spontaneous magnetization. No significant frequency-dependence of the position of the in- and out-of-phase maxima with the temperature was observed.

At this point, it is worth mentioning that magnetic ordering in the nitrate-intercalated NiAl–LDH analogue takes place at almost the same temperature, 3.8 K. This is rather interesting as previous findings indicate that the increase of the distance separating the hydroxide layers modifies their magnetic behaviour by controlling the intensity of the dipolar interactions operating between layers, as depicted in the previous chapter.[122] In turn, the T_M for NiAl–NO_3 and the CuPcTs-intercalated hybrid remain close to 4 K despite the intercalation of the complex promotes an expansion of around 9.4 Å in the *BS* of the latter.

According to the hysteresis loop measured at 2 K (**Figure 10**), **4** shows a small coercive field of 80 G and thereby can be classified as a soft ferromagnet. In the light of the magnetic studies, the insertion of paramagnetic units between

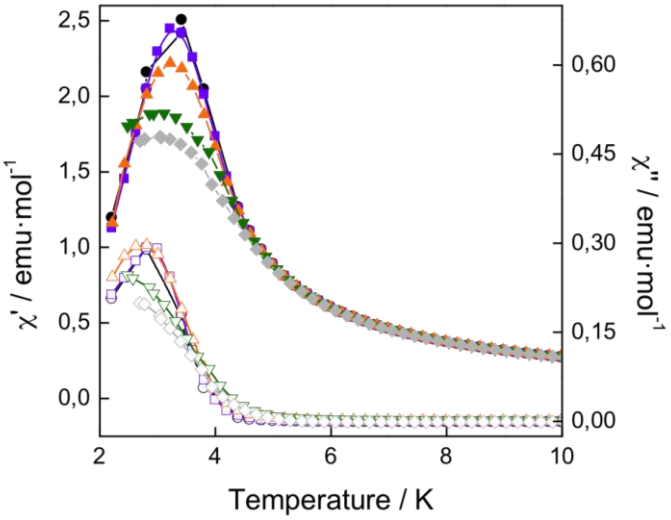

Figure 9. Alternating-current susceptibility in the 100–10000 Hz of **4**. In-phase susceptibility is represented by filled symbols, whereas empty ones represent out-of-phase susceptibility. Solid lines are only a guide to the eye.

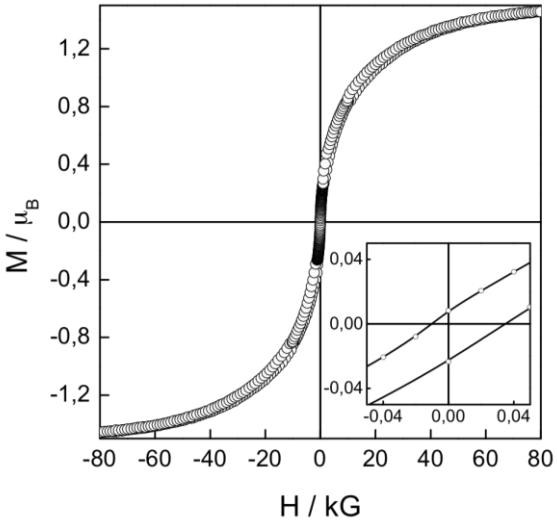

Figure 10. Hysteresis loop of **4** measured at 2 K. Inset highlighting the low-field area.

the ferromagnetic layers of the LDH does not seem to exert remarkable changes on the overall magnetism of the NiAl–LDH host. A similar behaviour has been already described for the intercalation of $[Cr(ox)_3]^{3-}$ complexes into ferromagnetic NiFe–LDH hosts, and more recently for a family of homometallic Ni(II) hydroxides intercalated with different phthalocyanines.[212,213]

5.2.6. ESR Studies

The ESR spectrum at room temperature of the pristine nonintercalated CuPcTs complex shows a single line with asymmetric shape from which an axial *g*-factor with $g_{//} > g_{\perp}$ ($g_{//}$ = 2.1039 and $g_{\perp}$ = 2.0361) can be extracted. The absence of resolved hyperfine structure in the ESR spectrum of Cu (II) (I = 3/2) probably arises from the intermolecular exchange coupling between neighboring CuPcTs complexes. This results in an average of the line splitting on the magnetic copper nuclei.[214,215] Whilst ZnAl–LDH is ESR silent, the powder spectrum of NiAl–LDH displays a rather complex structure, thus making difficult to extract any useful spectral information (**Figure 11**). Nevertheless, specific information on the magnetic behaviour of the NiAl–LDH can be obtained from studying the variation of the doubly integrated ESR intensities with the temperature where the intensity of ESR signal increases upon cooling down (**Figure 12**), in good agreement with the SQUID measurements.

The ESR spectra at room temperature of the intercalated hybrids still show a single line with the absence of the hyperfine splitting, thus confirming the presence of intercalated CuPcTs complexes in **3** and **4** and discarding the demetalation of the host in the anion-exchange step (**Figure 13**).[215]

The extracted ESR parameters for the systems under consideration are summarized in **Table 4**. The absence of hyperfine splitting and the large line width of the ESR spectra are probably originated by the presence of dipolar interactions operating between the paramagnetic copper centers in the confined space offered by the LDH hosts; this assumption seems to be supported by the UV–Vis diffuse reflectance spectra of both hybrids (see **Figure 14**) that suggest dimerization. Concretely, the spectrum shows the two characteristic phthalocyanine absorption bands: *B* band (or Soret band) at about 320 nm and the *Q* band at 675–690 nm. These bands are attributed to π–π^* macrocycle ring

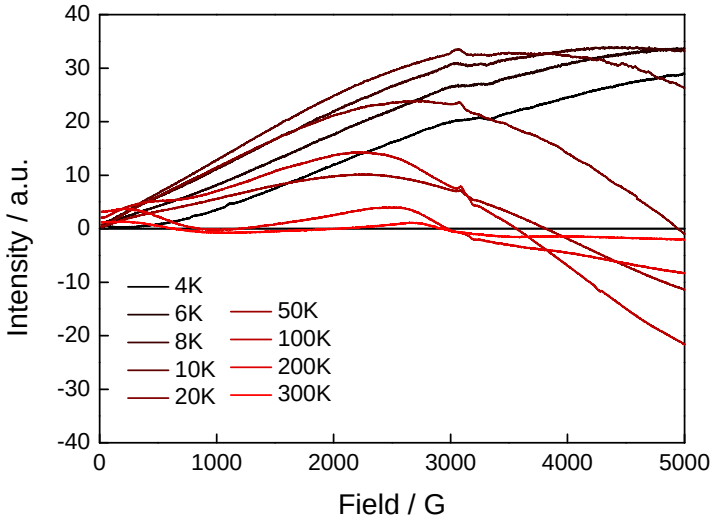

Figure 11. X-band ESR spectra of NiAl–LDH (**2**) recorded at different temperatures.

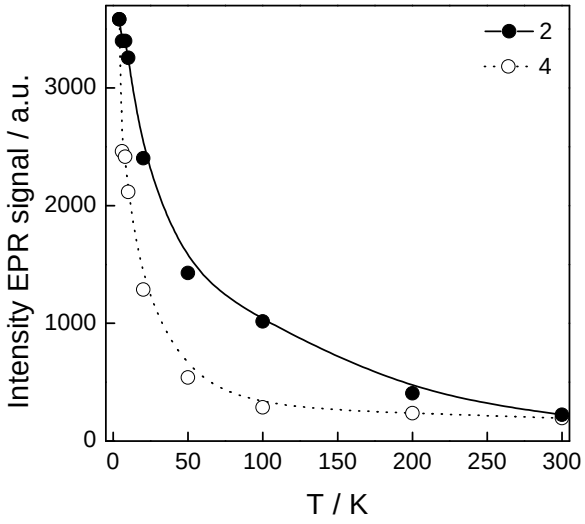

Figure 12. Plot of the ESR signal intensities of NiAl–NO_3 (**2**) (filled symbols, solid line) and NiAl–CuPcTs (**4**) (empty symbols, dashed line) as a function of temperature.

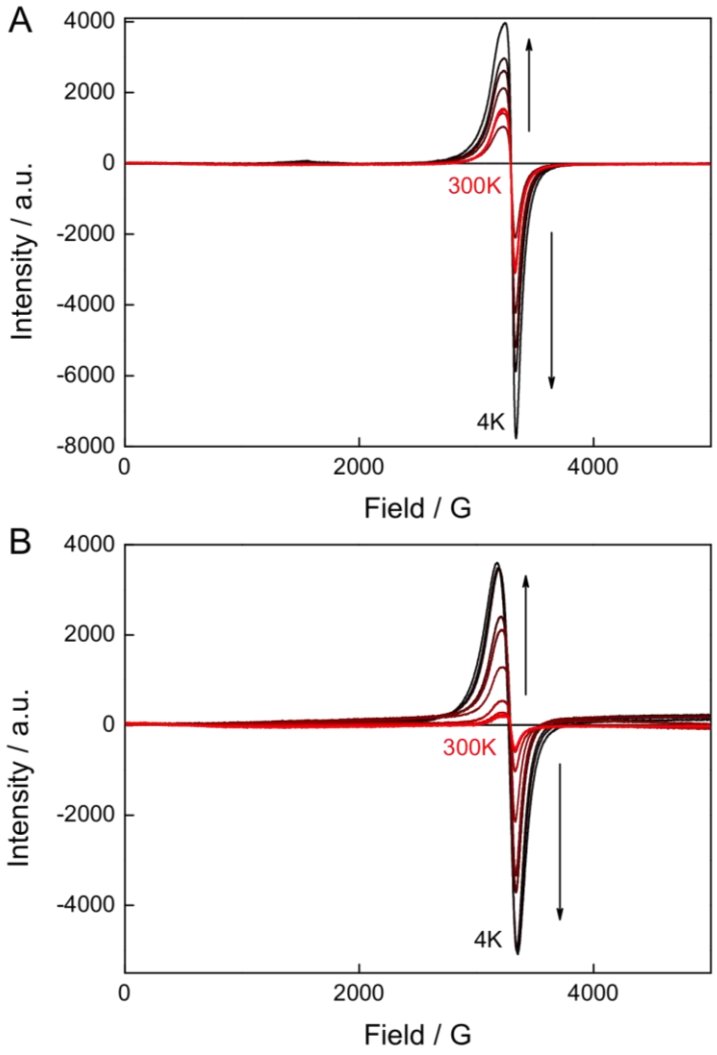

Figure 13. (A) X-band ESR spectra of ZnAl–CuPcTs (**3**) and (B) NiAl–CuPcTs (**4**) recorded at different temperatures.

transitions. Besides, likely due to the formation of dimeric species, a broad absorption band appears at *ca.* 610 nm. Dimerization is probably favoured by the perpendicular arrangement adopted by the macrocycles in the interlamellar space offered by the LDH layers (**Figure 14**). In addition, we detect in the ESR spectra a minor change of the *g*-factor of the CuPcTs complex in **3** and **4** in

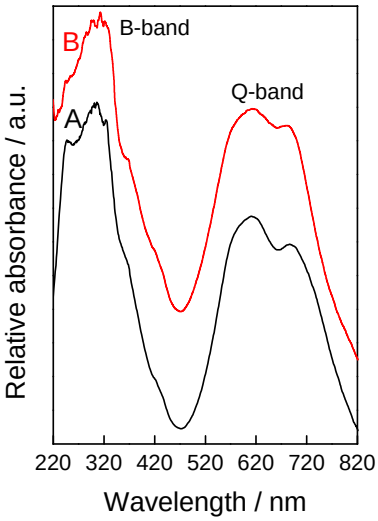

Figure 14. UV-Vis diffuse reflectance spectra of (a) ZnAl–Pc (**3**); and (b) NiAl–Pc (**4**).

Table 4. ESR parameters for CuPcTs and the two LDH–CuPcTs materials at room temperature, powder.

Sample	g	$g_{\perp}$	$g_{//}$	$W_{//}$ (G)	$W_{\perp}$ (G)
CuPcTs	2.1039	2.0361	2.0603	68	41
3	2.0954	2.0331	2.0559	62	40
4	2.0883	2.0306	2.0584	37	45

comparison with the nonintercalated material. According to previous works,[211] this slight change might be associated with small distortion from the planarity of the phthalocyanine ring induced by the confinement in the restricted space offered by the LDH matrix.

The spectrum of **4** can be described as the combination of two signals: a well-defined more intense response associated with the Cu (II) ions superimposed on a broader poorly defined signal, which shows a continuous increase with the field and stands for the presence of the NiAl–LDH layers (see **Figure 15**). This result seems to indicate that despite the magnetic interaction between the two spin sublattices remains weak, still some interactions may be present in **4** as shown by the small *g*-shift observed in the ESR signal associated with Cu(II) (see **Figure 16**).

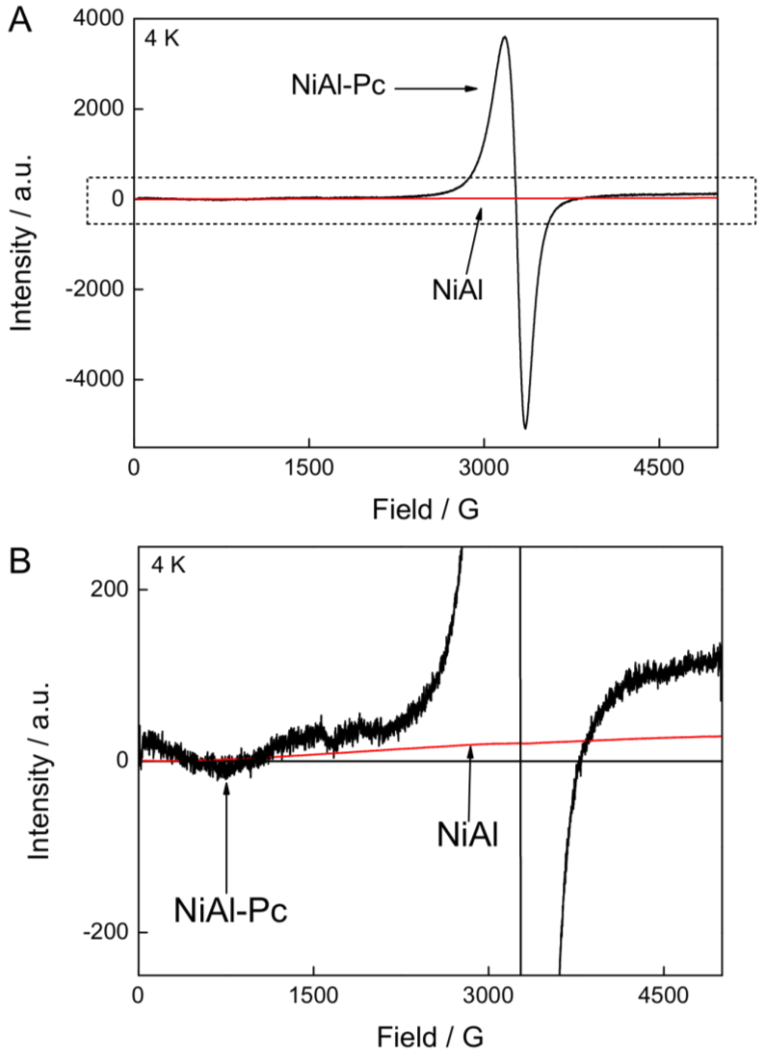

Figure 15. Left: X-band ESR spectra of NiAl–LDH (**2**; red) and NiAl–CuPcTs (**4**; black), at 4 K. Right: zoom-in of the selected area.

5.3. Conclusions

In summary, we have shown how the intrinsic flexibility of LDH materials can be used for the fabrication of hybrid magnetic multilayers by substitution of

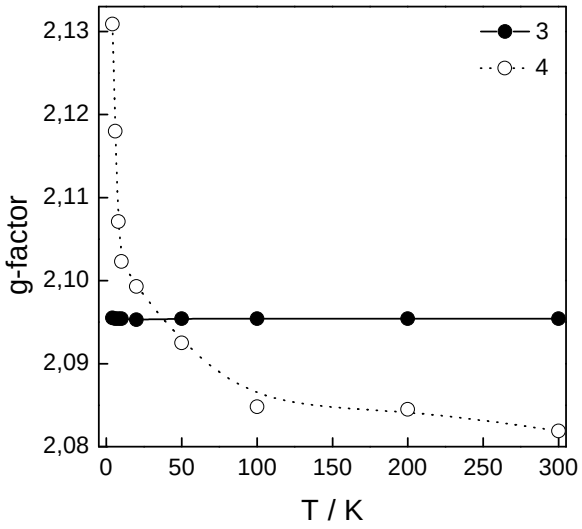

Figure 16. Variation of the *g*-factor value with temperature for the diamagnetic ZnAl–CuPcTs (**3**) and the magnetically active NiAl–CuPcTs (**4**) hybrids.

simple nitrate anions with the paramagnetic phthalocyaninetetrasulfonate (CuPcTs) complex via anion-exchange reactions.

First, the use of the diamagnetic ZnAl–LDH has permitted to extract the magnetic response of the paramagnetic complex in the confined medium offered by the layered host. Next, intercalation in the ferromagnetic NiAl–LDH has revealed that the presence of sandwiched copper(II) centers between the magnetic layers does not affect the overall magnetic response of the hybrid that is mainly controlled by the NiAl host. The T_M for NiAl–NO_3 and the hybrid NiAl–CuPcTs remain almost the same at around 4 K despite the intercalation of the complex promotes an expansion in the *BS* from 8.9 Å in **2** to 18.3 Å in **4**. While previous results on NiFe–LDHs have shown how the increase of the distance separating the hydroxide layers has a drastic impact on their magnetic behaviour due to differences in the interlayer interactions,[122] such change seems to be attenuated by the introduction of paramagnetic units between the layers.

This work represents the first step in the design of more advanced LDH-based hybrid materials in which the introduction of other anionic moieties having interesting magnetic properties (single molecule magnetic behaviour or spin-crossover, for example), may give rise to the isolation of more complex

magnetic materials. As a matter of fact, some attention has already been drawn on this work as illustrated by very similar systems consisting on a family of homometallic $Co_2(OH)_3$–Pc hybrids recently reported by G. Rogez and co-workers, in which the *Q*-band of the ESR spectra has been used for estimating the dipolar field strength operating in the interlamellar space (*i.e.* B_{dip} ~ 30 mT).[213]

5.4. Experimental Section

5.4.1. Synthesis

All chemicals $NiCl_2{\cdot}6H_2O$, $Zn(NO_3)_2{\cdot}6H_2O$, $Al(NO_3)_3{\cdot}9H_2O$, $AlCl_3{\cdot}6H_2O$, $NaNO_3$, HNO_3, $C_6H_{12}N_4$ (hexamethylenetetraamine, HMT), and copper(II) phthalocyaninetetrasulfonate (CuPcTs, tetrasodium salt, 85%, Aldrich) were used as acquired from commercial suppliers. All the experiments were carried out under an argon atmosphere.

5.4.2. Synthesis of ZnAl–LDH

*Synthesis of ZnAl–NO_3 LDH (**1**).* $[Zn_{0.64}Al_{0.36}(OH)_2](NO_3)_{0.36}{\cdot}0.4H_2O$ was synthesized according to the classical coprecipitation method first described by Miyata.[38] The respective metal nitrate salts were dissolved in Milli-Q purged water to reach a total metal cation concentration of 1 M in the final solution and fixing their stoichiometric coefficient at a value of x = 0.33 (equivalent to a Zn/Al molar ratio of 2:1). The reaction was carried out with excess of nitrate to make sure that it was the only specie present as interlamellar counter-anion. Two different solutions were dropwise added at room temperature: (a) 1 M solution of Zn^{2+} and Al^{3+} and (b) 1 M solution of NaOH and $NaNO_3$. The resulting mixture, with a pH of 8.2, was transferred to a Teflon-lined stainless steel autoclave and heated up to 80 °C on a preheated oven under autogenous pressure for 4 days. Finally, the resulting white precipitate was filtered, washed thoroughly with distilled water and ethanol, and dried at room temperature under vacuum.

5.4.3. Synthesis of NiAl–LDH

*Synthesis of NiAl–NO_3 LDH (**2**).* First, NiAl–CO_3 was synthesized following a homogeneous precipitation method, using HMT as ammonia releasing reagent (ARR). Accordingly, the chloride salts of the metals were dissolved in Milli-Q purged water, reaching a total metal cation concentration of 0.15 M in the final solution and keeping the stoichiometric coefficient constant at a value of x = 0.33 (equivalent to a Ni/Al molar ratio of 2:1). Next, an aqueous solution of HMT, whose concentration was fixed to be 3 times that of Al^{3+}, was added. The resulting green mixture was transferred to a stainless steel Teflon-lined autoclave and heated up to 140 °C in a preheated oven. After 4 days, the

autoclave was cooled on a bench to room temperature, and the resulting finely divided powder was filtered, washed thoroughly with distilled water and ethanol, and dried at room temperature under vacuum. The pH value of the remaining solution was found to be around 8.

$[Ni_{0.65}Al_{0.35}(OH)_2](NO_3)_{0.35}{\cdot}0.2H_2O$ (**2**) was prepared by carbonate exchange of the as-prepared NiAl–CO_3 LDH in presence of an excess of nitrate anions. In a typical procedure, 1 g of NiAl–CO_3 LDH was immersed in a round-bottom flask containing 1 L of an aqueous solution of $NaNO_3$ (1.5 M) and HNO_3 (0.005 M). This mixture was mechanically stirred under an inert atmosphere for 48 h. Afterward, the resulting green product was filtered, washed thoroughly with Milli-Q water and ethanol, and dried under vacuum at room temperature.

5.4.4. Anion Exchange

*Phthalocyanine Intercalation: ZnAl–CuPcTs (**3**) and NiAl–CuPcTs (**4**).* In a typical procedure, 300 mg of ZnAl–NO_3 (**1**) or NiAl–NO_3 (**2**) was finely powdered and transferred to a round-bottom flask. Then, 200 mL of a 0.005 M aqueous solution of Na_4CuPcTs was slowly added under an inert atmosphere. In addition, 30 mL of ethylene glycol (swelling agent) and 30 mL of ethanol (fluidizing agent) were added to the reacting mixture to favour the anion-exchange process. The mixture was sonicated for 10 min to obtain a homogeneous dispersion and then was vigorously stirred at 900 rpm for 3 days. Finally, the blue precipitate was filtered under an inert atmosphere, cleaned with a Soxhlet extractor to fully remove nonintercalated contaminant moieties, washed thoroughly with distilled water and ethanol until the presence of nonintercalated phthalocyanine in the washing residues was discarded, and dried at room temperature under vacuum.

$[Zn_{0.65}Al_{0.35}(OH)_2](CO_3)_{0.05}(CuPcTs)_{0.06}{\cdot}0.7H_2O$ (**3**) Anal. Calcd. for $C_{2.04}H_{4.20}O_{3.63}N_{0.50}Zn_{0.65}Al_{0.35}Cu_{0.06}S_{0.25}$ (FW = 157.63): C, 15.53; H, 2.66; N, 4.44; S, 5.08. Found: C, 16.72; H, 2.79; N, 4.53; S, 4.97.

$[Ni_{0.66}Al_{0.34}(OH)_2](CO_3)_{0.01}(CuPcTs)_{0.08}{\cdot}0.6H_2O$ (**4**) Anal. Calcd. for $C_{2.57}H_{4.18}O_{3.60}N_{0.64}Ni_{0.66}Al_{0.34}Cu_{0.08}S_{0.32}$ (FW = 164.91): C, 18.72; H, 2.55; N, 5.44; S, 6.22. Found: C, 20.12; H, 2.82; N, 5.87; S, 6.03.

5.4.5. Physical Characterization

Carbon, hydrogen, nitrogen, and sulfur contents were determined by microanalytical procedures using an EA 1110 CHNS-O elemental analyzer from CE Instruments. Metallic atomic composition of bulk samples was determined by means of electron probe microanalysis (EPMA) performed in a Philips SEM-XL30 equipped with an EDAX microprobe. Particles morphologies and dimensions were studied with a Hitachi S-4100 scanning electron microscope at an accelerating voltage of 20 keV over metalized samples with a mixture of gold and palladium for 30 s. Infrared spectra were recorded in a FT-IR Nicolet 5700 spectrometer in the 4000–400 cm^{-1} range using powdered samples diluted in KBr pellets. Thermogravimetric analyses of all compounds were carried out with a Mettler Toledo TGA/SDTA 851 apparatus in the 25–800 °C temperature range under a 10 °C min^{-1} scan rate and an air flow of 30 mL·min^{-1}. Powder X-ray diffraction patterns were collected with a Siemens d-500 X-ray diffractometer (Cu K_α radiation = 1.5418 Å) equipped with a rotating anode D-max Rigaku operating at 80 mA and 45 kV. Samples were mounted on a flat sample plate. Profiles were collected in the $2.5° < 2\theta < 70°$ range with a step size of 0.05°. HRTEM studies of the intercalated samples were carried out on a Technai G2 F20 microscope operating at 200 kV. Samples were prepared by dropping a suspension of the sample in ethanol on a lacey Formvar/carbon copper grid (300 mesh). Magnetic susceptibility measurements were performed on polycrystalline samples with a Quantum Design PPMS-9 model instrument. The susceptibility data were corrected by removing the diamagnetic contributions as deduced by using Pascal's constant tables. The dc data were collected in the range 2–300 K upon decreasing temperatures with an applied field of 1000 G, and hysteresis loops were collected between −8 and +8 T at 2 K. The ac data were collected in the range 2–30 K with an applied alternating field of 3.95 G at different frequencies in the range 10–10000 Hz. ESR experiments were performed by Dr. Filippo Busolo at ICMoL. ESR spectra were performed on powdered samples at X-band with a Bruker ELEXSYS E580 Oxford Instruments spectrometer equipped with a TE102 resonator and a helium cryostat to study the thermal dependence between 3 and 300 K. UV–Vis diffuse reflectance spectra of the powdered samples were recorded in a Jasco V-600 spectrophotometer equipped with an integration sphere.

6. Hybrid Magnetic Multilayers by Intercalation of Cobalt(II)-tetraphenylporphine Tetrasulfonate Complex in NiFe–LDH[†]

Hybrid magnetic multilayers have been synthesized by means of intercalation of [5,10,15,20-tetrakis(4-sulfonatophenyl)porphyrinato]cobalt(II) (CoTPPS) complex in the interlayer space of a $Ni^{II}Fe^{III}$ layered double hydroxide through anion-exchange reaction. A sebacate ($^{-}OOC–(CH_2)_8–COO^{-}$) intercalated NiFe–LDH have been used as precursor, facilitating the anion exchange reaction, thus permitting the inclusion of a paramagnetic macrocycle inside the ferrimagnetic NiFe–LDH layers. The material has been characterized by XRD, FT-IR, SEM, SQUID and ESR. For the hybrid NiFe–CoTPPS the temperature at which spontaneous magnetization is observed, *ca.* 11–12 K, is very close to that shown by the precursor, despite that the intercalation of the complex promotes an expansion in the basal space from 15.4 to 22.4 Å.

[†] Abellán, G.; Coronado, E.; Gómez-García, C. J.; Martí-Gastaldo, C.; Ribera, A. *Polyhedron* **2013**, *52*, 216.

6.1. Introduction

The ability of LDHs to accommodate a wide variety of functional molecules has currently opened the door for a myriad of applications. Concerning layered hydroxide–porphyrin hybrids, the attention has recently focused on their possible photophysical, photochemical, catalytic, and sensing applications.[216] If compared to free porphyrin and phthalocyanine molecules, these sort of hybrids exhibit several potential advantages, *i.e.* improved thermal and chemical stability, reduction of aggregation, tuning by layered hydroxide composition, and arrangement in transparent films.[216]

With respect to magnetism, the existing examples are very scarce. Thus, we have described in the previous Chapter the magnetic properties of paramagnetic copper phthalocyanine complexes inserted in two different LDHs, the diamagnetic ZnAl and the ferromagnetic NiAl. These studies have shown that the paramagnetic complex does not affect the magnetic ordering in the LDH layers.[165] In this context, mononuclear magnetically active macromolecules like porphyrins are promising candidates to obtain hybrid magnetic materials. Porphyrin-intercalated LDH materials were extensively considered[71,196,205] at the beginning of 90's in view of their appealing catalytic properties. Several synthetic approaches have been used to obtain porphyrin–LDH materials, but to the best of our knowledge this is the first work regarding the anion exchange intercalation and magnetic characterization of a CoTPPS guest in a magnetic NiFe–LDH host.

The prepared NiFe–CoTPPS material has been fully characterized including ESR and magnetic measurements that confirm the presence of ferrimagnetic NiFe layers coexisting with paramagnetic CoTPPS intercalated anions.

6.2. Results and Discussion

The hybrid NiFe–CoTPPS material has been synthesized using a NiFe–Seb LDH as precursor (Seb = $^{-}OOC–(CH_2)_8–COO^{-}$). The large basal spacing offered by this compound has proven to be an advantage for further intercalation of variable molecular entities. In fact, this approach allows for the intercalation of large molecules in short periods of time and avoiding the use of additional swelling agents, in contrast to the synthetic methodology described in the previous Chapter for the intercalation of Pc moieties. On the other hand, suffers from having worst crystallinity and morphologies. The NiFe–Seb precursor has been synthesized by using a modified co-precipitation method that maintains a constant pH value in the reaction medium to avoid the formation of contaminant non-LDH phases.

The inclusion of the as-synthesized CoTPPS complex has been made by anion exchange reaction under inert atmosphere with continuous stirring. Thus, a suspension of the NiFe–Seb precursor has been purged with Argon and a solution of the CoTPPS was added dropwise. A scheme of the synthesis is shown in **Figure 1**. This straightforward strategy has already been successfully used by our group for the insertion of oxalate complexes.[212] Still, in the present study we develop the intercalation of a large complex, taking advantage of the intrinsic flexibility of the LDH host to accommodate a wide variety of organic molecules. This increase in the separation of the magnetic layers offers us an ideal scenario for the insertion of many different magnetic compounds in between ferrimagnetic LDH layers.

6.2.1. Structural Characterization

X-ray diffraction patterns of the NiFe–Seb precursor and its corresponding NiFe–CoTPPS are shown in **Figure 2**. They show a typical XRD pattern with sharp and symmetric peaks corresponding to (00*l*) reflections (indexed assuming a 3*R* symmetry) and broad and less intense peaks at high 2Θ values, corresponding to (0*kl*) reflections.[8] The broad reflection around 60º could be indexed as (110), with respect to the hexagonal axes.

After the intercalation process, the mild conditions associated to the anion exchange reaction have permitted us to obtain a material without any significant loose of crystallinity.

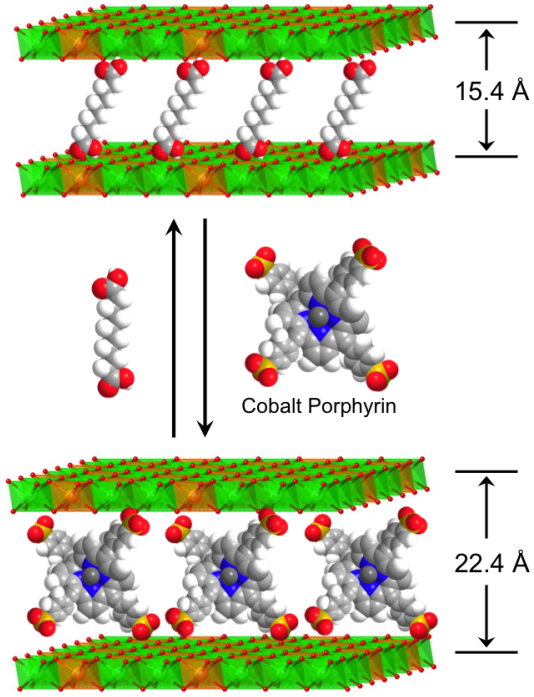

Figure 1. Schematic representation of the synthesis of the CoTPPS intercalated NiFe–LDH, illustrating the anion exchange reaction from the initial NiFe–Seb precursor.

The final material shows a large increase in the basal space, from 15.4 Å in the NiFe–Seb precursor to 22.4 Å, in the NiFe–CoTPPS sample as expected for the inclusion of a large macrocycle such as porphyrin (see **Table 1**). The as-obtained basal space is in excellent agreement with previous reported values in the literature.[217–219] By subtracting the thickness of the brucite-like LDH layer (*ca*. 4.8 Å), a *BS* of 17.6 Å could be obtained, similar to the estimated size of CoTPPS (18 x 18 Å).[218,219] These results suggest a perpendicular orientation of the CoTPPS anions in the interlamelar space of the LDH, in excellent accordance with the values reported by Taviot-Guého et al. for a Zn and Fe–TPPS,[212] and related precedents for cobalt porphyrins.[217]

FT-IR spectroscopy is a very useful technique to determine intercalated molecules in LDH materials. The as-recorded spectrum shows how the characteristic vibration modes associated to the cobalt porphyrin between 1600 and 1000 cm^{-1} are present in the NiFe–CoTPPS material.

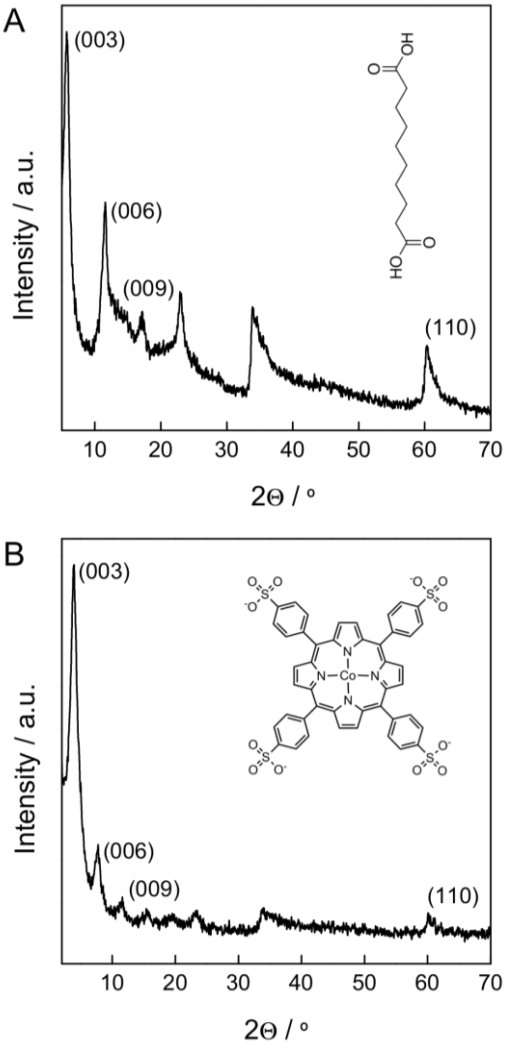

Figure 2. Powder X-ray diffraction patterns of the NiFe–Seb (A) and NiFe–CoTPPS (B) samples. The inset represents the corresponding interlamellar anion molecular structure.

The sulfonate bands of the product appear at 1208, 1180, 1125 and 1037 cm^{-1} (see **Figure 3**). Moreover, characteristic absorption bands could be observed at 1006, 882 and 855 cm^{-1} (C–H pyrrole bending) and at 1407, 1349 and 1311 cm^{-1} (C–N stretching). Both LDH materials exhibit broad intense peaks between

Table 1. X-ray diffraction data and unit cell parameters for NiFe–Seb and NiFe–CoTPPS.

	2Θ [°] (*hkl*)					Calc param[a] [Å]		
Sample	**(003)**	**(006)**	**(009)**	**(110)**	$d_{(110)}$	***a***	***c***	***BS***
NiFe–Seb	5.75	11.55	17.20	60.26	1.54	3.07	46.17	15.39
NiFe–CoTPPS	3.80	7.75	11.60	60.05	1.54	3.08	67.38	22.40

[a] $a = 2d_{110}$; $c = d_{003} + 2d_{006} + 3d_{009}$; $BS = c/3$.

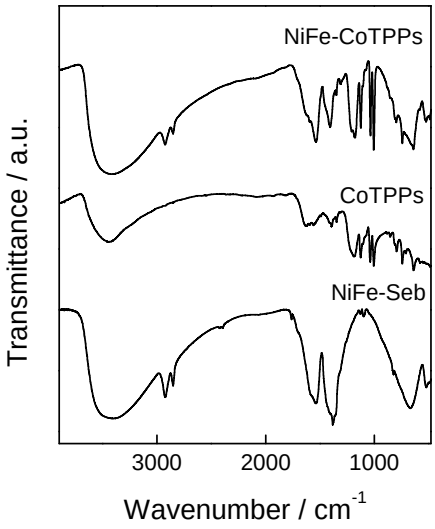

Figure 3. From *top* to *bottom*: FT-IR spectra of NiFe–CoTPPS, CoTPPS and NiFe–Seb compounds.

3430 and 3400 cm^{-1}, related with the O–H stretching vibration mode of the water molecules intercalated within the interlamellar space. In addition, the presence of residual sebacate anions can be confirmed by the doublet in the 2925–2850 cm^{-1} range, related with the C–H stretching mode of the $–CH_2$ alkyl groups of the dicarboxylic acid. This assumption seems to be supported by an AEC value of 69.9 % according to the metal composition estimated from EDAX, as expected for this kind of hybrid complex-LDH systems. Finally, the bending vibrational modes of the hydroxometallic octahedral complexes can be observed at lower wavenumbers (in the 540–480 cm^{-1} range).

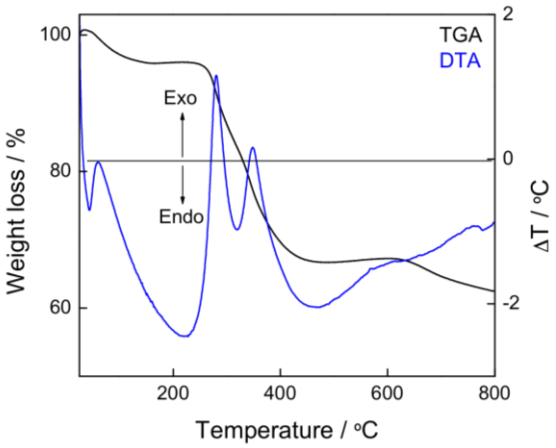

Figure 4. Representative TG/DTA curves of the NiFe–CoTPPS.

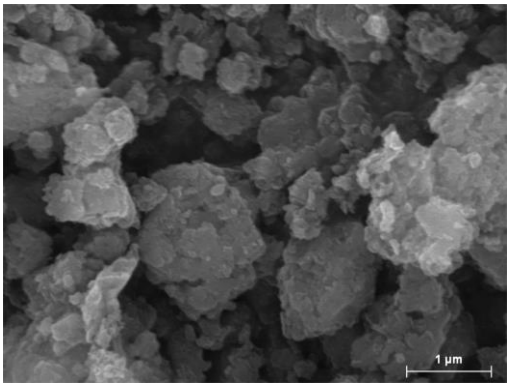

Figure 5. Representative SEM image of the NiFe–CoTPPS material.

Thermogravimetric analyses have been carried out for all the samples under an air atmosphere in the 25–850 °C range. The TG/DTA curve of NiFe–Seb exhibits an initial low-temperature mass loss in the 90–200 °C region, related with the thermal desorption of surface and intercalated water molecules (**Figure 4**). In contrast with the thermal behaviour observed in cobalt porphyrins intercalated in non-magnetic MgAl–LDHs, a decrease in the decomposition temperature of both the LDH matrix and the CoTPPS units can be observed.

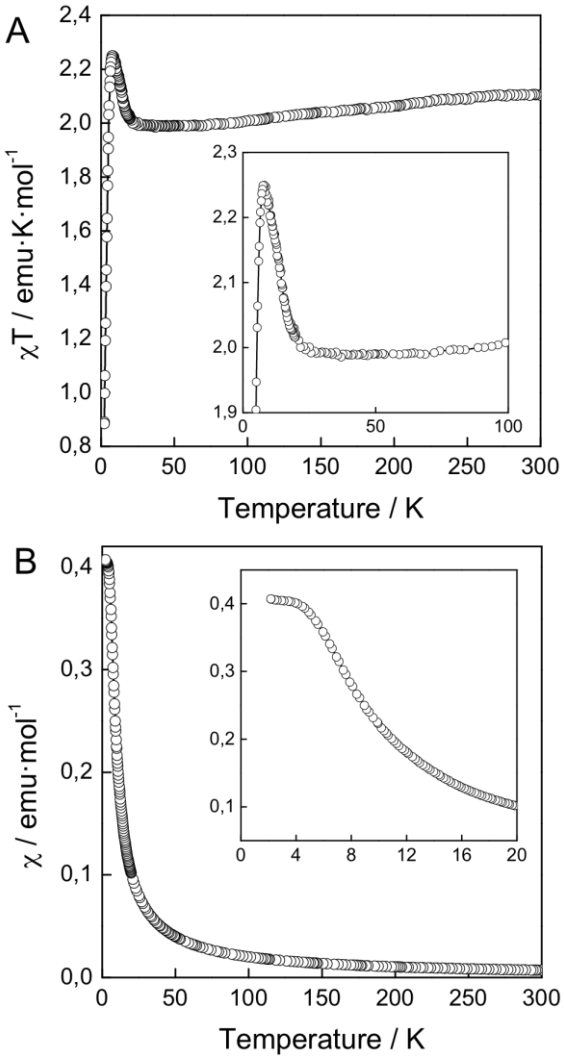

Figure 6. Thermal variation of the $\chi_M T$ product (A) and χ_M (B) for NiFe–CoTPPS. Solid lines are only a guide to the eye. Insets show the low temperature regions.

Thus, in the 200–400 ºC range, the dehydroxylation of the LDH matrix and the decomposition of the porphyrin take place. These processes are probably related with the catalytic activity of the metal nanoparticles formed *in situ*, as reflected in the exothermic peak centered at around 280 ºC in the DTA plot.[201]

Scanning electron microscopy of the intercalated NiFe–CoTPPS reveals a homogeneous material consisting of aggregates of round-shaped platelets, as expected for anion exchanged LDH (see **Figure 5**).

6.2.1. Magnetic Properties

The product of the molar magnetic susceptibility times the temperature of NiFe–CoTPPS shows a room temperature value of 2.11 emu·K·mol^{-1} (**Figure 6A**) close to the expected value for isolated Ni^{II}, Fe^{III} and Co^{II} ions with the metal composition estimated with EDAX. When the temperature is decreased, the $\chi_M T$ value smoothly decreases to reach a broad minimum of *ca.* 2.0 emu·K·mol^{-1} at *ca.* 40 K. At lower temperatures $\chi_M T$ shows an abrupt increase to reach a maximum of *ca.* 2.25 emu·K·mol^{-1} at *ca.* 8 K (inset in **Figure 6A**). Below 8 K, $\chi_M T$ decreases very sharply to reach a value of *ca.* 0.9 emu·K·mol^{-1} at 2 K. The thermal variation of the magnetic susceptibility shows a continuous increase when the temperature is decreased with a larger increase at *ca.* 10–12 K, corresponding to the abrupt increase in the $\chi_M T$ plot (**Figure 6B**). At low temperatures χ_M shows a reduced slope and reaches a plateau below *ca.* 4 K (inset in **Figure 6B**). The smooth decrease in the $\chi_M T$ plot at high temperatures suggests the presence of a weak antiferromagnetic interaction in the NiFe–CoTPPS sample, as also suggested by the negative Weiss constant value (θ = –5.4(2) K) obtained by fitting the Curie plot above 40 K (**Table 2** and **Figure 7**). This antiferromagnetic coupling between the Ni(II) and Fe(III) ions through the oxo bridges in the LDH layers is similar in nature although slightly higher than the one observed in the NiFe–Seb sample (θ = –2.67 K),[122] probably due to the presence of a spin–orbit coupling in the CoTPPS units that results in a decrease of the magnetic moment of the sample even if the Co(II) ions are magnetically isolated. The minimum observed in the $\chi_M T$ plot at *ca.* 40 K confirms the low dimensional ferrimagnetic behaviour of the NiFe layer, whereas the sharp increase of $\chi_M T$ at low temperatures suggests the presence of a long range ferrimagnetic ordering. Finally, the sharp decrease at low temperatures is simply due to the saturation observed in the χ_M plot at low temperatures (that becomes a sharp decrease in the $\chi_M T$ plot).

Table 2. Main magnetic data and parameters for NiFe–CoTPPS.

$\chi_M T_{rt}$	C (emu·K·mol^{-1})	C_{so} (emu·K·mol^{-1})	Θ (K)	T_M (K)	M_S[a] (μ_B)	M_R (μ_B)	H_{Coer} (G)
2.11	2.13	2.35	–5.4	12.5	2.12	0.02	280

[a] Magnetization saturation (*Ms*) has been estimated by extrapolation to $1/H = 0$ of the magnetization *vs.* $1/H$ plot at 2K.

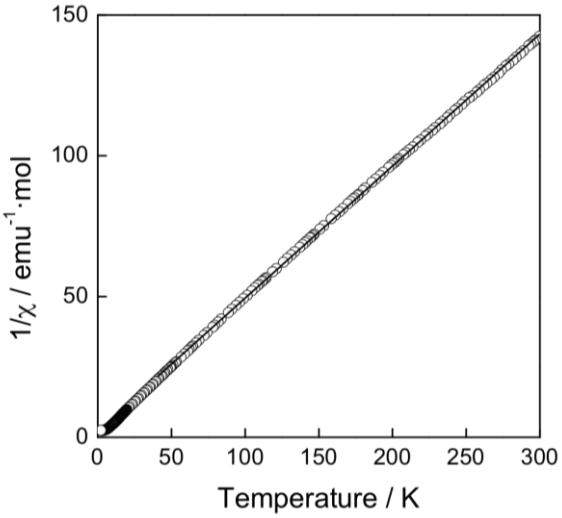

Figure 7. Best fitting (solid line) of the magnetic susceptibility data to a Curie–Weiss law.

A further confirmation of the antiferromagnetic interactions in the NiFe layer is provided by the isothermal magnetization at 2 K (**Figure 8**), that shows a lack of saturation even at magnetic fields as high as 80 kG. Moreover, the isothermal magnetization at 2 K also confirms the presence of a "long range ordered state" since it shows at 2 K a hysteresis cycle with a coercive field of *ca.* 280 G (inset in **Figure 8**). Note that this behaviour is similar to that observed in NiFe–Seb with similar coercive fields (280 G compared to 200 G).[122]

The presence of a magnetic "ordering" was further confirmed with ac susceptibility measurements under an oscillating field of 16 G in the frequency range 10–10000 Hz (**Figure 9**). These measurements show a frequency dependent maximum in the in phase (χ_M') signal at *ca.* 4.5–5.3 K together with

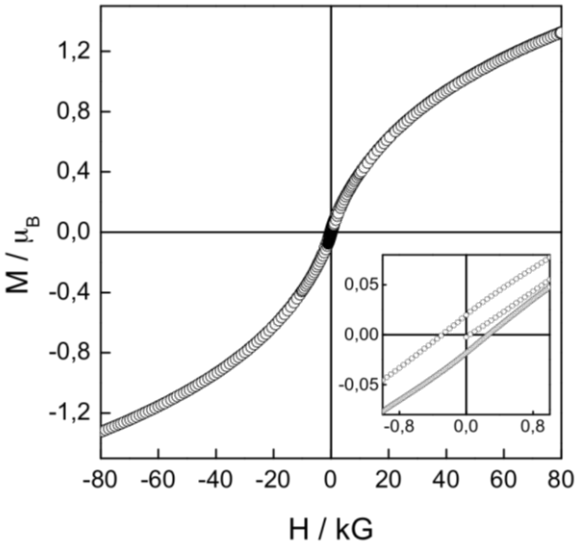

Figure 8. Hysteresis loop of NiFe–CoTPPS measured at 2 K. Inset shows the low field region.

a shoulder at higher temperatures (9.5–11.0 K). These in-phase features are accompanied by two out-of-phase (χ_M") peaks, one at low temperatures (3.5–4.4 K) and a broader one at higher temperatures (8.9–10.5 K). The high-temperature (χ_M") peak may be attributed to a "ferrimagnetic ordering", in agreement with the dc susceptibility measurements (see above) and with the behaviour observed in the related NiFe–Seb and NiFe–$Cr(ox)_3$ layers, that show T_M values at *ca.* 11.0 and 12.0 K, respectively.[122,212] Note that the large frequency dependence exhibited by the ac susceptibility signals prevents us to get an accurate estimate of T_M in the NiFe–CoTPPS sample. In any case, a value for T_M in the range 12–13 K can be estimated from the temperature at which χ_M" becomes non-zero. The proximity of this value with those estimated for the other two compounds despite the large differences in the interlayer distances (15.4, 9.9 and 22.4 Å in the NiFe–Seb, NiFe–$Cr(ox)_3$ and NiFe–CoTPPS samples, respectively) confirms the 2D nature of the magnetic ordering. The frequency dependence of the high temperature χ_M" signal is easy to analyze. Thus, this peak shows a frequency dependence whose normalized variation, measured as the peak shift per decade of frequency, $\Delta T_{max}/T_{max}\Delta(\text{Log } \nu)$, is

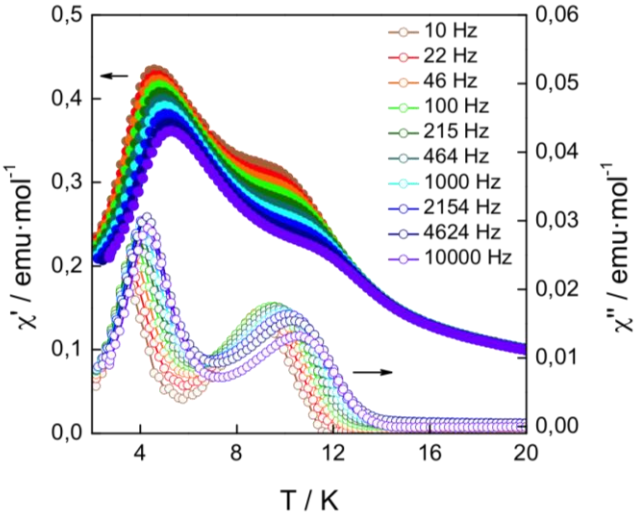

Figure 9. Thermal variation of the in phase (χ_M', full symbols, left scale) and out-of-phase (χ_M", empty symbols, right scale) ac magnetic susceptibility for NiFe–CoTPPS at different frequencies in the 10–10000 Hz range.

0.053–0.063 (depending on the T_{max} value used). Note that this value is much larger than the typical values observed in canonical spin glasses (0.005–0.018) and it is smaller than the typical values observed in superparamagnets (*ca.* 0.30), but lies within the normal range observed for spin glass-like materials (0.06–0.08).[163] Therefore, we can conclude that the NiFe–CoTPPS sample behaves as a spin glass-like system and we can attribute the slight frequency dependence of the high temperature χ_M" signal to the presence of some structural disorder in the ferrimagnetic layers. This disorder is most probably due to Ni^{II}/Fe^{III} exchanged positions, as detailed in previous Chapters, and/or vacancies compensated with the corresponding vacancies in the organic layers, in agreement with the chemical analysis. On the other side, the low temperature χ_M" peak may be related to the movement of the domain walls in the ordered ferrimagnetic phase. This assumption is confirmed by the analysis of the frequency dependence of the low temperature peak that follow an Arrhenius law, $\nu = \nu_0 \cdot \exp(-E_a/kT)$, with an activation energy of 132 K for the χ_M" peak (**Figure S1**).

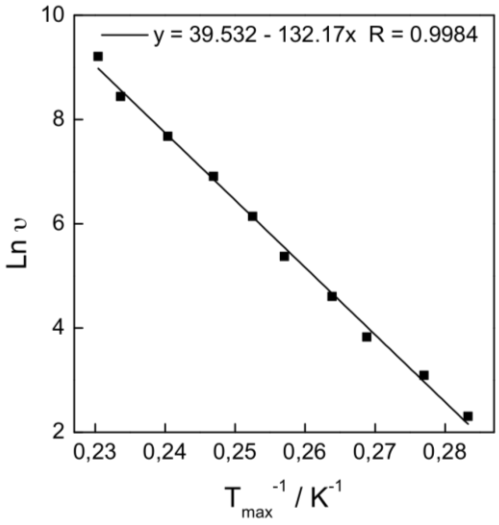

Figure 10. Arrhenius plot of the low temperature peak in the χ_M" signal.

A value close to those observed for this kind of domain wall movement in other similar 2D magnets.[119,220–222]

6.2.2. ESR Studies

An indication of the presence of magnetically isolated CoTPPS units in the hybrid is provided by the electronic spin resonance (ESR). Thus, the NiFe–CoTPPS sample shows a narrow line ($\Delta H_{p\text{-}p} \approx 20$ mT) at $g_{//} = 2.006$ which is similar to the one observed in the Co–TPPS sample ($\Delta H_{p\text{-}p} \approx 10$ mT) at $g_{//} = 2.018$ arising from the unpaired electron in the low-spin Co(II) complex located on the d_{z2} orbital.[218,219,223] The main difference between the spectra of CoTPPS and the NiFe–CoTPPS samples is the presence of a hyperfine structure in the perpendicular component of the NiFe–CoTPPS sample that appears at *ca.* 2450 G ($g_{\perp} = 2.74$, $\langle g \rangle = 2.49$). This hyperfine structure, composed by eight signals, comes from the coupling of the electronic spin S = 1/2 of the Co^{II} with its $I = 7/2$ nuclear spin. It has already been observed in other CoTPPS derivatives.[223] Its presence in the CoTPPS units inserted between the NiFe layers suggests that the CoTPPS anions are much more isolated in the NiFe–CoTPPS compound that in the pristine CoTPPS sample. This is in agreement with the low anion loading imposed by the cationic NiFe layers. In fact, the Co:Fe ratio is below the

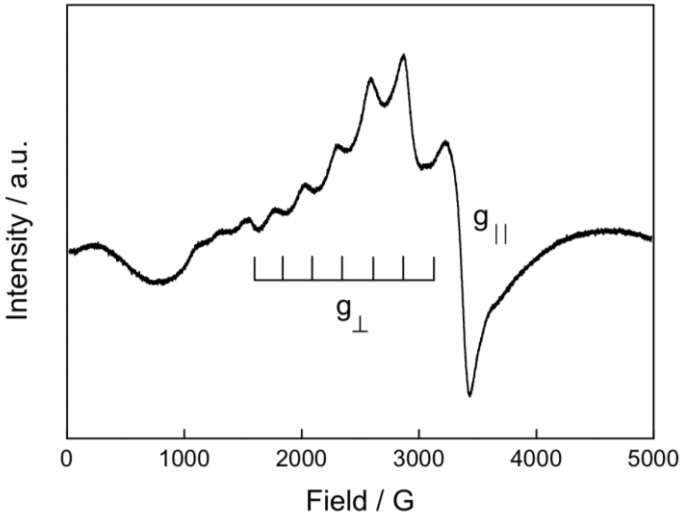

Figure 11. X-band ESR spectra of the NiFe–CoTPPS at 10 K.

maximum theoretical value (1:4), indicating that the CoTPPS units are quite well isolated.

6.3. Conclusions

We have demonstrated that it is possible to intercalate paramagnetic CoTPPS anionic units in between cationic NiFe–LDH. This intercalation process has not significantly modified the NiFe layers and thus, the NiFe–CoTPPS sample presents a "ferrimagnetic behaviour" similar to the one observed in the sebacate-intercalated NiFe precursor, as previously observed with the copper phthalocyanine complex.[165] Magnetic dc and ac susceptibility and magnetization measurements have confirmed the ferrimagnetic "ordering" in the NiFe–CoTPPS compound with a temperature for the onset of spontaneous magnetization of *ca.* 12 K and a coercive field of *ca.* 28 mT at 2 K. Additionally, ac measurements agree with a spin glass-like behaviour, coming probably from the cation disorder in the layers.[31,179] These measurements also show the presence of an activated domain wall movement inside the layers in the ordered phase.

6.4. Experimental

6.4.1. Synthesis of NiFe–Sebacate

All chemicals, $Ni(NO_3)_2{\cdot}6H_2O$, $Fe(NO_3)_3{\cdot}9H_2O$, $HO_2C(CH_2)_8CO_2H$ (sebacic acid), NaOH, (Sigma–Aldrich) and ethanol (Fluka) were used as received without further purification.

The precursor LDH material NiFe–Sebacate (NiFe–Seb) was prepared following the general method described previously by our group,[201] using sebacic acid/NaOH. In a typical synthesis, the salts of nickel and iron were dissolved in deionized water, keeping the stoichiometric coefficient $x = M^{III}/(M^{II} + M^{III}) = 0.33$, and the total metal concentration constant at 1 M. A second solution of NaOH and sebacic acid was also prepared using deionized water. Both solutions were mixed together by dropwise addition to form a thick slurry with a pH of 7. Subsequently, the slurry was heated up to 80 °C under constant stirring, and kept at this temperature for 4 days at atmospheric pressure. The solid was then filtered, abundantly washed with water and ethanol, and dried at room temperature under vacuum. All procedures were carried out under argon atmosphere to avoid incorporation of carbonate anions adsorbed from atmospheric CO_2 into the final precursor. Furthermore, the pH of the synthetic gel was controlled to avoid formation of solid phases different from LDH.

6.4.2. Synthesis of CoTPPS

All chemicals, 5,10,15,20-tetrakis(4-sulfonatophenyl)porphyrin (TPPS), NaOH, $Co(OAc)_2$ and EtOH where purchased from Sigma–Aldrich and were used as received without further purification. In the present investigation CoTPPS was prepared as reported elsewhere.[223] An aqueous solution of TPPS (0.25 g) was converted into the tetrasodium salt by adition of NaOH 2 M at a controlled pH value in the 7.5–8.0 range. An aqueous solution of cobalt(II) acetate (0.6 g) was slowly added and the reaction mixture was heated at 60 °C for 1 h. Finally, the cobalt(II) chelate was purified by recrystallization from ethanol–water.

6.4.3. Anion Exchange

In a typical procedure, 200 mg of NiFe–Seb was finely powdered and transferred to a round bottom flask. Then, 50 mL of a 0.003 M aqueous solution of CoTPPS was slowly added under inert atmosphere. The suspension was stirred at 70 °C

for 24 h. Finally, the NiFe–CoTPPS precipitate was filtered under inert atmosphere, washed thoroughly with distilled water and ethanol, and dried at room temperature under vacuum.

6.4.4. Physical Characterization

Carbon, hydrogen, nitrogen and sulphur contents were determined by microanalytical procedures using an EA 1110 CHNS-O Elemental Analyzer from CE instruments. Metallic atomic composition of bulk samples was determined by means of electron probe microanalysis (EPMA) performed in a Philips SEM-XL30 equipped with an EDAX microprobe. Particles morphologies and dimensions were studied with a Hitachi S-4100 scanning electron microscope at an accelerating voltage of 20 keV, over metalized samples with a mixture of gold and palladium during 30 s. Infrared spectra were recorded in a FT-IR Nicolet 5700 spectrometer in the 4000 to 400 cm^{-1} range using powdered samples diluted in KBr pellets. Thermogravimetric analysis of all compounds were carried out with a Mettler Toledo TGA/SDTA 851 apparatus in the 25–800 °C temperature range under a 10 $°C \cdot min^{-1}$ scan rate and an air flow of 30 $mL \cdot min^{-1}$. Powder X-ray diffraction patterns were collected with a Siemens d-500 X-ray diffractometer (Cu K_α radiation =1.5418 Å) equipped with a rotating anode D-max Rigaku operating at 80 mA and 45 kV. Samples were mounted on a flat sample plate. Profiles were collected in the $2.5° < 2\theta < 70°$ range with a step size of 0.05°. The magnetic measurements were performed on a polycrystalline sample with a Quantum Design MPMS-XL-5 SQUID magnetometer in the temperature range 2–300 K with an applied magnetic field of 1000 G. The isothermal magnetization measurements were done at 2 K with fields from –8 to +8 T in a Quantum Design PPMS-9 equipment. AC susceptibility measurements were performed on the same sample in the temperature range 2–20 K with an oscillating magnetic field of 1.6 mT in the frequency range 10–10000 Hz with the PPMS equipment. Susceptibility data were corrected for the sample holder and for the diamagnetic contribution of the sample using Pascal's constants.[224] ESR experiments were carried out by Prof. Carlos J. Gómez-García at ICMol. ESR spectra were performed on powdered samples at X-band (9.47 GHz) in the temperature range 4.2–300 K with a Bruker ELEXSYS E580 spectrometer equipped with a helium cryostat.

7. Photo-Switching in a Hybrid Material Made of Magnetic LDHs Intercalated with Azobenzene Molecules[†]

We report a magnetic photoresponsive hybrid material prepared by intercalation of a switchable trans-azobenzene-4,4′- dicarboxylate guest in the interlamellar space offered by a ferromagnetic $Co^{II}Al^{III}$–LDH host. Exposure to UV light triggers a compression/modification of the in-plane structure of the layered hybrid as result of the guest isomerization, causing a drop of the magnetization at 2 K close to 27% and an increase in the T_M of *ca.* 1 K. This photo-induced change can be reverted by means of proton assisted thermal isomerization in the presence of water acting as proton carrier, thus enabling reversible switching of the magnetism of the solid. A mechanism for the *cis* to *trans* isomerization is proposed.

[†] Abellán, G.; Coronado, E.; Martí-Gastaldo, C.; Ribera, A.; Jordá, J. L.; García, H. *Adv. Mate*r. **2014**, *26*, 4156. This work has been carried out in collaboration with Prof. H. García at the Instituto de Tecnología Química (CSIC-Universitat Politécnica de València)

7.1. Introduction

Multifunctional hybrid materials currently represent a hot topic in materials science. The so-called hybrid approach has been widely explored as an efficient route to chemically design this type of materials that can display unprecedented combination of desirable physical properties. In a first approach, these solids can be made up from the combination of two components that possess different intrinsic functionalities and can be combined into a single material. Still, these components behave as independent networks in these chemically assembled layered superstructures and display poor physical interaction.[69,74,124,225–227] A more sophisticated case arises when both components are coupled and new properties appear from their mutual interaction. This can be achieved by introducing a stimulus responsive molecule in a functional framework so that its ability to undergo physical change can modify the properties of the host.[228–230] In this last case, LDHs offer a broad range of possibilities.[27,73] The versatility of LDHs enables chemical design of a broad range of hybrid functional materials by deliberate choice of the guest whose physical properties can be then combined with the intrinsic magnetism of the host.[120,124,128,152,165,201,231]

In this context, the introduction of anionic photo-switchable molecules in the interlamellar space of the LDH host to produce a photoresponsive material whose magnetism can be reversibly changed with light through the switching of the guest molecule represents an open challenge. Among the potential candidates, azobenzenes are arguably the best examples of photo-switchable molecules as these molecules undergo photoinduced *trans-cis* isomerization in solution upon UV light irradiation.[232,233] Related, photoresponsive inorganic-azobenzene nanocomposites have been reported for layered silicates or hexaniobates.[234–240] Still, the performance of these hybrid solid matrices is generally limited by the restricted switching ability of the intercalated molecules in a confined space and light scattering, that reduces the radiation that the guests can absorb.[241] Notwithstanding these problems, we have shown that azobenzene-4,4′-dicarboxylic acid can be reversibly isomerized when embedded in silica gels, an intermediate state between solution and solid state (see **Appendix I** for a complete description of the preliminary photochemical studies underlying this chapter).[242] Although there is a vast number of reports

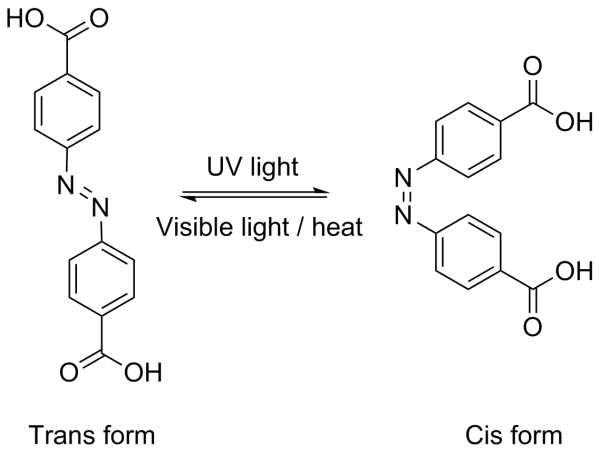

Figure 1. The photochemical isomerization of azobenzene-4,4'-dicarboxylic acid (T1).

describing an enhancement in the thermal stability of azo dyes when intercalated in LDHs,[81,243–246] when it comes to photo-isomerization, the list of examples is very scarce and is almost limited to organic polymers doped with azo dyes,[247] where the porous nature of the host and flexibility of the guest lead to enlarged gallery void and better mobility.

We describe a layered hybrid built from the intercalation of trans-azobenzene-4,4′-dicarboxylic acid (T1) molecules in a ferromagnetic CoAl–LDH. The magnetism of the host is substantially modified upon light irradiation as result of the partial photo-isomerization of the guest to the corresponding *cis* isomer (See **Figure 1**).[242] This triggers a structural rearrangement of the layers that compresses the gallery height and modifies their internal structure that alters the overall magnetic behaviour of the hybrid. This structural/magnetic change is reversible in the presence of moisture. A plausible mechanism to understand the role of the water in the *cis* to *trans* isomerization is proven.

7.2. Results and Discussion

$CoAl–NO_3$ LDH was prepared by a modified homogeneous precipitation method that involves the addition of urea to an aqueous solution containing the metal salts followed by carbonate-exchange reaction.[45,46,144] CoAl–T1 was then obtained by exchange reaction of the nitrate form of CoAl–LDH with the photoactive guest T1 (azobenzene-4,4′-dicarboxylic acid; $C_{14}H_{10}N_2O_4$) (See **Figure 2A**).

7.2.1. Structural Characterization

As confirmed with field emission scanning electron microscopy (FE-SEM), this mild route enables quantitative intercalation of the guest without affecting the original size and morphology of the pristine lamellae (**Figure 2B**). Intercalation of T1 was monitored with X-ray powder diffraction (XRPD) (**Figure 2A**, **Table 1**). Here, the exchange of NO_3^- with bulkier T1 molecules increases the basal space (*BS*) from 8.88 to 20.00 Å, in good agreement with the dimensions of T1 (see **Figure 3**). The estimated molecular length of the T1 molecule (15.17 Å) has been calculated by optimizing the azobenzene structure with molecular dynamics, and performing a DFT minimizing energy/geometry job (B3LYP/6-31G; developed using the ChemBio 3D Ultra software supplemented with GAMESS, CambridgeSoft).

The high crystallinity of CoAl–T1 is confirmed by the presence of sharp (00*l*) diffraction peaks that can be observed even at high 2θ angular values. We estimate an empirical formula of $[Co_{0.65}Al_{0.35}(OH)_2](C_{14}H_{10}N_2O_4)_{0.17}{\cdot}0.5H_2O$ from CHN, thermogravimetric analysis and energy-dispersive analysis of X-rays, which confirms that the anion-exchange reaction proceeds with a 100 % yield. The characteristic thermogravimetric profile of CoAl–T1 also reveals the presence of T1 in the lamellae with a sharp exothermic peak at 311 °C, which accounts for the combustion of 27 % of the mass in agreement with the experimental T1 content (*cf.* 26.7 %; **Figure 4**). In addition, the gradual weight loss of about 10% that corresponds to water desorption below 200 °C.

The specific surface area and therefore and indirect measurement of the degree of anion exchange can be determined be N_2 adsorption and desorption experiment.[208,248] The N_2 adsorption and desorption isotherms of the pristine $CoAl–NO_3$ and the CoAl–T1 hybrid material are shown in **Figure 5**.

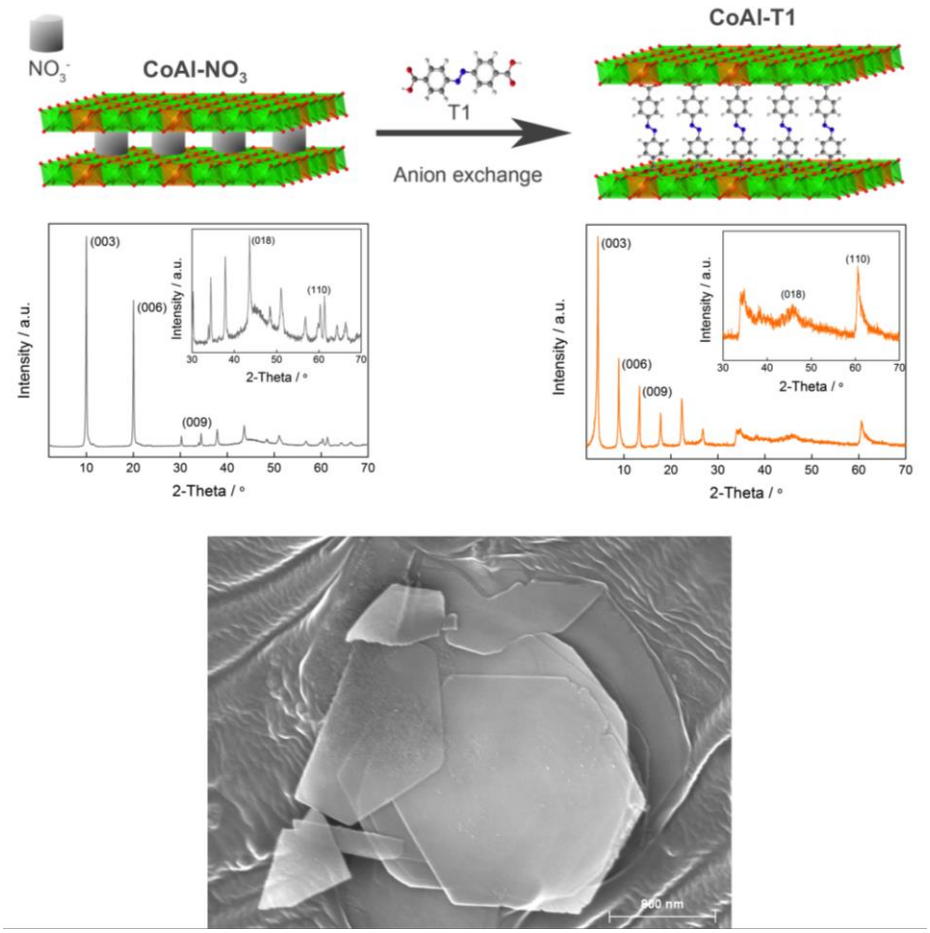

Figure 2. (*top*) Schematic representation of the parent and intercalated materials, and their powder X-ray diffraction patterns. (*bottom*) FE-SEM image of CoAl–T1 showing thin crystals with well-defined hexagonal morphology.

Table 1. Summary of the unit cell parameters of CoAl–NO_3 and CoAl–T1 as extracted from the refinement of PXRD data using the program Fullprof.

	Calc param[a] [Å]		
Sample	***a***	***c***	***BS***
CoAl–NO_3	3.070(1)	26.650(1)	8.88(1)
CoAl–T1	3.040(1)	60.001(1)	20.00(1)

[a] $BS = c/3$.

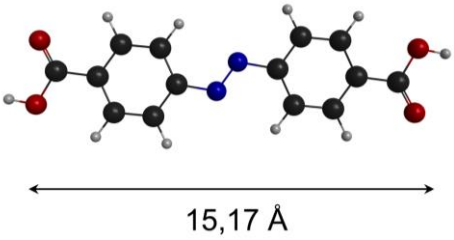

Figure 3. Optimized structure for the T1 molecule.

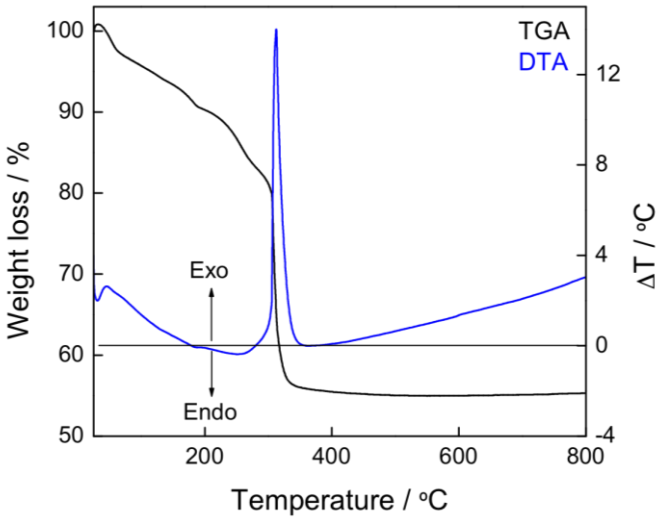

Figure 4. TGA/DTA curve of the CoAl–T1 hybrid material.

Both samples belong to Brunauer, Deming, Deming and Teller (BDDT) type II isotherms with a small hysteresis loop, which corresponds to nonporous or macroporous structures (additionally, it is possible to assign these isotherms as a IUPAC type IV with H3-type hysteresis loop ($P/P_0 > 0.4$), which suggests the presence of mesopores; however, the fraction of mesopores is not so large because the hysteresis loop is not so clear compared with those in typical mesoporous materials). The BET surface areas are 45 and 17 $m^2 \cdot g^{-1}$ respectively. The microporous areas are 27 and 0.6 $m^2 \cdot g^{-1}$ respectively, highlighting that a partial contribution to the surface area corresponds to the microporosity, if we consider the interlamellar space as a source of microporosity. This porous

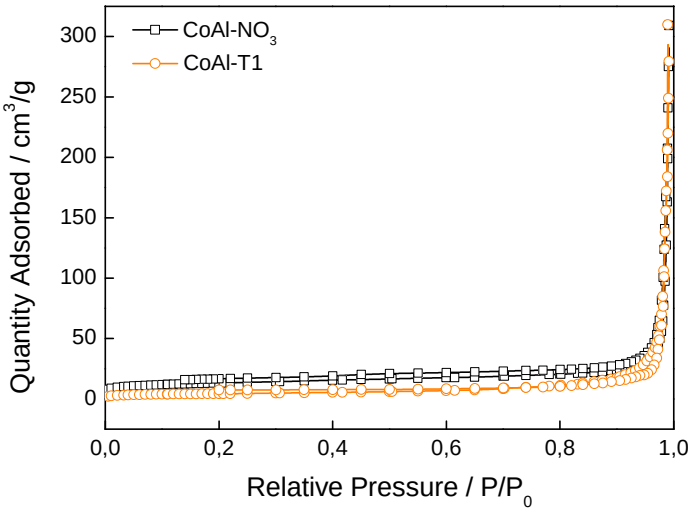

Figure 5. N_2 adsorption-desorption isotherm of as-synthesized sample CoAl–NO_3 and the subsequent anion-exchanged CoAl–T1.

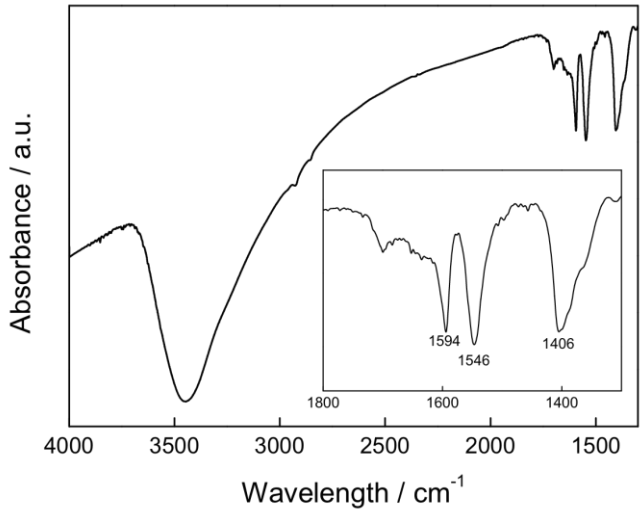

Figure 6. FT-IR spectra of compound CoAl–T1. The inset is a magnification of the 1300–1800 cm^{-1} region.

behaviour recalls that reported for NiTi–LDH,[249] microporous MgFeAl–LDH[250] or MgAl–LDH.[251]

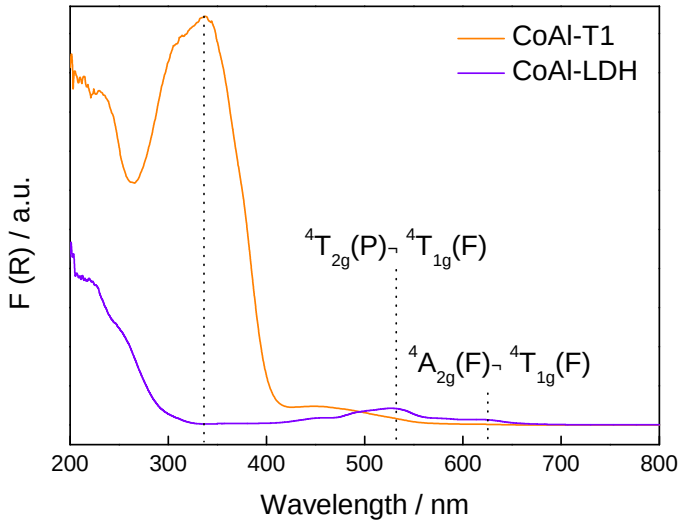

Figure 7. UV-Vis/diffuse reflectance spectra of the pristine CoAl-LDH and the hybrid CoAl–T1.

FT-IR also displays several vibrational modes at 1406, 1546 and 1594 cm^{-1} characteristic of the aromatic ring of azobenzene, which confirm the presence of T1 in the hybrid (**Figure 6**), discarding the presence of residual nitrate anions.

7.2.2. Photochemistry

Bulk UV-Vis studies of pressed pellets of pristine CoAl–NO_3 and CoAl–T1 LDHs show the appearance a strong absorption band between 300–400 nm with a maximum centered at 340 nm that confirms the presence of the *trans* isomer of T1 in the hybrid (**Figure 7**).[233] This is accompanied by a much weaker absorption band between 420 and 550 nm that corresponds to a minor proportion of the *cis* isomer. Furthermore, the UV cut-off effect of CoAl–LDH was discarded, as the absorption of *trans* azobenzene-4,4'-dicarboxylic acid (T1) is centered at 340nm (this is why we chose a 355nm cut-off filter for the bulk UV-Vis studies) whereas the diffuse reflectance of CoAl–LDH (purple colour) without intercalated azobenzene molecules absorbs at *ca.* 525 and 620 nm.[252] See comparison and characteristic transitions of CoAl–LDH in **Figure 7**.

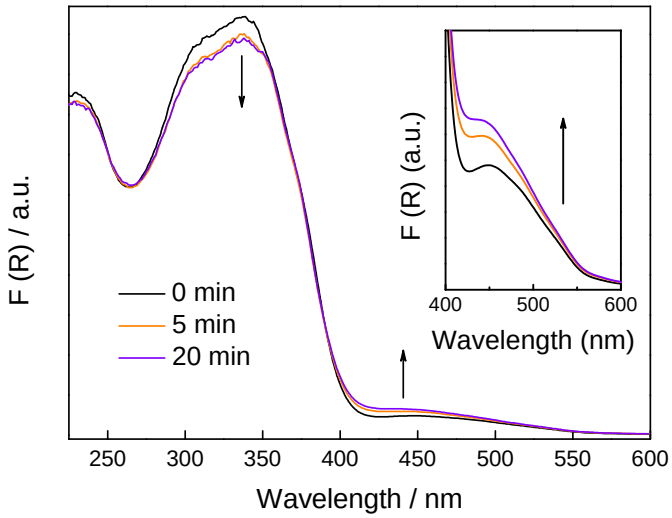

Figure 8. UV–Vis absorption spectra for CoAl–T1 at different irradiation times. The peaks at about 340 nm are characteristic of the *trans* isomer, while the peaks at about 430 nm correspond to the *cis* isomer. The presence of isosbestic points also supports *trans* (higher extinction coefficient) to *cis* (lower extinction coefficient) isomerization. The series of spectra presented correspond to the photoisomerization of the *trans* isomer of T1 to *cis* in UV light.

Irradiation with UV light using a pass band filter centered at 355 nm leads to an increase of the band corresponding to the *cis* isomer that is accompanied by a decrease of the intense 340 nm band (**Figure 8**).[253] Analogous experiments were carried out with CoAl–T1 sample deposited as thin film (about 1 μm determined by optical profilometry) on a transparent quartz substrate. In this case, transmission measurements permit registering the optical spectra with higher sensitivity, thus providing a more clear evidence of the spectroscopic changes triggered by UV-light irradiation.[240] The results obtained are presented in **Figure 9A** and show the presence of two isosbestic points at 310 and 375 nm, this being compatible again with the occurrence of photoinduced *trans* to *cis* isomerization of intercalated T1. The occurrence of this *trans-cis* photoswitching has been firmly established upon irradiation of T1 in aqueous solution (see **Figure 9B**) and the change in the optical spectra shown

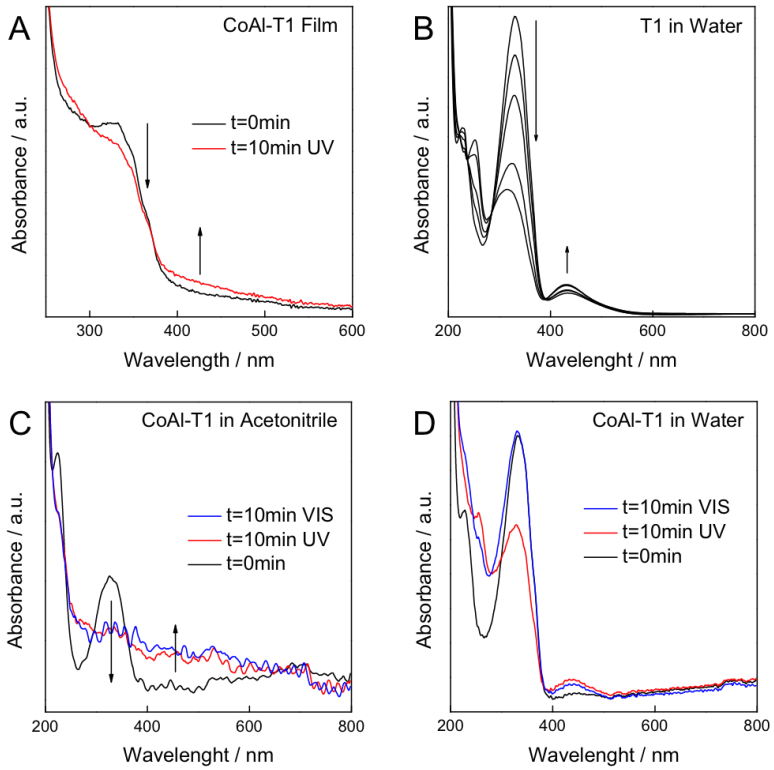

Figure 9. (A) UV–Vis absorption spectra for CoAl–T1 deposited as a thin film (1 μm) on Suprasil quartz at different irradiation times. (B) UV–Vis absorption spectra for T1 under UV-irradiation in water. The peaks at about 340 nm are characteristic of the *trans* isomer, while the peaks at about 430 nm correspond to the *cis* isomer. The presence of isosbestic points also supports *trans* to *cis* isomerization. (C) The plot shows the absorption spectra of a suspension of CoAl–T1 in acetonitrile, showing the characteristic bands of T1. After UV irradiation, the band corresponding to the *trans* isomer dissappears, and cannot be recovered by subsequent Vis irradiation, due to the absence of moisture. (D) UV-Vis spectra after addition of water to the suspension. Clear reversible *cis-trans* photoisomerization can be observed, highlighting the importance of the presence of water.

in **Figure 9A** is similar to that observed for isomerization of T1 in silica gels (see **Appendix I**)[242] and other azo compounds in solid samples.[253] To gain further insights into the photoisomerization mechanism, a powdered sample of CoAl–T1 was suspended in anhydrous acetonitrile and the changes in optical spectros-

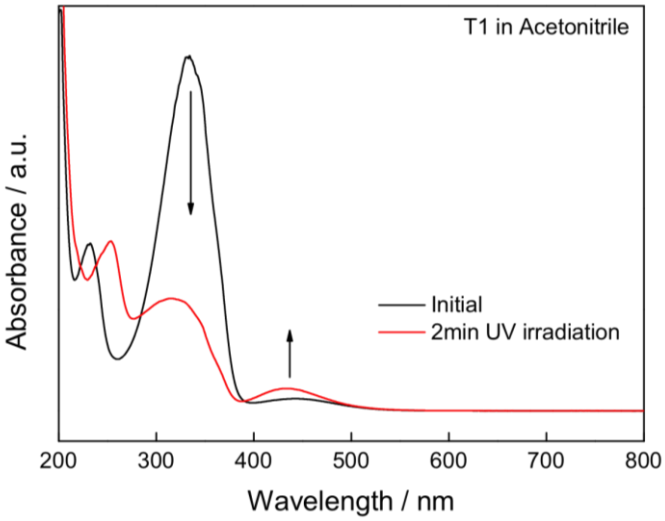

Figure 10. UV-Vis absorption spectra for T1 (previously basified with NaOH 2M for deprotonation of the dicarboxylic acid to obtain homogeneous solutions) in acetonitrile. T1 shows reversible *cis-trans* behaviour after 2 min of UV irradiation, with the presence of well-defined isosbestic points.

copy upon irradiation monitored (see **Figure 9C**). The sample was first irradiated with UV light leading to a significant decrease in the intensity of the 330 nm band characteristic of the *trans* isomer, with the concomitant increase of the absorption at 430 nm band specific of the *cis* isomer. Under these conditions, irradiation with visible light did not cause any change. However, addition of water to the acetonitrile suspension under irradiation driven the expected increase of the 330 nm band of the *trans* isomer in detriment of the intensity of the *cis* 430 nm band (See **Figure 9D**). This is consistent with the fully reversible behavior of T1 in acetonitrile (see **Figure 10**). As shown in **Figure 9D**, the presence of water allows for reversible cycles of *trans-cis* isomerization upon consecutive visible irradiation of the solid. This suggests the occurrence of a proton-assisted isomerization facilitated by the presence of water. The proposed mechanism is a thermal dark process that does not require visible irradiation to take place, consistent with our experiments that confirm *cis* to *trans* isomerization of the solid in the dark (**Figure 11**).

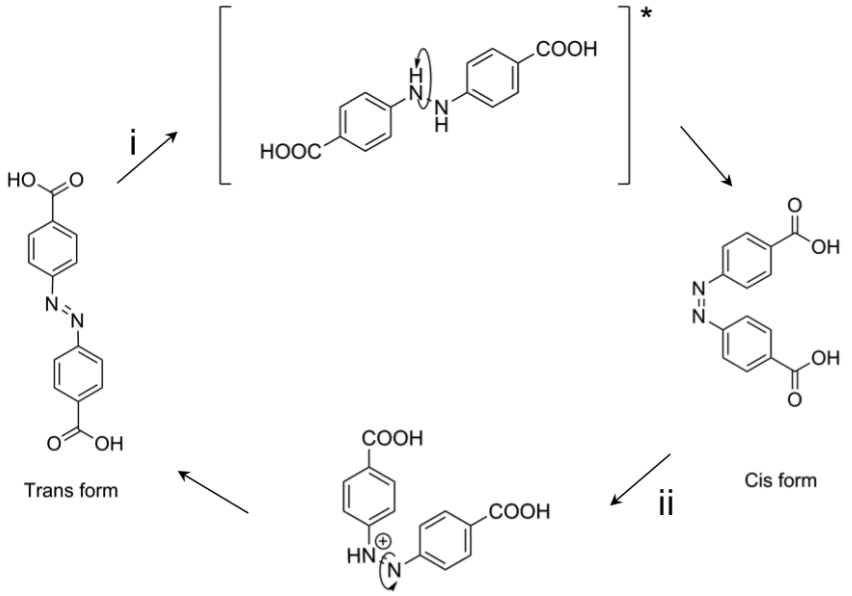

Figure 11. Schematic illustration highlighting the proposed mechanism for the isomerization of T1: i) UV photoisomerization through an electronic excited state. ii) Proton assisted thermal or photoinduced isomerization.

7.2.3. X-ray Diffraction Studies

UV irradiation of the as-prepared films was also monitored by XRD to study the influence of isomerization of the guest on the layered structure of the LDH hybrid. The initial sharp peaks corresponding to (00*l*) lines shift towards higher 2θ angles with UV light, decreasing the interlayer distance in the hybrid. (**Figure 12**). The *BS* extracted from the first three (00*l*) peaks shifts reversibly between 20.29(2) and 20.18(2) Å. This compression of the interlayer separation is consistent with a cooperative rearrangement of the host trying to accommodate the smaller *cis* isomer of T1.

Our study also reveals that the structural change in CoAl–T1 cannot be reversed by irradiation with visible light using a 450 nm cut-off filter in the absence of moisture. The optical spectrum and the PXRD remains unchanged indicating that the initial system, featuring longer interlayer distances, cannot be obtained photochemically if water is absent. In bulk samples, this compressed

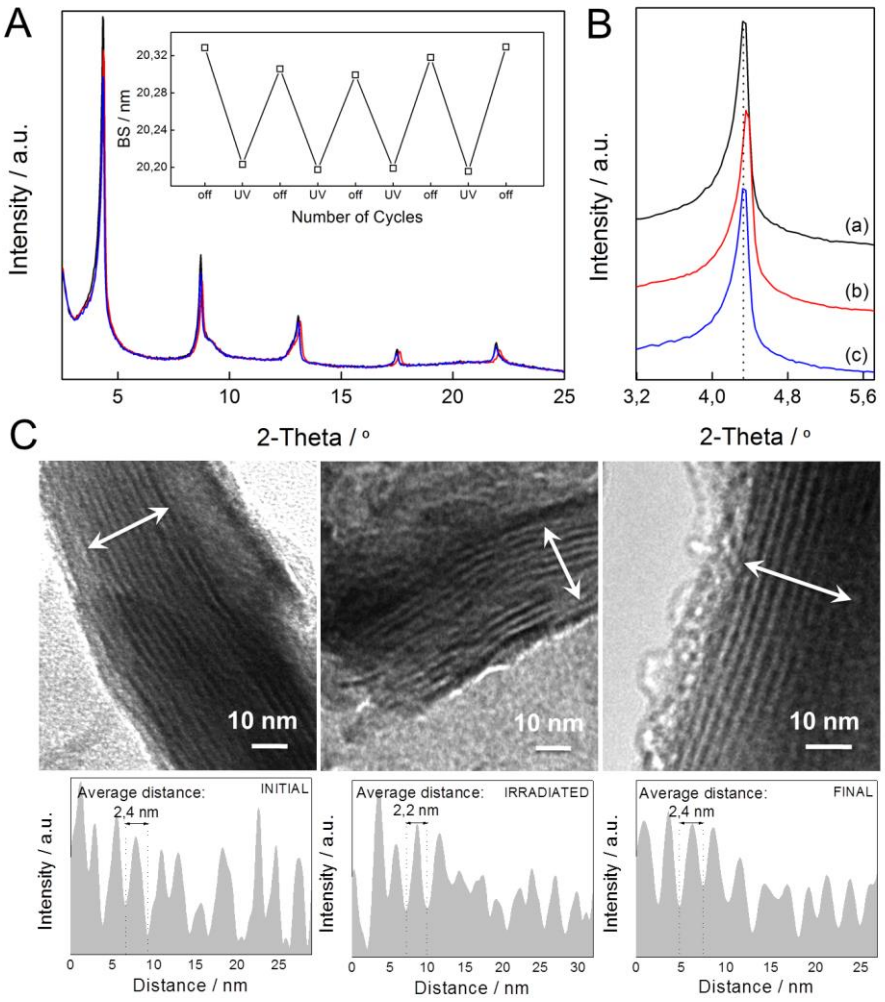

Figure 12. (A) The reversible change in the XRD pattern of CoAl–T1 upon UV irradiation and proton assisted thermal isomerization. The inset shows the variation in the d_{003} value during several cycles. (B) Zoom in highlighting the movement of the (003) peak, a) before irradiation, b) UV irradiated and c) final. (C) HRTEM images showing a cross view of CoAl–T1 crystals. (left) Initial, (center) irradiated and (right) final. The insets represent the indicated average profile, showing the average distance between fringes, that is an indication of the basal space.

state remains stable for days without reverting to the initial state when stored in a sealed vial in the absence of moisture. This is confirmed by the intensity of the

absorption band at 450 nm, which remains constant and equal to the maximum value after irradiation. Exposure of the solid irradiated with UV to a controlled atmosphere of water promotes an expansion of the *BS* associated to the shift of the (00*l*) peaks back to the original position in the pristine material. This is also consistent with the occurrence of proton-assisted *cis* to *trans* isomerization (**Figure 12B**).

7.2.1. Electron Microscopy

Structural changes of CoAl–T1 after UV irradiation and exposure to water were also confirmed by HR-TEM. It is worth mentioning that the identification of changes in the layered structure of this type of materials is seriously limited by their hexagonal morphology and 2D nature (base-to-height ratio close to 100). Hence, most of the TEM images correspond to frontal views in which no apparent changes upon irradiation-relaxation could be identified. However, the search of smaller crystals with suitable orientations enabled study of the cross section of the particles. **Figure 12C** shows selected cross section views of the particles of CoAl–T1 in which the layered structure can be associated to the parallel dark and bright fringes that correspond to high (LDH layer) and low (T1) electronic density, respectively. An estimation of the *BS* values can be directly calculated from HRTEM images by measuring the average distance between two consecutive clear regions, which corresponds to the interlayer separation. Our study reveals that the average distances observed, before (24 Å), after UV irradiation (22 Å) and upon rehydration (24 Å), are consistent with a reversible structural change.[147,254] The presence of two carboxylate anchoring groups in the azobenzene molecules leads, upon irradiation, to a distortion/tension of the layers as consequence of the *trans-cis* isomerization.

7.2.2. Magnetic Properties

We next performed magnetic measurements at low temperatures to correlate these structural changes with the overall magnetism of CoAl–T1. The combination of superexchange ferromagnetic interactions between the Co^{II} centers through –OH bridges and dipolar interactions between neighboring magnetic layers triggers the appearance of spontaneous magnetization below a critical temperature T_M in CoAl–LDHs. Whilst $\chi_M T$ in pristine CoAl–T1 reaches a maximum of 6.33 emu·K·mol^{-1} at 2.9 K, this value decreases down to 3.55

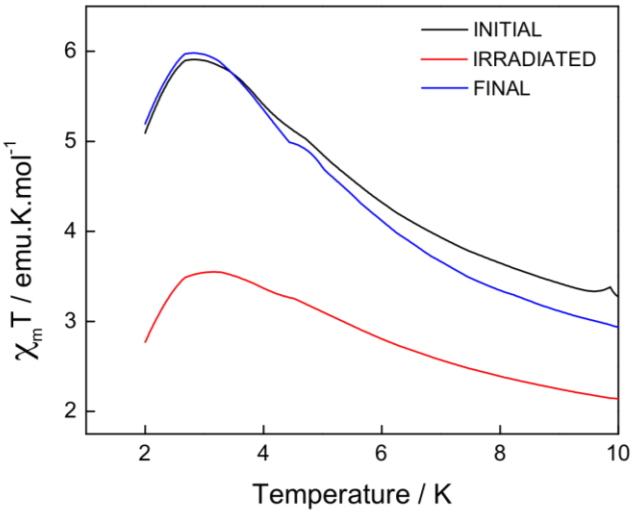

Figure 13. Thermal variation of the $\chi_M T$ product for the pristine CoAl–T1 compound, the irradiated and the hydrated one, in the low temperature region.

Table 2. Magnetic parameters for the pristine compound CoAl–T1, the irradiated and the hydrated.[a]

Sample	$\chi_M T_{rt}$	C_{so} (emu·K·mol^{-1})	C (emu·K·mol^{-1})	Θ (K)	M_S (μ_B)	H_{Coer} (kG)	T_M (K)
Initial	1.83	0.96	1.63	–2.58	1.27	<1	4.5
Irradiated	1.62	0.96	1.48	–9.71	0.77	<1	5.2
Final	2.02	0.96	1.98	–6.21	1.15	<1	4.5

[a] Expected spin-only value of the Curie constant [C_{so}, (emu·K·mol^{-1})], experimental Curie constant [C, (emu·K·mol^{-1})], Weiss constant [Θ, (K)], saturation magnetization [M_S, (μ_B)], coercive field at 2 K [H_{Coer}, (kG)] and temperatures for the appearance of the spontaneous magnetization from χ_M'' plots (T_M). S(Co^{2+}) = 3/2.

emu·K·mol^{-1} upon UV irradiation, and can be reverted back to 5.93 emu·K·mol^{-1} by exposure of the solid to water (**Figure 13** and **Table 2**). These maxima in the $\chi_M T$ product correspond to a steep jump in the thermal dependence of χ_M, suggesting the occurrence of long-range magnetic correlation between the spins at low temperatures (**Figure 14A**). The ob1served decrease in the magnetic signal upon irradiation can be initially linked to the compression

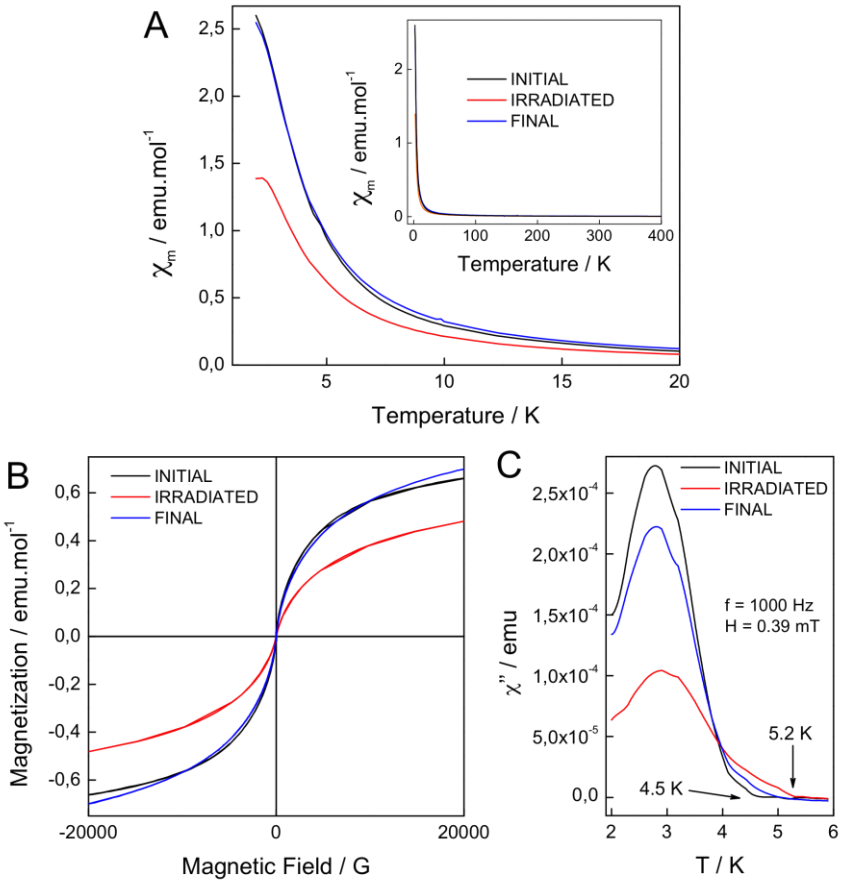

Figure 14. (A) Thermal variation in the low-temperature region of χ_M for the initial CoAl–T1 (black), and the corresponding irradiated (red) and final (blue) samples. The whole temperature range is shown in the inset. (B) Hysteresis cycles of the corresponding samples. (C) Out-of-phase signal (χ_M'') of the corresponding samples under an oscillating field of 0.39 mT at a frequency of 1000 Hz. Arrows indicate T_M temperatures.

of the host that will affect magnetization. Still, the decrease of the distance separating the LDH layers seems too small (~0.1 Å) to affect the magnetic behaviour through dipolar interactions. In fact, the observed magnetic changes are likely too dramatic to be ascribed to this effect and might in turn originate from changes of the exchange pathways and magnetic correlation within the layers. Photoinduced isomerization of the guest might trigger elastic structural

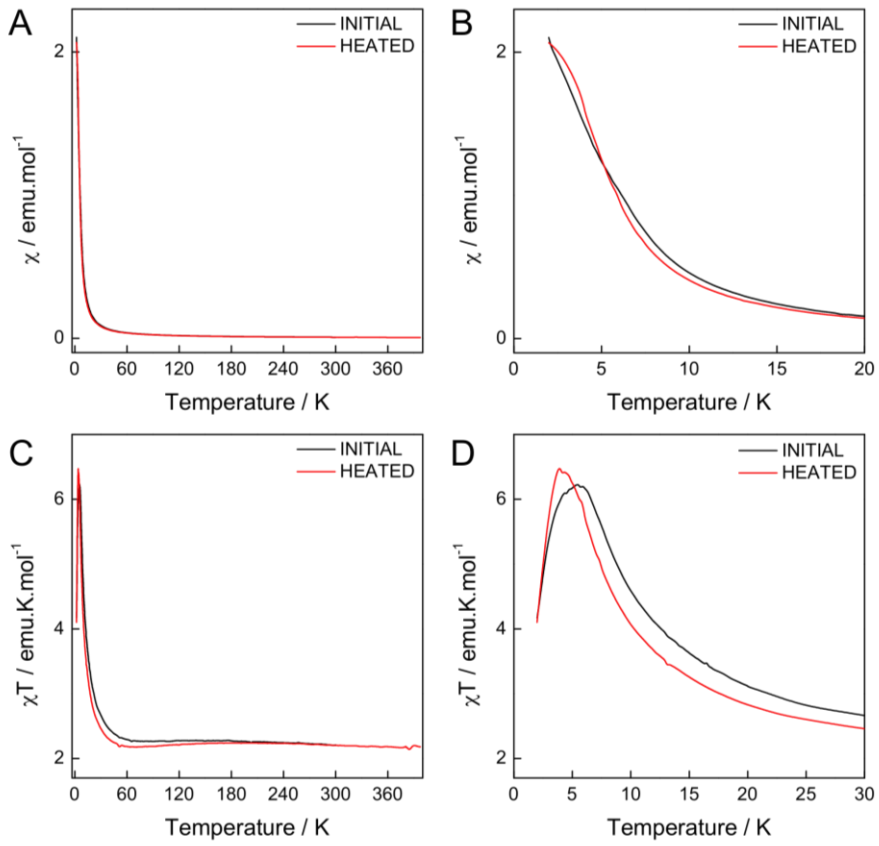

Figure 15. (A) Thermal variation of χ_M for the initial CoAl–T1 (black), and the sample heated in the SQUID at 400 K (red). (B) Zoom-in showing the low-temperature region. (C) Thermal variation of the $\chi_M T$ product at low temperatures (D). In-situ heating of as-made CoAl–T1 sample in the SQUID magnetometer at 400 K for 10 min leads to slight variations in the $\chi_M T$ product, discarding the dehydration as the origin of the changes in the magnetic behaviour of the irradiated samples.

changes in the coordination environment of the metal octahedra across the layers, affecting angles and bond distances, which would result in more acute magnetic changes. This is consistent with the HRTEM images showing a cross view of CoAl–T1 crystals (**Figure 12C**). Whereas the structure of the initial and final states looks almost identical featuring a parallel arrangement of planar fringes, irradiation provokes substantial changes characterized by a more corrugated profile and local distortions in the internal structure of the layers

that deviate from planarity and adopt more strained configurations. Theoretical studies reveal that, although not as flexible as graphite, LDHs are considerably more flexible than smectite clays like montmorillonite.[35] This structural elasticity has been more recently proven for surfactant intercalated LDHs.[36]
This scenario can be reverted upon back *cis* to *trans* isomerization as the *BS* reaches a value similar to that present in the original host. This hypothesis is consistent with the variation of the Weiss constants for the three states of the solid as estimated from the fitting of $1/\chi_M$ to the Curie-Weiss law in the high-temperature paramagnetic regime (100–400 K). The Θ values are negative for all the samples, due to strong spin-orbit coupling introduced by Co^{II} ions, but become more negative for the irradiated sample (**Table 2**).

Figure 14B shows the field dependence of the magnetization for the different states of CoAl–T1 at 2 K. As expected for ferromagnetic interactions, a rapid increase of the magnetization is observed at low-fields. The saturation values show a drastic decrease in the magnetization from 0.66 to 0.48 emu·mol^{-1} after irradiation at 2 T, that increases back to 0.57 emu·mol^{-1} at the final stage. The total photo-induced changes in the magnetization values are estimated to be of 27 % at 2 K. This variation is much larger than those reported for azobenzene-containing smectite clays and Prussian Blue analogues (*cf.* 11 % measured at 2 K under 100 Oe) or multi-bilayered vesicles of azobenzene embedded in a poly(vinylalcohol) matrix.[238,255]Furthermore, to discard the effect of dehydration or solvent on the magnetic switching we also measured the thermal variation of χ_M and the $\chi_M T$ product after heating the sample at 400 K in the SQUID magnetometer. The experiments showed almost negligible variations before and after heating, ruling out any influence of dehydration on the observed magnetic changes (See **Figure 15**).

The appearance of spontaneous magnetization was next confirmed with ac dynamic measurements with an applied field of 3.95 G with frequencies oscillating between 10 and 10000 Hz. **Figures 16** reveals the appearance of peaks for the initial, irradiated and relaxed states in both, the in-phase (χ_M') and out-of-phase (χ_M'') signals. The position of the maxima in χ_M' and χ_M'' displays clear dependence with the frequency of the oscillating field, therefore suggesting glassy-like relaxation. Analogous behaviors have been described in previous chapters for other magnetic LDHs and its origin attributed to the statistic

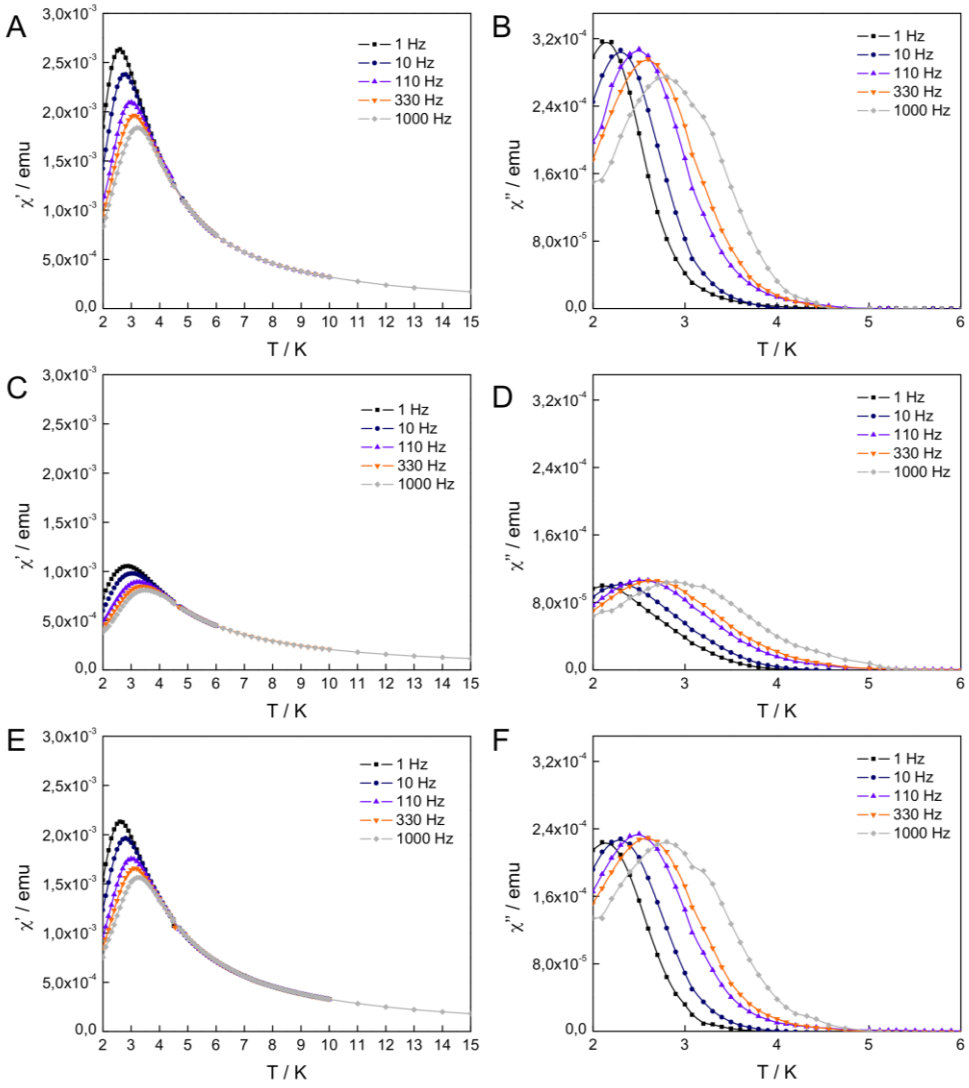

Figure 16. (A) Thermal dependence of (left) the in-phase signal (χ_M') and (right) the out-of-phase signal (χ_M'') at different frequencies from 1 to 1000 Hz of initial CoAl–T1, (B) CoAl–T1 after UV irradiation, and (C) CoAl–T1 after re-hydration. Solid lines are visual guides.

distribution of spin carriers across the layers or ion clustering.[122,123,164,165,179] **Figure 14C** shows clear differences in the temperatures for which spontaneous magnetization arises in the original sample T_M = 4.5 K, and after irradiation, 5.2

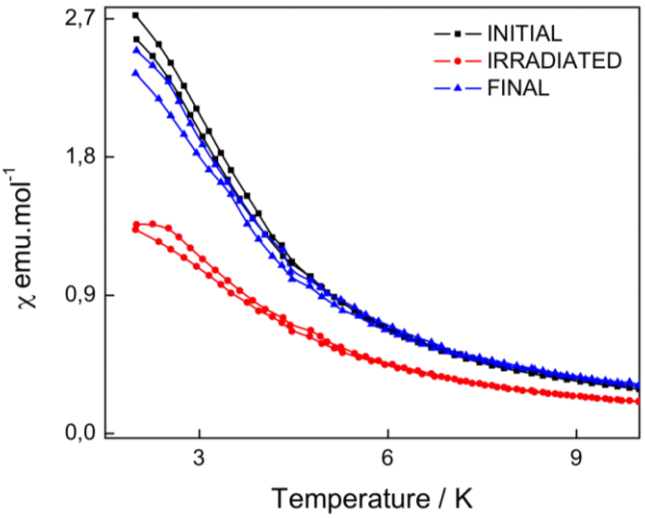

Figure 17. Low temperature FC and ZFC molar magnetization measured at 100 Oe of the pristine compound CoAl–T1, the irradiated and the hydrated one.

K. This increase in T_M is consistent with the proposed model in which the photo-induced compression/modification of the host will trigger more intense AF interactions leading to a higher T_M value. Next, restoration of the host by exposure to water weakens these interactions thereby decreasing T_M to 4.7 K, close to the original value. It is worth outlining that the ZFC and FC magnetic susceptibility measurements do not show a clear bifurcation below an irreversibility temperature T_{irr} (**Figure 17**). These data are similar to those previously obtained by O'Hare and co-workers for $Co_{1.8}Al_{1.1}(OH)_6(DDS)_{0.9}{\cdot}mH_2O$ (DDS = dodecylsulphate) bulk hydrotalcite, in which no clear bifurcation was observed in the FC/ZFC measurements at 100 Oe.[161]

7.3. Conclusions

Herein, we have described a hybrid multifunctional photoactive and magnetic layered material that makes use of the switching ability of azo molecules to effectively modulate the magnetism of a layered double hydroxide host.

Azobenzene-4,4'-dicarboxylic acid was intercalated into the magnetic layers of CoAl–LDH, and the solid irradiated with UV light to photochemically induce

a partial *trans*-to-*cis* isomerization of the guest. This promotes a small contraction (from 20.29(2) to 20.18(2) Å) of the basal distance separating the LDH layers in the host as result of the cooperative rearrangement of the non-isomerized *trans* molecules, from perpendicular to tilted orientation to accommodate their structure to the reduced interlamellar space available. More important, it also induces a distortion within the layers. This is facilitated by the T1 molecule, which acts as a bridge linking two adjacent layers through the carboxylic groups. In fact, it is presumably this distortion the main responsible for the sharp changes observed in the magnetic behaviour of the material upon irradiation (a drop of M of ca. 27 % and an increase of T_M close to 1K). Thus we propose that isomerization leads to an appreciable modification in the exchange pathways and magnetic correlation lengths by in-plane structural changes enabled by the intrinsic flexibility of LDH slabs. This photo-induced change can be reverted by exposure of the solid to water or air moisture, which permits recovering the original basal space upon rehydration through a proton-assisted thermal *cis*-to-*trans* isomerization, thus enabling reversible switching of the magnetic response of this layered hybrid. This work paves the way for the intercalation of related photoactive molecules showing thermo or photochromism between the layers of these metal hydroxides. It shows an interesting approach for the development of stimuli-responsive materials based on these inorganic magnetic lamellae.[256,257]

7.4. Experimental Section

7.4.1. Synthesis of CoAl–LDHs

Materials: All chemicals $Co(NO_3)_2{\cdot}6H_2O$, $Al(NO_3)_3{\cdot}9H_2O$, $NaNO_3$, HNO_3, $CO(NH_2)_2$ (urea) and azobenzene-4,4′-dicarboxylic acid, were used as received from commercial suppliers (Sigma-Aldrich, Fluka and TCI) without further purification. All the experiments were carried out under inert atmosphere to prevent carbonate contamination.

Synthesis of CoAl–CO_3 LDH: $[Co_{0.66}Al_{0.33}(OH)_2](CO_3)_{0.16}{\cdot}mH_2O$ was synthesized according to the homogeneous precipitation method by using urea as ammonia releasing reagent (ARR).[45,246,247] in this sense, the nitrate salts of the metals were dissolved in Milli-Q purged water to reach a total cation concentration of 0.15 M in the final solution and keeping the stoichiometric coefficient constant at a value of x = 0.33 (equivalent to a Co/Al molar ratio of 2:1). Next, an aqueous solution of urea (three times the $[Al^{3+}]$) was added. The resulting pink mixture was transferred to a round bottom flask and heated up to 97 °C under reflux conditions. After 48 hours, the resulting finely divided pink powder was filtered, washed thoroughly with distilled water and ethanol, and dried at room temperature under vacuum. The pH value of the remaining solution was found to be around 7.5.

$[Co_{0.66}Al_{0.34}(OH)_2](CO_3)_{0.33}{\cdot}0.33H_2O$ Anal. calc. for $H_{2.66}C_{0.33}O_{3.32}N_0Co_{0.66}Al_{0.34}$ (MW = 98.235): H, 2.61; N, 0; C, 1.96. Found: H, 2.58; N, 0.14; C, 1.98.

Preparation of CoAl–NO_3 LDH: $[Co_{0.66}Al_{0.33}(OH)_2](NO_3)_{0.33}{\cdot}mH_2O$ was obtained by carbonate-exchange of the as-synthesized CoAl–CO_3 LDH in presence of an excess of nitrate anions. In a typical procedure, 1 g of CoAl–CO_3 LDH was immersed in a round-bottom flask containing 1 L of an aqueous solution of $NaNO_3$ (1.5 M) and HNO_3 (0.005 M). This mixture was mechanically stirred under inert atmosphere during 48 h. Afterwards, the resulting pink solid was filtered, washed thoroughly with Milli-Q water and ethanol and dried under vacuum at room temperature.

$[Co_{0.67}Al_{0.33}(OH)_2](NO_3)_{0.33}{\cdot}0.31H_2O$ Anal. calc. for $H_{2.62}C_0O_{3.3}N_{0.33}Co_{0.67}Al_{0.33}$ (MW = 108.534): H, 2.42; N, 4.97; C, 0. Found: H, 2.26; N, 3.69; C, 0.18.

7.4.2. Anion Exchange

Azobenzene-4,4′-Dicarboxylic Acid Intercalation, CoAl–T1: In a typical procedure, 200 mg of CoAl–NO_3 was finely powdered and transferred to a round bottom flask. Then, 90 ml of a 0.03 M aqueous solution of azobenzene-4,4′-dicarboxylic acid, previously basified to pH 7.5 by addition of aqueous solution of NaOH 2 M, was slowly added under inert atmosphere and continuous stirring. The mixture was sonicated during 5 minutes to produce a homogeneous dispersion and then was vigorously stirred at 900 rpm for 20 h under continuous argon bubbling. Finally, the orange precipitate was filtered under inert atmosphere, washed thoroughly with distilled water and ethanol, and dried at room temperature under vacuum.
$[Co_{0.65}Al_{0.35}(OH)_2](C_{14}H_{10}N_2O_4)_{0.17}\cdot 0.51H_2O$ Anal. calc. for $H_{4.77}C_{2.45}O_{3.21}N_{0.35}Co_{0.65}Al_{0.35}$ (MW = 138.227): H, 3.47; N, 3.55; C, 21.28. Found: H, 3.31; N, 3.29; C, 20.26.

7.4.3. Physical Characterization

Carbon, nitrogen and hydrogen contents were determined by microanalytical procedures using an EA 1110 CHNS-O Elemental Analyzer from CE instruments. Metallic atomic composition of bulk samples was determined by means of electron probe microanalysis (EPMA) performed in a Philips SEM-XL30 equipped with an EDAX microprobe. Particle morphologies and dimensions were studied with a Hitachi S-4100 scanning electron microscope at an accelerating voltage of 20 keV, over metalized samples with a mixture of gold and palladium during 30 s. HRTEM studies of the intercalated samples were carried out on a Technai G2 F20 microscope operating at 200 kV. Samples were prepared by dropping a suspension of the sample in ethanol on a lacey formvar/carbon copper grid (300 mesh).
Infrared spectra were recorded in a FT-IR Nicolet 5700 spectrometer in the 4000–400 cm^{-1} range using powdered samples diluted in KBr pellets. Thermogravimetric analysis of all compounds were carried out with a Mettler Toledo TGA/SDTA 851 apparatus in the 25–800 °C temperature range under a 10 °C·min^{-1} scan rate and an air flow of 30 mL·min^{-1}. X-ray powder diffraction patterns of the precursor materials were collected with a Phillips X'Pert-MPD diffractometer provided with a graphite monochromator, operating at 40 kV

and 20 mA and employing nickel-filtered Cu-K_α radiation (λ = 1.5418 Å). Profiles were collected in the 2.5° < 2θ < 70° range with a step size of 0.05°. UV-Vis spectra were conducted using a Varian Cary-5G UV-Vis spectrophotometer. Room temperature diffuse reflectance UV-Vis-NIR spectra of solid samples were recorded with a Varian Cary 5000 UV-Vis-NIR scanning spectrophotometer. The irradiation experiments were carried out using the output of a 200 W xenon-doped mercury lamp (Hamamatsu Lightningcure LC8). Cut-off filters were employed for ultraviolet and visible light irradiation (Hamamatsu), and an optical fiber was employed to direct the irradiation beam to the respective sample holders. This experimental irradiation setup reduces considerably the nominal power of the xenon-doped mercury lamp, leading to cold light. In fact, the temperature of the sample in all the experiments was always lower than 35 ºC as determined by means a digital temperature controller.

Irradiations were carried out for powders compressed on a diffuse reflectance cell holder or by suspending the powder (5 mg) in anhydrous acetonitrile (3 ml). In the last case the sample was sonicated to favor dispersion of the powder and the suspension was maintained by magnetic stirring. For the UV-Vis reversibility studies, 100 µL of Milli-Q water were added to the suspension by means of a syringe under continuous stirring.

Additionally, thin films of CoAl–T1 were also submitted to irradiation. The films (on quartz Suprasil substrates) were prepared by drop casting on a hot plate (80 ºC) at under ambient conditions a paste of CoAl–T1 (about 40 mg) in terpineol-acetone (1.5 ml of a 1:2 mixture of terpineol:acetone) that was sonicated to obtain a good dispersion. Once the solvent was evaporated the thickness of the layer was measured with an Ambios Xi-100 Non-Contact Optical Profilometer with nanometric vertical resolution. The thickness of the films was about 1 micron.

Irradiations were carried out in situ while the sample was placed on the holder of the spectrometer or XRD difractometer at ambient conditions. XRD patterns of the irradiated samples were obtained using a PANalytical X'Pert PRO diffractometer using copper radiation (Cu K_α = 1.5418 Å) with an X'Celerator detector, operating at 40 mA and 45 kV. Profiles were collected in the 2° < 2θ < 30° range with a step size of 0.017° 2θ. Samples were irradiated in situ during the

measurements. Cell parameters refinements of the bulk samples were carried out with the Fullprof suite programs using the TCH pseudo-Voigt function to fit the experimental profiles and considering the R-3m space group.

The N_2 adsorption isotherms were recorded at 77 K with a Micromeritics ASAP 2000 instrument. The specific surface area was determined by the BET method. Magnetic measurements were carried out with a Quantum Design superconducting quantum interference device (SQUID) MPMS-XL-5. The susceptibility data were corrected from the diamagnetic contributions of the atomic constituents of the samples as deduced from Pascal's constant tables and the sample holder. The dc data were collected under an external applied field of 100 G in the 2–400 K temperature range. Magnetization studies were performed between −5 and +5 T at a constant temperature of 2 K. The ac data were collected in the range 2–15 K with an applied alternating field of 3.95 G at different frequencies in the range 1–1000 Hz. The powders for the magnetic measurements (*ca.* 20 mg) were placed in an Eppendorf container that was sealed to avoid changes in the water content before and after irradiation. Magnetization measurements in the SQUID apparatus of irradiated samples were carried out by submitting the samples to irradiation at room temperature before performing the measurements. Additional controls show that the powder diffraction patterns of the irradiated samples remain constant for a period of time much longer than the *ca.* 8 h required for the magnetic measurement, confirming that their structure is retained during those measurements.

7.5. Appendix I. On the Photochemical Behaviour of Azobenzene Having Acidic Groups. Preparation of Photoresponsive Gels[†]

7.5.1. General Overview

Photochemical isomerization of *trans* azobenzenes to the *cis* isomers and the corresponding dark, (thermal) or photochemical relaxation to the most stable *trans* isomer of the azocompound has attracted a considerable attention from the fundamental and applied points of view.[232,233,258–260] In general this photoisomerization can be conveniently followed by monitoring the optical spectrum since *trans* isomers absorb at around 350 nm, while the *cis* isomers typically exhibit a less intense absorption band at longer (around 450 nm) wavelengths.[232,258,259] The significant variation of the absorption band from trans to *cis* is useful, not only to follow the photoisomerization, but also to induce specifically the transformation of the *trans* into the *cis* (with UV light) and the conversion of the *cis* into the *trans* (with visible light), that can be employed to control at will the configuration of the molecule.[232]

One of the most notable consequences of the *trans* to *cis* isomerization is the dramatic change of molecule's length, that for the parent azobenzene changes from 9.0 Å for the *trans* isomer to 5.5 Å of the *cis* azobenzene isomer, this change in the molecular dimensions is among the largest possible for a reversible reaction.[258]

Recently, sol-gel derived inorganic matrices have been used as hosts due to their good chemical and mechanical stability and moreover, the synthesis is performed at low temperature, which is appropriated for the thermal stability of organic molecules.[261] In this sense, we have studied the photochemical behaviour of the azobenzene molecules in a more viscous ambient. Herein, this study present data of photoisomerization of three 4,4' azobenzenes having acid groups as substituent (**Figure 1**), showing the influence of the solvent, as well as the viscosity when the azobenzene is dispersed in a gel matrix. Our study is complemented with laser flash photolysis data and analysis of the photoreaction process to rationalize the results presented. The three azobenzenes under study

[†] Abellán, G.; García, H.; Gómez-García, C. J.; Ribera, A. *J. Photochem. Photobiol. Chem.* **2011**, *217*, 157.

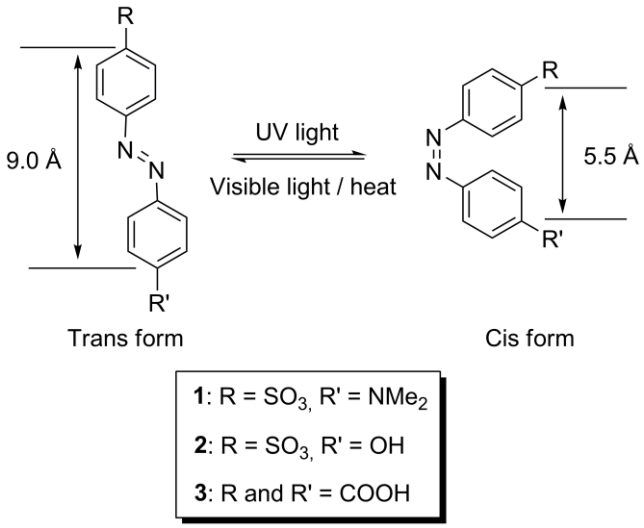

Figure 1. Variation in the molecular dimensions upon *cis–trans* isomerization and structure of the three azocompounds under study.

have in common the possession of acids groups, whose presences will make possible to complete the *trans*/*cis* isomerization with the use of these molecules as ligand of LDH systems.

7.5.2. UV–Vis Study

Samples were prepared by dissolving the compounds **1**–**3** in Milli-Q water, reaching a concentration 10^{-5} M. In the particular case of compound **3**, it was necessary to add a base to dissolve the sample correctly. For this purpose we employed 2 M sodium hydroxide. A Luzchem photoreactor equipped with 10 tunable quasi-monochromatic mercury lamps emitting between 300 nm and 355 nm were used for most of the *trans–cis* reactions. For *cis–trans* isomerization a visible light projector equipped with a 200 W mercury lamp was used. The temperature of the sample was always lower than 35 ºC by means a digital temperature controller.

All UV–Vis spectra were conducted using a Varian Cary-5G UV–Vis spectrophotometer. The samples were measured in 10 mm light path Hellma quartz precision cell in the case of azobenzene solutions and in a 1 mm light path Hellma quartz precision cell in the case of gel. Spectra of all the samples

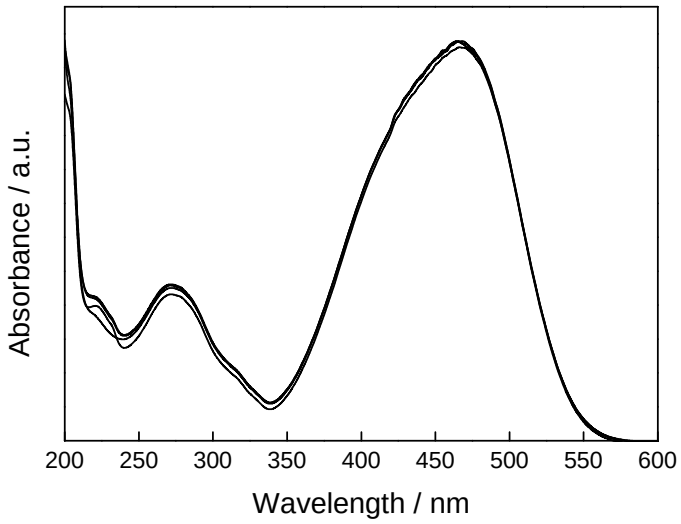

Figure 2. Absorption spectra of **1** under UV irradiation in water. The arrows indicate the growth or decrease of the absorption band upon UV irradiation.

were measured in transmission mode against air in the reference path. Preliminary studies with the three azobenzenes in aqueous solutions (about 10^{-5} M) were carried out under steady state irradiation. Although some minor changes were observed in the 210–240 nm region for **1**, this azocompound basically does not undergo any change in the optical spectrum under these conditions (**Figure 2**). Considering the short wavelenght in wich the changes are observed (< 250 nm) these small variations could be due to some impurities formed in small amounts during the photochemical treatment and unrelated to the *cis*/*trans* isomerization.

In the case of 4 hydroxy, 4' sulfonic substituted azocompound **2**, irradiation at 355 nm with quasi monochromatic mercury lamps in water (pH 6.3) leads to relatively minor changes in the 380–520 nm region that are compatible with the occurrence of some photoisomerization to reach a photostationary *trans*/*cis* mixture different from the initial statement. In addition also some minor variations in the 200–240 nm region were also observed (**Figure 3**). As commented in the case of compound **1**, variation of the absorbance in such short wavelength region, particularly if they are reversible, are most likely due to the formation of impurities, even in threat amounts and for the solvent, during

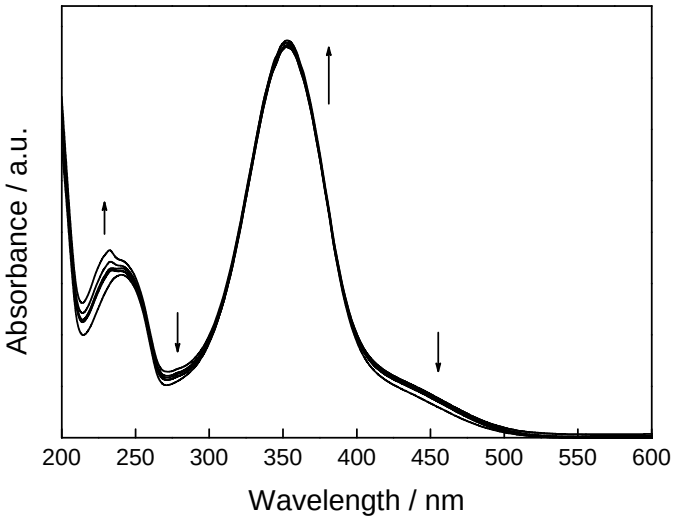

Figure 3. Absorption spectra of **2** under UV irradiation in water, showing some minor variations in the 200–240 nm region upon UV irradiation.

the photochemical irradiation. More interesting from the point of view of the photochemical isomerization under amenable conditions was the behavior of symmetric 4,4'-dicarboxilate azobenzene **3**. In this case it has to be noted that the pH of the aqueous solution was set to 11 to facilitate the solubility of the azobenzene **3**.[262] As it can be seen in **Figure 4**, 355 nm steady state irradiation of compound **3** leads to a gradual decrease of the 330 nm band and 228 nm corresponding to the *trans* isomer accompanied by a concomitant increase of the 430 nm and 250 nm bands of the *cis* isomer. Observation of four isosbestic points at 226, 238, 284 nm and 393 nm indicates the interconversion of the initial *trans* isomer to the *cis*. It should be noted that compounds **1** and **2** even at pH 11 exhibit exactly the same behavior (*i.e.* lack of evidence for *trans-cis* photoisomerization) that was observed when these compounds were irradiated at the pH that results from adding the compounds to solution. After photochemical isomerization using quasi-monochromatic UV-lamps, the course of thermal isomerization of the photogenerated *cis* isomer to the more stable *trans* isomer was followed in the dark (< 35ºC) monitoring the broad of the band corresponding to the *trans* isomer (330 nm). Fitting off the experimental data to a first order kinetics (see inset of **Figure 4**) has allow to

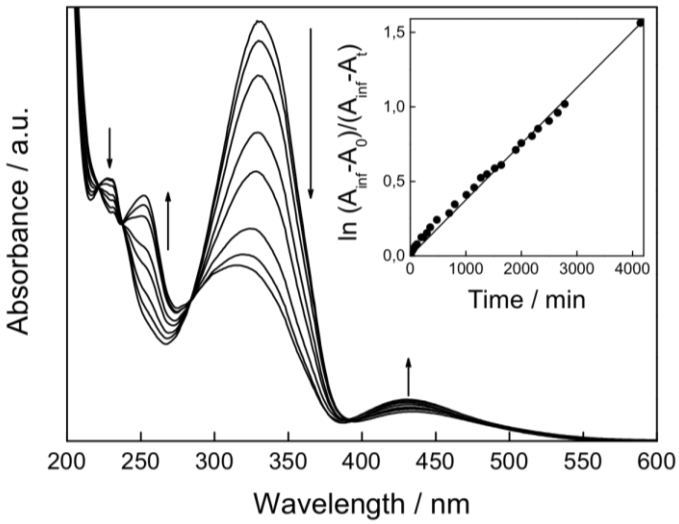

Figure 4. Absorption spectra of **3** under UV irradiation in water. The peaks at about 330 nm are characteristic of the *trans* isomer, while the peaks at about 430 nm correspond to the *cis* isomer. The series of spectra presented correspond to the visible light photoisomerization of the *cis* isomer into the *trans*. The inset shows a first order plot for *cis* to *trans* thermal isomerization.

estimate the value of the *cis* to *trans* thermal isomerization of $3.8E^{-4}$ min^{-1}.

7.5.3. Laser Flash Photolysis

Laser flash photolysis experiments were carried out in a Luzchem ns laser flash system using the third (355 nm) harmonic of a Q-switched Nd:YAG laser for excitation (pulse ≤ 10 ns) and a 175 W ceramic Xenon Fiberoptic Lightsource, Cermax, perpendicular to the laser beam, as a probing light. The signal from the monochromator/photomultiplier detection system was captured by a Tektronix TDS 3032B digitizer. Laser system and digitizer are connected to a PC computer via GPIB and serial interfaces that controlled all the experimental parameters and provided suitable processing and data storage capabilities. The software package has been developed in the LabVIEW environment from National Instruments and compiled as a stand-alone application. The samples contained on Suprasil quartz 0.7×0.7 cm^2 cuvettes capped with septa were purged with a N_2 or O_2 flow for at least 15 min before laser experiments.

Since in the case of methyl orange (**1**) we have not been able to obtain any evidence of the photoisomerization using conventional spectroscopy, we have submitted an aqueous solution of **1** irradiated at the open air after 15 min purging with oxygen, to laser flash photolysis using a nanosecond system and operating at 355 nm as excitation wavelength. The presence of oxygen during the experiment should suppress the formation of any triplet-excited state that could mask the spectral changes of the isomerization. In principle *trans-cis* isomerization should occur independently of the presence of oxygen. Under these conditions we have been able to record a transient spectrum showing an absorption band from 340–400 nm accompanied by an intense bleaching of the ground state absorption peaking at 455 nm and a continuous absorption from 500 to 800 nm (see **Figure 5**). The temporal profile of the signals in the 500–800 nm broad band is identical showing that this absorption corresponds to a single species that do not correspond to the *cis* isomer. For the *cis* isomer a narrower band from 500–600 nm should that been recordered. Based on precedents in the literature we attribute the continuous 500–800 nm absorption to a photochemical proton shift mediated by the solvent in wich, at the pH studied, a proton from the dimethyl amino substituent move to the azo group.[263] Similarly laser flash photolysis of azobenzene **2** in water was performed in the presence of oxygen to avoid the interference of triplet excited state. **Figure 6** shows the corresponding transient spectrum recordered upon 355 nm excitation. As it can be seen there this transient spectrum has many similarities with that previously commented from azobenzene **1**, narrow absorption peaking at 260 nm, bleaching off the trans isomer at 360 nm and a continuous from 470 to 800 nm, and it was again attributed to photoinduced proton transfer from the phenolic to the azo group mediated by the solvent. One interesting difference between azobenzenes **1** and **2** is the lifetime of the initial *trans* isomer. This increase lifetime of the species arising from phototropism of compound **2** must have to be related with the stability of the corresponding phenolate with respect to the acid/base equilibrium corresponding to azobenzene **1**. In any case for azobenzene **1** and **2** under the conditions studied, laser flash photolysis clearly rules out the occurrence of *trans* to *cis* photoisomerization.

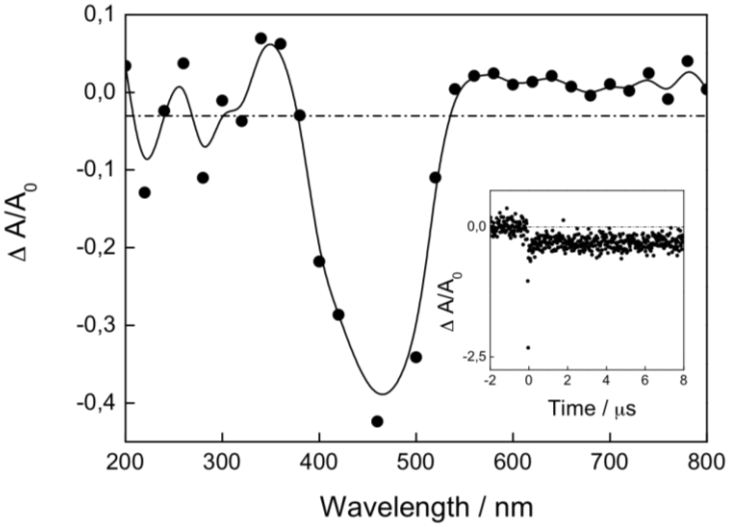

Figure 5. Transient absorption spectra given as variation of absorbance, Δ*A*, divided by the initial absorption of an O_2-purged **1** solution recorded 1 μs after 355 nm laser excitation. The inset shows the temporal signal decay measured at 460 nm.

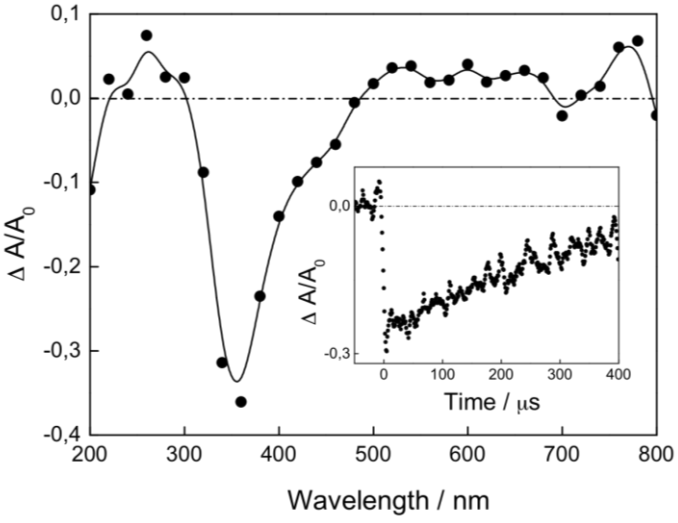

Figure 6. Transient absorption spectra given as variation of absorbance, Δ*A*, divided by the initial absorption of an O_2-purged **2** solution recorded 250 μs after 355 nm laser excitation. The inset shows the temporal signal decay measured at 360 nm.

7.5.4. Silica Gels

The azobenzene-containing gels were synthesized by mixing an aqueous solution of **1**–**3** (10^{-4} M) previously alkalinized with sodium hydroxide (2 M) in the case of azocompound **3**, until the sample was completely dissolved (final pH = 11, yellowish solution). Then 5 g of Aerosil were added to the initial solution (100 mL) and the mixture was vigorously stirred during 5 minutes. Finally the sample was placed on a preheated oven at 70 ºC for 3 hours to generate a yellowish dense and viscous gel that does not fall down upon turning the vial upside down.

Compounds **1**, **2** and **3** were used to prepare gels that could exhibit photoresponse as consecuence of the *trans*/*cis* isomerization. As observed in aqueous solution only compound **3** exhibit reversible photoisomerization upon UV irradiation (see **Figure 7**). In contrast to solutions, the much higher viscosity of gels allows the formation of thick films and other bulky systems containing indefinitely persistent suspended micro-/nano particles. The reduced diffusion and mobility of suspended particles occurring in gels is not possible in solution. In our case the gels were obtained by suspending Aerosil (5% weight) in water containing **3**, then the suspension was vigorous stirred and mild heated at 70 ºC until thick gel was obtained. Irradiation of this gel containing **3** leads to changes in the optical spectrum, compatible with the occurrence of *trans-cis* isomerization observed for this compound in aqueous solution. The two main differences of the photoisomerization in gel and in liquid phase are the extent of the decrease/increase of the bands corresponding to the *trans-cis* isomers (which is smaller in gel than in solution), and the kinetics of the reverse *cis* to *trans* isomerization that is much slower in the gel than in solution. Consecutive cycles of *trans* to *cis* isomerization irradiating at 300 nm and *cis* to *trans* by irradiation in the visible were performed up to 10 times, without observing significant fatigue in the system. Considering that the increase viscosity of gels could favor the *trans* to *cis* isomerization of azobenzenes **1** and **2** despite that these process that not occur in aqueous solution, we also studied the photochemical behavior of two analogous gels prepared by incorporating azobenzene **1** or **2** however also for the gels, we have not been able to obtain any spectroscopic evidence that

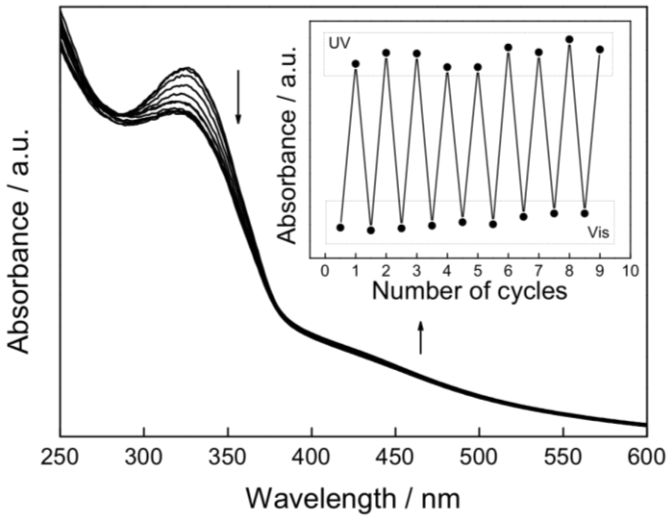

Figure 7. Absorption UV-Vis spectra of the photoresponsive gel prepared with molecule **3**. The peak at about 330 nm is characteristic of the *trans* isomer, while the peak at about 430nm corresponds to the *cis* isomer. The inset shows the reversibility data monitored at 324 nm to 327 nm after successive cycles of irradiation with UV and visible light.

could support the occurrence of *trans* to *cis* photoisomerization, and therefore, no further studies with these two azobenzenes were pursued.

8. Thermo-Responsive Breathing in Hybrid Magnetic Multilayers Based on LDHs[†]

A hybrid magnetic multilayer material having micrometric size, highly crystalline hexagonal crystals consisting on CoAl–LDH ferromagnetic layers intercalated with a mixture of flexible sodium dodecylsulphate surfactant and thermoresposive 4-(4-anilinophenylazo)benzenesulfonate (AO5) molecules (proportion 9:1) has been obtained. The resulting material exhibits thermochromism attributable to the isomerization between the azo (prevalent at room temperature) and the hydrazone (favoured at higher temperature) tautomers, leading to a thermomechanical response. In fact, these crystals exhibited thermally induced motion triggering dramatic changes in the crystal morphology and volume. *In-situ* variable temperature XRD of these thin hybrids shows that the reversible change into the two tautomers is reflected in a shift of the position of the diffraction peaks at high temperatures towards higher interlayer spacing for the hydrazone form as well as a broadening of the peaks reflecting lower crystallinity and ordering due to non uniform spacing between the layers. These structural variations between room temperature (*BS* = 25.91 Å) and 100 ºC (*BS* = 25.05 Å) are also reflected in the magnetic properties of the LDH due to the variation of the magnetic coupling between the layers. Overall, our study constitutes one of the few examples showing a fully reversible thermo-responsive breathing in a 2D hybrid material. In addition, the magnetic response of the hybrid can be modulated due to the thermotropism of the organic component that, by influencing the distance and in-plane correlation of the inorganic LDH, modulates the magnetism of the CoAl–LDH sheets in a certain range.

[†] Abellán, G.; Carrasco, J.A.; Coronado, E.; Ribera, A.; Varela, M.; Jaafar, M.; Gómez-Herrero, J.; Zamora, F.; Atienzar, P.; Jordá, J. L.; García, H. *submitted*. This work has been carried out in collaboration with: Prof. H. García at the Instituto de Tecnología Química (CSIC-UPV), Prof. F. Zamora and Prof. J. Gómez-Herrero at Universidad Autónoma de Madrid, and Dr. M. Varela at Oak Ridge National Laboratory, Materials Science and Technology Division, USA.

8.1. Introduction

As we have seen in the previous Chapter, intercalation of a azobenzene-4,4'-dicarboxylate molecule leads to photoinduced *trans-cis* isomerization with a remarkable reduction of the length of the molecule that is reflected in the interplanar distance of the ferromagnetic CoAl–LDH.[181] The system undergoes a reversible shift to the initial state upon *cis*-to-*trans* proton-assisted, thermal isomerization triggered by moisture. Apart from this example, we are aware of no other works dealing with the reversible photo-switching of micrometric LDH systems. In that example azobenzene-4,4'-dicarboxylate is connected through the two extremes to the layers leading to a "rigid" system in which the *cis-trans* photoinduced isomerization is almost unable to change the interlayer distances; in turn, it produces a sharp tension within the layers including distortion, which lead to significant changes in the magnetic properties. Here we will explore the use of a photoactive molecule, which is designed to be connected by one of the two extremes to the system. This modification is expected to lead to more flexibility (**Figure 1**).

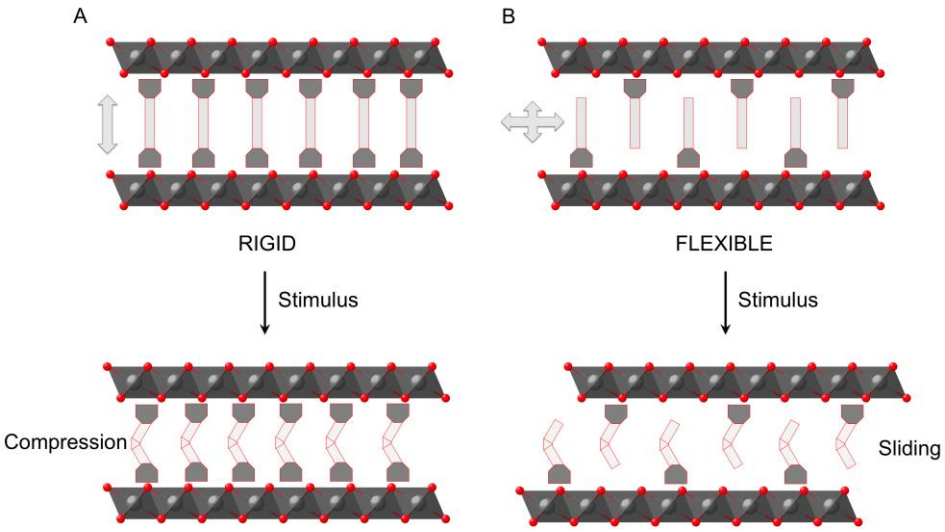

Figure 1. Schematic diagram of the LDH nanosheet compression/sliding movement and interlayer distance change by application of an external stimulus to: (A) a rigid system consisting on two anchoring groups; and (B) a more flexible one having only one anchoring group.

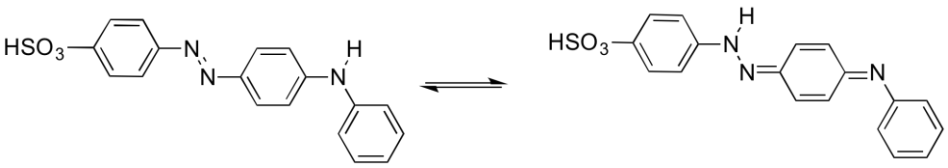

Figure 2. Tautomeric equilibrium between the *A*– and the *H*–form of the 4-(4-anilinophenylazo)benzenesulfonate.

Inoue and co-workers have reported the only example based on inorganic niobate nanosheets that exhibits macroscopic morphological change originated by reversible photoinduced sliding of the layers.[264] In this sense, the more versatile LDHs offer a broader range of possibilities to develop responsive materials that are almost unexplored at the present.[7,73,81]

Herein, we report the behaviour of a different LDH hybrid containing thermochromic 4-(4-anilinophenylazo)benzenesulfonate (AO5) molecules together with flexible SDS surfactant moiety that exhibits upon heating at moderate temperatures a reversible change in the structure and, therefore, in the magnetic properties. This hybrid shows temperature-responsive breathing, with drastic structural transformations. We have selected the AO5 thermochromic molecule on the basis of its optimal tautomeric behaviour (**Figure 2**).[265] Using the reversible equilibrium between the two tautomers of the azobenzene triggered by temperature at the nanometric scale, we have varied the interlayer distance of the inorganic component allowing modulating the magnetic behaviour and the change being reflected at the micrometric scale in the morphology of the crystals. As demonstrated by means of variable temperature PXRD and AFM, this layered hybrid molecular system exhibits a reversible morphological change, and can be considered as a thermoactivated responsive material.

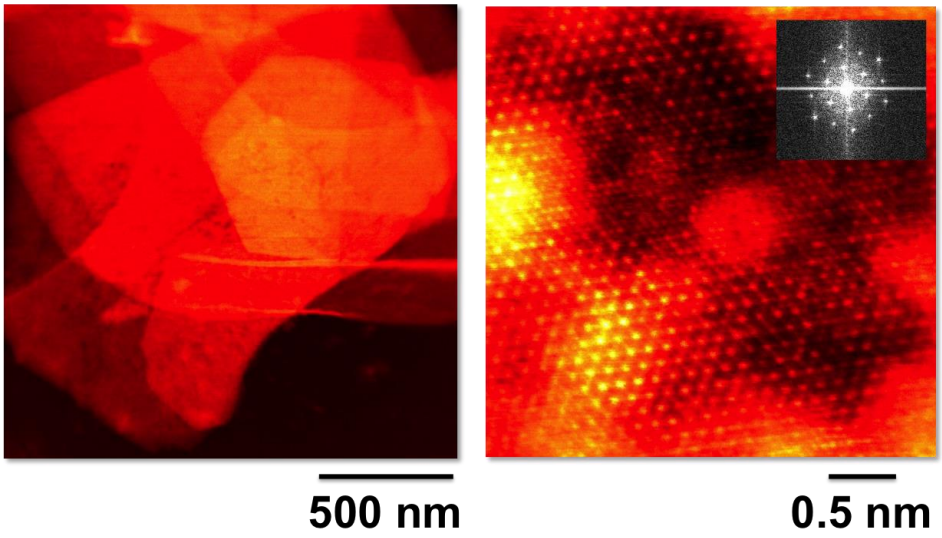

Figure 3. (*left*) Low magnification image of the platelets, which are 500–1000 nm in size. (*right*) High magnification HAADF image. The inset shows the image fast Fourier transform, which exhibits the hexagonal symmetry of the crystal.

8.2. Results and Discussion

8.2.1. Structural Characterization

A CoAl–CO_3 material with very high crystallinity and defined hexagonal morphology was herein obtained by means of a modified homogeneous precipitation method using urea as ARR and subsequently, submitted to ion exchange to obtain the NO_3^- form. To gain further insight on the microstructure of the initial platelets, we analysed the sample by aberration-corrected STEM-EELS at 60 kV.

The crystals were in the range of microns in size, as depicted in the low magnification HAADF image of **Figure 3** (left). An atomic resolution high angle annular dark field (HAADF) STEM image of the CoAl sample is shown on the right panel, acquired with the electron beam perpendicular to the platelet plane. The sample is highly crystalline and a clear hexagonal atomic structure can be observed with well-defined edge-sharing metallic octahedra that clearly indicate the brucite-like structure of the layers (see the Fourier transform in the inset). Some stacking faults are also observed with occasional lack of periodicity in the

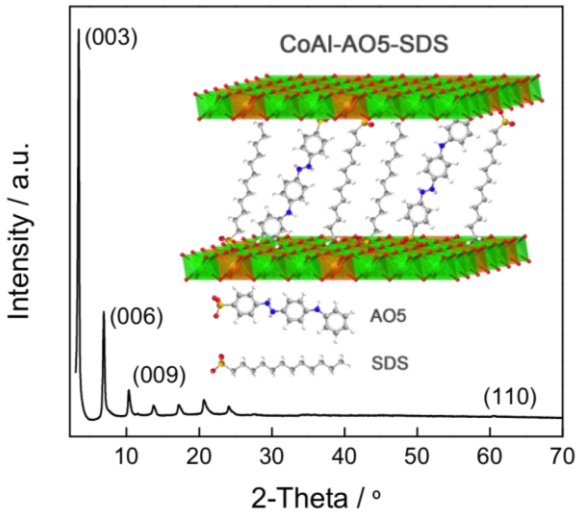

Figure 4. X-ray diffraction pattern of CoAl–AO5.

atomic chains, probably related to some disruptions in the cation ordering of the samples.[31,154,179] Unfortunately, the samples were quite sensitive to electron beam irradiation and did damage too fast under the electron beam to acquire meaningful spectroscopic data that would allow a detailed chemical quantification.

The preparation of the ferromagnetic LDH incorporating the combination of the two organic anions —one of them with a thermotropic tautomeric equilibrium— has been carried out by nitrate-exchange under mild conditions. Specifically, the CoAl–NO_3 was modified by co-incorporation of sulfate dodecyl and AO5 molecules in the appropriate SDS/AO5 ratio to achieve the optimal tautomeric behaviour (*i.e.* 9:1) to give the sample CoAl–AO5. It is worth mentioning the high crystallinity of the final hybrid material, as depicted in **Figure 4**.[265] A similar material in which AO5 accompanied by sodium benzene dodecyl sulfonate surfactant has been incorporated in the intergallery space of a diamagnetic ZnAl–LDH have been reported by Wei and co-workers.[265] These authors have shown that the role of the surfactant is to dilute the aromatic azo compound providing a flexible hydrophobic environment making possible the operation of a reversible cycle between the azo and the hydrazone tautomeric forms of the thermoresponsive azo compound. They have also reported that

under optimal compositions the solid can behave as a thermochromic material useful for sensing purposes, among others.

Chemical analysis and infrared spectroscopy confirm the absence of carbonates and nitrates indicating that the ion exchange steps have been performed completely. Moreover, CoAl–AO5 was characterized by thermogravimetric analysis under air atmosphere. There was an initial loss of desorption of water taking place in two steps corresponding to weakly physisorbed water (T < 100 ºC) and strongly chemisorbed water molecules that desorb at temperatures up to 200 ºC. After this initial weight loss due to water desorption, a considerable multi-step jump of about 25 % attributable to combustion of organic anions takes place in the temperature range from 200 ºC to 500 ºC.

FESEM provides images showing the hexagonal morphology of the LDHs (**Figure 5**). Well-developed hexagonal crystals of about 4.5 μm diagonal were determined for both the CoAl–NO_3 and CoAl–AO5 LDHs. Moreover, a precise correlation between the thickness of the platelets and their composition has been observed (**Figure 6**). In fact, while the hexagonal morphology was retained, the thickness of the platelets increased by the anion exchange from NO_3^- to AO5. The ratio of the average particle thickness (from 71 to 197 nm; 2.8 times) before and after the exchange of NO_3^- with the AO5/SDS mixture was consistent with the ratio of the basal spacing (from 0.88 to 2.59 nm; 2.9 times) before and after the anion exchange determined by PXRD. These measurements confirm the topochemical reaction of the intercalation, as recently reported by Ogawa et al.[59]

This platy morphology of CoAl–AO5 is especially suited for the preparation of thin films coating flat substrates. These films were obtained by spraying a paste of CoAl–AO5 suspended on acetyl acetonate using α-terpineol and carboxymethyl cellulose as thickener, followed by evaporation of these additives. Profilometric analyses of these films are shown in **Figure 7** that also shows a photograph of the films on high-quality suprasil quartz. As it can be seen in this Figure, the film is highly homogeneous without formation of pinholes, cracks or crevices on it. The average thickness is around 1.5 μm.

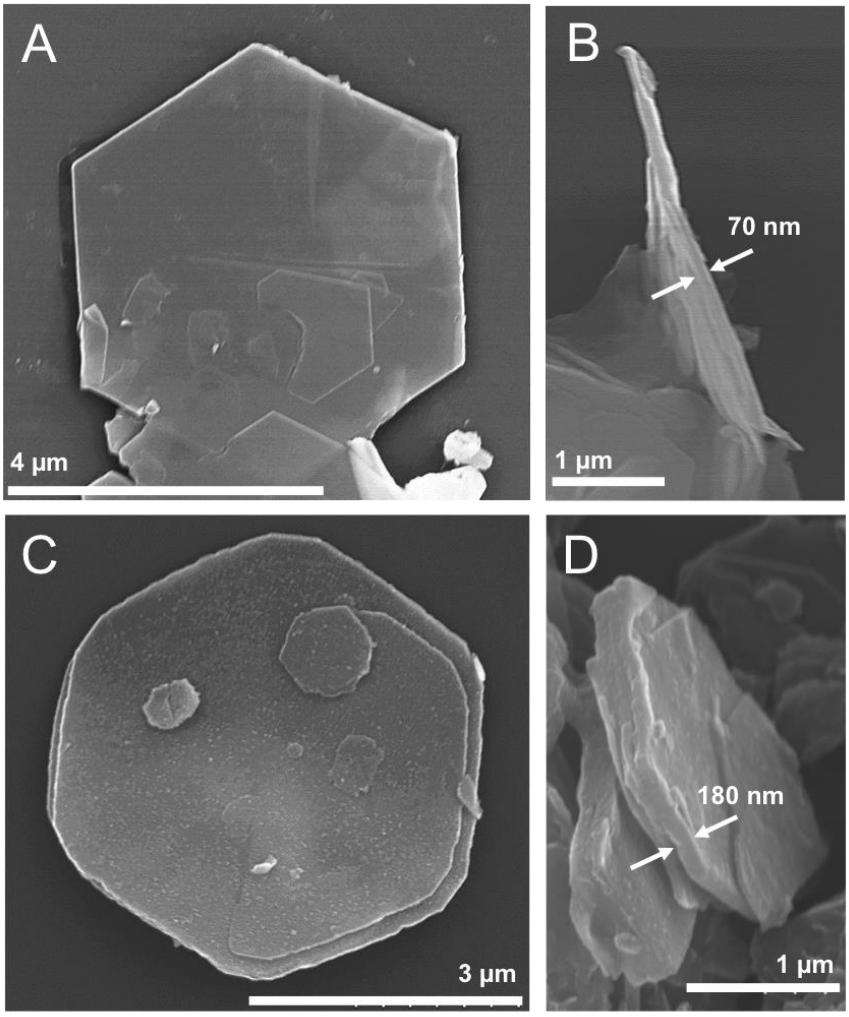

Figure 5. FESEM images of the CoAl–NO_3 (A and B) and CoAl–AO5 (C and D) samples, showing hexagonal well-defined morphology and their thickness.

8.2.1. Photochemistry

These films have allowed us to perform a spectroscopic study of the reversible photochromism exhibited by CoAl–AO5. Heating of the film from room temperature to > 65 ºC produces a significant visual change in the color from yellow to red.

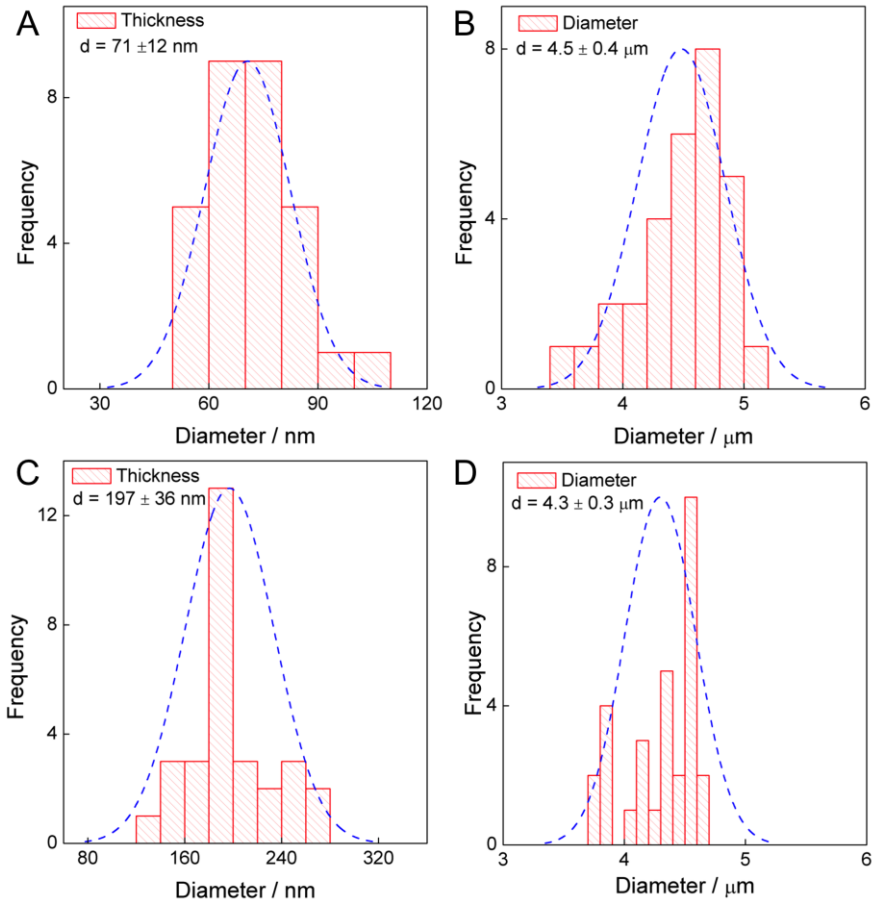

Figure 6. Particle size distribution highlighting the average values for the diameter and thickness of CoAl–NO_3 (A and B) and CoAl–AO5 (C and D), respectively.

This visual change can be quantified by the corresponding variation in the UV-Vis absorption spectrum of the material (**Figure 8**). The fact that the CoAl–AO5 material is in the form of thin film, allows recording absorption spectra by transmission mode, a technique that is not possible working with opaque powders. The state exhibiting yellow color has an absorption band at λ_{max} = 365 nm that has been attributed to the azo tautomer (*A*) of AO5. Upon heating, a broader band at longer wavelengths (λ_{max} = 445 nm) that has been ascribed to the hydrazone form of AO5 (*H*) develops.[232] This change in colors were reversible and is compatible with the proposed shift in the equilibrium between

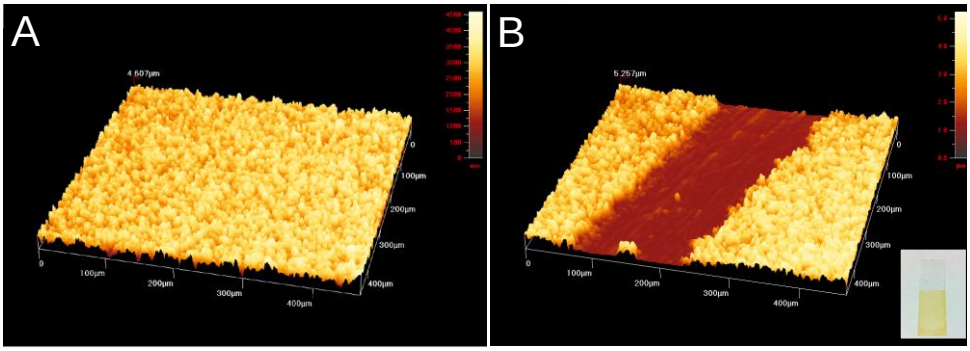

Figure 7. (A) Surface and (B) profilometric characterization of the CoAl–AO5 films prepared using acetyl acetonate, α-terpineol and carboxymethyl cellulose. The inset presents a digital photograph of the as-obtained film on suprasil quartz substrate.

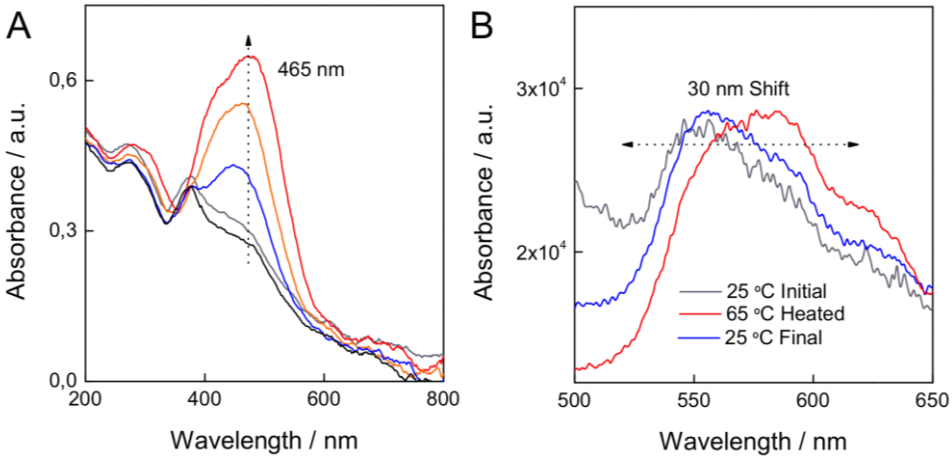

Figure 8. (A) In-situ transmission absorption spectra of the CoAl–AO5 film during heating in the temperature range 25–80 °C. (B) The corresponding in-situ fluorescence spectra showing the reversible peak shift after heating at 65 °C.

the two forms of AO5 as depicted in **Figure 2**. The changes in the UV-Vis absorption spectra are accompanied by parallel changes in fluorescence spectroscopy. Although the emission from the material is weak due to the transparency and thinness of the film, photoluminescence was observed both for the yellow AO5–*A* and the red AO5–*H*. At room temperature excitation at

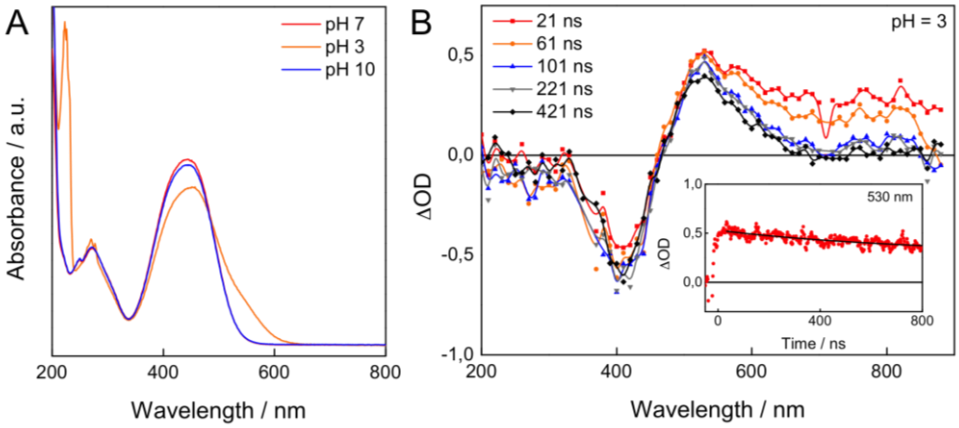

Figure 9. (A) UV-Vis absorption spectra of aqueous solutions of AO5 at different pH, namely, 3 (ocre), 7 (red) and 10 (blue). (B) Laser flash photolysis absorption spectra of an acidic solution of AO5 (pH = 3), depicted spectral traces are from 21 to 421 ns after the laser pulse (λ_{exc} = 355 nm). The inset represents the decay spectra at 530 nm, highlighting the presence of long live transient ascribed to the formation of the *cis* isomer.

370 nm gives an emission peaking at about 550 nm. When the film is heated, and the 465 nm band develops, the photoluminescence shifts to the red exhibiting the maximum at 585 nm. **Figure 8** illustrates the changes in the emission spectra accompanying to the variation in the absorption spectra.

In order to provide some additional spectroscopic data to understand the changes occurring in the absorption optical spectra of the CoAl–AO5 material, we undertake a study of the UV-Vis absorption spectra of pure AO5 molecules in solution as well as some laser flash transient spectroscopy. While in acetonitrile solution compound AO5 exhibit a band with absorption maximum at 463 nm, in aqueous solution the absorption maximum in the range of pH values from 3 to 10 was between 465 nm (acid pH) to 450 (basic pH). According to these spectra it seems that the tautomerization observed upon heating and cooling is related to changes with the polarity of the tautomeric equilibrium of AO5 between *A* and *H*, as previously suggested.[265] In fact, when an acid aqueous solution (pH = 3) of AO5 (λ_{max} = 465 nm) is photolyzed with 355 nm laser pulse under argon atmosphere, generation of a lived long transient with a

characteristic band at 530 nm is observed (see **Figure 9**). This transient observed in water with characteristic λ_{max} red-shifted with respect to the absorption of the starting isomer is compatible with the generation of the *cis* isomer of the azo compound that is a general photochemical transformation of azo compounds.[233,242] Observation of this *cis* isomer at 530 nm seems to rule out the involvement of this isomer in the reversible thermal changes observed for the CoAl–AO5 material. Therefore, in view of the previous proposal on the occurrence of *A* to *H* reversible thermal tautomerisation for AO5 and our observation of a band at 530 nm upon photolysis of AO5, the most likely rationalization for the changes observed in the optical spectrum upon heating is, then, the conversion between the *A* and the *H* forms of AO5.

8.2.2. X-ray Diffraction Study

The most relevant feature of CoAl–AO5, related to the reversible thermochromism attributable to the mesomeric proton shift, is the change inthe spacing between the layers that accompanies the reversible tautomerization from the *A* to *H* forms. X-ray diffraction of CoAl–AO5 at room temperature gives the characteristic pattern expected for highly crystalline LDH with up to eight sharp (00*l*) diffraction peaks, presenting a *BS* of 25.91 Å in excellent accordance with previous reports on SDS intercalated LDHs.[59]

We were interested in determining if the reversible changes into the two isomeric forms that presumably should have different molecular dimensions are reflected also in changes into the structure, *i.e.* the interplanar distance of LDH. The study was performed with thin films of CoAl–AO5 supported on quartz. We followed the changes in the XRD upon heating from room temperature to 100 °C. The configuration of the cell holder for thin films did not allowed to monitor 2θ angles smaller than 5° and, therefore, we were limited to study the second (00*l*) harmonic and higher peaks. It was observed that also for these films the diffraction pattern changes shifting the position of the (00*l*) peaks towards higher angles as well as the peaks become broader. The broadening should indicate a more disordered stacking of the layers in CoAl–AO5. Based on recent similar finding for niobate[240,264] we propose that this disorder should be a consequence of a random sliding of the constituting hydroxide layers (*vide infra*), a fact that is triggered by the partial isomerization of *A* into *H* forms

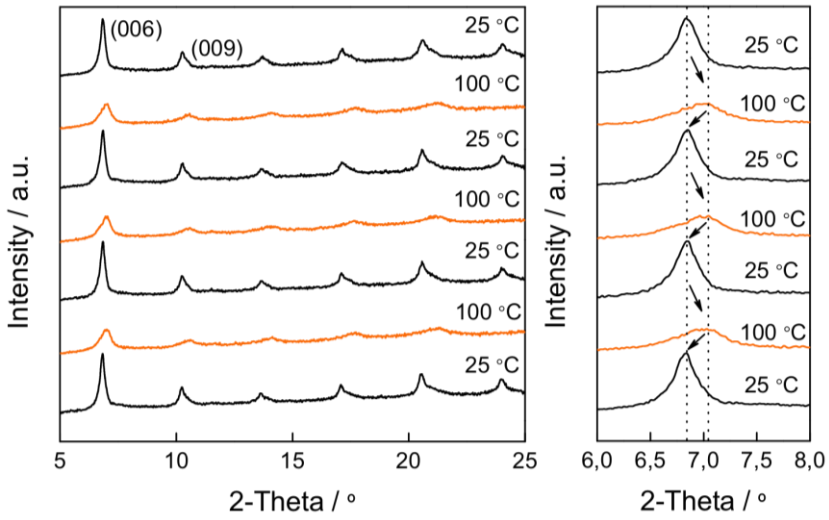

Figure 10. (A) In-situ transmission absorption spectra of the CoAl–AO5 film during heating in the temperature range 25–80 °C. (B) The corresponding in-situ fluorescence spectra showing the reversible peak shift after heating at 65 °C.

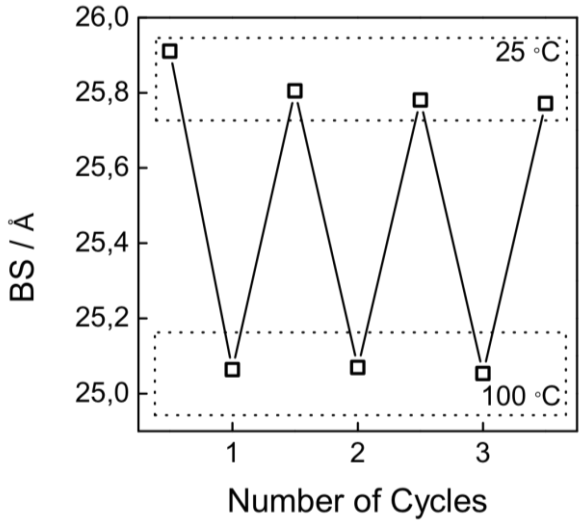

Figure 11. The variation of the basal space during several cycles of heating and cooling.

leading to a distribution of interlayer distances around a maximum value. These changes were reversible upon heating and cooling cycling, in accordance with the changes previously observed in transmission absorption spectroscopy for the isomerism between the azo and hydrazone forms. **Figure 10** shows a series of X-ray diffraction patterns recordered at 25 or 100 ºC illustrating the changes observed. While for room temperature the position of the (006) peaks is around 6.8º, at 100 ºC the broader peak has the maximum shifted towards higher values in 2θ, corresponding with a change in the basal spacing from 25.91 to 25.05 Å (**Figure 11**). The assumption that the mechanism of isomerization by proton shift involves water —probably as shuttle of the protons following a Grotthuss-type proton migration mechanism, as previously proposed (**Figure 12**)[11,265]— is reflected by the fact that this cycling between the two diffraction patters shown in **Figure 11**, can also be achieved by submitting the cell chamber to vacuum to desorb water and, then, exposing the sample to moist air. It is worth to comment that if instead of moist air, dry nitrogen is introduced into the chamber, the position of the peaks remain as in vacuum at 2-Θ value of *ca.* 7.1º, these changes between moist (006 peak 6.7º), and dry (006 peak 7.1º) states, were also reversible as already observed for thermochromism and for the heating in XRD.[78]

8.2.3. AFM Study

Besides XRD and crystallinity we also investigated the variations in the morphology of the CoAl–AO5 crystals by means of a variable temperature atomic force microscope, mounted in a standard high vacuum chamber. Heating and cooling were achieved by thermal contact to the sample holder. The sample temperature was measured with a thermocouple. We prepared a diluted ethanol suspension of CoAl–AO5 crystals by sonication and, afterwards, we deposited a drop on a silicon wafer having markers. AFM imaging of the surface revealed platy CoAl–AO5 crystals of reduced dimensions (*ca.* 0.5–1.5 μm) probably due to the sonication. **Figures 13–15** shows AFM images of CoAl–AO5 acquired at ambient conditions, heating the sample at 80 ºC and then cooled again at RT. In each image we can distinguish a particle and a reference marker that safely identifies the particle throughout the experiments. Zoom-in images allows the observation of the evolution of the shape of the particle,

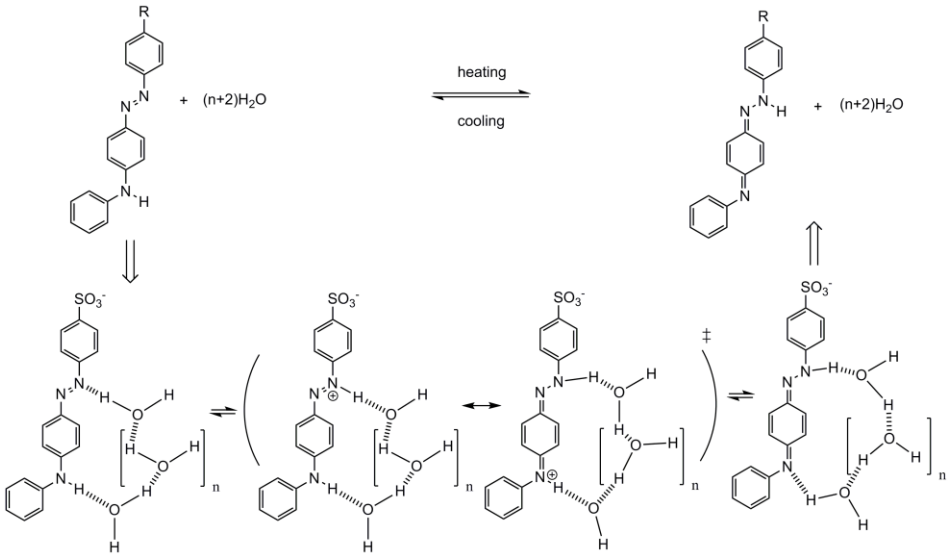

Figure 12. Representation of the tautomerization of AO5 upon heating and cooling in the interlayer space of CoAl–AO5 following a Grotthuss-type proton migration mechanism. Adapted from Wang et al.[265]

exhibiting a pronounced compression upon heating, that is partially reverted freezing to RT.

Moreover, as can be observed in **Figure 13**, the histogram of the volume indicates a decrease in the overall volume of the particle with heating, which is also partially reversible after freezing. The images clearly reveal notable changes in its morphology and volume of the particle, probably due to the random sliding of the hydroxide sheets, in accordance with the broadening and decreased interlayer spacing previously observed in X-ray diffraction experiments. These experiments provide a direct evidence of the thermo-responsive breathing of the hybrid at the microscale as consequence of the isomerization of the AO5 at the nanoscale in the LDH.

8.2.1. Magnetic Properties

Another effect of the *A–H* isomerization of AO5 incorporated on LDH is that due to the composition of the CoAl–AO5 LDH, the magnetic response should change reversibly between two states. The precedents showing fully reversible magnetic properties between two states in a hybrid materials are scarce,[181,238,255,266] and the reversible structural transformations associated to the

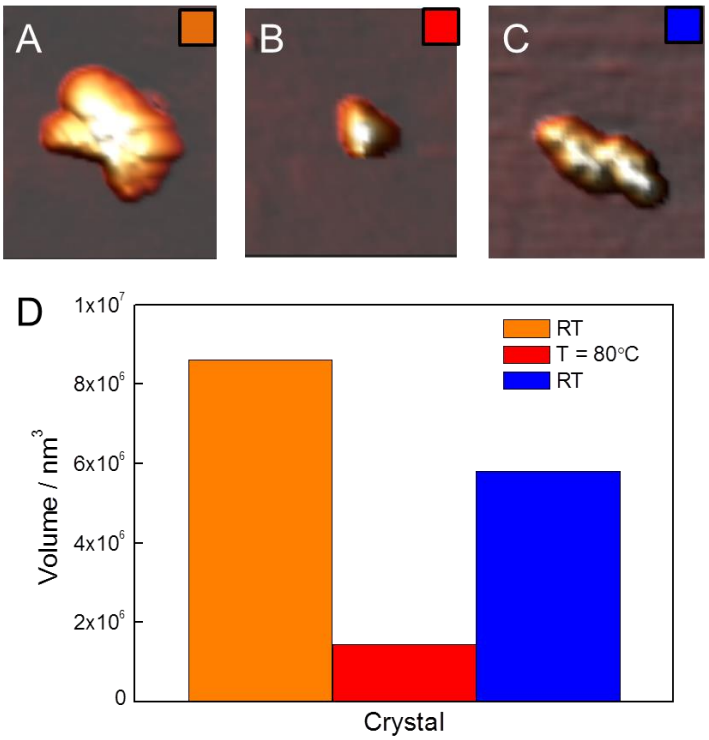

Figure 13. AFM images of CoAl–AO5 acquired at (A) RT; (B) 80ºC; (C) RT after heating the sample at 80ºC. The scanning area is exactly the same in all images. Image size: 1.7 μm × 1 μm. (D) Histogram of the volume of CoAl–AO5 measured by AFM.

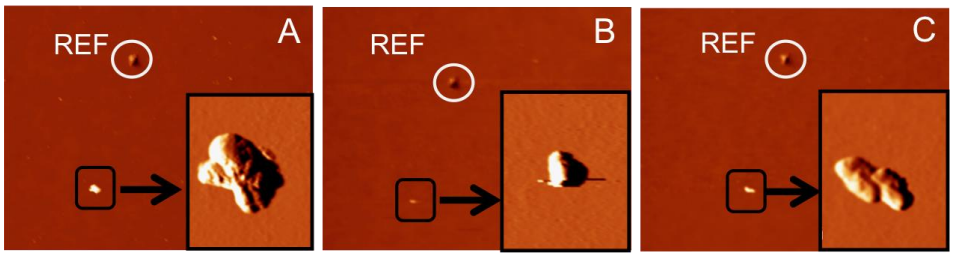

Figure 14. Topography images of CoAl–AO5 acquired at ambient conditions and different temperatures. In each image we can distinguish a crystal and a reference marker: (A) RT; (B) 80 ºC; (C) RT after heating the sample at 80 ºC. Images size: 13 μm × 9 μm. Insets are the same images of **Figure 13A–C**, respectively. In order to enhance the details of the crystal the derivative of the topography is shown.

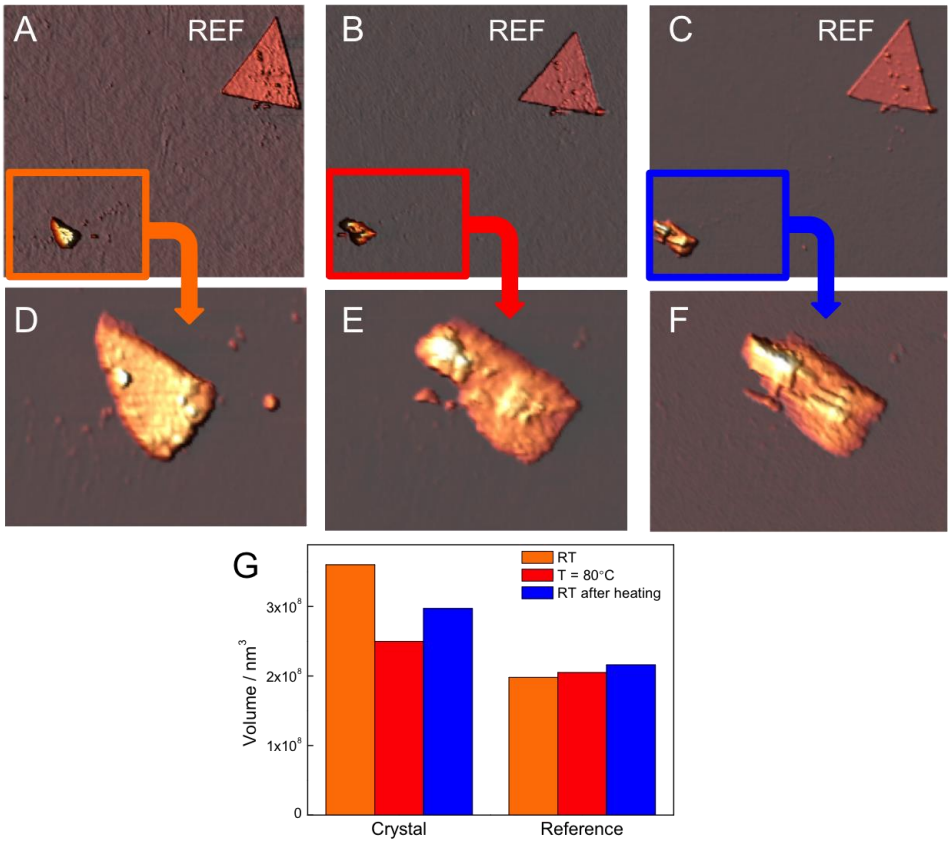

Figure 15. AFM images of CoAl–AO5 acquired at ambient conditions and different temperatures. In each image we can distinguish a crystal and a reference marker: (A) RT; (B) 80ºC; (C) RT after heating the sample at 80 ºC. Images size: 17 µm × 17 µm. (D), (E) and (F) corresponds to zooms of (A), (B), (C) images to observe in detail the evolution of the shape of the crystal. (g) Histogram of the volume of CoAl–AO5 and the referece measured by AFM.

thermoresponsive breathing of the crystals should be reflected in changes in their magnetic behaviour. As previously reported, the overall magnetic behaviour of LDH materials depends on the F in-plane superexchange pathways between Co metals and the AF interlayer dipolar interactions, resulting in a low-temperature spin-glass-like behaviour.[121,161,179,181] The reversibility between *A* and *H* forms of the incorporated guest leads to a more disordered state as confirmed by XRD (shift and broadening of the peaks) and AFM (morphological changes)

measurements that is in clear contrast to that reported for a CoAl–LDH having intercalated photoisomerizable trans-azobenzene-4,4′-dicarboxylic acid (T1), in which no clear modifications in the XRD peak broadening were observed after UV irradiation.[181] In addition, while AO5 possesses only one SO_3^- anchoring group, leading to a more flexible movement, T1 acts as a more rigid pillar of the structure due to the double anchoring. These structural differences are also reflected in the magnetic behaviour of CoAl–AO5 LDH compared to CoAl–T1 LDH. The magnetic properties of CoAl–AO5 LDH were measured in a SQUID before and after heating of the sample in a quartz capsule at 2 K. As depicted in **Figure 16**, the hysteresis cycle of the CoAl–AO5 reveals a fully reversible variation of the saturation magnetization values after heating and cooling the sample. The magnitude of this variation is *ca.* 8 %, notably smaller than that reported for the CoAl–T1 (27 %). This is probably due to the fact that the flexible environment provided by the SDS/AO5 molecules minimizes the induced structural stress of the layers upon stimulus, resulting in less-intense modifications of the magnetism of the layers. Moreover, there is also an observable slight variation in the coercive field of *ca.* 5 G, despite the superparamagnetic character of the field dependence of the magnetization. Finally; *ac* dynamic magnetic measurements with an applied field of 3.95 G with frequencies oscillating between 1 and 1000 Hz, confirmed the spontaneous magnetization of the hybrid in the three states, showing a clear dependence with the frequency of the oscillating field in both the in-phase and out-of-phase signals, with no significant differences in the T_M values.

8.1. Conclusions

We have described a hybrid multifunctional thermoactive and magnetic layered material that makes use of the switching ability of 4-(4-Anilinophenylazo)benzenesulfonate molecules to alter the morphology of the material exhibiting a thermo-responsive behaviour. The different molecular shape of the azo (stable at room temperature) and the hydrazine (favoured at high temperatures forms) tautomers is reflected in a variation in the intergallery spacing of the LDH material as evidenced by AFM and X-ray diffraction, and this change at the nanoscale has consequence in the microscale. The change in

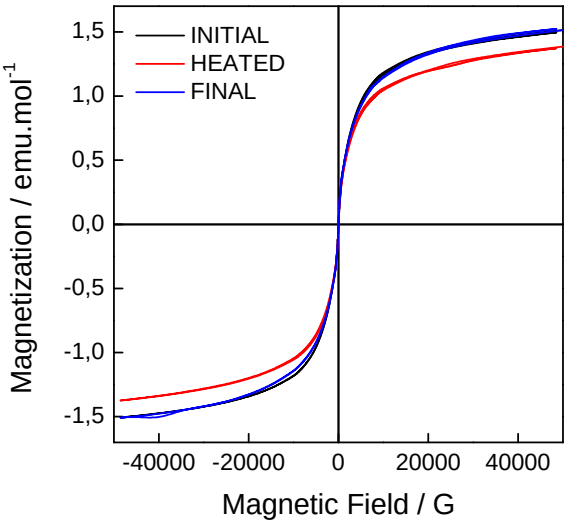

Figure 16. Hysteresis cycles for the initial CoAl–AO5 (black), and the corresponding heated (red) and final (blue) samples.

the morphology of the crystals and the macroscopic variations of their magnetic properties also depends on the state of the organic guest. Thus our study shows a case of control and tunabilty of the magnetic response between two different states by combining the thermotropism of the organic component with the magnetism of the inorganic LDH. Among others, the development of stimulus-responsive materials exhibiting reversible cycling (breathing) has been limited to the field of coordination polymers, or more specifically to MOFs[267] This work paves the way for the development of related "breathing" systems based on LDHs, paving the way for a plethora of possible applications in sensing,[268] magnetic switching,[230,269] heat storage/transfer,[270] or for temperature switchable devices.[271,272]

8.2. Experimental Section

8.2.1. Synthesis of CoAl–LDHs

Materials: All chemicals $CoCl_2{\cdot}6H_2O$, $AlCl_3{\cdot}9H_2O$, $NaNO_3$, HNO_3, $CO(NH_2)_2$ (urea), sodium dodecyl sulfate and 4-(4-anilinophenylazo)benzenesulfonate, were used as received from commercial suppliers (Sigma-Aldrich, Fluka and TCI) without further purification. All the experiments were carried out under inert atmosphere to prevent carbonate contamination.

Synthesis of CoAl–CO_3 LDH: $[Co_{0.66}Al_{0.33}(OH)_2](CO_3)_{0.16}{\cdot}mH_2O$ was synthesized according to the homogeneous precipitation method by using urea as ammonia releasing reagent (ARR).[45,246,247] Accordingly, the chloride salts of the metals were dissolved in Milli-Q purged water to reach a total cation concentration of 0.15 M in the final solution and keeping the stoichiometric coefficient constant at a value of x = 0.33 (equivalent to a Co/Al molar ratio of 2:1). Next, an aqueous solution of urea (three times the $[Al^{3+}]$) was added. The resulting pink mixture was transferred to a round bottom flask and heated up to 97 °C under reflux conditions. After 48 hours, the resulting finely divided pink powder was filtered, washed thoroughly with distilled water and ethanol, and dried at room temperature under vacuum. The pH value of the remaining solution was found to be around 7.5.

$[Co_{0.66}Al_{0.34}(OH)_2](CO_3)_{0.33}{\cdot}0.17H_2O$ Anal. calc. for $H_{2.66}C_{0.33}O_{3.32}N_0Co_{0.66}Al_{0.34}$ (MW = 98.235): H, 2.61; N, 0; C, 1.96. Found: H, 2.58; N, 0.14; C, 1.98.

Preparation of CoAl–NO_3 LDH: $[Co_{0.66}Al_{0.33}(OH)_2](NO_3)_{0.33}{\cdot}mH_2O$ was obtained by carbonate-exchange of the as-synthesized CoAl–CO_3 LDH in presence of an excess of nitrate anions. In a typical procedure, 1 g of CoAl–CO_3 LDH was immersed in a round-bottom flask containing 1 L of an aqueous solution of $NaNO_3$ (1.5 M) and HNO_3 (0.005 M).[143] This mixture was mechanically stirred under inert atmosphere during 48 h. Afterwards, the resulting pink solid was filtered, washed thoroughly with Milli-Q water and ethanol and dried under vacuum at room temperature.

$[Co_{0.67}Al_{0.33}(OH)_2](NO_3)_{0.33}{\cdot}0.31H_2O$ Anal. calc. for $H_{2.62}C_0O_{3.3}N_{0.33}Co_{0.67}Al_{0.33}$ (MW = 108.534): H, 2.42; N, 4.97; C, 0. Found: H, 2.26; N, 3.69; C, 0.18.

8.2.2. Anion Exchange

4-(4-anilinophenylazo)benzenesulfonate/SDS intercalation, CoAl–AO5: In a typical procedure, 200 mg of CoAl–NO_3 was finely powdered and transferred to a round bottom flask. Then, 45 ml of an aqueous mixture of 4-(4-anilinophenylazo)benzenesulfonate (0.02 M) and SDS (0.14 M), was slowly added under inert atmosphere and continuous stirring. The mixture was sonicated during 5 minutes to produce a homogeneous dispersion and then was vigorously stirred at 900 rpm for 20 h under continuous argon bubbling. Finally, the yellowish precipitate was filtered under inert atmosphere, washed thoroughly with distilled water and ethanol, and dried at room temperature under vacuum.

$[Co_{0.65}Al_{0.34}(OH)_2](C_{18}H_{14}N_3SO_3)_{0.033}(C_{18}H_{29}SO_3)_{0.297} \cdot 0.77H_2O$ Anal. Calc. (M_W = 204.401): H, 6.17; N, 0.68; C, 34.87; S, 5.17. Found: H, 5.6; N, 1.24; C, 25.46; S, 5.13

8.2.3. Physical Characterization

Carbon, nitrogen and hydrogen contents were determined by microanalytical procedures using an EA 1110 CHNS-O Elemental Analyzer from CE instruments. Metallic atomic composition of bulk samples was determined by means of electron probe microanalysis (EPMA) performed in a Philips SEM-XL30 equipped with an EDAX microprobe. Dr. M. Varela at Oak Ridge National Laboratory carried out atomic resolution studies in real space by aberration corrected scanning transmission electron microscopy (STEM) and electron energy-loss spectroscopy (EELS) in a Nion UltraSTEM100 operated at 60 kV equipped with a spherical aberration corrector and a Gatan Enfina EEL spectrometer. Samples were prepared by dropping a colloidal suspension of the fresh sample in formamide on a holey carbon-coated copper grid for STEM-EELS observation. Field emission scanning electron microscopy (FESEM) studies were performed on a Hitachi S-4800 microscope operating at an accelerating voltage of 20 kV over metallized (1 min of Au/Pd) samples.

Infrared spectra were recorded in a FT-IR Nicolet 5700 spectrometer in the 4000–400 cm^{-1} range using powdered samples diluted in KBr pellets. Thermogravimetric analysis of all compounds were carried out with a Mettler Toledo TGA/SDTA 851 apparatus in the 25–800 °C temperature range under a

10 °C·min^{-1} scan rate and an air flow of 30 mL·min^{-1}. X-ray powder diffraction patterns of the precursor materials were collected with a Phillips X'Pert-MPD diffractometer provided with a graphite monochromator, operating at 40 kV and 20 mA and employing nickel-filtered Cu-K_α radiation (λ = 1.5418 Å). Profiles were collected in the 2.5° < 2θ < 70° range with a step size of 0.05°. UV-Vis spectra were conducted using a Varian Cary-5G UV-Vis spectrophotometer. Room temperature diffuse reflectance UV-Vis-NIR spectra of solid samples were recorded with a Varian Cary 5000 UV-Vis-NIR scanning spectrophotometer. Steady-state photoluminescence measurements were recorded in a Photon Technology International (PTI) 220B spectrofluorimeter having a 75W Xe arc lamp light excitation and Czerny-Turner monochromator, coupled to a photomultiplier.

Thin films of CoAl–AO5. The films (on quartz Suprasil substrates) were prepared by drop casting on a hot plate (80 ºC) at under ambient conditions a paste of CoAl–AO5 (about 40 mg) in α-terpineol-acetone (1.5 ml of a 1:2 mixture of α-terpineol:acetone) acetyl acetonate using α-terpineol and carboxymethyl cellulose as thickener that was sonicated to obtain a good dispersion. Once the solvent was evaporated the thickness of the layer was measured with an Ambios Xi-100 Non-Contact Optical Profilometer with nanometric vertical resolution. The thickness of the films was about 1 micron.

Irradiations were carried out in situ while the sample was placed on the holder of the spectrometer or XRD difractometer at ambient conditions. XRD patterns of the irradiated samples were obtained using a PANalytical X'Pert PRO diffractometer using copper radiation (Cu K_α = 1.5418 Å) with an X'Celerator detector, operating at 40 mA and 45 kV. Profiles were collected in the 2° < 2θ < 30° range with a step size of 0.017° 2*θ*. Samples were heated in situ during the measurements between 25 and 100 ºC. Cell parameters refinements of the bulk samples were carried out with the Fullprof suite programs using the TCH pseudo-Voigt function to fit the experimental profiles and considering the R-3m space group.

AFM experiments were carried out in the laboratories of Prof. F. Zamora and Prof. J. Gómez-Herrero at Universidad Autónoma de Madrid. Variable temperature Atomic Force Microscope (AFM) images were acquired in dynamic mode using a Nanotec Electronica system operating in the 25–100 ºC

temperature range in ambient air conditions. For AFM measurements, Olympus cantilevers were used with a nominal force constant of 0.75 N/m. The images were processed using WSxM. The surfaces used for AFM were marked SiO_2 substrates. In order to obtain reproducible results, very flat substrates were used with precisely controlled chemical functionalities, freshly prepared just before the chemical deposition.

AFM Sample preparation: CoAl–AO5 (1 mg) was suspended in 1 mL of EtOH under Ar atmosphere. The resulting suspension was diluted to a concentration of about 10^{-3} mg·mL^{-1}. The diluted solution was deposited on SiO_2 (10 μL) by drop casting using a Hamilton syringe. Upon standing 1 h in a homemade Cryocool device the substrates were dried under an argon flow.

Magnetic measurements were carried out with a Quantum Design superconducting quantum interference device (SQUID) MPMS-XL-5. The susceptibility data were corrected from the diamagnetic contributions of the atomic constituents of the samples as deduced from Pascal's constant tables and the sample holder. The *dc* data were collected under an external applied field of 100 G in the 2–400 K temperature range. Magnetization studies were performed between −5 and +5 T at a constant temperature of 2 K. The *ac* data were collected in the range 2–15 K with an applied alternating field of 3.95 G at different frequencies in the range 1–1000 Hz. The sample was placed on a quartz tube that had been previously measured in the same conditions. In a first run the hysteresis cycle of the magnetization of the sample was measured at 2 K and then the sample was submitted to room temperature and heated with an electrical heater at 100 °C during several minutes. After this heating, the sample was immediately inserted in the SQUID magnetometer at 100 K and cooled to 2 K in less than 30 min and the hysteresis cycle was repeated. Finally, the sample was submitted again to room temperature during several minutes and measured at 2 K to finish the reversibility measurements. Furthermore, the reproducibility of the measurements was checked for up to three different samples that gave very similar results.

3 Applications of LDH–Based Hybrids

9. Dual-Function Supercapacitive and Water Oxidation Electrocatalysts Based on Graphene/NiFe–LDH Hybrids[†]

In this chapter, we have explored the electrochemical behaviour of NiFe–LDHs, that show superb electrocatalytic properties towards the Oxygen Evolution Reaction. Moreover, as the electrochemical performance of LDH modified electrodes is often limited by their low intrinsic electronic conductivity, we have also investigated the effect of their hybridization with reduced graphene oxide, to render better electronic mobility. The incorporation of graphene leads to an increase in the supercapacitive properties of the hybrid whereas limits their oxygen evolution reaction (OER) activity due to the decrease in the active surface exposed to the electrolyte. A thorough study has been performed to unveil the insights into the electrochemistry of these appealing LDH–graphene hybrids.

[†] Abellán, G.; Martinez, J. G.; Bosch-Navarro, C.; Romero, J.; Marti-Gastaldo, C.; Otero, T. F.; Coronado, E. *submitted.* This work has been carried out in collaboration with Prof. T. F. Otero at the Group of Electrochemistry Intelligent Materials and Devices (Universidad Politécnica de Cartagena)

9.1. Introduction

The rapid increase in energy demand of the last few years has prompted the search of new cost-effective ways of storing energy.[273,274] The challenge is to develop new electrochemical supercapacitors, lithium ion batteries or water splitting devices in which chemical energy could be directly converted and stored. In order to increase the energy density a promising strategy is the design of new nanomaterials with controlled architectures.[102] In this sense, two-dimensional materials (*e.g.* transition-metal chalcogenides, graphene, layered double hydroxides) could play a key role as they possess unique physical properties and have been successfully employed for many different energy-related applications.[103,275]

Electrocatalytic water splitting (WS) drives the conversion of water into hydrogen fuels and arguably qualifies as the most promising source of limitless, clean, renewable energy. The Oxygen Evolution Reaction (OER) ($2\ H_2O \rightarrow O_2 + 4H^+ + 4e^-$) is the key limiting process as it is energetically disfavored by the thermodynamic stability of water.[273,274]. It involves the transfer of 4-electron per molecule with a complex mechanism affecting the overall energy conversion efficiency.[113] Practical electrochemical H_2 production is generally limited by the high overpotentials necessary, imposed by the slow kinetics of O_2 evolution, and the poor stability of electrode materials under alkali conditions. To date, the dominant electrocatalysts for OER are based on oxides of precious metals like Iridium (IrO_2) or Ruthenium (RuO_2) oxides based on their efficiency and sustainability.[276] Their high cost and scarcity nonetheless has hindered integration into commercial electrolysers and prompted the search of inexpensive, more abundant alternatives featuring similar efficiencies —high current densities at low overpotentials— and chemical stabilities. Starting with crystalline metal oxides like perovskites,[277] spinels[278] and amorphous metal oxides,[279,280] following with molecule-based polyoxometalate clusters[281–283] or Prussian Blue Analogues,[284] all have shown promising OER electrocatalytic activities. Among these materials, LDHs have been recently postulated as bimetallic earth-abundant electrocatalysts, giving new impetus to the rational design of sustainable catalytic materials.[115,116,285]

The interlayer anions of LDHs can be easily exchanged by soft chemistry routes. The composition of the metal layers can be also tuned chemically to introduce relevant properties like photocatalytic activity (e.g. ZnCr– or ZnTi–LDH)[249,286] or magnetism (e.g. NiAl– or NiFe–LDH).[122,179] Nanosheets of NiFe–LDH display very high OER activity in alkali solutions and has been postulated as excellent electrodes for ultrafast Zn–air batteries,[116,287] however their poor electrical conductivity and tendency of the layers to re-pack could lower the stability of the electrode featuring poor sustainability. This can be overcame by combining the electrocatalyst with conducting counterparts like carbon nanoforms to produce strongly coupled inorganic/nanocarbon hybrids with higher electrical conductivities and chemical robustness as result of the hybridation between components.[82,113] In this line, Graphene (G) and reduced graphene oxide (rGO), prepared by oxidation of graphite followed by exfoliation and chemical reduction, are playing an important role in the development of nanostructured hybrid catalyst assemblies provided their high surface area, outstanding electronic properties and two-dimensional geometry that favour redox surface events and water oxidation catalysis (WOC).[288,289]

Based on these principles, G/LDH strongly coupled hybrids have already shown higher efficiencies and stabilities when used as batteries, supercapacitors or pollutant removers.[87,101,106,110,111,290–297] Very recently, Dai and co-workers reported a nanosized NiFe–LDH (5:1 metal ratio, synthesized via sol-gel approach) hybridized with multiwall carbon nanotubes, exhibiting excellent OER activity.[116,287] However, there are no reports regarding the hybridization with graphene. Moreover, in a recent precedent published while our work was in progress, Liu, Kang and co-workers reported a material consisted of a nanosized NiFe–LDHs (5:1 metal ratio) hybridized with carbon quantum dots whose efficiency is strongly dependent on the size of the carbon nanoform (the hybrid being worse than the bare NiFe–LDH as the size of QDs is increased from 5 to 100 nm).[298] In all these previous studies, very small nanoparticles of NiFe–LDHs (< 100 nm in size, *ca.* 1 nm thick) with a rather unusual metallic composition (outside from the typical $0.20 < x < 0.33$ range)[11] were employed.

Furthermore, the ability of LDHs to undergo topochemical transformations after calcination opens the door for the study of the derived mixed metal oxides. In the specific case of NiFe–LDH, the thermal treatment leads to 2D nanoplates

consisting of NiO and $NiFe_2O_4$, which are expected to exhibit excellent performances as water oxidation electrocatalyst based on previous reports.[280,299]

We report a complete OER study of highly crystalline NiFe–LDH (x = 0.20, synthesized via ARR approach) exhibiting superb efficiencies, giving values higher than 20 mA·cm^2 after more than 20 days of continuous working at 1.6 V *vs.* RHE at basic pH. We also report the one-pot formation of a hybrid nanocatalyst by in-situ hybridization of crystalline NiFe–LDH platelets with rGO, which also exhibits high OER catalytic activity. Finally, we show that by a low-temperature annealing under nitrogen these materials give rise to an electrochemically active 2D strongly coupled bi-component NiO–$NiFe_2O_4$/rGO hybrid.

9.2. Results and Discussion

9.2.1. Synthesis and Characterization of rGO Hybrids

Hybrid NiFe–LDH/rGO (**1**) was obtained in one step by formation of the LDH in the presence of templating rGO layers. GO was added to a solution of Ni^{2+} and Fe^{3+} nitrates in water and the mixture was transferred to a Teflon liner, sealed in a solvothermal vessel and heated under autogenous pressure at 125 ºC. Heating triggers the hydrolysis of urea that progressively increases the pH up to a final value close to 8. This enables in-situ reduction of GO layers into rGO[300,301] whilst assisting the formation of NiFe–LDH. Magnetic measurements reveal the formation of spinel nanoparticles as a side-product of the reaction (*vide infra*).[116] Previous works report the formation of comparable impurities of $NiCo_2O_4$ spinel and iron oxide FeO_x in CoAl–LDH/rGO and NiFe–LDH/MWCNTs composites.[116,151,302] In a second stage, **1** was transferred to a tubular furnace, purged with nitrogen and heated to 250 ºC to generate NiO–$NiFe_2O_4$/rGO (**2**) in which only a bi-component-active mixture of NiO and $NiFe_2O_4$ is coupled to rGO.[105] The annealing temperature was optimized in order to avoid metal reduction at expense of graphene that can act as a nanometallurgic agent (see **Figure 1A**).[297] The formation of the hybrids was further corroborated by FT-IR analysis, showing the characteristic bands of rGO and those related with NiFe–LDH and NiO-$NiFe_2O_4$ (see **Figure 2**).

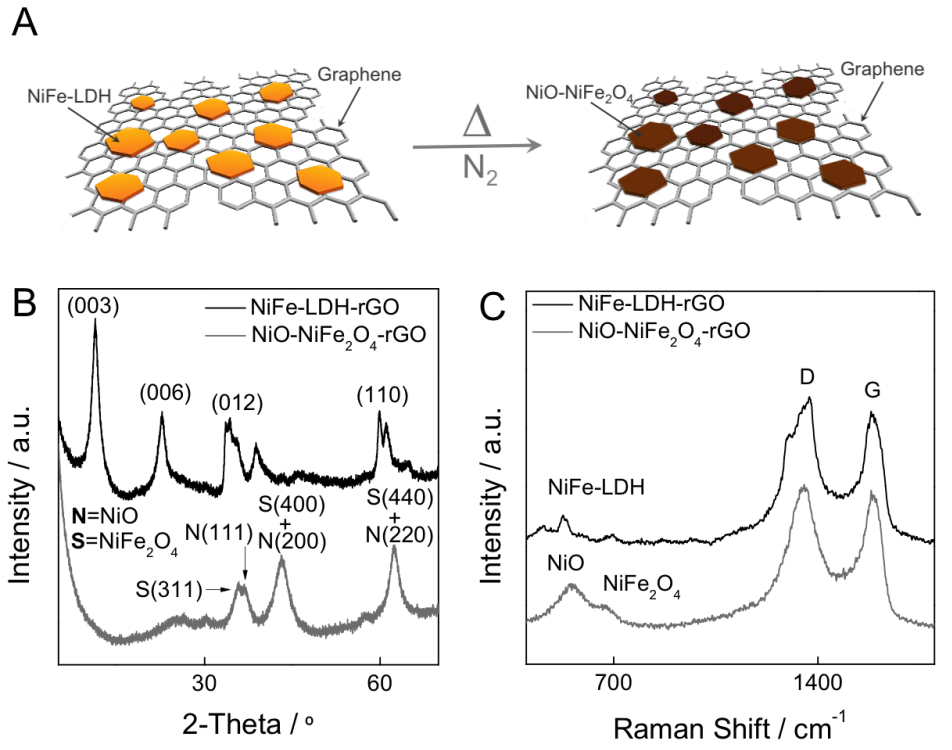

Figure 1. Structural characterization of the hybrids. (A) Idealized model for the *in-situ* growth of strongly coupled nanohybrids of NiFe–LDH and graphene and its thermal annealing to obtain a hybrid with NiO–$NiFe_2O_4$ platelets decorating the surface of graphene. (B) PXRD patterns of **1** and **2** showing the characteristic diffraction lines of NiFe–LDH (black), and NiO–$NiFe_2O_4$ (grey) phases. The N, S and C accounts for NiO, $NiFe_2O_4$ and Graphene phases, respectively. (C) Raman spectra of **1** (black) and **2** (grey).

Figure 2 shows the FT-IR spectra of GO, **1** and **2**. GO displays signals at 1100 cm^{-1} (ν(C–O)), 1410 cm^{-1} (δ(C–OH)), 1621 cm^{-1} (δ(OH_2)) and 1720 cm^{-1} (ν(C=O)), that are consistent with the presence of oxygenated moieties. The broad band between 3100 and 3600 cm^{-1} is associated to water, COOH, hydroxyl groups and aromatic C–H.[301] These bands disappear after thermal treatment and are replaced by broad bands between 1600 and 1150 cm^{-1} that can be associated to the recovery of the sp^2 conjugation in rGO. The peak at 3162 cm^{-1} also indicates the formation of C–H aromatic bonds probably by reduction of oxygen species at the sheet rims. The presence of NiFe–LDH in **1**

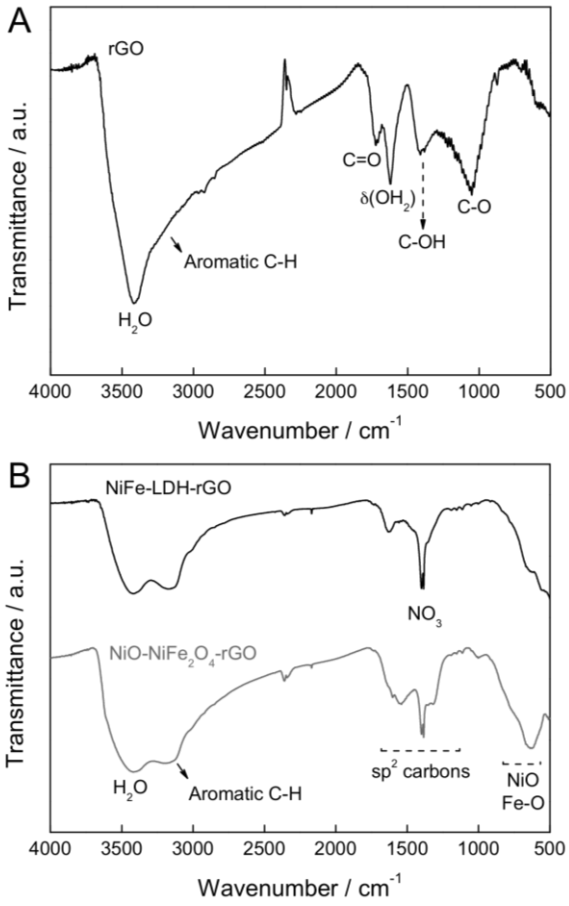

Figure 2. FT-IR analysis. (A) FT-IR spectra of rGO. (B) FT-IR spectrum of hybrids **1** (black) and **2** (red), highlighting the main absorption bands described in the text.

and metal oxides in **2** is consistent with the vibration modes at low wavenumbers linked to metal-oxygen bonds alongside with the characteristic ν_3 vibration mode of the nitrate anion interleaved between LDH layers.

Powder X-ray diffraction (PXRD) of 1 (**Figure 1B**) shows (00*l*) Braggs peaks characteristics of NiFe–LDHs.[179] The absence of diffraction lines around 25º rules out the presence of graphite-like structures from the stacking of graphene sheets.[303] LDH characteristic (00*l*) diffraction disappears upon annealing confirming the structural transformation of the LDH phase that evolves into

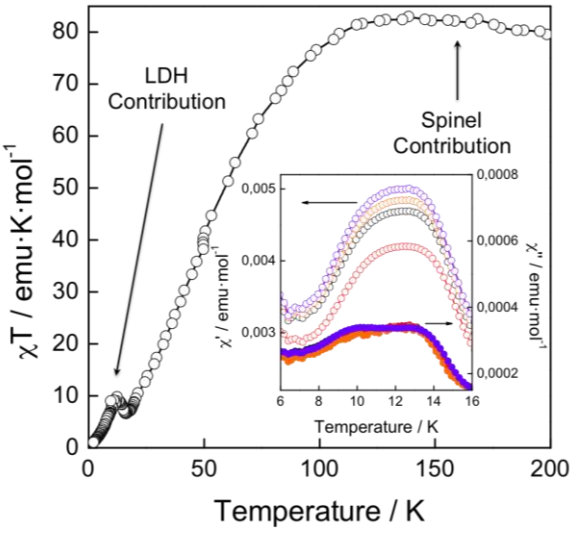

Figure 3. Magnetic measurements. Temperature dependence of the $\chi_M T$ product of **1**. Inset stands for dynamic ac susceptibility of **1** at low temperatures: in-phase (open symbols) and out-of-phase (closed symbols) at 10, 22, 46 and 464 Hz (purple, green, black and orange, respectively).

broad peaks of low intensity which correspond to a superposition of the characteristic reflections of $NiFe_2O_4$ and NiO.[304] Moreover, according to microanalysis, the Ni/Fe molar ratio is *ca.* 2.5, suggesting a final $NiFe_2O_4$/NiO molar ratio of about 1:4. To further confirm the presence of NiFe–LDH and NiO/$NiFe_2O_4$ we studied the magnetism of the hybrids (**Figure 3**). **1** displays a low-temperature ferromagnetic response featuring frequency-dependence and spontaneous magnetization at *ca.* 15.5 K (T_M), characteristic of NiFe–LDH, and high-temperature ferromagnetism that stands for the presence of iron rich spinel impurities.[151,179] The subsequent appearance of room temperature magnetic behaviour corresponding to a crystallized NiO and $NiFe_2O_4$ phases in individual platelets,[304] exhibiting a visible heterojunction nanostructure as previously observed for LDH-derived bi-component NiO/$NiFe_2O_4$ or CoO/$CoFe_2O_4$ nanocomposites, demonstrates the formation of **2.**[105,304]

As shown in **Figure 1C**, the first order Raman of **1** and **2** shows the typical G and D bands of graphitic-like species, and are very similar to the spectrum of GO. The first order Raman of graphene is characterized by having a G band

(1580 cm^{-1}), which is associated with E_{2g} vibrational modes of the aromatic domains, and a D band (1340 cm^{-1}) that arises from the breathing modes of the graphitic domains in presence of defects: it disappears in defect-free graphitic materials. Although the I_G/I_D ratio has been traditionally used to compare the structural order between graphitic and amorphous graphitic systems,[305] it can just be used to estimate the average size of C sp^2 domains for very defective systems.[306] In our case, I_G/I_D ratios are 1.136 for GO, 0.89 for **1** and 0.98 for **2**, which means that GO possesses bigger graphitic domains, but does not provide information on their level of reduction. **1** also shows characteristic signals of low intensity for NiFe–LDH in the low-frequency region (*ca.* 500 cm^{-1}). After the annealing, these low frequency signals evolve into two main bands that points to the formation of NiO and $NiFe_2O_4$ in hybrid **2**.[307–309]

The nature of the carbon component in the hybrids was studied by X-ray photoelectron spectroscopy (XPS) (**Figure 4**). GO features four dominant peaks in the C1s XPS centered at binding energies (*BE*s) of 284.8 eV (C–C sp^2), 286.2 eV (C–O), 287.8 eV (C=O) and 289.0 eV (C(O)O) (**Figure 4**).[310] The three last peaks which correspond to oxygenated carbons, cover a much higher effective area than the non-oxygenated signal at 284.8 eV, confirming the high degree of oxidation of the GO used in the fabrication of the hybrids. As shown in **Figure 4**, the hydrothermal treatment used to synthesize **1** triggers a substantial increase of the C–C sp^2 band at expense of the reduction the oxygenated peaks to the C1s spectrum. That is consistent with the reduction of the GO layers in-situ to form rGO. The spectrum of **2** (**Figure 4B**) is very similar to that of **1** with a slightly higher C–O:C–C sp^2 relative ratio that stands for a higher reduction of the rGO component connected to the thermal annealing.[311] The Ni 2p and Fe 2p high resolution XPS spectra of the hybrids reveals the presence of Ni(II) and Fe(III) in both. Ni 2p spectra (See **Figure 4C** and **D**) display two dominant peaks between 856 and 880 eV that can be assigned to the spin-orbit splitting into the Ni($2p_{3/2}$) and Ni($2p_{1/2}$), with an splitting energy of 17.2 eV. Each peaks is accompanied by a less intense satellite peak at ~6 eV higher *BE*s, in agreement with that expected for Ni^{2+} ions.[312] Fe 2p XPS spectra (**Figure 4E** and **F**), feature two dominant peaks centered at *BE*s of approximately 711 and 725 eV, as expected for NiFe–LDH and $NiFe_2O_4$–NiO mixed oxides.[116,313]

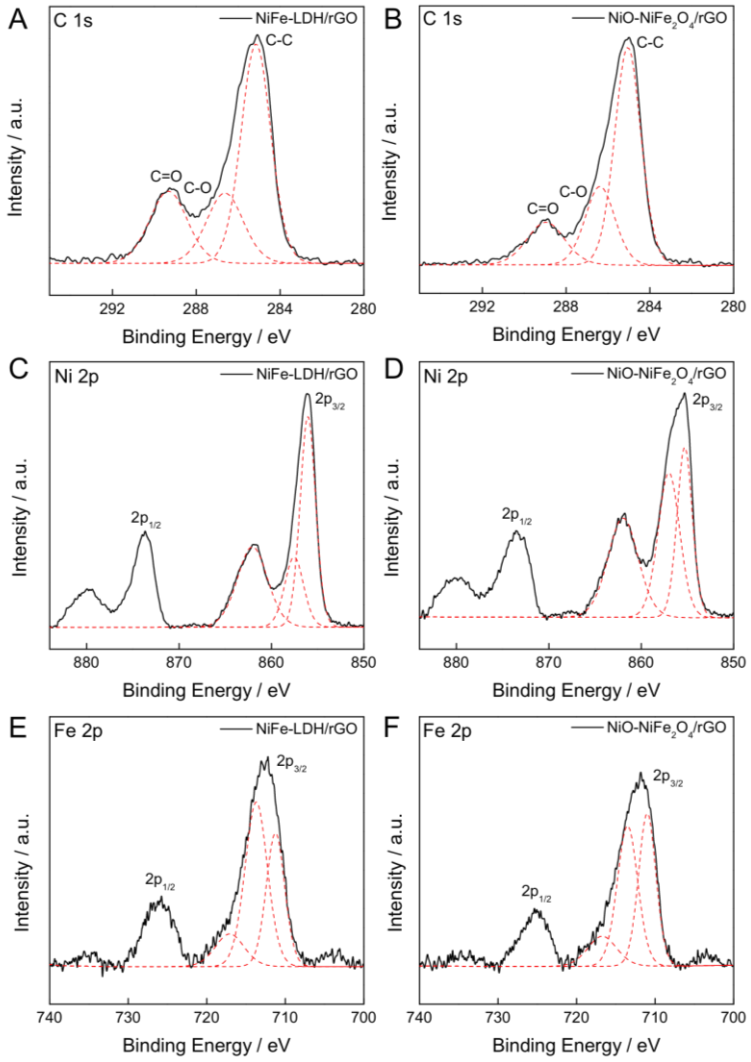

Figure 4. XPS analysis. High-resolution XPS spectra for **1** and **2**. (A and B) C 1s, (C and D) Ni 2p and (E and F) Fe 2p.

Figure 5 illustrates the thermal decomposition in air of GO, **1** and **2**. GO decomposes almost completely at 200 ºC (70 % weight loss) as result of the big extent of defective sp^3 carbon positions across the layers that correspond to oxygenated moieties. As 10 % of the sample corresponds to water (weight loss at 100 ºC), only 20 % of the total mass can be assigned to sp^2 carbon atoms that

Table 1. The binding energy values (eV) and the relative area (%) extracted from the high resolution XPS spectra.

	C1s XPS		
Sample	**Csp^2**	**C–O/C–N**	**C=O/CO_3**
GO	285 eV / 34.5 %	285.6 eV / 4.2 %	289 eV / 56.7 %
1	285.1 eV / 54.9 %	286.63 eV / 23 %	289.3 eV / 23 %
2	285.05 eV / 59.2 %	286.38 eV / 24.3 %	289 eV / 16.5 %

Sample	**Fe2p XPS**			**Ni2p XPS**		
1	711.25 eV / 34.6 %	713.7 eV / 52.3 %	717.07 eV / 13 %	856.05 eV / 46.5 %	857.55 eV / 19.1 %	862.06 eV / 34.4 %
2	711 eV / 41.4 %	713.52 eV / 45 %	716 eV / 13.5 %	855.29 eV / 30 %	857.01 eV / 35.7 %	861.97 eV / 34.3 %

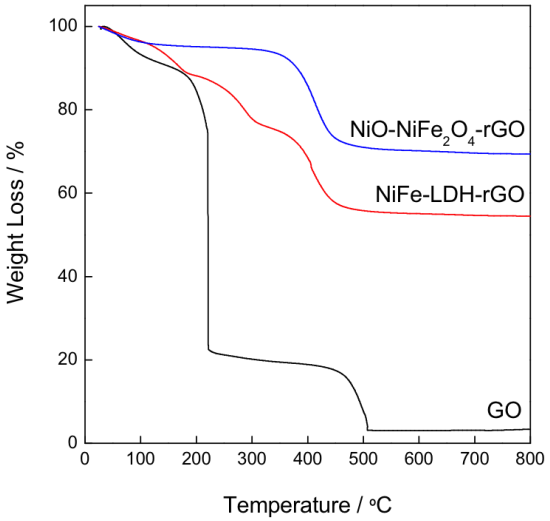

Figure 5. Thermogravimetric analysis. Thermal decomposition in air of GO (black), **1** (red) and **2** (blue) collected at a scan rate of 10 °C min^{-1}.

start to decompose at T ~ 500 °C.[296] The thermal decomposition of the hybrids is substantially different. Hybrid **1** shows a multistep decomposition pattern recalling that shown by pure NiFe–LDH: release of physisorbed and chemisorbed water followed by dehydroxilation of the layers, although the hybridization with rGO triggers increased thermal stability.[101,106,144] Water

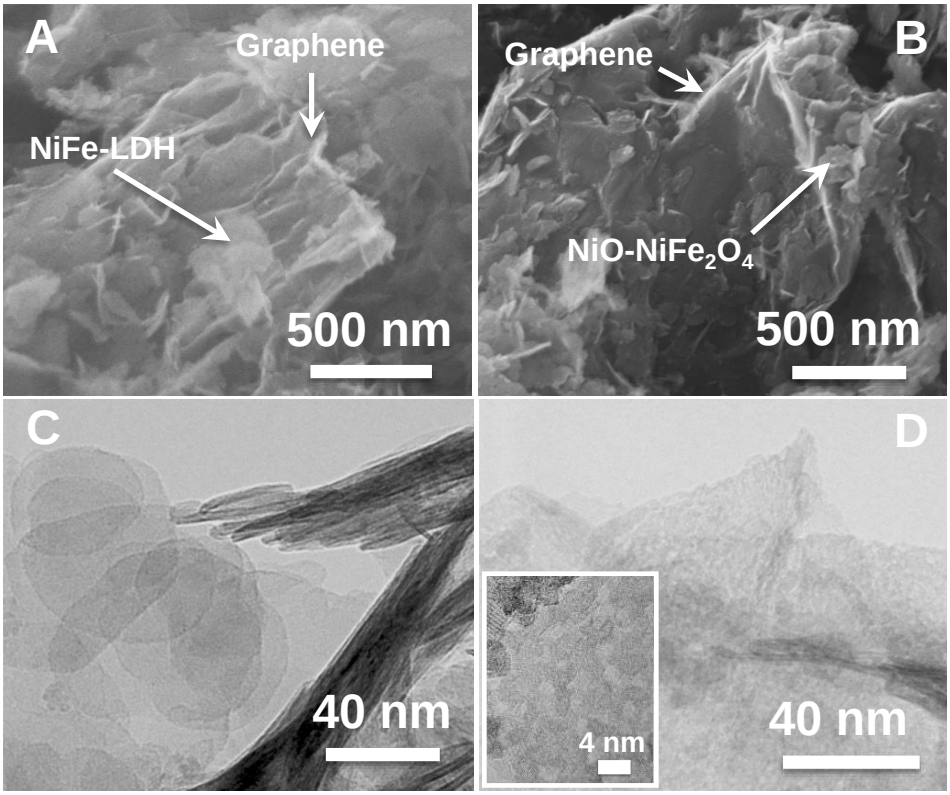

Figure 6. Electron microscopy study. (A) FESEM image of NiFe–LDH platelets grown on graphene sheets. (B) FESEM image highlighting the presence of NiO–$NiFe_2O_4$ platelets decorating the surface of the graphene sheets. (C and D) TEM images of the hybrids **1** and **2**. Inset in (D) represents a HRTEM image showing the lattice fringes of the porous and rough surface induced during the topotactic transformation.

desorption is almost negligible for **2**, which shows a single weigh loss of 25% at around 420 ºC that can be linked to the combustion of rGO.[106] From the remaining solid at 800 ºC we estimate a metal content of 70%.

The morphology of the hybrids was studied by FESEM (**Figure 6**). Images of **1** show a uniform material constituted by corrugated carbon sheets with smooth edges on top of which several morphologically distinct NiFe–LDH platelets can be observed (**Figure 6A**). After annealing, **2** show the presence of $NiFe_2O_4$–NiO platelets and rGO with the characteristic silk-like appearance (**Figure 6B**). The structure of the hybrids was further studied by HRTEM (**Figures 6C** and **D**). **1**

shows a complex structure in which the rGO layers appear decorated by a big number of NiFe–LDH platelets. **2** present a better-defined morphology in which $NiFe_2O_4$–NiO platelets with smooth borders can be observed over the carbon layers. A higher magnification of one of these platelets reveals lattice fringes, despite the porous rough surface induced during the formation of nickel oxide and spinel 2D heterojunction nanostructures (**Figure 6D**).[105,314]

Nitrogen adsorption-desorption isotherms yield BET surfaces areas of 79 and 169 $m^2 \cdot g^{-1}$ for **1** and **2**, respectively (**Figure 7**), consistent with the values reported for similar LDH–GO hybrids.[294–296] The annealing doubles the value of the surface area due to the greater contribution of the porous $NiFe_2O_4$–NiO platelets. Both hybrids exhibit Brunauer-Deming-Deming-Teller (BDDT)-type I and IV isotherms, suggesting the formation of micro- and mesopores. This type of isotherm is frequently observed for the mesoporous stacking structure of sheet-like 2D materials.[296,315] The pore-size distribution confirms the formation of mesoporous solids showing an average of 30–32 nm for both samples. This mesoporosity is linked to the typical house-of-cards-type stacking structure and the intrinsic mesoporosity of the layered constituents.[315] The presence of micropores was further confirmed with CO_2 isotherms, which reveals an increase in the micropore volume for hybrid **2**.

9.2.2. Supercapacitive Properties

We tested the electrochemical behaviour of the **1**, **2**, NiFe–LDH and NiO–$NiFe_2O_4$ samples in a conventional three-electrode cell. The powdered samples were mixed with acetylene black and PVDF at a mass ratio of 80:10:10 with ethanol. The resulting slurry was cast on a 1 cm^2 Ni-foam, dried and pressed to minimize the loss of the active material during the electrochemical testing. The electrochemical properties were measured by means of cyclic voltammetry (CV) using 6 M KOH as electrolyte under an applied voltage range of –1.0 to 0.4 V (*vs.* Ag/AgCl). CV in **Figure 8** reveals a complex pseudocapacitive behaviour with redox contributions from Ni, Fe (similar to the bare NiFe–LDH and NiO–$NiFe_2O_4$ samples) and graphene. Indeed, Fe(II)/Fe(III) (reduction peak at *ca.* –0.6 V), and Ni(II) to Ni(III) (reduction peak at *ca.* +0.2 V) redox pairs can be appreciated. Moreover, an oxidation peak at *ca.* –0.2 V appeared for both hybrids. Experiments at different anodic and cathodic potential limits revealed

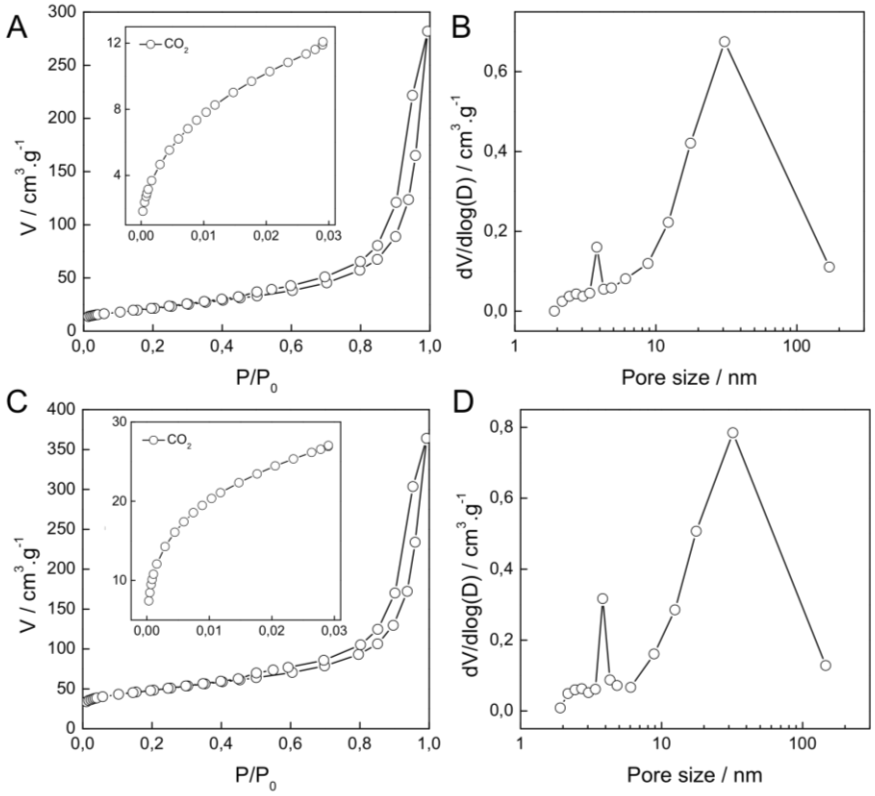

Figure 7. Gas adsorption/desorption analysis. (A) N_2 adsorption-desorption isotherm of hybrid **1** (SSA ~ 79 $m^2 \cdot g^{-1}$) (77.4 K). (Inset) The CO_2 (273.2 K) isotherm. (B) Pore-size distribution for N_2 (calculated by using Barrett-Joyner-Halenda (BJH) method. (C) N_2 isotherm of hybrid **2** (SSA ~ 169 $m^2 \cdot g^{-1}$). (Inset) The CO_2 (273.2 K) isotherm. (B) Pore-size distribution for N_2 (BJH).

that the –0.2 V and –0.6 V peaks are coupled in a reverse oxidation/reduction process, and are probably related with graphene.

Galvanostatic charge–discharge cycling was also measured in order to study the specific capacitance of the materials (**Figure 9**). Obviously, **1** and **2** hybrids show higher electrochemical activity than NiFe–LDH and NiO–$NiFe_2O_4$, respectively. **Figures 8C** and **D** show the galvanostatic discharge curves and the excellent capacity retention of hybrid **1**, respectively. Large discharge capacities

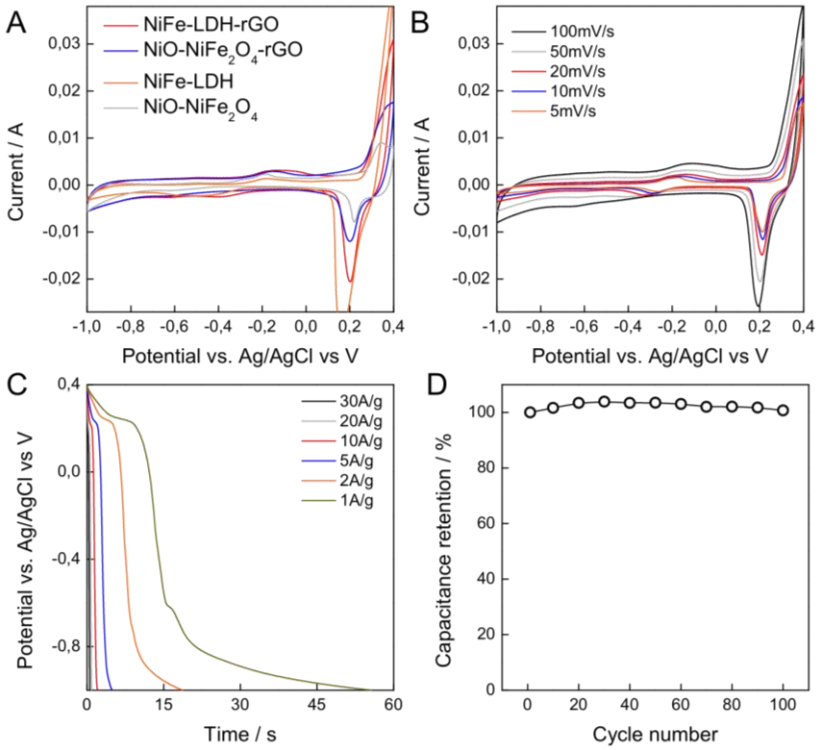

Figure 8. Electrochemical properties of **1**, **2**, NiFe–LDH and NiO–$NiFe_2O_4$ samples. (A) CV at 50 $mV{\cdot}s^{-1}$ for all the samples in a 6 M KOH aqueous solution. (B) CV curves for hybrid **1** at various scan rates. (C) Galvanostatic discharge curves and (D) specific capacity *vs.* cycle number at a current density of 30 $A{\cdot}g^{-1}$.

of *ca.* 605 $F{\cdot}g^{-1}$ and 217 $F{\cdot}g^{-1}$ were obtained for a current density of 2 $A{\cdot}g^{-1}$ for **1** and **2**, respectively (**Figure 8C**), overpassing that recently reported for a $NiFe_2O_4$–rGO material[316] (345 $F{\cdot}g^{-1}$ at 1 $A{\cdot}g^{-1}$), or for a NiO–rGO nanocomposite (525 $F{\cdot}g^{-1}$ at 0.2 $A{\cdot}g^{-1}$).[317] This improvement of the supercapacitive properties by means of hybridization is in excellent accordance to that observed for several LDH/rGO nanocomposites,[110,111,291,295,318–320] suggesting that these hybrids can be used as good electrode materials for supercapacitors.

However, what is really remarkably in the NiFe–LDH phases are their electrocatalytic properties, behaving as dual-function composites for battery and OER application.

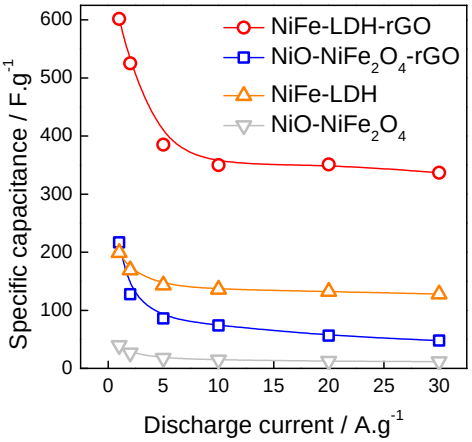

Figure 9. Specific capacitance of the studied materials at different discharge current densities, highlighting the increase in the specific capacitances promoted by the hybridization with graphene.

9.2.3. Electrocatalytic Properties

The electroctalytic OER activity of **1** and **2** in 1M KOH was evaluated at room temperature using a standard three-electrode cell with Ag/AgCl (0.3M) as the reference electrode. The catalysts (*ca.* 1 mg) were loaded into 1 cm^2 Ni-foam and used as working electrodes. In addition, pure NiFe–LDH platelets, as benchmark material, NiO–$NiFe_2O_4$ 2D platelets and a Platinum electrode for comparative purposes were measured under the same conditions. Each electrode was controlled by cyclic voltammetry at 5mV·s^{-1}. The voltammetric responses in **Figures 10A** and **B** show electrolytic oxygen evolution at the lowest onset potential for pristine NiFe–LDH (*ca.* 1.48 V *vs.* RHE), whereas hybrid **1** exhibits *ca.* 1.50 V *vs.* RHE. (See **Table 2**) The potentials needed to reach a current density of 10 mA·cm^{-2} are also reduced to 1.49 V *vs.* RHE. For **1**, **2**, or the Pt anodes these potentials are: 1.54 V, 1.51 V, and 1.63 V, respectively. All the tested electrodes show the evolution of oxygen bubbles immediately after applying an anodic potential. Voltammetric responses from the two hybrids also reveal the presence of a redox peak at around 1.35 V, that can be assigned to the Ni(II)/Ni(III or IV) redox processes, probably related with the transformation between $Ni_{1-x}Fe_x(OH)_2$ and $Ni_{1-x}Fe_xOOH$.[116,321,322] The mixed NiO/$NiFe_2O_4$

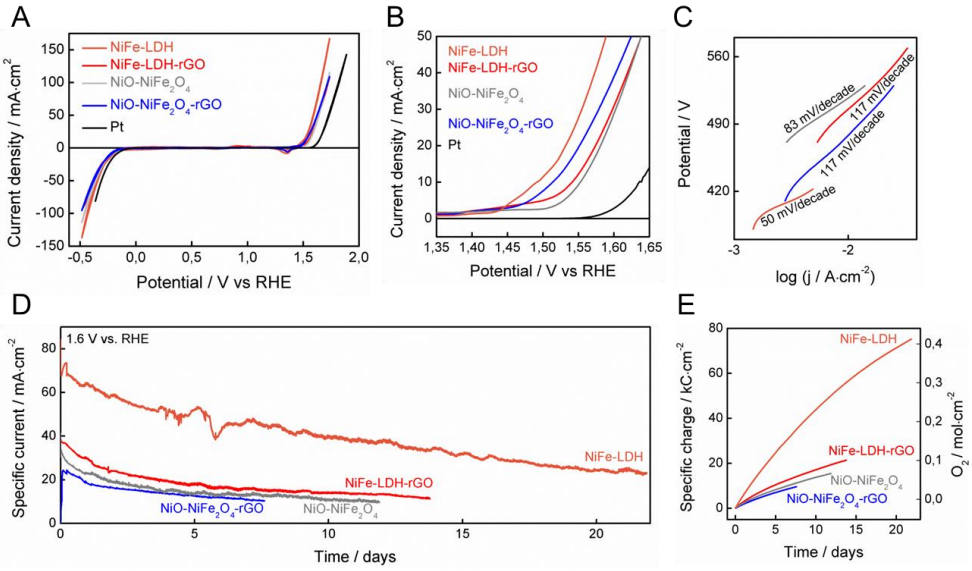

Figure 10. Electrochemical properties. (A) Cyclic voltammograms obtained at room temperature at 5 $mV \cdot s^{-1}$ in 1 M KOH aqueous solution from electrodes having 1 cm^2 of: clean Pt (black); highly crystalline NiFe–LDH (ocre); NiO–$NiFe_2O_4$ (grey); hybrid **1** (NiFe–LDH/rGO; red); and hybrid **2** (NiO–$NiFe_2O_4$/rGO; blue), deposited in nickel foam electrodes. Ag/AgCl was employed as reference electrode, and all the potentials are referred to the RHE. (B) Linear sweep voltammetry curves for all the measured electrodes. (C) The corresponding Tafel plots of NiFe-LDH (ocre), NiO–$NiFe_2O_4$ (grey), hybrid **1** (NiFe–LDH/rGO; red) and hybrid **2** (NiO–$NiFe_2O_4$/rGO; blue). (D) Current responses obtained when a constant potential of 1.6 V (vs. RHE) was applied for several weeks. (E) Consumed charge, or oxygen released, during chronoamperograms shown in (D).

phases, not hybridized with G, also behave as a good catalyst for water oxidation, exhibiting a potential of *ca.* 1.55 V to reach 10 $mA \cdot cm^{-2}$.[299,313]

To gain more insights into the OER activity, the polarization curves recordered at 5$mV \cdot s^{-1}$ under N_2 purged solutions of 1 M KOH were fitted to the Tafel equation: $\eta = b \log (j/j_0)$, where η is the overpotential applied to the electrode, b is the Tafel slope, j the current density flowing at each overpotential and j_0 the exchange current density (**Figure 10C**). The resulting Tafel slope for NiFe–LDH sample was of *ca.* 50 $mV \cdot decade^{-1}$, which was smaller that those exhibited by **1** and **2** (117 $mV \cdot decade^{-1}$) or by NiO–$NiFe_2O_4$ (83 $mV \cdot decade^{-1}$).

These behaviours indicate unique efficient electrocatalytic behaviour towards OER: when the overpotential is increased by 50, 87 and 117 mV, the current consumed to generate oxygen increases by 10. The Tafel slope of the pristine NiFe–LDH is smaller than that reported for Ir/C catalyst (*ca.* 60 mV·decade^{-1} at KOH 0.1 M),[321] or Pt/IrO_2 (51 mV·decade^{-1}), or Pt/Ir-IrO_2, (54 mV·decade^{-1}) in H_2SO_4 0.5 M, respectively. These systems were considered for many years to be the best electrocatalysts for the oxygen evolution reaction.[323]

In addition, the potential required to oxidize water at the current density of 10 mA·cm^{-2} is commonly used to evaluate the OER activity. As observed in **Table 2**, the NiFe–LDH promotes the OER current density to 10 mA·cm^{-2} at a potential of 1.49 V, which is significantly better than other LDHs reported to date (namely, ZnCo–,[115] CoNi–,[285] MnAl–,[294] and CoFe–LDHs[154]), and comparable to that of IrO_2/C materials (*ca.* 1.61 V, pH=13).[324,325] Moreover, the rest of the studied electrodes exhibited comparable OER activity, revealing that the high electrocatalytic property was primarily attributed to the NiFe–LDH phase. In this sense, $Ni_{1-x}Fe_xOOH$ oxyhydroxide is probably the active phase. It is believed that, if compared to $Ni(OH)_2$, the more complex local environment around Ni–O pairs in NiFe–LDHs plays a crucial role on the OER activity, increasing the NiOOH conductivity >30-fold. In fact, Fe exerts a partial-charge-transfer activation effect on Ni, as recently reported by Boettcher and co-workers.[322] Tentatively, this phenomenon could be related with the distorted metallic octahedra exhibited by LDHs. Furthermore, the efficiencies of 5:1 NiFe–LDHs, exhibiting low crystallinity and nanosized dimension, are slightly higher than those exhibited by the highly crystalline micrometric 4:1 LDHs samples, suggesting that highly defective Fe-doped LDHs are the best catalyst towards OER.

The stability of our material under oxygen evolution was checked applying a constant potential of 1.6 V (*vs.* RHE) during several weeks to the different electrodes —it is worth mentioning that, to the best of our knowledge, this is the longest operational evolution reported to date for LDH and related materials—. A higher current was always obtained for the NiFe–LDH, followed by the hybrid **1** electrode (**Figure 10D**). A current higher than 20 mA·cm^{-2} was flowing through the electrode for > 20 days. The observed slow deactivation could be due to the mechanical loss of a few poorly attached particles.[284] By integration of

Table 2. OER activities of various LDH-based catalyst reported to date.

Sample	Electrolyte	OER onset	Current density	Overpotential	Stability	Ref.
NiFe–LDH	1M KOH	1.48 V	10 $mA{\cdot}cm^{-2}$	1.49 V	23 $mA{\cdot}cm^{-2}$ after 22 days at 1.635 V	This work
NiO–$NiFe_2O_4$	1M KOH	1.55 V	10 $mA{\cdot}cm^{-2}$	1.55 V	10 $mA{\cdot}cm^{-2}$ after 12 days at 1.635 V	This work
NiFe–LDH–rGO	1M KOH	1.50 V	10 $mA{\cdot}cm^{-2}$	1.54 V	12 $mA{\cdot}cm^{-2}$ after 14 days at 1.635 V	This work
NiO–$NiFe_2O_4$/rGO	1M KOH	1.51 V	10 $mA{\cdot}cm^{-2}$	1.51 V	11 $mA{\cdot}cm^{-2}$ after 7 days at 1.635 V	This work
ZnCo–LDH	1M KOH	1.63 V	10 $mA{\cdot}cm^{-2}$	1.63 V	1 $mA{\cdot}cm^{-2}$ after 10 h at 1.656 V	[115]
CoNi–LDH	0.1 M K_2PO_4	1.62 V	1 $mA{\cdot}cm^{-2}$	2.12 V	3 $mA{\cdot}cm^{-2}$ after 400 s at 2.023 V	[285]
MnAl–rGO	1M NaOH	1.67 V	NA	NA	0.1 $A{\cdot}g^{-1}$ after 500 cycles	[294]
CoFe–LDH	1M KOH	1.53 V	10 $mA{\cdot}cm^{-2}$	1.57 V	10 $mA{\cdot}cm^{-2}$ after 10000 s at 1.576 V	[154]
NiFe–LDH–CNT	1M KOH	1.45 V	10 $mA{\cdot}cm^{-2}$	1.48 V	4.3 $mA{\cdot}cm^{-2}$ after 12000 s at 1.44 V	[116]

the consumed current, the consumed charge is attained. Considering that each O_2 molecule requires four electrons to be electrogenerated from basic media ($4\ OH^- \rightarrow O_2 + 2H_2O + 4e^-$), and using the Faraday constant (F = 96485 $C{\cdot}mol^{-1}$), the number of electrogenerated moles of oxygen was estimated (**Figure 10E**). Interestingly, at 1M KOH concentrations, the pristine NiFe–LDH exhibited a superior performance. This clearly indicates that the more accessible the active metal centres are, the highest efficiency is observed. This is not surprising. In fact, Liu, Kang and co-workers, reported similar findings for carbon quantum dots/NiFe–LDH hybrids. Concretely, they observed that the OER efficiency decreased with the size of the carbon counterpart. Indeed, for quantum dots bigger than 100 nm, the onset of the oxygen evolution was worse than bare NiFe–LDH nanoplatelets. Taking into account that our rGO flakes are of micrometric size, and that the specific surface area is reduced, the improvement of the electronic conductivity induced by rGO cannot be reflected in a better efficiency of the catalyst.

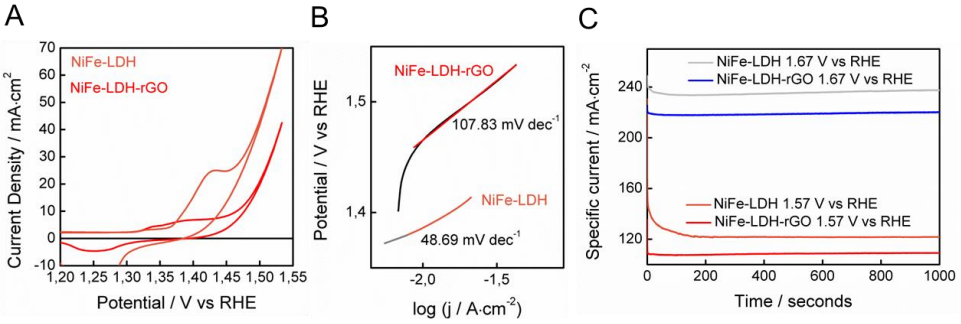

Figure 11. Electrochemical properties of NiFe–LDH and NiFe–LDH/rGO hybrid **1** in 6 M KOH. (A) Cyclic voltammograms obtained at room temperature at 5 $mV{\cdot}s^{-1}$. (B) Tafel plots and (C) Current-time curves at different applied voltages, namely 1.57 and 1.67 V vs RHE, highlighting the high values of current densities obtained.

However, increasing the OH^- concentration (using 6M KOH solutions which is typical for Zn–Air batteries), a different behaviour is observed (**Figure 11A**). In this case, the differences in the onset potentials are dramatically reduced to 1.37 V for NiFe–LDH and 1.41 V for hybrid **1**. Moreover, the Tafel slopes values are 48 and 107 $mV{\cdot}decade^{-1}$, respectively (**Figure 11B**). Finally, we have developed chronoamperometric studies at very high voltages highlighting the steady remarkable current densities delivered by the electrodes (**Figure 11C**). It should be further pointed out that the present electrocatalytic behaviour can be probably improved by directly growing the LDHs on the surface of a conductive electrode, or by generating a conductive porous matrix allowing a better accessibility to the active metal centers in order to facilitate electrolyte diffusion. In this sense, a major goal in the future will involve the preparation of hybrid structures formed by high quality graphene films decorated with unilamellar LDH nanosheets to develop electrocatalytic devices with large surface areas.

9.3. Conclusions

The OER electrocatalytic response of highly crystalline NiFe–LDH (x = 0.4) has been studied. In addition, the NiO–$NiFe_2O_4$ platelets obtained by thermal treatment of the pristine materials have been also analysed, showing that the most active specie is the LDH. Moreover, NiFe–LDH/rGO and NiO–$NiFe_2O_4$/rGO hybrids have been produced by the direct nucleation and growth

of the LDH platelets on the rGO sheets, originating a strong coupling only for direct contact sheets between the carbon layer and the platelets through oxygen functionalities. These hybrids exhibit dual-function in a single material. In this sense, the electrical properties of graphene seem to improve the supercapacitive behaviour of the hybrids whilst graphene plays a negative role on the OER activity as it reduces the accessibility of electrolyte to the active metal centers. In this sense, a system consisting of exfoliated NiFe–LDH nanosheets could be more efficient towards OER. These studies confirm that NiFe–LDH is a better catalyst than other related LDH phases. Even most surprising is the excellent stability of these materials under continuous oxygen production for many weeks. Therefore, it can be pointed out that these cost-effective materials could represent an excellent alternative to traditional precious metals, underscoring a promising future as electrodes in energy-storage devices.

9.4. Experimental Section

9.4.1. Synthesis

General synthesis remarks: Graphite powder was purchased from Fisher Scientific (G/0900/60). Tubular furnace (Gallur) and Brandsonic 5510 sonifier were used.

Synthesis of GO: GO was obtained by the Hummers method.[326] In a typical experiment, to a flask containing 6.5 g of graphite and 3.3 g of $NaNO_3$ at 0 ºC, 150 mL of H_2SO_4 65% were carefully added. Once the ice bath was removed, 19.6 g of $KMnO_4$ were added rising up the temperature to 50 ºC and maintaining it with continuous stirring for additional 30 minutes, after which, 300 mL of water were added slowly, increasing the temperature to 90 ºC. After 20 minutes of vigorous stirring, 600 mL of water were added. Finally, 50 mL of H_2O_2 were added, and the slurry centrifuged and filtered under vacuum.

*Synthesis of hybrids **1** and **2***: To a solution of 0.95 g of nickel (II) nitrate and 0.45 g of iron (III) nitrate in a mixture of 0.15 mL of triethaolamine and 5.6 mL of water, 200 mg of GO were added.[144] Next, 0.45 g of urea in 5.6 mL of water was added, and the pH adjusted to 7 by adding NaOH 6M. The mixture was sonicated during 30 minutes and then transferred to a Teflon-line autoclave. After heating it at 125 ºC during 48 hours, the sample was filtered and washed first with a great amount of Milli-Q water, secondly with a few milliliters of ethanol and then dried under vacuum (**1**). Finally, the brown solid obtained was placed inside a tubular oven, which was purged with nitrogen and heated at 250 ºC during 15 hours so **2** was obtained.

9.4.2. Physical Characterization

IR spectrum was taken using FT-IR Nicolet 5700 spectrometer in the 4000–400 cm^{-1} frequency range, using powdered samples diluted in KBr pellets.

Magnetic measurements were collected with Quantum Design PPMS-9 equipment. The dc static data were collected in the 2–300 K range with an applied field of 1000 G. The *ac* dynamic susceptibility measurements were performed on powdered samples in the temperature range 2–17 K with an oscillating magnetic field of 1.6 mT in the frequency range 10–464 Hz.

Susceptibility data were corrected for the sample holder and for the diamagnetic contribution of the sample using Pascal's constants.

HR-TEM images were obtained using a TECNAI G2 F20 microscope. Field Emission Gun (FEG) 200 kV. FESEM studies were performed on a Hitachi S-4800 microscope operating at an accelerating voltage of 20 kV and without metallization of the samples. Thermogravimetric analysis was carried out with a Mettler Toledo TGA/SDTA 851 apparatus in the 25–800 ºC temperature range under ambient conditions and at 10 $K \cdot min^{-1}$ scan rate. XRD patterns were obtained using a Philips X'Pert diffractometer using the copper radiation (Cu-Kα radiation, λα = 1.54178 Å). Profile was collected as step scans in the $5^o < 2\theta < 70^o$ range with a spot size of 0.02º. XPS measurements were performed in an ultra-high vacuum system ESCALAB210 (base pressure 1.0×10^{-10} mbar) from Thermo VG Scientific. Photoelectrons were excited by using the Mg–Kα line (1253.6 eV). All spectra have been referred to the Fermi level. μ-Raman measurements at room temperature were performed with a dispersive Jobin-Yvon LabRam HR 800 microscope, working with an excitation line of 532 nm. The scattered light was detected with a thermoelectric cooled (–70 ºC) charge coupled device detector (CCD). It also has an Olympus BXFM optic microscope. All the measurements were carried out directly over the sample. In the performed experiments, the power employed over the samples was of the order of 0.3mW, and the exposition time 60 seconds. The porous texture of all the materials prepared was characterized by N_2 adsorption at 77 K and CO_2 at 273 K in an AUTOSORB-6 apparatus. The samples were previously degassed for 4 h at 523 K and 5×10^{-5} bar. The desorption branch of the N_2 isotherm was used to determine the pore size distribution using the BJH method. The surface area was determined using the BET method. The micropores volumes were determined by applying *t*-plot and DR methods.

9.4.3. Electrochemical Measurements

Electrochemical Measurements: the electrochemical characterization has been carried out in collaboration with Prof. T. F. Otero at the Group of Electrochemistry Intelligent Materials and Devices (Universidad Politécnica de Cartagena). The materials were mixed with acetylene black and PVDF in a mass ratio of 80:10:10 in ethanol and deposited in a nickel foam electrode. The as-

prepared nickel foam electrodes were dried overnight at 100 °C and pressed. Each working electrode contained about 1 mg of electroactive material and had a geometric surface area of about 1 cm^2. A typical three-electrode experimental cell equipped with a stainless steel plate having 4 cm^2 of surface area as the counter electrode and a Metrohm Ag/AgCl (3 M KCl) as the reference electrode was used for the electrochemical characterization of the nanocomposite materials trapped by the working electrodes. All the electrochemical measurements were carried out in 6 M KOH aqueous solutions as the electrolyte. Ultrapure water was obtained from Milli-Q equipment. All the electrochemical experiments were performed at room temperature using an AUTOLAB PGSTAT 100 potentiostat–galvanostat controlled by GEPES electrochemical software.

10. Magnetic Nanocomposites Formed by $FeNi_3$ Nanoparticles Embedded in Carbon Nanoforms. Application as Supercapacitors[†]

In this chapter, a general family of magnetic nanocomposites formed by $FeNi_3$ ferromagnetic nanoparticles (NPs) embedded in a graphitized carbon matrix is described. The soft chemical approach used relies on the catalytic effect of the NPs resulting from the thermal decomposition of the layered double hydroxide precursor, which acts as a multilayered nanoreactor enabling the formation of a range of carbon nanoforms (CNFs). This can be followed by acid treatment of the as-obtained nanocomposites to isolate the different CNFs formed, from carbon nano-onions to graphene depending on the temperature of the thermal decomposition. This synthetic process paves the way for the rational design of metal–carbon nanocomposites with controllable composition as precursors of nanocarbons including graphene. The coexistence of metal NPs and nanostructured carbon is a major source of applications. As a proof of concept, the electrochemical performance of these metal–carbon hybrid supercapacitors is studied under high discharging current densities and they exhibit high values of specific capacitance and excellent rate capabilities.

[†] a) Abellán, G., Coronado, E., Ribera, A. Patent P201200188 (Spain). WO 2013124503 A1 (International). b) Abellán, G.; Coronado, E.; Martí-Gastaldo, C.; Ribera, A.; Sánchez-Royo, J. F. *Chem. Sci.* **2012**, *3*, 1481. c) Abellán, G.; Coronado, E.; Martí-Gastaldo, C.; Ribera, A.; Otero, T. F. *Part. Part. Syst. Charact.* **2013**, *30*, 853. This work has been carried out in collaboration with Prof. T. F. Otero at the Centro de Electroquímica, Materiales Inteligentes y Dispositivos (Universidad Politécnica de Cartagena) and Prof. J. F. Sánchez-Royo at the Instituto de Ciencia de los Materiales (Universitat de València)

10.1. Introduction

Functional nanocomposites based on LDH materials as inorganic component have attracted particular attention in the last few years because of their broad range of applications in magnetism, catalysis, biomedicine, chemical sensing, corrosion-resistance coatings, electrochemical batteries, ion exchangers, adsorbents, or even nanoreactors.[8,100,119,124,195,199,200,327–329] In addition, the chemical versatility of LDHs to accommodate different transition metal ions in a well-defined composition range[122,144] have been exploited to produce different metal oxides with nanometric size, thus expanding the possibilities of these materials.[99,330]

More recently, this focus of attention has shift to the synthesis of hierarchical nanocomposites derived from LDHs and nanocarbons illustrating the value of chemical design as a tool to improve the applications of LDHs.[82] In this context, the use of transition metal-based LDHs has enabled the chemical synthesis of carbon nanoforms, demonstrating the potential of LDH as precursors.[201,331–334] It is worth highlighting that, aside these works, all LDH-based nanocomposites had generally led to the formation of mixed metal oxides.[335,336] Great efforts on the hierarchical design of new hybrids are still needed to access the rational control of their properties. Here, the study of LDH-based nanocomposites represents a versatile vehicle to explore the impact of the structure-to-composition relationship in the properties of these hybrids. The possibility to control the chemical composition in LDHs is of utmost importance in their potential uses in areas such as nanoelectronics, magnetic devices, catalysis, separation, materials science, energy conversion and storage, environmental and biology. Among these, it is worthwhile outlining the use of hybrid organic–inorganic LDH materials as starting materials in the development of carbon-mixed metal oxides nanocomposites with electrochemical activity.[327,330] In particular, Leroux and co-workers[335,337] have described a series of mixed metal oxide nanoparticles (NPs), obtained by controlled pyrolysis of LDH hybrids, which, thanks to their porogen activity, display useful electrochemical properties. Additionally, high-performance capacitances have been described for a hybrid graphene–nickel/manganese mixed oxide nanocomposite derived from a NiMn–LDH when used as an anode material for Li-ion batteries.[106] In

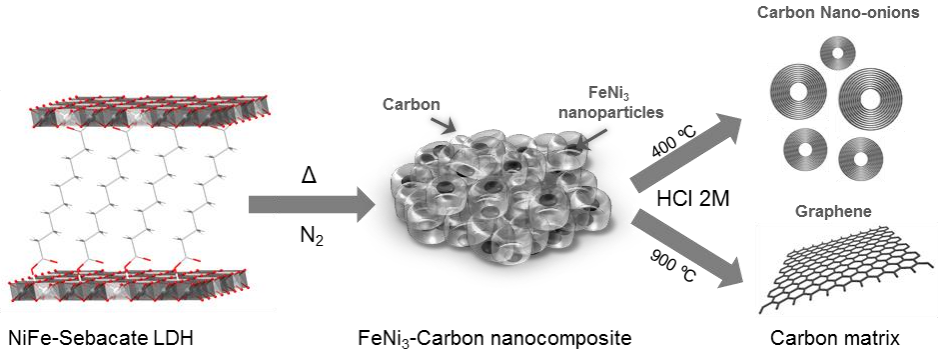

Figure 1. Schematic illustration of the formation of $FeNi_3$–Carbon nanocomposites and the corresponding CNFs obtained after the acid leaching procedure, *i.e.*, carbon nano-onions at 400 °C and graphene at 900 °C.

our opinion, these precedents illustrate the potential of LDH-based composites for developing more efficient supercapacitors. These electrochemical devices have attracted considerable interest in recent years because of their high power density, long cycle-life, and low maintenance cost.[338] Besides the classical electric double layer capacitance (EDLC), the pseudo-capacitance can be exploited to increase the capacitance of an electrochemical capacitor by as much as an order of magnitude over that of the EDLC. Such a type of capacitance is faradaic, *i.e.*, non-electrostatic in origin, arises when an electrochemical charge-transfer process takes place, and results from the introduction of redox centers in the device. Beyond this aspect, another requirements as for example, enhanced robustness, low cost, environmental friendliness, or good processability are equally necessary for the realization of higher performances in supercapacitors. Hence, metal–carbon nanocomposites are superior candidates as they can show both types of capacitances: EDLC associated to the nanostructured carbon and pseudo-capacitance from reversible redox reactions associated with the presence of metal NPs.

Herein, we take advantage of the possibility to use a sebacate-intercalated NiFe LDH as an inorganic multilayered nanoreactor (see **Figure 1**). Using the $Ni^{II}Fe^{III}$–LDH layers as precursor of $FeNi_3$ NPs, a magnetic alloy that has proved to be a good candidate for soft magnetic materials, due to its superior magnetic properties and thermal stability[339–341] and a double-functionalized aliphatic

chain with carboxylic groups as anchoring groups and carbon source. This choice could increase the carbon density present in the interlamellar space.

To the best of our knowledge, the synthesis of carbon-coated metal NPs by using LDHs remains unexplored. In this chapter, we report the physical characterization of a family of $FeNi_3$–C nanocomposites and its application as electrode materials in supercapacitors. We also describe the influence of calcination temperature on the electrochemical properties under high discharging current densities, exhibiting excellent values of specific capacitance and energy and power densities.

10.2. Results and Discussion

10.2.1. $FeNi_3$–C Nanocomposites

In this chapter, we decided to design a hybrid material combining $Ni^{II}Fe^{III}$–LDH layers —a source of catalytic mixed oxide nanoparticles— with interleaved sebacate anions, which can act as a carbon source. While the introduction of Ni(II) and Fe(III) in the LDH responds to the well-known catalytic activity of these transition metal ions in the synthesis of carbon nanoforms,[333,336] the use of a long carbon-chain dicarboxylic acid is to introduce carboxylic functionalities, which will act as anchoring points in the final nanocomposite, while increasing the carbon content present in the interlamellar space.

The thermal decomposition of this hybrid organic–inorganic compound under an inert atmosphere at 400 °C results in the formation of $FeNi_3$ nanoparticles, whose catalytic activity facilitates the decomposition of the confined organic moiety to grow carbon nanoforms on their surface, along with the formation of a graphitic shell around these metallic nanoparticles. These nanoparticles can be easily removed in a subsequent step by acid leaching of the hybrid composite with hydrochloric acid, to enable the insulation of free-standing carbon nanoforms. Hence, here we describe how NiFe–Sebacate LDH can be used as a hybrid organic–inorganic precursor for the low-temperature synthesis of carbon nanoforms.

Starting NiFe–Sebacate LDH (NiFe–Seb-0.20, **1**, NiFe–Seb-0.25, **2**, NiFe–Seb-0.33, **3**) was synthesized by coprecipitation under controlled heating conditions at 80 °C for 4 days following a reported procedure.[122,201] As

Table 1. Elemental Chemical Analysis Data for NiFe–Seb-0.20 (1), NiFe–Seb-0.25 (2), and NiFe–Seb-0.33.

		x[a]		water	
Sample	**Molecular formula**	**exp**[b]	**theor**	**[%]**[c]	**molec**
1	$[Ni_{0.78}Fe_{0.22}(OH)_2](C_{10}H_{16}O_4)_{0.11}\bullet 1.0H_2O$	0.22	0.20	13.8	1.0
2	$[Ni_{0.74}Fe_{0.26}(OH)_2](C_{10}H_{16}O_4)_{0.13}\bullet 1.2H_2O$	0.26	0.25	15.9	1.2
3	$[Ni_{0.67}Fe_{0.33}(OH)_2](C_{10}H_{16}O_4)_{0.16}\bullet 1.4H_2O$	0.33	0.33	16.7	1.4

[a] $x=[Fe^{III}]/([Ni^{II}]+[Fe^{III}])$. [b] Obtained with EPMA. [c] Water content derived from thermogravimetric analysis.

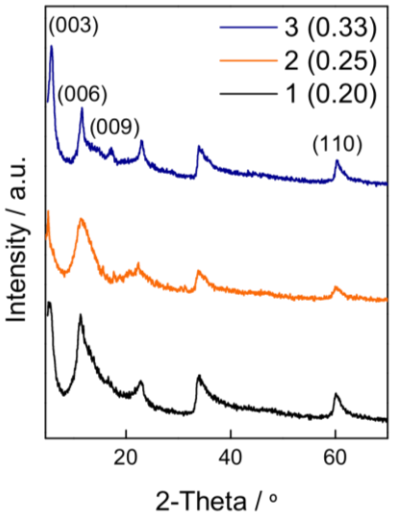

Figure 2. PXRD patterns for compounds **1**–**3**. Note that the silicon grease used to support the powder on the sample holder contributes to the diffraction pattern with a broad band centered at around 11–12°.

summarized in **Table-1**, the experimental metal ratios are in good agreement with the theoretical values. The $FeNi_3$–C composites ($FeNi_3$–C-0.20, **4**, $FeNi_3$–C-0.25, **5**, $FeNi_3$–C-0.33, **6**) are directly obtained by calcination of the as-made precursor at 400, 650, or 900 °C under inert atmosphere (every sample will be named by the composition number (**4**, **5**, or **6**) followed by the calcinations temperature, **4**–400 °C, **4**–650 °C, **4**–900 °C, and so on).

Table 2. X-Ray diffraction data and unit cell parameters for 1–3.

	2Θ [°] (*hkl*)					Calc param[a] [Å]		
Sample	**(003)**	**(006)**	**(009)**	**(110)**	$d_{(110)}$	***a***	***c***	***BS***
1	5.24	11.48	17.10	60.18	1.54	3.07	47.82	15.94
2	5.14	11.50	17.67	60.20	1.54	3.07	47.63	15.88
3	5.75	11.55	17.20	60.26	1.54	3.07	46.17	15.39

[a] $a = 2d_{110}$; $c = d_{003} + 2d_{006} + 3d_{009}$; $BS = c/3$.

According to their powder X-ray diffraction patterns (PXRDs; see **Figure 2** and **Table 2**) **1**, **2**, and **3** exhibit the classical profile for LDH materials with high-intensity diffraction lines associated to (00*l*) reflections appearing at low angles, whereas they become broader and poorly defined at higher angular values. Analysis of the PXRD of **4**, **5**, and **6** (see **Figure 3**) permits their identification as (FCC)–$FeNi_3$ composites (JCPDS file N°. 38–0419). Although the compositional range for which pure crystalline phases of LDHs can be formed (typically, $0.33 \geq x = M^{II}/M^{II}+M^{III} \geq 0.20$) is very close to the ideal metal ratio necessary for formation of the $FeNi_3$ phase ($x = 0.25$), it is not possible to discard residual formation of contaminant phases in the NiFe alloys due to slight deviations from this stoichiometry (**Table 3**). From now on, we will focus the discussion on the samples with ideal stoichiometry (**5**), generally named $FeNi_3$–C for clarity. Weak reflection lines can be observed at $2\theta = 37.3°$, 62.7° in the **5**-400 °C sample, indicative of the residual formation of Fe_3O_4 as a secondary phase.[342] Moreover, small broad peaks at $2\theta = 35.8°$, 43.5° can be related with the presence of NiO can be detected. This is likely due to the presence of oxygen derived from the hydroxide layers in the LDH and carboxylate groups from the sebacate, which might facilitate the formation of Fe_3O_4 and NiO upon calcinations. These residual impurities disappear for higher calcination temperatures, which also trigger more intense and narrower diffraction lines, with no peaks denoting the presence of either α-Fe (*i.e.* at 2θ of 65.2°) or (FCC)-Ni (*i.e.* at 2θ of 44.5°, 51.8° and 76.4°).[343] PXRDs of **4**, **5** and **6** show analogous evolution with the temperature with increasing intensity of the diffraction lines corresponding to the $FeNi_3$ phase and progressive disappearance of the contaminant Fe_3O_4 and NiO (**Figure 3**). The particle size in sample **5** has been estimated by applying the Scherrer equation to the Bragg reflection (111),

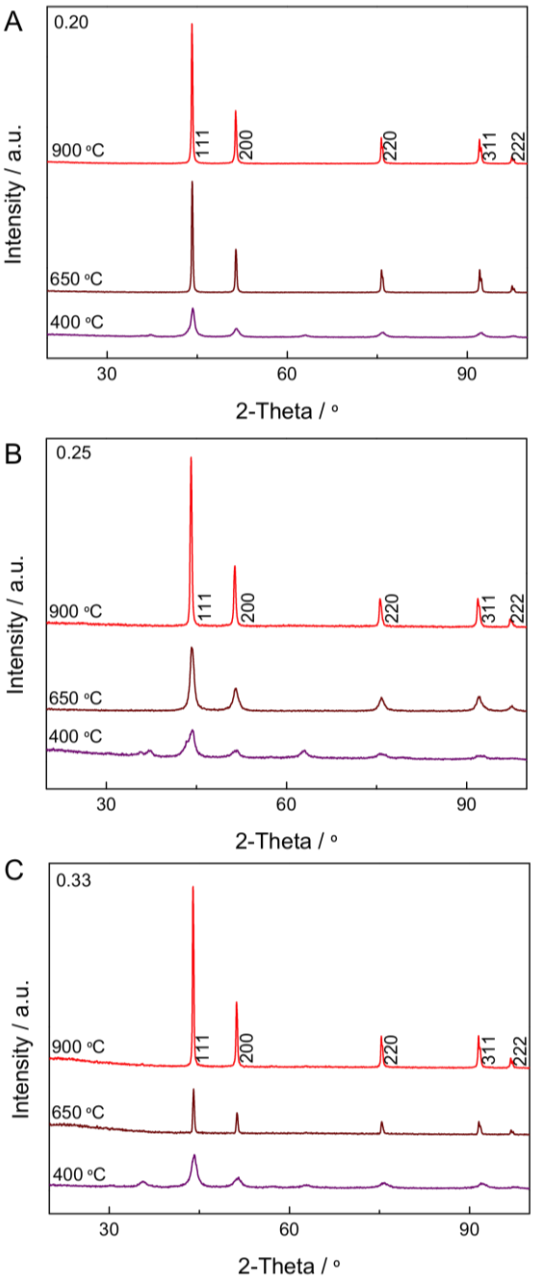

Figure 3. PXRD patterns for $FeNi_3$–C nanocomposites: (A) $FeNi_3$–C-0.20 (**4**), (B) $FeNi_3$–C-0.25 (**5**) and (C) $FeNi_3$–C-0.33 (**6**) at different temperatures ranging from 400 to 900 °C.

Table 3. Metal composition data for $FeNi_3$–C-0.20 (4), $FeNi_3$–C-0.25 (5), and $FeNi_3$–C-0.33 (6) calcined at 400 and 900 °C.

	400 °C			900 °C		
Sample	**Fe[at.%]**	**Ni[at.%]**	**Fe:Ni ratio**	**Fe[at.%]**	**Ni[at.%]**	**Fe:Ni ratio**
4	25.15	74.85	0.336	23.75	76.25	0.311
5	27.80	72.20	0.385	27.05	72.95	0.371
6	36.88	63.12	0.584	36.02	63.98	0.563

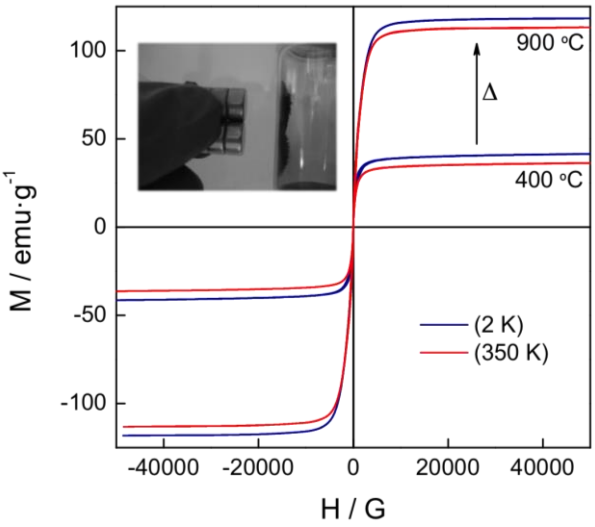

Figure 4. Magnetization *vs*. field data for $FeNi_3$–C nanocomposite calcined at 400 and 900 °C measured at both 2 and 350 K, highlighting their ferromagnetic character. The upper inset shows a photograph of a selected sample under an external magnetic field.

obtaining values of 6, 13 and 30 nm for the samples synthesized at 400, 650 and 900 °C, respectively, in good agreement with the values observed by HRTEM (*vide infra*). Moreover, the temperature has a tremendous impact on the morphology of the resulting CNFs as detailed below.

The presence of $FeNi_3$ NPs in the $FeNi_3$–C nanocomposites was further confirmed by magnetic measurements. Thus, sample **5**–400 °C display a hysteresis loop at 350 K (**Figure 4**) with a saturation value of the magnetization of 42 emu·g^{-1}, in excellent agreement with the values reported for $FeNi_3$ nanoplatelets,[344] $FeNi_3/SiO_2$ and $FeNi_3/Al_2O_3$ core/shell NPs.[345,346] Surface oxidation at

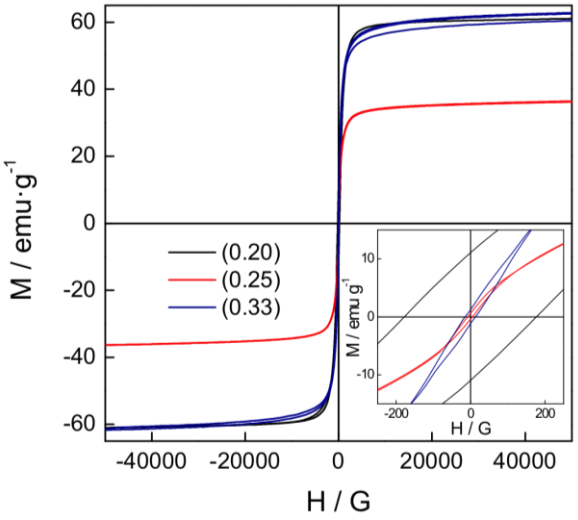

Figure 5. Magnetization at 350 K versus field data for $FeNi_3$–C nanocomposites **4**, **5** and **6** synthesized at 400 ºC. The lower inset shows the enlarged M-H curves at low applied fields.

grain boundaries may be the reason to cause a decrease in saturation magnetization with respect to the bulk permalloy (92 emu·g^{-1} for $Fe_{20}Ni_{80}$).[347] As expected for this type of ferromagnets, small coercive fields are observed for **4**, **5**, and **6** (see **Figure 5**), but no significant differences with temperature can be measured, supporting the residual character of the Fe_3O_4 impurities.[348,349]

Moreover, a dramatic increase in the saturation magnetization is observed after heating at 900 °C, reaching *ca.* 113 emu·g^{-1}, in excellent agreement with the value of bulk $FeNi_3$ alloys, the same behavior can be observed for the rest of the compositions. This increase is related with the growing of the metal NPs, favored at higher temperatures. The saturation magnetization (M_s), remnant magnetization (M_r), and coercivity (H_c) values for all the nanocomposites at representative temperatures 400 and 900 °C to illustrate the most drastic changes on magnetization, are shown in **Table 4**. No significant differences in the magnetic properties are observed at lower temperatures confirming the ferromagnetic character of these nanocomposites.[350]

It is worth mentioning that the high crystallinity obtained with the highest temperatures allows for the protection of some of the metal NPs against acid

Table 4. Summary of magnetic properties of $FeNi_3$–Carbon nanocomposites synthesized at 400 and 900 °C.[a]

Calcination temperature	400 °C						900 °C					
Measuring temperature	2 K			350 K			2 K			350 K		
Sample	M_S	M_r	H_c	M_S	M_r	H_c	M_S	M_r	H_c	M_S	M_r	H_c
4 (0.20)	65	16	360	61	11	177	103	6	40	96	4	40
5 (0.25)	42	5	25	37	1	10	118	4	60	113	6	57
6 (0.33)	66	1	20	60	1	20	128	1	15	109	1	10

[a] Saturation magnetization (M_S; emu·g^{-1}), remnant magnetization (M_r; emu·g^{-1}), and coercive field at 2 K (H_{Coer}; G).

damage, thanks to the graphene carbon matrix formed in these conditions.[351] In fact, one needs more than 48 h of acid leaching for the isolation of free-standing graphene sheets on the surface of the acid bath. This is supported by the magnetic measurements. Thus, whilst 400 °C samples are diamagnetic, the rest are still magnetic due to the extreme stability of the NPs that cannot be removed by acid leaching.

The graphitic nature of the shells coating the NPs was confirmed by Raman spectroscopy. Two mean features, namely G and D bands, characterize Raman spectrum of graphene. G band represents the in-plane bond-stretching motion of the pairs of C sp^2 atoms (the E_{2g} phonons); whereas D band corresponds to the breathing modes of rings, or κ-point phonons of A_{1g} symmetry. The Raman spectra of as-prepared nanocomposites exhibit the presence of a G-band centered at 1581–1593 cm^{-1} and a D-band centered at 1339–1350 cm^{-1}, depending on the sample (**Figure 6A**).[306] The intensity ratio of these bands (I_D/I_G) increases with temperature, suggesting the presence of more disorder in the carbon matrix. As shown in **Figure 6A**, the appearance of 2D bands for the samples calcined at 900 °C is consistent with the presence of graphene sheets. When the acid leaching takes place, a decrease in the I_D/I_G ratio indicates the partial restoration of the electronic conjugation in graphene sheets by repairing defects (**Figure 6B**). Those facts indicate for all the cases an increase in the sp^2-graphitic domains and enhanced crystallinity of the materials upon acid leaching. Interestingly, the shift in the G band from *ca.* 1590 to *ca.* 1580 cm^{-1}

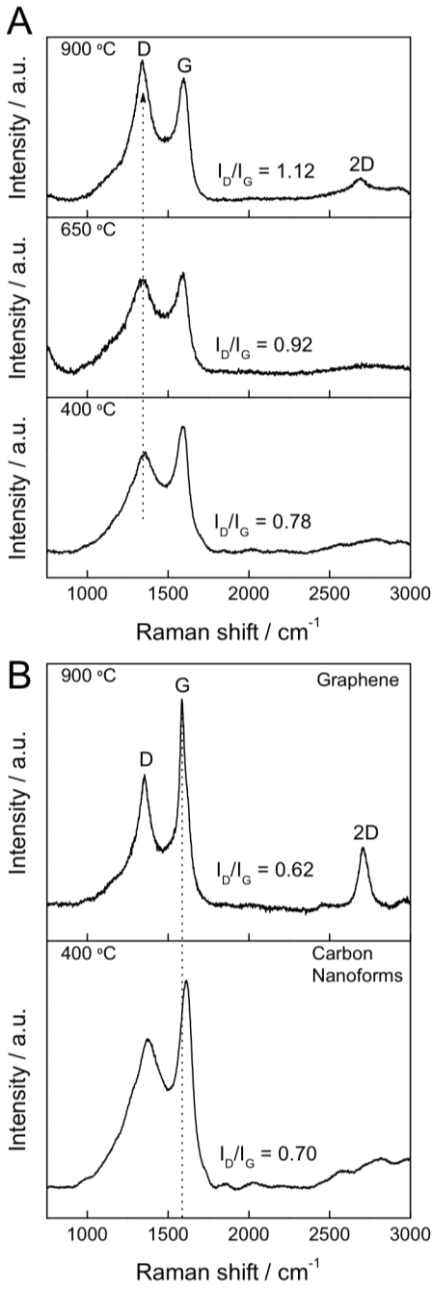

Figure 6. (A) Raman spectra of $FeNi_3$–C nanocomposites at different temperatures ranging from 400 to 900 °C. (B) Raman spectra of the resulting carbon matrix after the acid leaching of the samples synthesized at 400 °C (CNFs) and 900 °C (graphene).

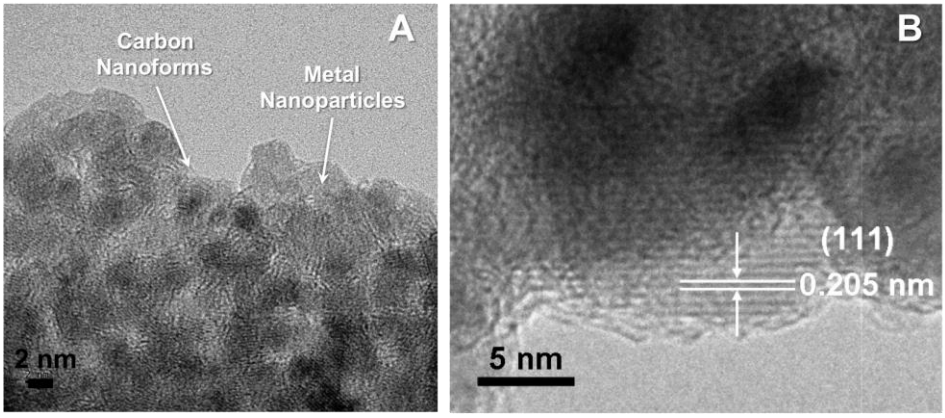

Figure 7. (A) HRTEM image of $FeNi_3$–C nanocomposite synthesized at 400 °C, CNFs and $FeNi_3$ NPs have been highlighted with arrows. (B) Zoomed-in HRTEM image of the $FeNi_3$–C nanocomposite showing the lattice spacing between two adjacent planes.

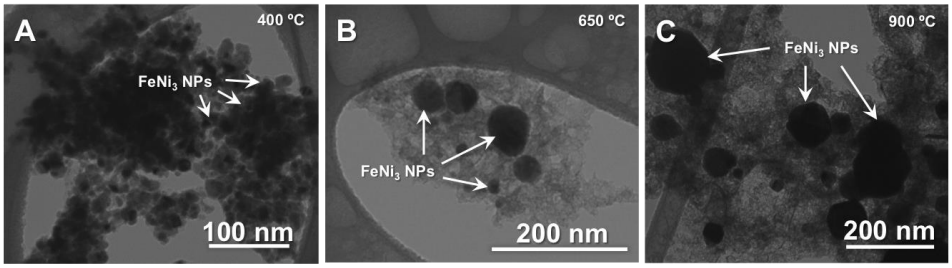

Figure 8. HRTEM images of $FeNi_3$–C nanocomposite synthesized at (A) 400 °C, (B) 650 °C, and (C) 900 °C, showing the increase in the NP's size. $FeNi_3$ NPs have been highlighted with arrows.

and the decrease of the I_D/I_G ratio related with the large number of disordered edge sites expected in the carbon nano-onions (CNOs) is in good agreement with the evolution of the CNOs and related multiwalled materials to graphene sheets (*vide infra*). Moreover, the presence of the 2D band centered at 2700 cm^{-1} in the graphene sample can be observed and is narrow enough to support the presence of aggregates formed by a few layers of graphene.

The morphology of the nanocomposites was studied by means of HRTEM. **Figure 7A** shows a HRTEM selected image of the as-obtained nanocomposite **5**–400 °C, presenting well-dispersed NPs of small dimension (average size *ca.* 2–

5 nm) embedded into a graphitized carbon matrix.[201] These graphitic shells are presumably responsible for the enhanced stability of the metal NPs against oxidation.[351] The increase in the thermal decomposition temperature is reflected in the size of the NPs. Actually, $FeNi_3$ NPs of *ca.* 50 nm can be observed in the HRTEM images of the sample calcined at 900 °C (see **Figure 8**). Moreover, a detailed HRTEM image of the NPs of the **4**–400 °C composite (**Figure 7B**) indicates that the lattice spacing between two adjacent planes corresponds to 0.205 nm, in good agreement with the distance separating the (111) planes of $FeNi_3$.[340]

XPS was used to confirm the presence of Ni and Fe in the $FeNi_3$–C nanocomposites before and after acid treatment (**Figure 9** and **Table 5**). We observe that the surface of the samples is dominated by Ni(II) and Fe(II) centers. Each one of the two spin-orbit components of the Ni 2p spectra shows three resolved features. However, only one asymmetric feature can be resolved for the spin-orbit doublet of the Fe 2p spectra. For the deconvolution and fitting of these spectra, a Shirley background[352] has been taken into account. Deconvolution of the Ni 2p spectra has been carried out by considering three Gaussian line-shape spin-orbit doublets (with a spin-orbit splitting of around 18 eV). The Fe 2p survey revealed photoelectron peaks at around 711 and 725 eV correspond to the binding energies of $2p_{3/2}$ and $2p_{1/2}$ of oxidized iron Fe(II) and/or Fe(III). These have been reproduced by considering one spin-orbit doublet (with a spin-orbit splitting of 13.2 eV) whose components appear to be well described by Doniach-Sunjic line-shapes.[353] A smaller peak at 707.7 eV suggests the existence of zerovalent iron (Fe $2p_{3/2}$). The shoulder at 721 eV is likely the result of two overlapping components: the shakeup satellite $2p_{3/2}$ for oxidized iron and $2p_{1/2}$ for zerovalent iron.[354–357] The presence of a relatively small amount of zerovalent iron and large fraction of oxidized iron indicate extensive oxidation of iron at the surface.

Regarding the three components detected for the Ni $2p_{3/2}$ spectra, these located at 853.2 and 856.4 eV can be attributed to metallic and divalent Ni, respectively, whereas that located at 862.5 eV can be attributed to the so-called 6-eV Ni satellite.[312,358] The Fe(II) peak is in accord with the presence of Fe_3O_4 (detected in the PXRD of **4–6** synthesized at 400 °C, *vide supra*), which coexists with the $FeNi_3$ nanoparticles in the composite, while Ni(II) may indicate the

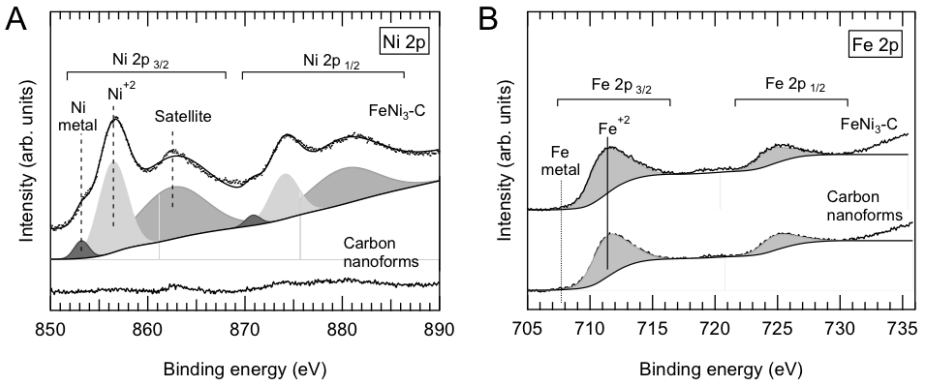

Figure 9. (A) Ni 2p and (B) Fe 2p XPS spectra for $FeNi_3$–C nanocomposite and CNFs.

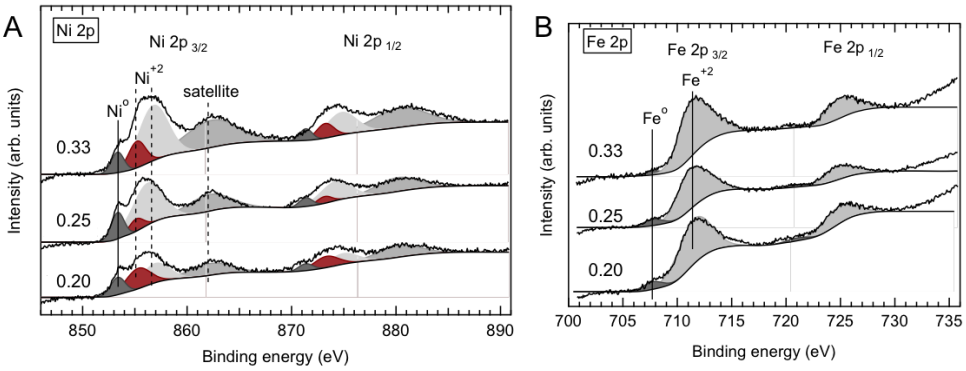

Figure 10. (A) Ni 2p and (B) Fe 2p XPS spectra for $FeNi_3$–graphene nanocomposites **4**–900 °C, **5**–900 °C and **6**–900 °C.

presence of a nickel oxide shell.[359] It is worth noting that, despite the presence of these oxidation states, it is also possible to detect the presence of Ni(0) (Ni $2p_{3/2}$, BE = 853.2 eV) and Fe(0) (Fe $2p_{3/2}$, BE = 707.7 eV) from the graphene-containing nanocomposites synthesized with different composition —namely: **4**–900 °C, **5**–900 °C and **6**–900 °C— (**Figure 10**). The corresponding CNFs show the absence of Ni but a residual presence of Fe(II), arising from Fe_3O_4 impurities not removed by acid (Fe $2p_{3/2}$, BE = 711.5 eV) (see **Table 5**). In turn, the carbon matrix derived from the acid leaching of the 900 °C samples (*i.e.* graphene) shows the presence of Ni(0) and Ni(II), probably related with the presence of carbon-encapsulated NPs as demonstrated by the magnetic measurements.

Table 5. XPS study of selected compounds 4–400 ºC, 4–900 ºC, 5–900 ºC, 6–900 ºC and its corresponding carbon nanoforms and graphene matrix.[a]

Sample	Ni $2p_{3/2}$ Binding energy (eV)				Fe $2p_{3/2}$ Binding energy (eV)		Ni/Fe ratio
	Ni^0	Ni^{II} (1)	Ni^{II} (2)	Ni satellite	Fe^0	Fe^{II}	
4–400 ºC	853.2	0	856.4	862.5	0	711.2	1.71
4–900 ºC	853.4	855.3	856.9	862.2	707.7	711.5	0.8
5–900 ºC	853.3	855.1	856.2	862.1	707.7	711.2	1.1
6–900 ºC	853.4	855.2	856.8	862.3	707.8	711.4	1.33
CNFs	–	–	–	–	–	711.5	0
Graphene[a]	853.2	854.9	856.6	861.3	–	–	inf

[a] Magnetic residue obtained from the acid leaching of the **4**–900 ºC sample.

10.2.2. Carbon Nanoforms

At this point, a detailed HRTEM study of the as-obtained CNFs is needed. In this sense, we have studied the selected sample **6**–400 ºC, on the basis of their highest carbon content (higher sebacate content in the initial precursor). **Figure 11** shows the presence of various nanoforms in the carbon phase upon removal of the metallic template, including empty multi-walled CNFs with fullerene-type structure, such as CNFs or multiwall carbon nanotubes (MWNT), some of them with bamboo-like or polyhedral structures. The average inter-wall distance estimated from the images is *ca.* 0.34 nm, in good agreement with that expected for the distance separating two adjacent (200) planes of graphite.[360] The CNFs are heterogeneously disposed over graphitized sheets and present variable size, with the diameter of the CNOs varying between 15 and 40 nm and the length corresponding to the MWNTs ranging from 75 to 200 nm.

At this point it is interesting to compare our results with previous works reporting the synthesis of CNFs from other carbon-intercalated LDHs. For example, Zeng et al. detected the formation of what they defined as "carbon nanoparticles" —fullerenic nanoforms with multiwalled structure— as a result of the thermal decomposition of terephthalate-intercalated CoMgAl–LDHs.[331] In our opinion, these nanoforms should be considered as intermediates towards the formation of either MWNTs or CNOs rather than as final products. This assumption seems to be supported by the amorphous carbon matrix surrounding the reported nanoparticles whereas our nanoforms are grown over

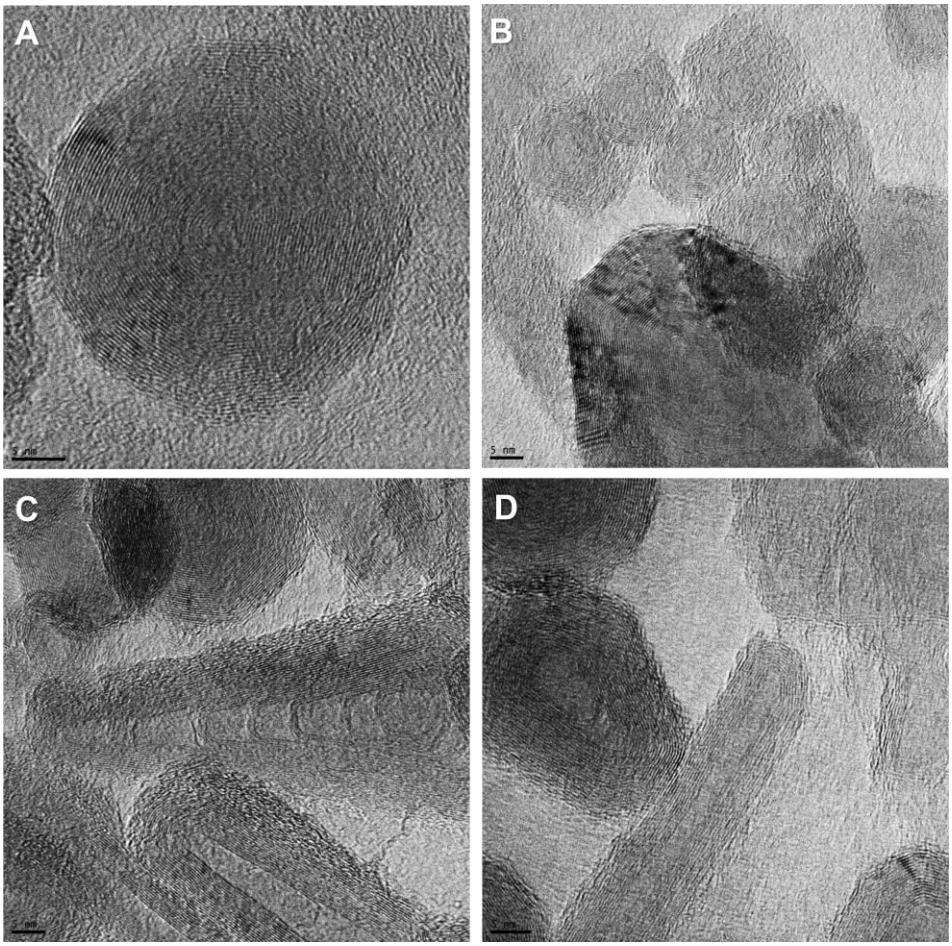

Figure 11. (A) HRTEM image of CNFs showing a well-defined carbon nano-onion, obtained after acid leaching of the nanocomposites with 2 M HCl. (B) HRTEM image showing some CNOs. (C and D) HRTEM images showing some fullerene-type CNFs; specifically a bamboo-like nanotube and some multiwall nanotubes can be observed.

graphitic layers, suggesting a less efficient graphitisation process after decomposition of the intercalated anions for the previous work. This process is vital for the quantitative formation of these nanoforms and must be considered as the key difference between the reported results. The use of a CoMgAl–LDH host, with only cobalt centres being catalytically active, results in a more dilute distribution of catalytic sites within a non-catalytic matrix. This results only in a

poorly efficient graphitisation process. Here, the use of a NiFe–LDH, leads to a very high density of catalytic active sites, therefore favouring subsequent formation of CNFs.

Let us now compare our chemical method with the most employed physical method developed for CNO preparation.[361,362] Both give a mixture of CNOs with amorphous carbon, graphitic carbon, nanotubes and nanorods. In both cases well-defined spherical CNOs with an average size of *ca.* 20 nm are obtained. However, while the physical method seems to give large amounts of amorphous carbon and starting graphite, which require further purification to extract the nanoforms, in our method carbon nanoforms are the dominant species. Further, while the physical method requires the use of complex equipment (arcing of high purity graphite under water), our method is cheap, simple and can easily be upscaled to give large amounts of CNFs (of the order of grams).

The use of LDH nanocontainers as sacrificial inorganic templates might explain the appearance of CNFs thanks to the periodic distribution of catalytic centres at the atomic scale inherent to these layers. This scenario favours the controlled formation of nanometric inorganic particles, whose catalytic activity in the thermal decomposition process, leads to the formation of the observed carbon nanoobjects. This assumption seems to be supported by the thermogravimetric profile of the decomposition of the NiFe–Seb LDH precursors, which shows an abrupt mass loss around 250 ^{o}C accompanied by a high-intensity exothermic peak centred at around 299 ^{o}C in the DTA plot (not shown). It is worth mentioning that both the dehydroxylation of the LDH layers and the decomposition of the organic phase takes place in this narrow temperature range, thus suggesting that both processes are coupled as a result of the catalytic activity of the metal nanoparticles being formed *in situ*. This temperature is close to that reported elsewhere for the pyrolysis of the intercalated organic molecules (< 400 ^{o}C). The formation of metallic nanoparticles could decrease the temperature of this process and the resulting reducing gases would probably assist the reduction of Ni and Fe.

From a morphological point of view, the carbon matrix displays important changes upon increasing calcination temperatures (see **Figures 12A** and **B**). Hence, whilst the black carbon matrix obtained after acid leaching of **5**–400 °C is dominated by the presence of CNOs, these nanoforms evolve to form

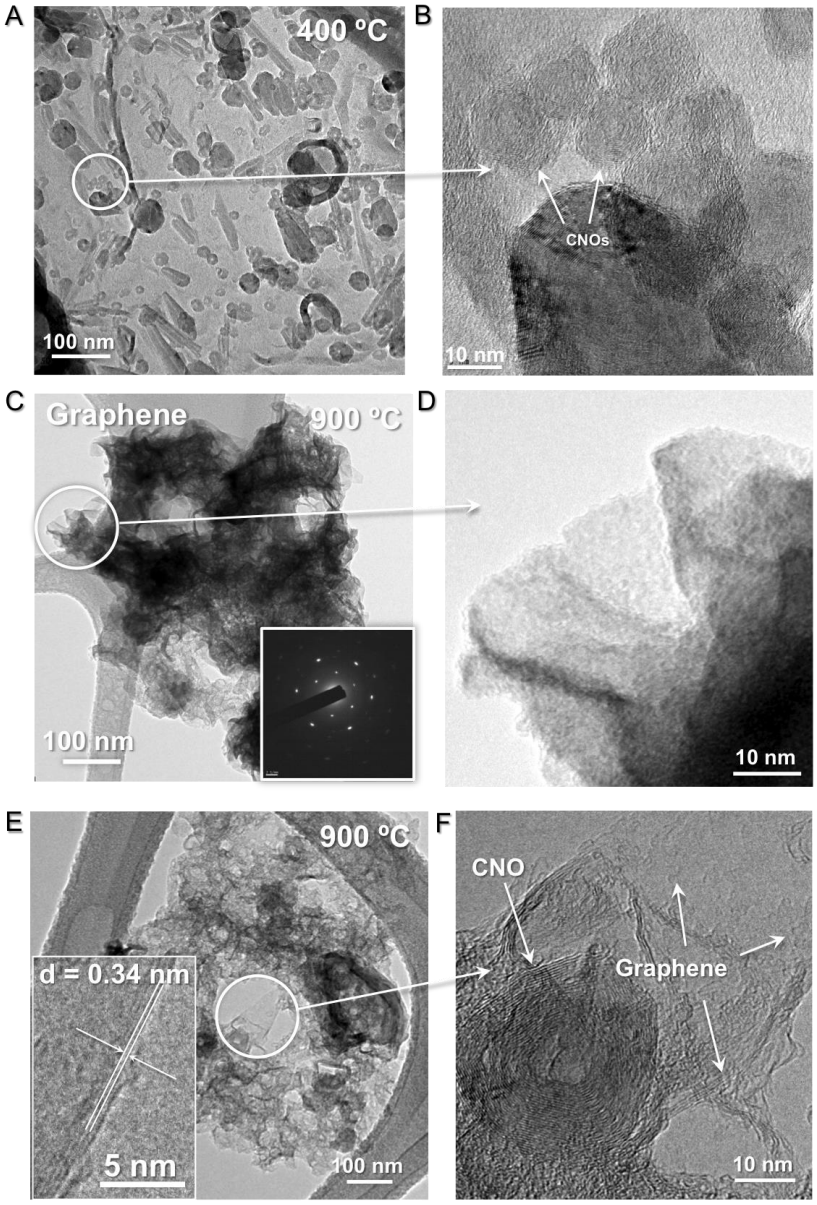

Figure 12. (A, B) TEM image of the as-obtained CNFs after the acid leaching procedure of $FeNi_3$–C nanocomposite synthesized at 400 °C (A, B) showing several CNFs including CNOs. (C, D) HRTEM images of graphene obtained from the $FeNi_3$ nanocomposite synthesized at 900 °C and its corresponding SAED pattern. (E, F) Selected area showing the evolution of a CNO into graphene layers.

graphene at 900 °C, as previously evidenced by Raman spectroscopy (see **Figure 6**). For the samples obtained at intermediate temperatures (650 °C), a quasi-2D graphitic morphology in which several CNFs coexist can be observed, recalling an intermediate scenario between the extreme temperatures. Moreover, for the samples calcined at 900 °C, the synthesis of graphene from the sebacate-intercalated LDH precursor is supported by the presence the characteristic hexagonal pattern in the selected area electron diffraction (SAED) image (inset of **Figure 12C**). Additional HRTEM images show the typical corrugation morphology of graphene flakes. These graphene sheets are randomly aggregated and closely associated with each other to form a disordered solid (see **Figure 12D**). In a higher magnification of the graphene sheets, single and double lines (with an interlayer distance of *ca.* 0.34 nm) corresponding to one or two graphene layers, were observed (inset in **Figure 12E**). Remarkably, in some areas we have been able to observe the coexistence of graphene sheets and residual CNOs, which are probably the seeds from which graphene is formed (**Figure 12F**). This straightforward procedure allows for the selective synthesis of both CNOs and graphene by simple tuning the calcination temperature. In the case of using high temperatures, only free standing sheets of graphene can be obtained, probably due to the carbon consumption arising from some reduction processes at high temperatures.[297]

FESEM images confirm the hierarchical structure of the nanocomposites. **Figure 13** is a set of FESEM images of sample **5** under different calcination conditions. In the 900 °C sample, the catalytic $FeNi_3$ NPs are highly visible inside the graphene matrix indicating the intimate contact between graphene and the NPs (**Figure 13C**). This carbon matrix shows the typical corrugation of graphene.

10.2.3. Textural Properties

The textural properties of the samples were evaluated by means of nitrogen adsorption/desorption isotherms. As shown in **Figure 14A**, the $FeNi_3$–C nanocomposite show a type IV isotherm with low specific surface area, since it is composed by metal NPs embedded in the carbon matrix, with a considerable contribution of the microporosity arising from the carbon constituent, that becomes larger as the iron content increases.[363] As expected, the same behaviour

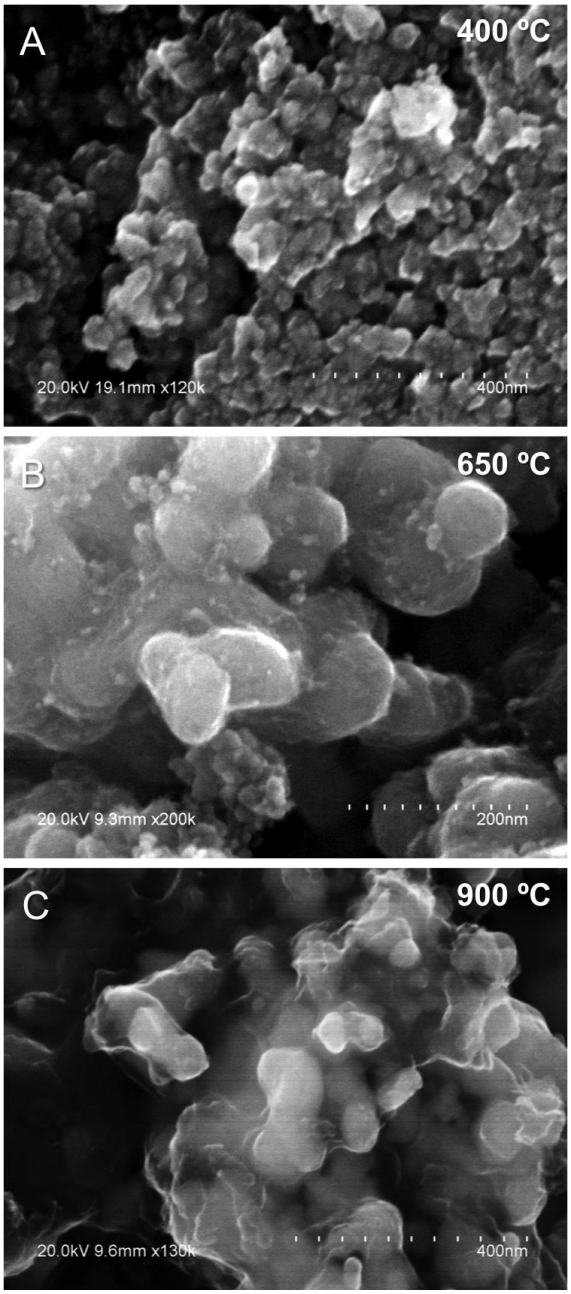

Figure 13. FESEM images of $FeNi_3$–C nanocomposites synthesized at (A) 400 °C, (B) 650 °C, and (C) 900 °C.

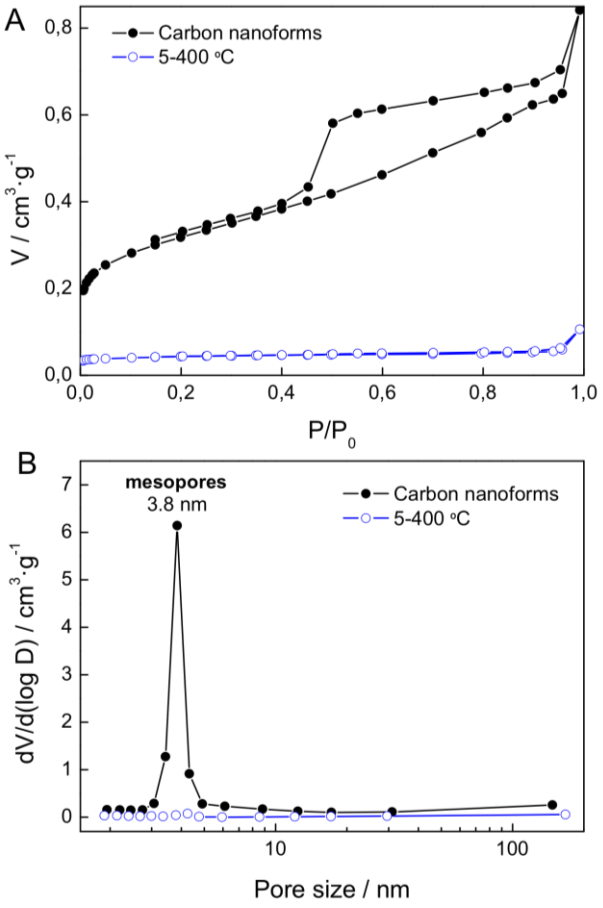

Figure 14. (A) Nitrogen adsorption/desorption isotherms at 77 K of $FeNi_3$–C nanocomposite obtained at 400 °C and its corresponding CNFs obtained after acid leaching. (B) Pore size distributions calculated from the desorption branch of the N_2-isotherm using Barret–Joyner–Helender (BJH) method. The corresponding textural parameters are shown in **Table 1**.

is observed for the rest of the compositions (*vide supra*), showing values below 90 $m^2 \cdot g^{-1}$ (**Table 6**). The pore size distributions exhibit both mesoporous and interparticle pores. The increase in the calcination temperature, leads to a marked mesoporosity, as can be observed for sample **5** (**Figure 15**).

After acid leaching, the whole adsorption/desorption curve steep rises indicating a dramatic increase in the porosity and surface area. As illustrated in

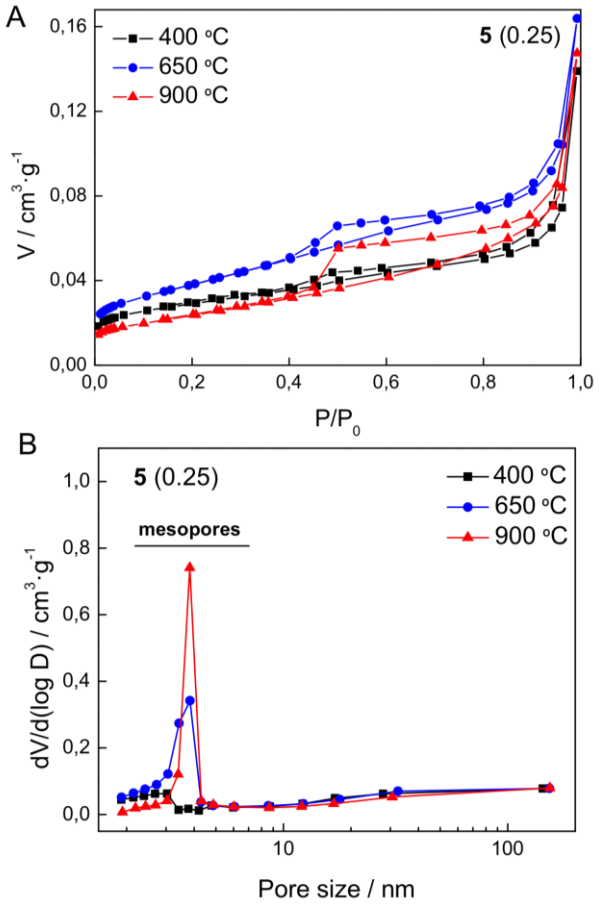

Figure 15. (A) Nitrogen adsorption/desorption isotherms at 77 K for the ideal stoichiometric sample **5** (0.25) calcined at 400, 650 and 900 °C. (B) Pore size distributions calculated from the desorption branch of the N_2-isotherm using BJH method. The corresponding textural parameters are shown in **Table 1**.

Figure 14A, the carbon matrix shows a type IV isotherm with a H3 hysteresis loop (according to the IUPAC classification).[363] Above the monolayer formation P/P_0 > 0.1, a drastic change in the curvature takes place indicating the adsorption on the external surface. This value is measured by S_T. In turn, below P/P_0 = 0.1 the adsorption occurs on the micropore surface (S_μ). Direct comparison of the porosity of **5** before and after the acid treatment clearly demonstrates the mesoporous nature of the carbon matrix and its enhanced

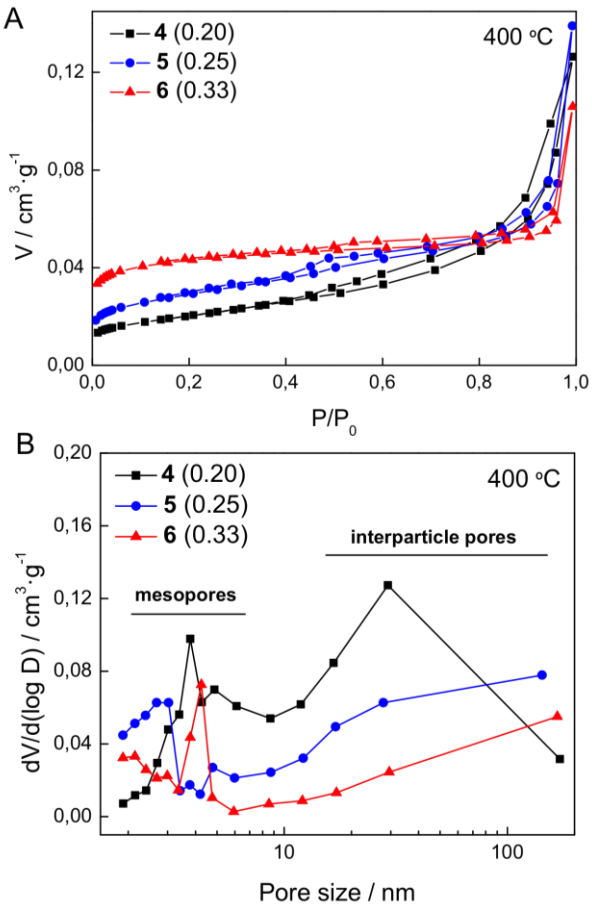

Figure 16. (A) Nitrogen adsorption/desorption isotherms at 77 K for $FeNi_3$–C nanocomposites **4**, **5** and **6** calcined at 400 °C. (B) Pore size distributions calculated from the desorption branch of the N_2-isotherm using BJH method.

porosity, as evidenced by the increase in the BET surface area (685 $m^2 \cdot g^{-1}$) and its narrow pore size distribution centered at *ca.* 3.8 nm.[364] The corresponding pore size distribution and textural parameters of these materials and those corresponding with the samples **4**, **5** and **6** calcined at different temperatures are summarized in **Figures 15**, **16** and **Table 6**, respectively. One of the most appealing features of these materials is that in these nanocomposites the carbon matrix and, more specifically graphene, is not acting as a 2D support but as a

Table 6. Textural parameters for $FeNi_3$–C nanocomposites 4, 5 and 6 calcined at 400 °C, the nanocomposite 5 calcined at different temperatures, and the carbon nanoforms obtained after acid treatment of the sample 5–400 °C.

Sample	S_{BET}[a] [$m^2 \cdot g^{-1}$]	*t* plot		$V\mu_{(<0.7\ nm)}$[b] [$cc \cdot g^{-1}$]	$V\mu_{DR}$[c] [$cc \cdot g^{-1}$]	$V\mu_{(0.7–2\ nm)}$[d] [$cc \cdot g^{-1}$]	V_{meso}[e] [$cc \cdot g^{-1}$]
		$S\mu$[a]	S_T[a] [$m^2 \cdot g^{-1}$]				
4–400°C	46	4	42	0.01	0.02	0.01	0.07
5–400°C	64	13	51	0.02	0.02	0	0.03
6–400°C	80	73	7	0.03	0.04	0.01	0.01
5–650 °C	88	<1	88	0.01	0.03	0.02	0.04
5–900 °C	55	0	55	0.01	0.02	0.01	0.04
CNF[f]	685	199	486	0.16	0.23	0.12	0.35

[a] Data obtained from N_2-adsorption. Specific surface area calculated by BET method, and *t*-plot for the microporous surface contribution $S\mu$ and external surface S_T; [b] Data obtained from CO_2-adsorption. Micropore volume (<0.7 nm) calculated according to the Dubinin–Radushkevich (DR) method; [c] Micropore volume calculated from N_2-adsorption using DR method; [d] Micropore volume in the 0.7–2 nm range calculated according to: $V\mu_{(0.7–2\ nm)} = V\mu_{DR} - V\mu_{(<0.7\ nm)}$ values; [e] Mesopore volume was calculated according to: $V_{meso} = V_{(P/P0\ =\ 0.7)} - V\mu_{DR}$ values. f) Carbon nanoforms deriver from the acid leaching of **5**–400 °C.

hierarchical shell covering the metal NPs and improving its interfacial interaction.[365]

10.2.4. Electrochemical Properties

One of the most relevant aspects of hybrid inorganic-nanocarbon materials is their applicability in energy storage devices like Li-ion batteries, super-capacitors (SCs) or water splitting devices.[12,365]

We tested the $FeNi_3$–C nanocomposites as the electrode materials for SCs in a conventional three-electrode cell. **Figure 17** shows the stationary cyclic voltammograms and cyclic chronopotentiometric plots of the electrodes prepared with the ideal stoichiometric metal composition (0.25) of sample **5** after calcination at different temperatures. The nanocomposite **5** clearly exhibits a Faradaic contribution to capacitance. The morphology of the voltammograms does not change with the scan rate. Among the three studied nanocomposites, the $FeNi_3$–graphene electrode (**5**–900 °C) showed the highest current response during both, voltammetric and galvanostatic cycling. Thus, as plotted in **Figure 18**, a maximum value of *ca.* 343 $F \cdot g^{-1}$ (6.24 $F \cdot m^{-2}$) at a high value of current

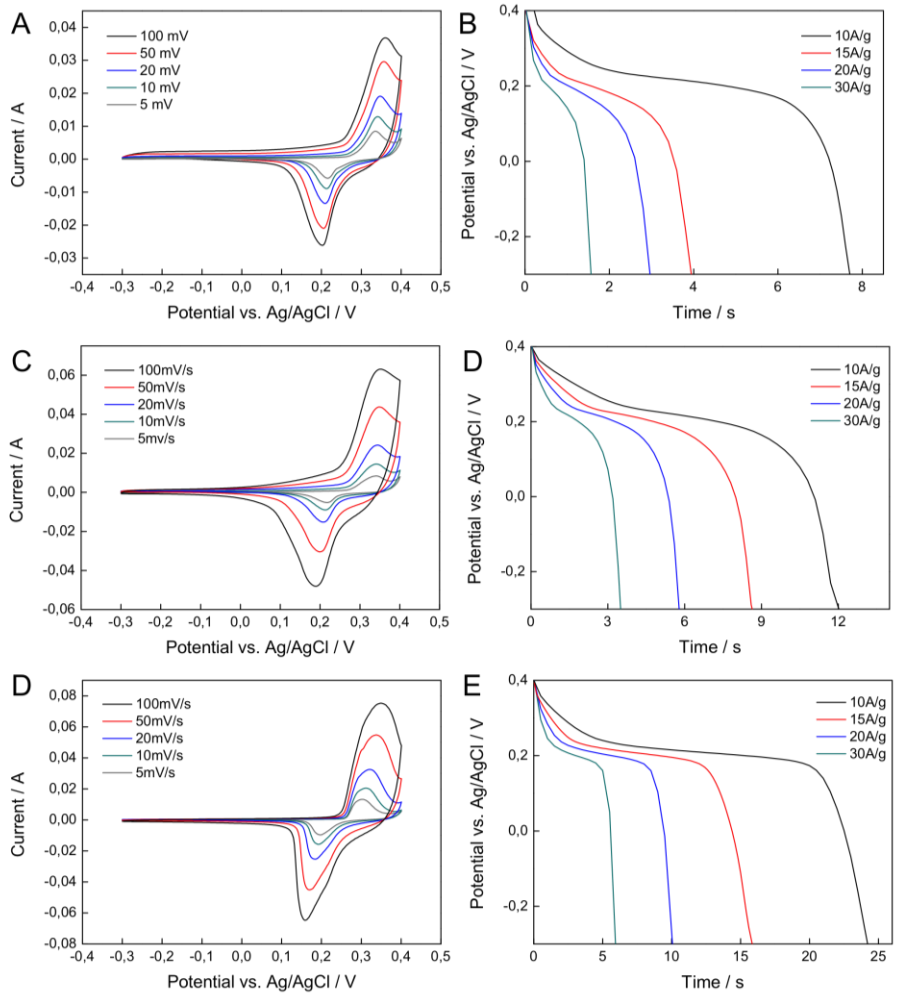

Figure 17. Stationary CV at various scan rates for the $FeNi_3$–C nanocomposite in 6 M KOH aqueous solution and his corresponding stationary galvanostatic discharge curves at various discharge current densities within the potential window of 0.4 to –0.3 V (*vs.* Ag/AgCl) of (A, B) **5**–400 °C, (C, D) **5**–650 °C, and (E, F) **5**–900 °C.

density of 10 $A \cdot g^{-1}$ has been obtained. The specific capacitance increases with the temperature more than 300 % as a result of the presence of graphene in the nanocomposites synthesized at the highest temperatures. This high pseudocapacitive behavior is due to the combination of mesoporosity[366–369] and solid-state redox centers, mainly nickel and its corresponding oxidized shells

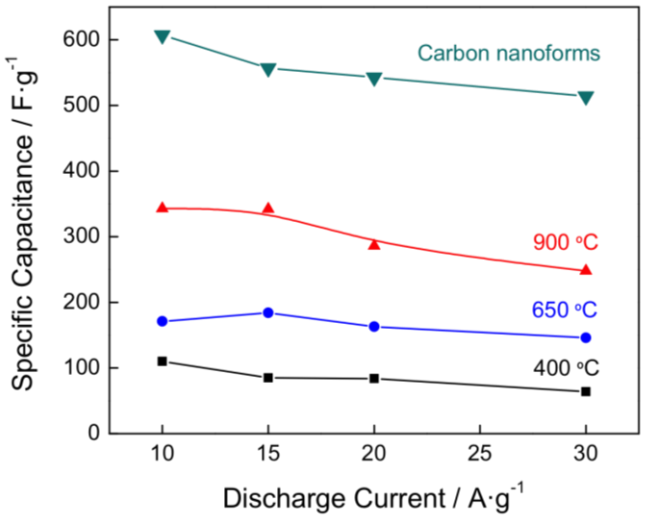

Figure 18. Specific capacitance of the electrodes prepared with $FeNi_3$–C nanocomposite synthesized at different temperatures and its corresponding CNFs derived from **5**–400 °C at different discharging current densities.

(NiO) in the used potential window. This oxidized shell (and that corresponding to iron, Fe_3O_4) are a superior source of capacitance.[370,371] It is worth mentioning that the galvanostatic curve shows a defined plateau during the cathodic swep. This is a clear evidence of the pseudocapacitive character of the nanocomposite material. Moreover, the intrincate morphology of the conducting graphene matrix promotes the electrolyte penetration improving the electrochemical performance of the material, which behave as a 3D electrodic material at the nanometric level.

In the studied potential window, the main contribution to the electrochemical properties arises from the NiO shell and the graphene layers. Concretely, a reversible process of insertion and extraction of OH^- ions should be expected, according with the reaction: $Ni^{II}O + OH^- \leftrightarrow Ni^{III}OOH + e^-$.[103] Moreover, the presence of $FeNi_3$ metal cores provides good conductive networks in addition to the graphene layers, improving the electronic transfer and therefore in the performance of the electrode.[370] In addition, the presence of Fe species could be of interest from an electrochemical point of view. In this

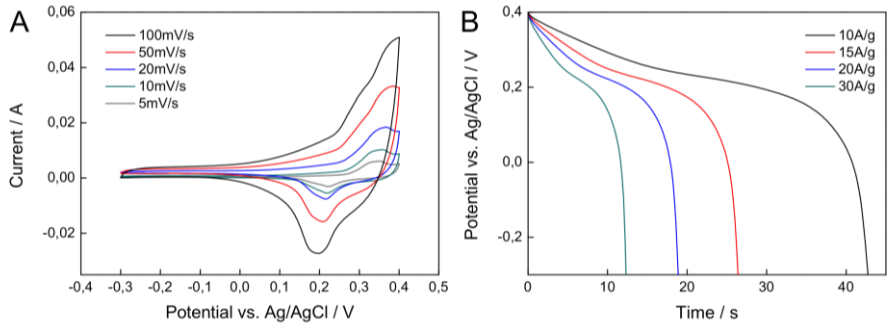

Figure 19. Stationary CV curves at various scan rates for the CNFs derived from **5**–400 °C nanocomposite in KOH 6 M electrolyte and his corresponding galvanostatic discharge curves at various discharge current densities within the potential window of 0.4 to −0.3 V (*vs.* Ag/AgCl).

direction, a nanocomposite material acting as a chemical memory device could be envisioned (see **Appendix II**).

Our capacitance values (≈248 $F{\cdot}g^{-1}$ at 30 $A{\cdot}g^{-1}$ current density) are remarkably higher than those previously reported for LDH-based mixed oxide-carbon composite materials. For example, values comprised between 65 and 94 $F{\cdot}g^{-1}$ have been recently reported for NiAl, CoAlFe, or CoAl nanocomposites under slow regime.[82,88,335] The hierarchical structure and the development of a highly graphitized carbon matrix for all the temperatures seems to be a key factor for improving the capacitance in this family of LDH-based materials.

The CV curve of the acid leaching carbon matrix (**Figure 19**) has also been measured. A value as high as ≈ 607 $F{\cdot}g^{-1}$ (0.89 $F{\cdot}m^{-2}$) at 10 $A{\cdot}g^{-1}$ was obtained (see **Figure 18**). The increase in the specific capacitance is probably due to the redox contribution arising from the residual metal oxide centers and the enhanced porosity. This behavior seems to indicate that the metal NPs play a crucial role in the pseudocapacitive contribution.[107]

Figure 20A shows the Ragone plots (energy density *vs.* power density plot) of the four electrodes showing high values of energy densities in rapid charging–discharging process (current density). $FeNi_3$–graphene nanocomposite exhibits an energy density of 16.9 $W{\cdot}h{\cdot}kg^{-1}$, with a corresponding power density as high as 10483.5 $W{\cdot}kg^{-1}$. Moreover, in the case of the CNFs, a superior value of energy

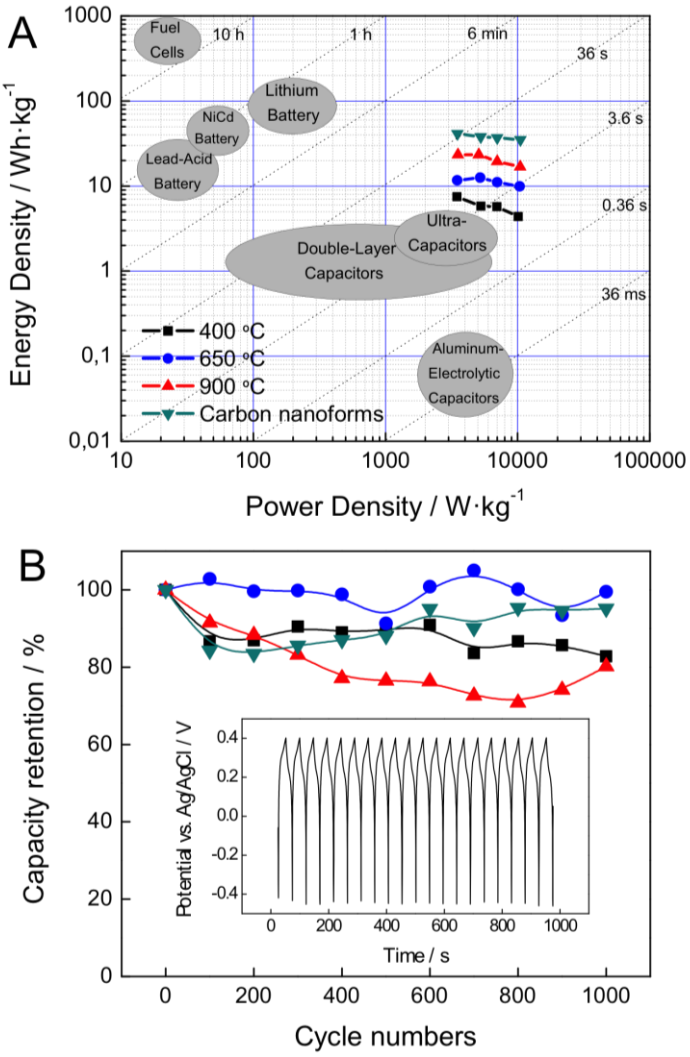

Figure 20. Energy storage performance of $FeNi_3$–C nanocomposites calcined at different temperatures and its corresponding CNFs derived from the acid leaching of the sample **5**–400 °C: (A) Ragone plot showing the performance of as-prepared supercapacitive electrodes among various commercial energy-storage devices (source data from US Defense Logistics Agency) and (B) cycling performance at 20 $A \cdot g^{-1}$. The inset shows the stationary galvanostatic charge and discharge curves of the CNFs derived from **5**–400 °C at a current density of 20 $A \cdot g^{-1}$.

density of 35 $W \cdot h \cdot kg^{-1}$ with a corresponding power density of 10503 $W \cdot kg^{-1}$ can be obtained. As expected for a graphene-based device, the energy density is comparable to that of modern nickel metal hydride battery used in hybrid vehicles.[372] Another important aspect in the development of efficient supercapacitive devices is the cycling capability. We perform the galvanostatic charge–discharge cycling in order to test the electrochemical stability (**Figure 20B**). The cycling life experiments were carried out at a current density of ±20 $A \cdot g^{-1}$. More than 80 % of its original capacitance is retained after 1000 cycles for all the studied materials, almost 99 % in the case of CNFs. Moreover, the plot shows also a coulombic efficiency close to 99 % (inset in **Figure 20B**). $FeNi_3$–C-based electrodes exhibits a good performance in durability and stability. All these features suggest that this kind of nanocomposites can be applied as electrode materials for supercapacitors.

10.3. Conclusions

We have synthesized a series of hierarchical structured $FeNi_3$–C nanocomposites. We have demonstrated how a sebacate-intercalated NiFe–LDH acts as an inorganic multi-layered nanoreactor, permitting the formation of CNF. Interestingly, the nature of the CNFs in this matrix can be tuned with temperature (ranging from carbon nano-onions at 400 °C to graphene in the case of 900 °C). This process is promoted by the catalytic activity of the $FeNi_3$ nanoparticles formed *in-situ*, which facilitate the synergistic decomposition of the confined sebacate molecules to produce carbon nanoforms embedded into a graphitic shell. The onset temperature for which the formation of multi-shell carbon nanoforms occurs —400 °C— is remarkably lower than that required for the catalytic synthesis of CNOs and related materials by using nano-particulate NiFe catalysts —typically ranging from 750 to 850 °C.[373] This drastic difference seems to indicate that both the nanometric distribution of catalytic metals in the 2D layers intrinsic to LDH materials and the intimate contact between these layers and the carbon precursors in a confined media, play a pivotal role in the low-temperature synthesis of carbon nanoforms.

Additionally, we have shown how the use of a NiFe–LDH host leads to the highest density of catalytic active sites permitted by LDH materials. Therefore this favours the graphitisation process and subsequent formation of carbon

nano- forms, in comparison with other LDHs used in this context. In our opinion, this result nicely illustrates the value of chemical design as a powerful tool to enhance the efficiency of a specific problem. In addition, this methodology opens the door for the low-cost and more environmentally friendly synthesis of these new forms of carbon.

Furthermore, these materials show $FeNi_3$ magnetic NPs embedded in a graphitized carbon matrix. The magnetic properties of this nanocomposites show that the $FeNi_3$ NPs are ferromagnetic in the 2–350 K temperature range. In addition, they show high-performance supercapacitive behaviour under high current densities as a result of the coexistence of both types of capacitances, EDLC and redox pseudo-capacitance, arising from nanostructured carbon and metal NPs, respectively. In view of their environmentally friendy character, low-cost, robustness and high energy and power density values, these nanocomposites can be envisioned as promising supercapacitors.

Carbon-based materials are expected to prevail in the future as an important component of commercial supercapacitors, in view of the low cost required for their processing.[107,374,375] In this sense, those based on LDH have been recently postulated as a cheap alternative with lower environmental impact for industrial companies.[12] This straightforward methodology is therefore suitable for preparing novel hybrid carbon nanocomposites with interesting functionalities arising from the different constituents, which can be useful not only in energy storage, but also in other areas of diverse interest such as biomedicine, spintronics, or catalysis. As a matter of fact, the synthetic methodology described here has been recently employed by Xu and co-workers for the development of carbon-encapsulated transition metal phosphide with improved cycle stability for lithium-ion batteries.[376]

10.4. Experimental Section

10.4.1. Synthesis

Chemicals: All chemicals, $Ni(NO_3)_2{\cdot}6H_2O$, $Fe(NO_3)_3{\cdot}9H_2O$, $HO_2C(CH_2)_8CO_2H$ (sebacic acid), NaOH, KOH, HCl, acetylene black, poly(vinylidene fluoride) (PVDF), and ethanol (Aldrich, Fluka, Alfa-Aesar) were used as received without further purification.

Synthesis of NiFe–Seb and $FeNi_3$–C: The precursor LDH material NiFe–Seb was prepared following the general method described previously by our group, using sebacic acid/NaOH.[122,201] The $FeNi_3$–C nanocomposites have been obtained by calcination under nitrogen atmosphere during 2 h at 400, 650, or 900 °C, depending on the sample, in a programmable oven with a 2 °C·min^{-1} scan rate and nitrogen flow of 40 mL·min^{-1}. The CNFs and graphene have been obtained by acid leaching of the nanocomposites with 2 M hydrochloric acid with magnetic stirring.

10.4.2. Physical Characterization

Metallic atomic composition of bulk samples was determined by means of electron probe microanalysis performed in a Philips SEM-XL30 equipped with an EDAX microprobe. Carbon, nitrogen, and hydrogen contents were determined by microanalytical procedures by using a LECO CHNS-932. HRTEM studies of the hybrid material were carried out on a JEM-2010 microscope (JEOL, Japan) operating at 200 kV. Samples were prepared by dropping a sonicated suspension of the material in ethanol on a carbon-coated copper grid. The digital analysis of the HRTEM images was done using DigitalMicrograph 1.80.70 for GMS 1.8.0 by Gatan. FESEM studies were performed on a Hitachi S-4800 microscope operating at an accelerating voltage of 20 kV and without metallization of the samples.

Thermogravimetric analysis (TGA) of all compounds were carried out with a Mettler Toledo TGA/SDTA 851 apparatus in the 25–800 °C temperature range under a 10 °C·min^{-1} scan rate and an air flow of 30 mL·min^{-1}. XRPD patterns were collected with a Siemens d-500 X-ray diffractometer (Cu-Kα radiation; λ = 1.5418 Å) equipped with a rotating anode D-max Rigaku operating at 80 mA and 45 kV. Samples were mounted on a flat sample plate. Profiles were collected in the $2.5° < 2\theta < 100°$ range with a step size of 0.05°. Magnetic susceptibility

measurements were performed on polycrystalline samples with a Quantum Design PPMS-9 model instrument. The susceptibility data were corrected by removing the diamagnetic contributions as deduced by using Pascal's constant tables. The *dc* data were collected in the range 2–300 K upon decreasing temperatures with an applied field of 1000 G, and hysteresis loops were collected between –5 and +5 T at 2 and 350 K. The Raman measurements (Jobin-Yvon LabRam HR 800 Raman Microscope) were carried out at room temperature with the 532 nm line of an Ar ion laser as an excitation source. XPS measurements were performed in the laboratory of Prof. J. F. Sánchez-Royo at the Instituto de Ciencia de los Materiales (Universitat de València). XPS measurements were performed in an ultra-high vacuum system ESCALAB210 (base pressure 1.0 × 10−10 mbar) from Thermo VG Scientific. Photoelectrons were excited by using the Mg-Kα line (1253.6 eV). All spectra have been referred to the Fermi level. The porous texture of all the materials prepared was characterized by N_2 adsorption at 77 K and CO_2 at 273 K in an AUTOSORB-6 apparatus. The samples were previously degassed for 4 h at 523 K and 5×10^{-5} bar. The desorption branch of the N_2 isotherm was used to determine the pore size distribution using the BJH method. The surface area was determined using the BET method. The micropores volumes were determined by applying *t*-plot and DR methods.

10.4.3. Electrochemical Measurements

The electrochemical characterization has been carried out in collaboration with Prof. T. F. Otero at the Group of Electrochemistry Intelligent Materials and Devices (Universidad Politécnica de Cartagena). The materials were mixed with acetylene black and PVDF in a mass ratio of 80:10:10 in ethanol and deposited in a nickel foam electrode. The as-prepared nickel foam electrodes were dried overnight at 110 °C and pressed. Each working electrode contained about 1 mg of electroactive material and had a surface area of about 1 cm^2. A typical three-electrode experimental cell equipped with a stainless steel plate having 4 cm^2 of surface area as the counter electrode and a Metrohm Ag/AgCl (3 M KCl) as the reference electrode was used for the electrochemical characterization of the nanocomposite materials trapped by the working electrodes. The electrochemical measurements were carried out in 6 M KOH aqueous solutions

as the electrolyte. Ultrapure water was obtained from Milli-Q equipment. All the electrochemical experiments were performed at room temperature using an AUTOLAB PGSTAT 100 potentiostat–galvanostat controlled by GEPES electrochemical software. The specific capacitance (C), energy density (E), and power density (P) were calculated from the cyclic chronopotentiometric curves according to Equations (1)–(3),

$$C=I\Delta t/m\Delta V \quad \text{eq. [1]}$$

$$E=1/2C(\Delta V)^2 \ (2) \quad \text{eq. [2]}$$

$$P=E/\Delta t \ (3) \quad \text{eq. [3]}$$

where I is the charge/discharge current, Δt is the time for a full charge or discharge, m the weight in grams of the active material in the electrode layer, and ΔV is the voltage change after a full charge or discharge.

10.5. Appendix II. Electrochemical Characterization of $FeNi_3$-Graphene Nanocomposites in Nonaqueous Media[†]

In general, all supercapacitive nanocomposites have been usually checked in aqueous electrolytes having limited potential window of *ca.* 1 V due to the thermodynamic electrochemical window of water (1.23 V).[377] Thus, when the potential window is increased up to 3 V in organic solutions new electrochemical processes in $FeNi_3$–graphene hybrid nanocomposite are expected. In this direction, we have measured the electrochemical properties of selected sample **5**–900 ºC in acetonitrile solutions. (see **Figure 1**).[378] For measuring the electrochemical behaviour of the $FeNi_3$–G powder, we spread the sample (*ca.* 1 mg) over a graphite paste, in order to avoid the use of Ni-foams and preventing any loss of the active material during the electrochemical control. The excellent electronic properties of the graphene matrix avoid the use of other conducting additives. Then, the electrode was dried at 100 °C overnight to evaporate any organic solvent coming from the graphite lacquer. We have obtained the voltammetric responses in a large potential window that exceed 3 V from 0.1 M lithium perchlorate acetonitrile solutions. The voltammetric responses, when the material was cycled at 50 $mV{\cdot}s^{-1}$ up to increasing anodic potential limits in the range from 1 V to 1.5 V keeping a constant cathodic potential limit of −1.8 V, reveals (**Figure 1A**) that two new peaks protrude from the general structure: I, for the material oxidation at 1.2 V and II, for the material reduction at −1.5 V separated over 2.4 V. These peaks are coupled correspondingly to a reverse oxidation/reduction process: when the potential sweep includes peak II and the cathodic potential limit is changed in the potential range of peak II, the increasing currents involved here are correlated with the increasing oxidation current for peak I (**Figure 1A**), and vice versa (**Figure 1B**). We can assume that they correspond to the simultaneous transitions $Fe^0/Fe^{II}/Fe^{III}$ and Ni^0/Ni^{II}, for peak I, and the reverse transitions for peak II.[114] The large displacement related to the redox potentials of each couple could be related to the strong graphene/nanoparticle interactions in addition to

[†] Abellán, G.; Martinez, J. G.; Otero, T. F.; Ribera, A.; Coronado, E. *Electrochem. Commun.* **2014**, *39*, 15

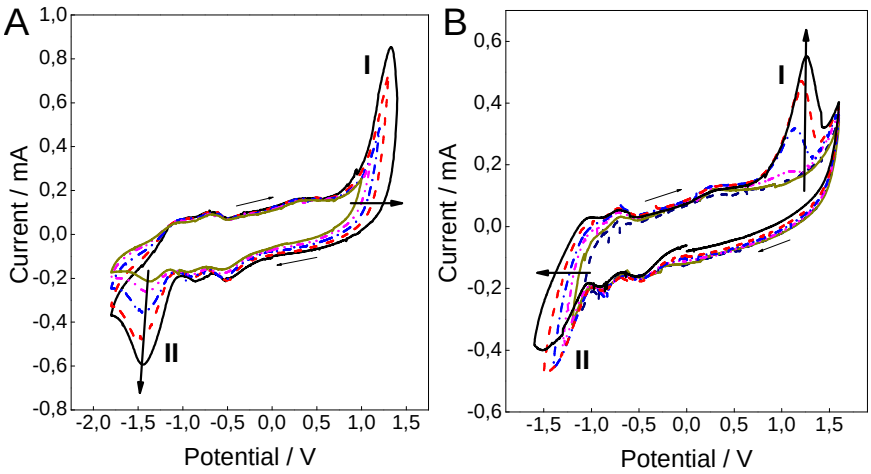

Figure 1. (A) Voltammograms obtained from $FeNi_3$–G nanocomposite between −1.8 V (*vs.* Ag/AgCl) and different anodic potential limits. (B) Voltammograms obtained from $FeNi_3$–G nanocomposite between different cathodic potential limits and 1.5 V (*vs.* Ag/AgCl).

some redox processes related with the chemical reactivity of graphene at surface defect sites, and in particular edge-plane-like defect sites.[379] These findings expand the possible application of these sorts of materials towards chemical memory devices.[378,380,381]

11. Giant Magnetoresistance with Temperature-Dependent Crossover in $FeNi_3$-Graphene Nanocomposites[†]

In this chapter we have thoroughly studied the magnetotransport properties of the $FeNi_3$–graphene nanocomposites synthesized in the previous section using NiFe–Seb LDH hybrids as precursors.

All our data suggest that we have ferromagnetic nanoparticles embedded in a graphene matrix forming a granular nanocomposite whose matrix conductivity can be tuned with temperature, thus offering the possibility of modulate the magnetoresistance (MR) behavior.

This hierarchical structure herein obtained exhibits giant MR (GMR) with temperature-dependent crossover and low-field MR (LFMR) in a synergistic way, arising from the correlation of the physical properties of its initial constituents, *i.e.*, electrical conductivity and ferromagnetism. In contrast to multilayered GMR materials, where a high magnetic field is required to saturate the MR, our GMR granular nanocomposites can operate at room temperature and low fields. This behaviour makes these materials promising for applications as GMR sensors, magnetically-controllable electrochemical capacitors, energy tuning devices for microelectronics and data storage devices.

[†] a) Abellán, G., Coronado, E., Ribera, A. Patent P201200188 (Spain). WO 2013124503 A1 (International). b) Abellán, G.; Coronado, E.; Prima-García, H. (manuscript in preparation)

11.1. Introduction

Magnetoresistance (MR) is a phenomenon that reflects the resistance change of a material when an external magnetic field is applied to it, and can be categorized into five distinct types including ordinary magnetoresistance (OMR), anisotropic magnetoresistance (AMR), giant magnetoresistance (GMR), tunneling magnetoresistance (TMR) and colossal magnetoresistance (CMR).[382] Since GMR was first discovered in magnetic multilayers[383] and subsequently in magnetic granular films,[384–386] a new perspective in the development of innovative materials for technological applications has been generated in areas such as biological detection,[387] magnetic recording and information storage systems.[388]

Especially, polymer nanocomposites with functional particles have created much interest due to their cost-effective processability and high flexibility rendering possible many applications such as microwave absorbers,[389] or smart stimuli-responsive materials.[390] These polymer nanocomposites can be considered as granular systems, in which the GMR originates from the spin-dependent scattering of conduction electrons at the interface between the ferromagnetic (F) particles and the nonmagnetic matrix, as well as within the F particles. Indeed, GMR has a close relationship with the local magnetization of F nanoparticles. However, the magnitude of MR depends on various factors, such as magnetic to non-magnetic constituent ratio, the chemical nature of the matrix, the size and shape of the particles and also the inter-particle (grain) distance.[384] Therefore, the nature of the nonmagnetic matrix plays a crucial role in these sort of nanocomposites.

Beyond traditional materials, graphene is being widely studied as a functional matrix due to its superior electronic properties. The direct exposure of the active-conducting area of graphene to the external world, and the expected long spin coherence lifetimes and lengths makes this 2D material suitable for spintronics.[391] Until recently, graphene has been considered a nonmagnetic material, but now numerous investigations are focused on studying its MR property.[392–395] In this sense, organic magnetoresistance (OMAR) has recently been found in graphene, and in few layers graphene, among other carbon-based materials.[396] Moreover, our group has recently

reported a study describing how the chemical doping of G with electronically active organic functionalities can modify its MR response.[397]

In view of these results, one can take advantage of graphene by using the electronic and structural properties of it as a conductive matrix in granular magnetic composites. Here graphene will be used not only as a source of conductivity but also as a hierarchical spacer. A first result along this line has recently reported by Guo et al., which found GMR in magnetic graphene nanocomposites, in which core-shell magnetic nanoparticles are disposed on the surface of graphene sheets showing high values for MR and negative permittivity.[398]

In the present Chapter we intend to go a step forward by studying the chemically-designed magnetic nanocomposites prepared in the Chapter 10, which are formed by magnetic nanoparticles embedded in a graphene matrix. In these hybrid materials the close proximity between the two components may lead to strong synergistic interactions between the electron transport and the magnetism, which may result in new MR effects. Thus, the results show that these hierarchically structured materials exhibit a temperature-dependent crossover MR operating at low magnetic fields up to 500 G.

11.2. Results and Discussion

11.2.1. Structural Characterization

As depicted in the previous section, the sample consisted on well-dispersed highly crystalline nanoparticles of small dimension (average size *ca.* 20–50 nm) embedded into a graphene matrix, which facilitated the imaging of lattice fringes and "graphitic" coatings (**Figure 1**). A detailed observation of the nanocomposite revealed that the nanoparticles are heterogeneously distributed on the graphene, forming a series of aggregates. The distance between these aggregates can be of several nanometers on the basis of HRTEM observation. The measured 0.34 nm spacing for the carbon coating is consistent with literature values for the interlayer spacing of graphene.[360,399] As evidenced by HRTEM, highly corrugated graphene sheets surrounding the metal nanoparticles can be observed (**Figure 1B–C**). The intricate structure of the graphene matrix is related with the evolution of the previous carbon nano-onions obtained at 400 ºC.[201,399] A clear evidence of this assumption could be obtained from HRTEM images of the hybrids depicted in **Figure 1D**, in which a deployed graphene monolayer from a CNO can be clearly seen. Highly corrugated single to few-layers graphene sheets surrounding the $FeNi_3$ NPs can be observed in several areas, having good flexibility, moreover this morphology reveals how close the particles are, showing a minimum carbon coating of *ca.* 2 nm. Thereby, this chemical approach allows for obtaining a convenient system for the study of the complex magnetoresistance phenomenology, due to the presence of ferromagnetic nanoparticles embedded in a conducting carbon matrix formed by corrugated graphene.

11.2.1. Magnetic Measurements

As depicted in the previous Chapter, we have performed magnetic measurements of the $FeNi_3$–G nanocomposite at different temperatures ranging from 350 K to 2 K. A ferromagnetic behaviour is observed with no significant differences as a function of the temperature.[350] The magnetization reaches a saturation value of 122 emu·g^{-1}, in excellent agreement with the values reported for bulk permalloy.[340,400] The coercive force is *ca.* 20 G being characteristic of soft ferromagnets.[342,344,345,401] The magnetic NPs are completely saturated at fields higher than 1.5 T in all the studied temperature range.

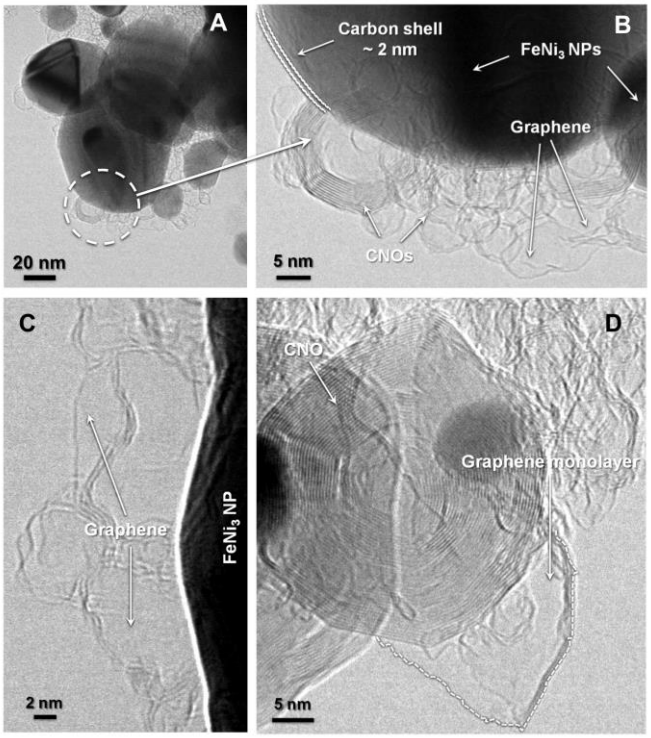

Figure 1. (A and B) High-resolution TEM micrographs of the $FeNi_3$-Graphene nanocomposite synthesized at 900 °C showing the carbon shell, the nanoparticles and the carbon nanoforms. (D) HRTEM image highlighting the morphology of the graphne surrounding the metal nanoparticles. (E) HRTEM image showing the deploy of a graphene monolayer from a carbon nano-onion.

11.2.2. Electrical Transport Measurements

The electrical conductivity is measured by a standard four-probe method in compressed pellets. **Figure 2A** shows the temperature dependent conductivity (σ) for the $FeNi_3$–G nanocomposite. Concretely, the sample has a σ of 3.09 $S \cdot cm^{-1}$ at 300 K and 0.078 $S \cdot cm^{-1}$ at 2 K, showing a decrease in the conductivity of two orders of magnitude in this temperature range. The conductivity shows a small decrease upon cooling from 300 K to *ca.* 50 K. Moreover, temperature dependent *I*–*V* measurements were taken from 300 K to 2 K for the $FeNi_3$–G nanocomposite in order to clarify its electrical behaviour (**Figure 2B**). The *I*–*V* characteristics curves show strong temperature dependence and are highly

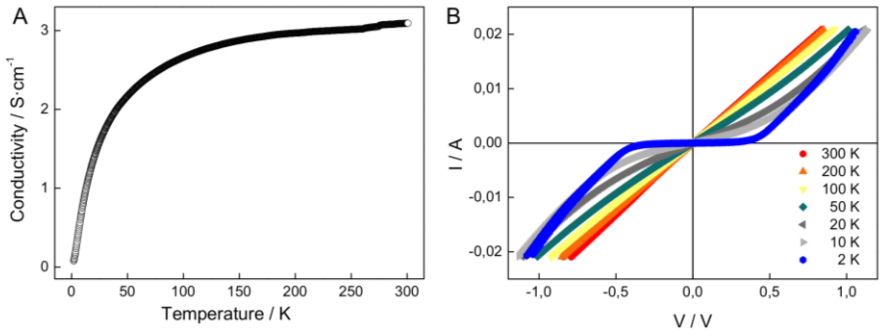

Figure 2. (A) Temperature dependence of the conductivity for the $FeNi_3$–G nanocomposite. (B) *I-V* curves for the $FeNi_3$–G nanocomposite.

symmetric. Below *ca.* 50 K, the conductivity diminishes dramatically exhibiting a thermal transition from metallic to semiconducting behaviour.[402] This abnormal behaviour is probably due to the specific hierarchical structure of the nanocomposite. At this point, is important to separatedly study both the $FeNi_3$ NPs and the carbon matrix in order to elucidate the conductivity mechanism of these nanocomposites.

11.2.3. $FeNi_3$ Nanoparticles

Firstly, we have synthesized monodisperse $FeNi_3$ nanoparticles following a sol-gel methodology described in detail in the experimental section and the **Appendix III**. The electrical transport in the temperature range 2–300 K confirms the metallic character of the NPs. The resistivity at room temperature of the $FeNi_3$ NPs is 4.24 10^{-4} Ohm·cm. In sharp contrast to $FeNi_3$–G nanocomposite, the *I–V* curves of the $FeNi_3$ NPs in **Figure 3** reaffirm their metallic behaviour in all the temperature range studied. The thermal variation of the resistivity for $FeNi_3$ NPs depicted in **Figure 3B** shows a decrease of the resistivity upon cooling down, indicative of metallic behaviour.[388] The electrical transport behaviour of ferromagnetic alloys below the Curie temperature is a result of different kinds of scattering processes such as electron–phonon, electron–magnon and electron–electron interaction.[403,404] For ferromagnetic alloys the electrical transport is dominated by magnon scattering and the temperature dependence of the resistivity can be written in the form:

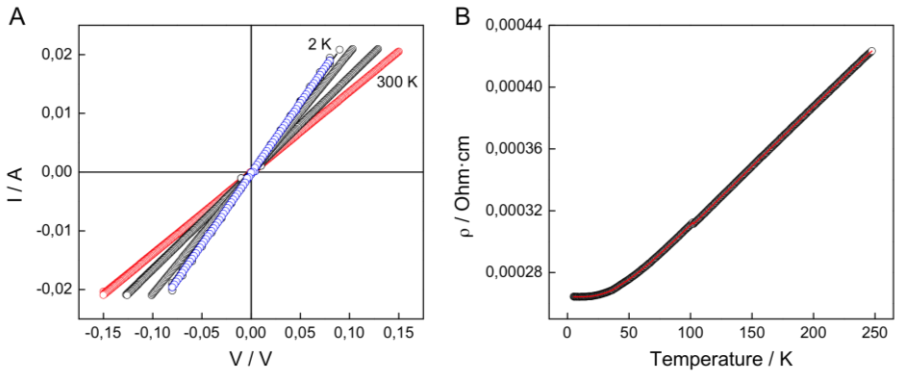

Figure 3. (A) *I–V* conductivity *vs.* voltage curves at different temperatures ranging from room temperature to 2 K. (B) The temperature dependence of resistivity obeys the behaviour predicted by Eq. (1). The symbols represent the experimental data and the solid line the fitted results.

$$\rho(T) = \rho_0 + \mathrm{A} \cdot \mathrm{T}^2 + \mathrm{B} \cdot \mathrm{T}^n \qquad \text{eq. [1]}$$

where ρ_0 is the residual resistivity due to impurities such as defects and grain boundaries, *A* is the electron-magnon scattering coefficient and *B* and *n* depend on higher order scattering mechanisms such as two magnon scattering or electron–phonon scattering. The results of the fit gives $n = 4.5$, meaning that the predominant processes in the electronic transport of the $FeNi_3$ NPs is two magnon scattering, in good accordance with the literature.[388] The *A* parameter is around 4.04 10^{-9} $\Omega{\cdot}cm{\cdot}K^{-2}$, which is high compared with the parameter for magnon scattering for bulk ferromagnetic metals like Fe, Ni or Co (of the order of 10^{-11} $\Omega{\cdot}cm{\cdot}K^{-2}$). This trend is the one expected for nanocrystalline systems with significant grain boundaries.

11.2.1. Carbon Matrix

Secondly, for comparative purposes, we have measured the electrical properties of the non-magnetic corrugated graphene matrix obtained from the acid leaching of the nanocomposite. The electrical conductivity of this blank is $1.3{\cdot}10^{-6}$ $S{\cdot}cm^{-1}$ at 300 K and *ca.* $9{\cdot}10^{-13}$ $S{\cdot}cm^{-1}$ at 2 K, exhibiting a typical semiconducting behaviour (**Figure 4**).

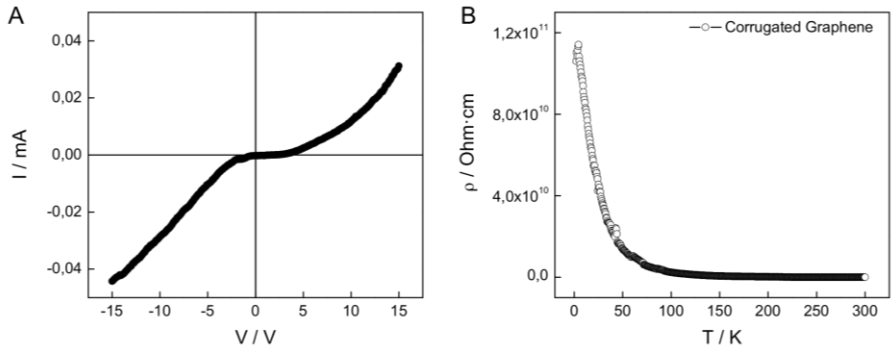

Figure 4. (A) *I-V* of the graphene matrix at 300 K, and (B) resistance *vs.* temperature.

These control experiments show that the graphene matrix surrounding the metallic nanoparticles exerts a crucial role in the electrical behaviour of the $FeNi_3$–G hybrid nanocomposites. The deviation from the metallic behaviour observed at low temperatures in the *I*–*V* curves is due to the semiconducting character of the graphene matrix.

11.2.2. Conduction Mechanisms

A good understanding of the conduction mechanisms is of crucial importance in order to elucidate the magneto-transport behaviour. Two different conduction mechanisms are directly deduced, which are strongly influenced by the temperature: (a) Ohmic region, where *I*(V) is linear with the voltage, for temperatures ranging from 300 K to below *ca.* 50 K. In this region a metallic conductance is observed. (b) Non-Ohmic region, where the *I*(V) curves have a non-linear behaviour, for temperatures lower than *ca.* 50 K. The same temperature regions are extracted for the *I-V* curves and the thermal variation of the conductivity, where the dramatic decrease in the conductivity around 50 K coincides with the appearance of a zero conductance (gap) in the low voltages area. The NPs are well described by arrays of localized electrons interacting through long-range Coulomb forces.[405] Notably, when the thermal energy is lower than the Coulomb interaction energy, electrical conduction is strongly reduced below a threshold voltage, a phenomenon known as Coulomb blockade (**Figure 5**).[405,406] In this sense, the transition to nonlinear *I*–*V* curves at low temperatures is expected when the conductance is limited by the Coulomb-

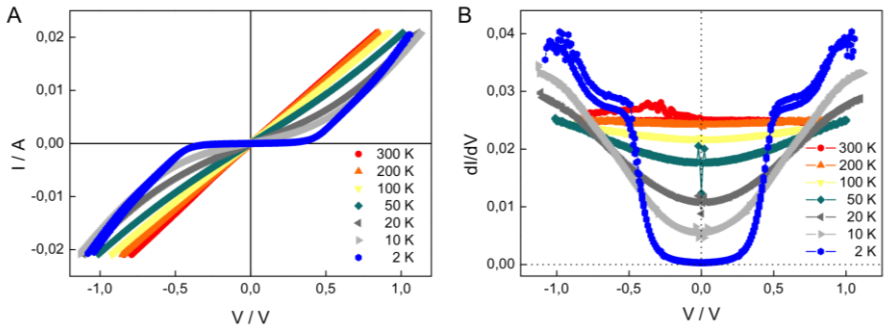

Figure 5. (A) *I-V* curves for the $FeNi_3$–G nanocomposite. (B) The corresponding calculated conductance d*I*/d*V* curves for all the studied temperature range.

blockade, as observed in **Figure 5A**. Similar transitions have been observed in nanocomposites and nanowires embedded in a carbon matrix.[404–411] In order to show the transition and Coulomb gap much more clearly, a plot of the calculated *dI*/*dV* differential conductance curves vs. V at temperatures ranging for 300 K to 2 K is represented in **Figure 5B**. The *dI*/*dV* curves have a pronounced minimum at low temperatures; the suppression of conductance around zero bias represents the Coulomb gap. The depletion of the differential conductance at low energies is widely reported and usually regarded as a signature of *e–e* interaction, in accordance with the gradual opening of a Coulomb gap at low temperatures. Above 10 K the Coulomb gap becomes filled by thermal excitations and almost vanishes at 50 K.

From a macroscopic point of view, the two different conducting regions can be described by two different conduction mechanisms: in the first region (50 < T < 300K) the conductivity follows a thermal activation mechanism given by the Arrhenius formula Eq. (2):

$$\sigma_1=\sigma_{01}\exp(-\Delta E/kT) \qquad \text{eq. [2]}$$

where σ_{01} is a constant and ΔE is the activation energy. This best fit of the data gives σ_{01}=3.33 S·cm^{-1} and ΔE=1.83 meV (**Figure 6A**). The value of Arrhenius activation energy is lower compared with other measurements on MWCNT composites,[411] in which it has been demonstrated that the activation energy is

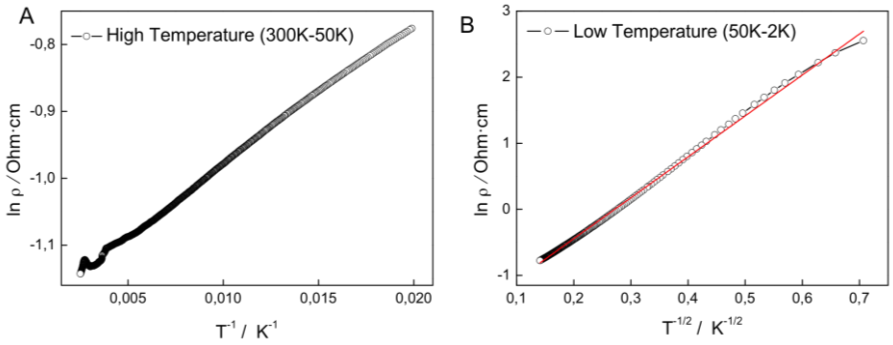

Figure 6. (A) Resistivity (logarithmic scale) as a function of $1/T$ for $FeNi_3$–G nanocomposite in the temperature range 300 K to 50 K. (B) Resistivity (logarithmic scale) as a function of $1/T^{-1/2}$ for $FeNi_3$–G nanocomposite in the temperature range between 50 K to 2 K.

reduced when the concentration of the more conducting MWCNT in the matrix is decreased. In our hybrid, the interfaces between the conductive NPs are relatively diffuse and hopping across them should not require much energy.

In the second region (2 < T < 50K) the conductivity shows a sharp decrease and the electronic transport is dominated by strong Coulomb interactions. Thus, it follows the Efros-Shklovskii Variable Range Hopping mechanism (ES-VRH) depicted in Eq. (3).[405,410]

$$\sigma_2=\sigma_{02}\exp\text{-}(T_0/T)^{1/2},\ (50\text{ to }2\text{ K}) \qquad \text{eq. [3]}$$

where T_0 is the characteristic temperature that determines the thermally activated hopping among localized states at different energies and considered as a measure of the disorder; and σ_{02} can be considered as the limiting value of conductivity in the high temperature limit. The observed linear relation between the logarithmic resistivity and the square root of temperature $T^{-1/2}$ is shown in (**Figure 6B**). The T_0= 39 K and σ_{02}= 5.4 S·cm^{-1} values obtained from the fit have been calculated from the slope and the intercept of the straight line, respectively. The temperature dependence of lnρ with $T^{-1/2}$ observed in our fitting is associated with the presence of Coulomb interactions in a low-temperature hopping process.[404,410,412,413] This charge transfer from one to other nanoparticle

through the graphene shell at very low temperatures is in good agreement with the values reported by Chauvet and co-workers for SWCNTs.[413] Once clarified the conductivity mechanisms, we have explored the electrical transport under a magnetic field.

11.2.3. Magnetotransport Measurements

Figure 7A-B shows the MR of the $FeNi_3$–G nanocomposites at temperatures of 300 K and 2 K calculated using Eq.(4):

$$MR(\%)=(R(H)-R(0))/(R(0))\cdot 100 \qquad \text{eq.[4]}$$

Where R(*0*) and R(*H*) are the resistance at zero and at an applied field *H*, respectively. We have measured MR curves several times in different samples showing a good reproducibility. The MR has been measured in the 300–2 K temperature range from pressed pellets, where the random orientation of the composite does not allow for any preferential symmetry direction.

Our sample exhibits a partial inversion of the MR as a function of the temperature. The MR reaches a negative value of *ca.* –4% at 300 K at an applied magnetic field of 40 kG, diminishing as the temperature is decreased (**Figure 7C**). When the temperature raised 50 K the MR changes from negative to positive value and starts increasing its magnitude as the temperature decreases until reach a positive value at around ~ 6 % at 2 K. Interestingly, Guo et al. have reported a series of particulate Fe/conducting-carbon hybrid materials in which they observe negative MR at room temperature and some transitions from semiconductor to conductor around 50 K for the highest NPs loadings.[412,414,415] This points to an optimal value of NPs loading in our nanocomposites. Remarkably, the MR presents a low field MR (LFMR) effect, reaching its maximum value at 2 K. The low-field effects are usually related with the presence of magnetic nanoparticles and the distances between them, which is established by the surrounding matrix. This distance is directly related with the spin-polarized tunnelling through electron barriers across the grain boundaries of nanoparticles.[416,417] In fact, Wang el al. have been reported the synthesis and characterization of core-shell structured $La_{0.7}Sr_{0.3}CoO_3$ nanoparticles, observing large LFMR at low temperatures (5 K) originated from the improvement of this

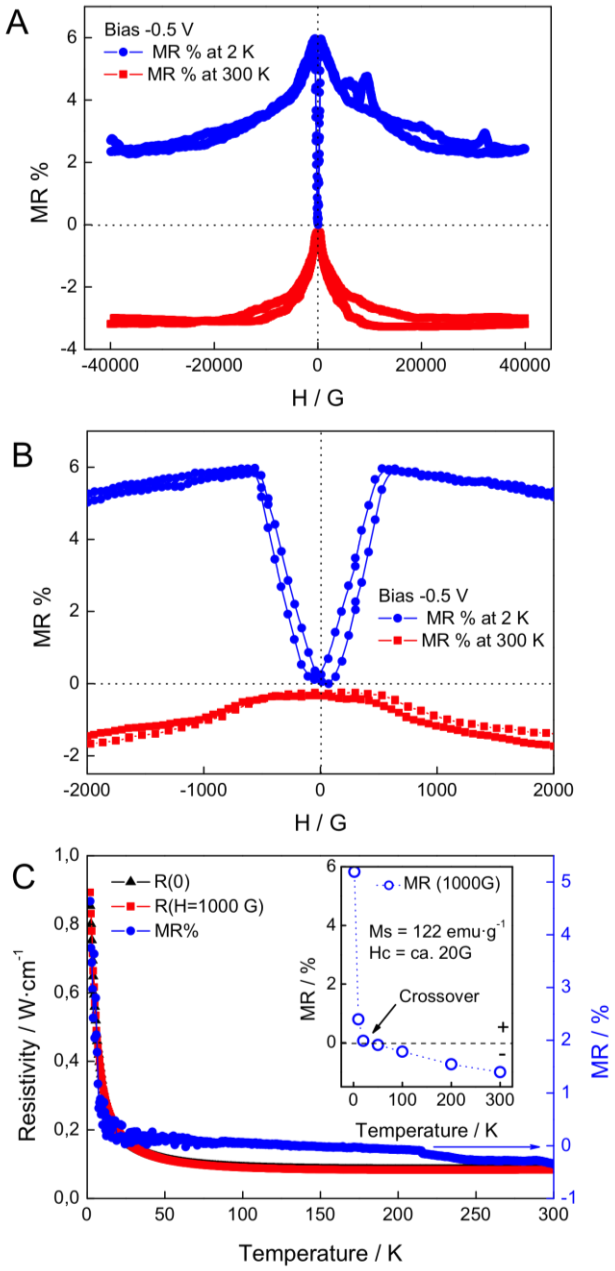

Figure 7. (A) Magnetoresistance versus applied magnetic field (H) curves measured at 2 and 300 K. (B) Zoom of the LFMR. (C) Temperature dependence of the resistivity at zero magnetic field, and with a magnetic field of 1000 G. In the inset the MR for all the temperature range is plotted.

interparticle tunneling due to the presence of noncrystalline insulating layers.[418] In our system, the interparticle tunnelling is governed by the surrounding graphene matrix, acting as an insulating layer at low temperatures.

For comparison, we have measured the MR behaviour of bare $FeNi_3$ NPs (**Figure 8**). We have observed that the nanoparticles only present MR at very low temperatures, showing the non-saturating MR behaviour characteristic for metals resulting from the ordinary MR, which is always positive and proportional to the quadratic magnetic field. At 2K a LFMR effect (that increases with the applied magnetic field up to *ca.* ± 500 G by the same way than the $FeNi_3$–G nanocomposites) could be observed, probably as a result of the improvement of spin-dependent interparticle tunneling due to the presence of insulating layer coming from the natural oxidation of the $FeNi_3$ NPs.

On the other hand, we have performed MR measurements for the graphene matrix obtained after acid leaching of the nanocomposite. It is worth to mention that the as-obtained matrix consists on a highly corrugated and defective graphene with a porous structure presenting a semiconducting behaviour, (*vide supra*). No MR has been found in all the temperature range studied —graphene is considered a non-magnetic material indeed, due to the presence of topological defects and coupling among the spins carriers, pure graphene has already been reported to show weak ferromagnetic long range ordering and MR effect—[392–394,419] the graphene MR reported in bibliography until now reveals positive values proportional to the quadratic magnetic field.[396]

This MR for the graphene is attributed mainly to the electron deviating from the electric field direction by the Lorentz force, with increasing magnetic field.[408] This is not the case for our nanocomposites, which exhibit a completely different shape, highlighting that the maximum change in the resistance happens at low magnetic fields for all the temperature range studied.

Interestingly, at low fields, the dependence of the resistance with the magnetic field for the $FeNi_3$ nanoparticles and the $FeNi_3$–G follows the same trend but the MR is six times stronger for the $FeNi_3$–G. The influence of the graphene matrix is also reflected in the saturate MR obtained at higher applied magnetic fields. Until now, this effect has not been observed in both pristine or crystalline graphene (**Figure 7C**).[393,396,397] Finally, a striking crossover from positive to negative magnetoresistance is observed for the $FeNi_3$–G

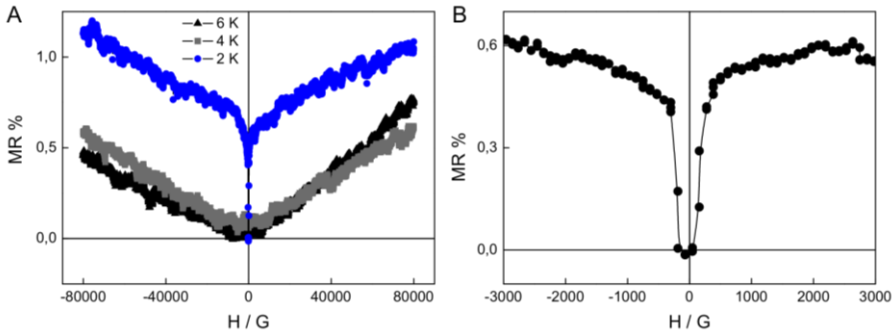

Figure 8. (A) Magnetoresistance *vs.* applied magnetic field curves measured at low temperatures of the $FeNi_3$ NPs. (B) Zoom of the LFMR for the magnetoresistance curves at 2 K.

nanocomposites. This is a clear demonstration of the optimal synergy between the NPs and the corrugated graphene.

11.2.4. Crossover Mechanism

Based on the above results, the proposed mechanism for the MR crossover can be summarized as follows:

i) *Negative MR*. For the high temperature range (from 300 K to 50 K) the resistance decreases when a magnetic field is applied (**Figure 6A**). Hopping between the localized states of the $FeNi_3$ nanoparticles, and hopping between different graphene sheets mainly govern the transport mechanism for this range. The MR measurement indicates that the surface spins of the $FeNi_3$ nanoparticles can be aligned by an external applied magnetic field, resulting in a significant reduction of the resistance. In contrast to bare polycrystalline systems (*e.g.* $Ni_{80}Fe_{20}$, Fe_3O_4, CrO_2 or Prussian Blue Analogues, among others), the incorporation of graphene appears to exert a crucial role, reducing the magnetic fields required to saturate the MR.[416,420–422]

ii) *Positive MR*. For the low temperature range (from 50 K to 2 K) the resistance increases when a magnetic field is applied (**Figure 6B**). The ES-VRH process due to the enhanced Coulomb interactions between charge carriers dominates the electronic transport of the $FeNi_3$–G nanocomposite at low temperatures. As consequence of this phenomenon, the presence of a magnetic field results in a

decrease in the hopping probability of the carriers transport, causing an increase in the resistance and finally originating positive MR.[405]

Examples describing crossover phenomena from positive to negative MR are very scarce. It has been discovered in spinels with magnetic phase transitions[423] and in G monolayers with controlled induced disorder.[424] As far as we know, this is the first example of a G-based nanocomposite showing this striking and unusual effect.

11.3. Conclusions

In conclusion, all of our data suggest that we have ferromagnetic nanoparticles embedded in a graphene matrix forming a granular nanocomposite whose matrix conductivity can be tuned with temperature, thus offering the possibility of modulate the MR behavior.

This unprecedented hierarchical structure herein obtained by a cost-effective chemical methodology exhibits GMR with temperature-dependent crossover and LFMR in a synergistic way, arising from the correlation of the physical properties of its initial constituents, *i.e.*, electrical conductivity and ferromagnetism. Our GMR granular nanocomposites can operate at room temperature and at low fields, in contrast to multilayered GMR materials, where a high magnetic field is often required to saturate the MR.[425,426] This behaviour offer an easy approach for the development of new systems, like magnetic sensors such as read head devices in computer hard disks, suggesting promising applications as GMR sensors, energy tuning devices for microelectronics and data storage devices. Moreover, as these nanocomposites have exhibited promising performances as electrochemical capacitors, a magnetic control over the charge or discharge process can be envisioned. Work is in progress aiming at developing a magneto-supercapacitive device.

11.4. Experimental Section

11.4.1. Synthesis

Materials: All chemicals, $Ni(NO_3)_2{\cdot}6H_2O$, $Fe(NO_3)_3{\cdot}9H_2O$, $HO_2C(CH_2)_8CO_2H$ (sebacic acid), $FeSO_4 \cdot 7H_2O$, $NiCl_2 \cdot 6H_2O$, $N_2H_4 \cdot H_2O$ (80%), NaOH, KOH, benzyl alcohol and ethanol (Sigma-Aldrich and Fluka) were used as received without further purification. Ultrapure water was obtained from Millipore Milli-Q equipment.

Preparation of $FeNi_3$–carbon nanocomposites: The precursor LDH material NiFe-Sebacate (NiFe–Seb) was prepared following the general method described previously by our group, using sebacic acid/NaOH. In a typical synthesis, the salts of nickel and iron were dissolved in deionized water, keeping the stoichiometric coefficient $x = M^{III} / (M^{II} + M^{III})$ at the value of $x = 0.33$, and the total metal concentration constant at 1 M. A second solution of NaOH and sebacic acid was also prepared using deionized water. Both solutions were mixed together by dropwise addition to form thick slurry with a fixed pH of 7. Subsequently, the slurry was heated up to 80 °C under constant stirring, and kept at this temperature for 4 days at atmospheric pressure. The solid was then filtered, abundantly washed with water and ethanol, and dried at room temperature under vacuum. All procedures were carried out under argon atmosphere to avoid incorporation of carbonate anions adsorbed from atmospheric CO_2 into the final precursor. Furthermore, the pH of the synthetic gel was controlled to avoid formation of solid phases different from LDH. The $FeNi_3$–G nanocomposite have been obtained by calcination under nitrogen atmosphere during 6 hours at 900 °C, focusing only in 900 °C, depending on the sample, in a programmable oven with a 1 °C·min^{-1} scan rate and nitrogen flow of 40 mL·min^{-1}. The carbon matrixes of the as-synthesized nanocomposites have been obtained by sonication and acid leaching of the same with 2M hydrochloric acid during 48 hours with magnetic stirring.

Preparation of $FeNi_3$ nanoparticles: In a typical procedure, 7.5 mmol of $FeSO_4{\cdot}7H_2O$ and 22.5 mmol of $NiCl_2{\cdot}6H_2O$ were dissolved in 50 mL of benzyl alcohol. After that, the mixture was heated up to 80 °C in a thermostatic bath. Afterwards, a NaOH 5 M solution was drop-wise added to the mixture until it reached a pH of *ca.* 11. Then, 13 mL of hydrazine hydrate was added, followed

by gas evolution, as well as the precipitation of small black particles. This reduction procedure was set for 30 min. Finally, the particles were collected by a magnet and washed with Milli-Q water and EtOH for several times, and then dried in an oven at 60 °C for 5 h. EDAX microanalysis gives a Ni:Fe ratio of 2.82(±0.06).

11.4.2. Physical Characterization

HRTEM studies of the hybrid material were carried out on a JEM-2010 microscope (JEOL, Japan) operating at 200 kV. Samples were prepared by dropping a sonicated suspension of the sample in ethanol on a carbon-coated copper grid. The digital analysis of the HRTEM micrographs was done using DigitalMicrographTM 1.80.70 for GMS 1.8.0 by Gatan. The magnetic properties of the nanocomposites at different temperatures where measured in a physical properties measurement system (PPMS-9) by Quantum Design. The susceptibility data were corrected by removing the diamagnetic contributions as deduced by using Pascal's constant tables. The temperature dependent conductivity (σ) and magnetoresistance (MR) have been measured using a standard four-probe method with Pt wire as leads in the same PPMS-9 equipment, in the temperature range between 2 K to 300 K using Keithley devices, a current source (model 2400) and an electrometer (model 6154). Electrical contacts were made with highly conducting silver paints. Samples sizes were approximately of 3 mm^2. The powders of nanocomposites were pressed into pellets for resistivity and MR measurements.

11.5. Appendix III – Synthesis and Characterization of $FeNi_3$ Nanoparticles[†]

The synthesis of the $FeNi_3$ NPs was performed at low temperature (80 °C) by using benzyl alcohol as solvent and hydrazine as reducing agent, concretely the metal salts were dissolved in benzyl alcohol and then the hydrazine was added with the consequent formation of nitrogen, indicative of the metal reduction at basic pH, as depicted in Eq. (1).[342]

$$3Ni^{2+} + Fe^{2+} + 2N_2H_4 + 8OH^- \text{ —> } FeNi_3 + 2N_2 + 8H_2O \text{ (pH = 11 ~ 13)} \quad \text{eq.[1]}$$

11.5.1. Structural Characterization

X-ray powder diffraction confirmed the formation of the NPs, **Figure 1** shows the characteristic diffraction pattern from face-centered cubic (FCC) (Joint Committee on Powder Diffraction Standards file No. 38-0419, *Pm3 m* space group, a = 3.545 Å), and no signature of the presence of either a α-Fe (*i.e.* at 2h of 65.2°), (FCC)-Ni (*i.e.* at 2h of 44.5°, 51.8° and 76.4°) or spinel impurities.[343,399] The crystallite sizes of the NPs calculated by Scherrer's equation was 13.4 nm, suggesting that the particles observed in electron microscopy were composed of small primary NPs (*vide infra*).[427] The formation of pure $FeNi_3$ phase was further confirmed by means of EDAX micro-analysis, giving values of Ni:Fe metallic composition of *ca.* 3 in perfect agreement with that expected for the nominal ratio.

The morphology of the NPs was examined by means of FESEM, which revealed spherical NPs with smooth surfaces (**Figure 2**). Low magnification images show homogeneous samples with no evidence of micrometric aggregates. The size analysis of several NPs revealed that the average particle size distribution was 206 nm.

Figure 3 shows selected HRTEM images and their corresponding selected area electron diffraction (SAED) pattern. Representative TEM images show particles with diameters comprised between 150 and 200 nm composed by

[†] Abellán, G.; Carrasco, J. A.; Coronado, E.; Prima-García, H. *J. Sol-Gel Sci. Technol.* **2014**, *70*, 292.

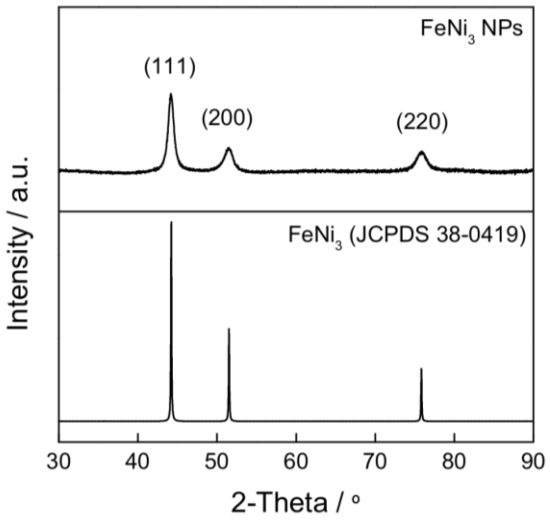

Figure 1. XRD pattern of the $FeNi_3$ nanoparticles synthesized via hydrazine reduction in benzyl alcohol. The inset represents the JCPDS data for (FCC) $FeNi_3$.

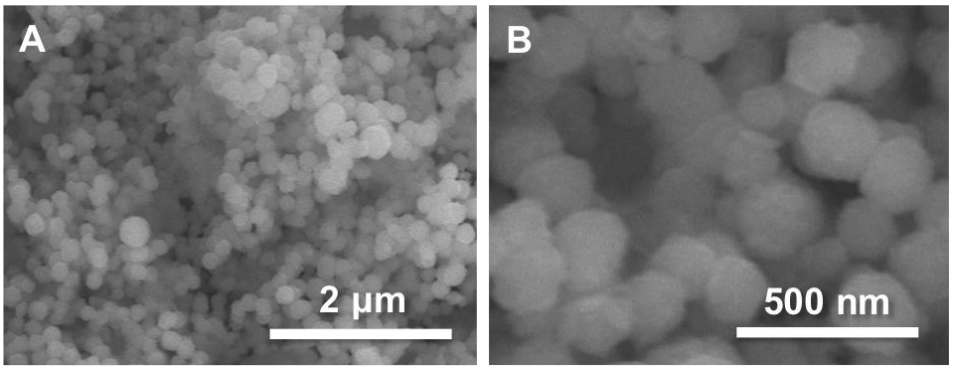

Figure 2. FESEM micrographs at different magnifications of the as-prepared $FeNi_3$ NPs.

smaller grains, in excellent agreement with XRPD and FESEM measurements. Moreover, higher magnifications revealed periodic fringe spacings of *ca.* 2.0 Å, in good accordance with interplanar spacing between (111) planes of the $FeNi_3$ phase.[201,339] The ED pattern exhibits the characteristic polycrystalline diffraction rings from (111), (200), (220), (311) and (222) planes of (FCC) $FeNi_3$, which corroborates the results of XRPD pattern.

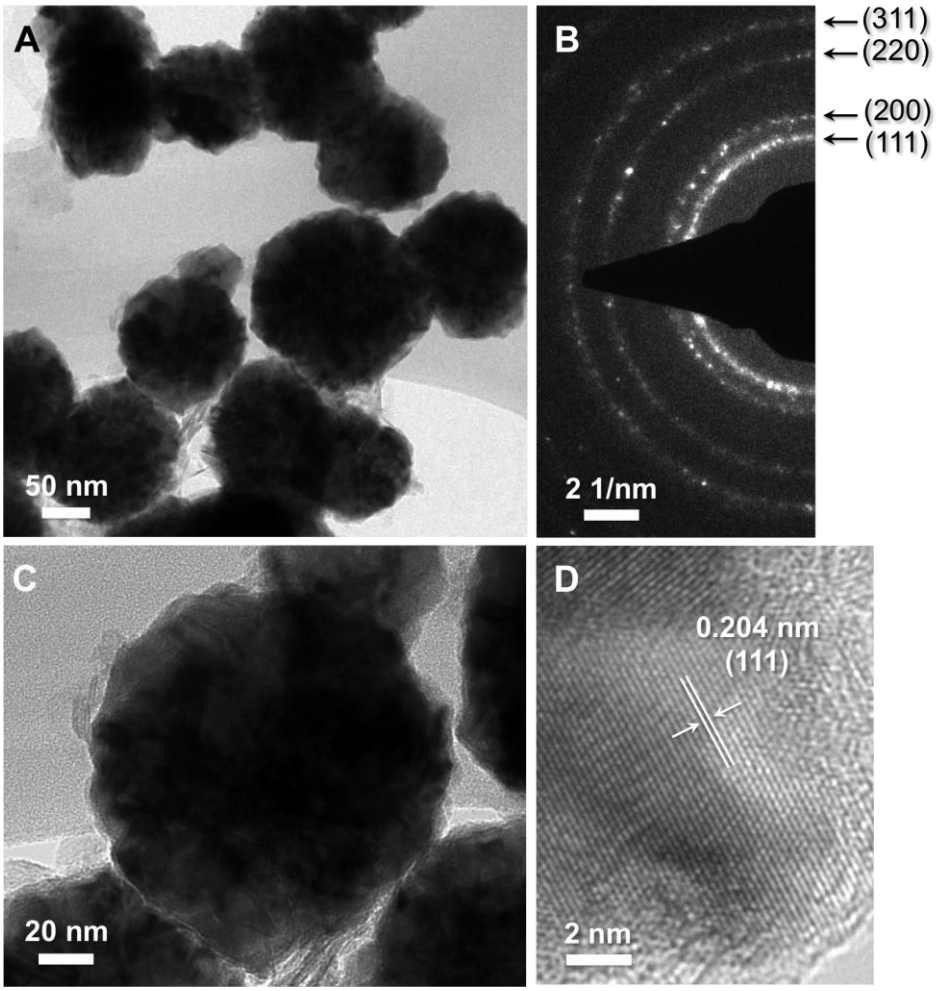

Figure 3. Typical TEM image (A) and electron diffraction pattern (B) of $FeNi_3$ NPs synthesized by hydrazine reduction in benzyl alcohol. (C) HRTEM image of a single $FeNi_3$ particle and (D) higher magnification showing the lattice spacing between two adjacent planes corresponding to the lattice spacing of (111) plane of (FCC) $FeNi_3$.

11.5.2. Magnetic Properties

Magnetic measurements performed in a superconducting quantum interference device at room temperature shows a ferromagnetic behaviour, as expected for these materials. **Figure 4** also demonstrates a strong response to an applied magnetic field, meaning that they can be rapidly separated from the solution.

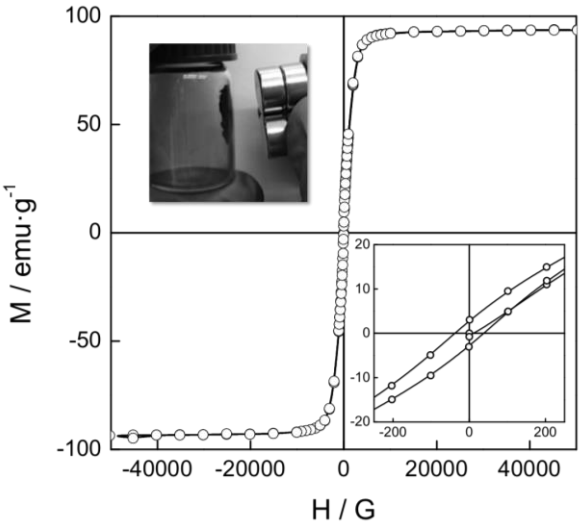

Figure 4. Magnetization versus field data for $FeNi_3$ NPs measured at 300 K. The *upper inset* shows a photograph of the sample under an external magnetic field. The *bottom inset* shows the low field region of the hysteresis cycle.

Hysteresis loops measured between -50 kG < *H* < 50 kG exhibited a saturated profile indicative of ferromagnetic interactions, with a saturation magnetization (*Ms*) of 95 emu·g^{-1}, a coercive force (*Hc*) of *ca.* 40 G and a remnant magnetization (*Mr*) of *ca.* 3 emu·g^{-1}, both indicative of soft magnetic behaviour. The large *Hc* value compared to that of the bulk $FeNi_3$ (0.5 Oe) is probably due to the large intrinsic magnetocrystalline anisotropy of ordered intermetallic compound (compared with the disordered $FeNi_3$ permalloy), internal strain, grain boundary effects and the high fraction of atoms at the NPs surface.[342,427]

Resumen

Los materiales híbridos multifuncionales constituyen una importante categoría dentro del mundo de la ciencia de materiales. En esta clase de materiales la interacción íntima entre los componentes trasciende la simple mezcla física, y por tanto, hace posible la conexión entre sus propiedades. Frente a las obras recientes, los orígenes de la ciencia de materiales híbridos se basan en algunos descubrimientos extremadamente antiguos marcados por la serendipia, que ilustran perfectamente la belleza de estos materiales. De hecho, el primer ejemplo de un material híbrido obtenido por intercalación data de aproximadamente dos mil años atrás, y se refiere a la intercalación de la caolinita (un aluminosilicato arcilloso), que explica el secreto que subyace detrás de la porcelana fina originaria de China. Por otra parte, se ha descubierto recientemente que el antiguo pigmento "Azul Maya", empleado en Mesoamérica aproximadamente desde el 300 al 1500 dC, y que exhibe una elevada resistencia química, consiste en un material nanoestructurado basado en la paligorskita (un material arcilloso microfibroso) y colorante índigo extraído de las plantas. Estas antigüedades siguen siendo una fuente de inspiración para los nuevos diseñadores de materiales híbridos.

Más recientemente, el desarrollo de procesos químicos inorgánicos suaves (también llamados "Chimie Douce") han permitido el crecimiento exponencial de la lista de materiales híbridos existente con el consiguiente desarrollo de sus aplicaciones. Durante el último siglo, las arcillas aniónicas, y más específicamente los hidróxidos dobles laminares, (layered double hydroxides LDHs) se han extendido como excelentes constituyentes para materiales híbridos funcionales, ofreciendo un escenario ideal para difuminar las fronteras entre química orgánica e inorgánica, mientras que la ciencia de materiales se erige como el último invitado a este fascinante campo de investigación.

Los LDHs son una vasta familia de arcillas aniónicas con estructura laminar equivalente a la del mineral brucita [$Mg(OH)_2$], en la que tiene lugar la sustitución parcial del metal divalente por otro trivalente, pudiendo ser formulados como $[M^{II}_{(1-x)}M^{III}_{x}(OH)_2][A^{n-}_{(x/n)}]\cdot y\ (H_2O)$, ($0.20 < x < 0.33$). Esto resulta en un exceso de carga positiva en las láminas que debe ser compensado con un anión interlaminar A^{n-} cuya naturaleza puede modularse a voluntad. Los LDHs sintéticos son materiales muy prometedores para un gran número de posibles aplicaciones debido a su bajo coste y su inusitada versatilidad química,

lo que se ve reflejado en sus propiedades fácilmente manipulables y su formidable rango de composición y variables sintéticas entre otros. Por lo tanto no es sorprendente que, *per se* o tras su descomposición térmica, susciten numerosas aplicaciones prácticas. A lo largo de los últimos años ha habido un inmenso auge en el número de publicaciones relacionadas con esas aplicaciones, siendo muchas de ellas de interés industrial.

El *leitmotiv* de la presente tesis son los LDHs magnéticos. La estructura del manuscrito se ha organizado en tres partes claramente diferenciadas. Se tratarán desde los aspectos sintéticos y físicos más básicos, hasta la preparación de materiales híbridos multifuncionales basados en LDHs, finalizando con algunas aplicaciones prácticas de interés en almacenamiento y conversión de energía y espintrónica.

La primera parte versa sobre el diseño químico, la síntesis, exfoliación y caracterización de las propiedades físicas de nuevos sistemas LDH magnéticos. El Capítulo 2 proporciona una visión en profundidad sobre la síntesis de LDHs altamente cristalinas de NiFe con morfologías hexagonales bien definidas y composición variable. La síntesis de este tipo de LDHs de NiFe ha sido esquiva durante mucho tiempo debido a la ausencia de Al como elemento constituyente de las láminas y, gracias al uso de un agente quelante adicional, la trietanolamina se han podido sintetizar satisfactoriamente controlando su composición. Adicionalmente se ha llevado a cabo por primera vez la exfoliación en formamida de estos LDHs magnéticos en nanoláminas de espesor inferior al nanómetro. Se ha desarrollado una exhaustiva caracterización de estas nanoláminas mediante microscopía de fuerza atómica, microscopía electrónica de alta resolución y espectroscopía ultravioleta-visible. El Capítulo 3 está dedicado al estudio de las propiedades físicas de estos nuevos sistemas laminares, desentrañando su comportamiento magnético que presenta magnetización espontánea en torno a 16 K y clarificando el orden catiónico de sus láminas, aspecto este último de vital importancia a la hora de esclarecer el origen del comportamiento como vidrios de espín de los LDHs. Para este fin se han empleado técnicas de espectroscopia Mössbauer además de medidas de susceptibilidad magnética dc y ac. Finalizando esta primera parte de la tesis, el Capítulo 4 aborda el profundo efecto ejercido por las impurezas extrínsecas de nanopartículas de óxidos metálicos en el comportamiento magnético de los

LDHs, expandiendo las posibilidades ofrecidas por este tipo de materiales magnéticos.

La segunda parte de la tesis explora la preparación de nuevos materiales híbridos basados en LDHs, con un énfasis especial en el control de sus propiedades magnéticas mediante estímulos externos. Estos híbridos han sido obtenidos mediante la inclusión de aniones orgánicos o metal-orgánicos en el espacio interlaminar de los LDHs. En este sentido, el Capítulo 5 se focaliza en la incorporación de ftalocianinas de Cobre en el espacio interlaminar de LDHs de ZnAl y NiAl, diamagnéticos y ferromagnéticos, respectivamente, estudiando cómo afecta la magnetización espontánea de las capas a las moléculas paramagnéticas incorporadas. Siguiendo esta dirección, el Capítulo 6 trata sobre la intercalación de otro macrociclo de gran interés: las porfirinas. Aquí se ha preparado un híbrido consistente en porfirina de cobalto intercalada en NiFe–LDH, estudiando el efecto ejercido por los LDHs. En ambos casos se observa cómo el confinamiento inducido por los LDHs evita la agregación de los macrociclos, y el campo magnético ejercido por las láminas puede ser detectado en las señales de espectroscopía de resonancia de espín electrónico.

Además también se ha explorado a lo largo de de estos capítulos el diseño, síntesis y caracterización de nuevos materiales híbridos que responden a estímulos externos, mostrando por primera vez ejemplos de conmutación reversible de las propiedades magnéticas en sistemas basados en LDHs. Abordando este objetivo, el Capítulo 7 versa sobre el control mediante luz de un material híbrido consistente en moléculas simétricas de azobenceno intercaladas en LDHs de CoAl ferromagnéticos. Estos aniones actúan como pilares de la estructura anclándose a las capas por sus dos extremos mediante grupos carboxilato. Los azobencenos presentan isomería *cis-trans* cuando son irradiados con una luz de longitud de onda apropiada; gracias a este fenómeno estos materiales híbridos exhiben un aumento reversible de la magnetización de *ca.* 27% debido a la compresión de las capas y las tensiones estructurales ejercidas por las moléculas fotoactivas. En cambio, en el Capítulo 8, se examina cómo controlar mediante la temperatura la morfología y el magnetismo de un híbrido basado en LDHs de CoAl intercalado con moléculas termocrómicas ancladas por un solo punto y un surfactante "inocente" como el dodecilsulfato de sodio. En este caso se ha observado mediante microscopía de fuerza atómica

una modificación drástica de la morfología de los cristales, debido al deslizamiento de las capas, que se ve también reflejada de forma reversible en la espectroscopia ultravioleta-visible, la fluorescencia, los rayos-X y el magnetismo del sistema.

Por último, la tercera parte de la tesis está dedicada a las aplicaciones de varios materiales basados en LDHs en diferentes campos de gran importancia, como son el almacenamiento y conversión de energía o la espintrónica. En el Capítulo 9 se han estudiado las propiedades electrocatalíticas intrínsecas de los NiFe–LDH para la oxidación de agua en condiciones básicas. También se ha estudiado el efecto de la generación *in-situ* de materiales híbridos con grafeno mediante la nucleación directa del LDH en la superficie de óxido de grafeno y su posterior reducción. La incorporación del grafeno en estos híbridos proporciona, entre otras, una propiedad complementaria a los LDHs: la conductividad, mientras que los LDHs contribuyen con una elevada actividad redox y catalítica. En este sentido, se ha explorado el comportamiento de estos híbridos como electrodos de supercapacitores y electrocatalizadores para la oxidación de agua, mostrando un comportamiento excelentes en ambos casos. El Capítulo 10 trata sobre el uso de híbridos de NiFe–LDH intercalados con moléculas con un alto contenido en carbono como nanorreactores catalíticos para la síntesis *in situ* de nuevos nanocomposites. Estos nanocomposites jerárquicos están formados por nanopartículas de $FeNi_3$ embebidas en una matriz grafitizada y pueden ser empleados como precursores para la obtención de nanoformas de carbono a baja temperatura, que van desde nanocebollas de carbono a grafeno. Además, se han probado estos nanocomposites como materiales para electrodos de supercapacitores, obteniendo altos valores de capacidad específica así como excelentes valores de densidad de energía y potencia operando a densidades de corriente elevadas.

Finalmente, se ha investigado la aplicación de estos nanocomposites de grafeno y nanopartículas magnéticas de $FeNi_3$ en el campo de la espintrónica. Concretamente el Capítulo 11 describe las propiedades de magnetotransporte de estos híbridos, que se ven marcadamente afectadas por los diferentes mecanismos de conductividad que presentan en función de la temperatura, mostrando un comportamiento sorprendente de cruce de magnetorresistencia positiva a negativa por encima de 50 K. A temperatura ambiente, estos sistemas

presentan saturación a bajos campos, ofreciendo una disminución de la resistencia. Este interesante comportamiento viene derivado de la correlación de las propiedades físicas de sus constituyentes de una forma sinérgica.

En resumen, la tesis plantea la síntesis de LDHs magnéticos mediante una aproximación novedosa que ha permitido modular la composición de los NiFe–LDHs, su exfoliación y el estudio de sus propiedades magnéticas. De este estudio se ha derivado una mejor comprensión del comportamiento de vidrio de espín que poseen los LDHs, y se ha podido determinar el origen de las impurezas magnéticas más habituales en estos sistemas. En base a estos conocimientos se han sintetizado una serie de nuevos materiales híbridos orgánico-inorgánicos, en los que se ha determinado la influencia que ejerce el magnetismo de las capas de LDH en sus moléculas huésped, así como la influencia de las moléculas intercaladas en las propiedades magnéticas de las láminas. En este sentido se han desarrollado los primeros ejemplos de modulación reversible de las propiedades magnéticas de sistemas LDH mediante estímulos externos como la luz y la temperatura respectivamente. Finalmente más allá de los estudios fundamentales y del interés básico de estos materiales, se han explorado diferentes aplicaciones que ilustran el gran potencial de los LDHs. Primero, como electrocatalizadores para la oxidación de agua, un proceso fundamental para la disociación de agua. En segundo lugar, como electrodos activos para supercapacitores, dispositivos electroquímicos de gran interés en vehículos eléctricos o dispositivos portátiles móviles, y por último, como materiales magnetorresistivos de interés en espintrónica.

References

1. Gómez-Romero, P. & Sanchez, C. *Functional Hybrid Materials.* (John Wiley & Sons, 2006).
2. Weiss, A. Organic Derivatives of Mica-type Layer-Silicates. *Angew. Chem. Int. Ed. Engl.* **2,** 134–144 (1963).
3. Ruiz-Hitzky, E., Aranda, P., Darder, M. & Rytwo, G. Hybrid materials based on clays for environmental and biomedical applications. *J. Mater. Chem.* **20,** 9306–9321 (2010).
4. Sánchez Del Río, M., Martinetto, P., Reyes-Valerio, C., Dooryhée, E. & Suárez, M. Synthesis and Acid Resistance of Maya Blue Pigment. *Archaeometry* **48,** 115–130 (2006).
5. Berke, H. The invention of blue and purple pigments in ancient times. *Chem. Soc. Rev.* **36,** 15–30 (2006).
6. Río, M. S. del *et al.* A combined synchrotron powder diffraction and vibrational study of the thermal treatment of palygorskite–indigo to produce Maya blue. *J. Mater. Sci.* **44,** 5524–5536 (2009).
7. Auerbach, S. M., Carrado, K. A. & Dutta, P. K. *Handbook of Layered Materials.* (CRC Press, 2004).
8. Cavani, F., Trifiro, F. & Vaccari, A. Hydrotalcite-type anionic clays : preparation, properties and applications. *Catal. Today* **11,** 173–301 (1991).
9. Rives, V. *Layered Double Hydroxides: Present and Future.* (Nova Publishers, 2001).
10. Forano, C., Hibino, T., Leroux, F. & Taviot-Guého, C. in *Dev. Clay Sci.* (Faïza Bergaya, B. K. G. T. and G. L.) **Volume 1,** 1021–1095 (Elsevier, 2006).
11. Duan, X. & Evans, D. G. *Layered Double Hydroxides.* (Springer, 2006).
12. Mousty, C. & Leroux, F. LDHs as Electrode Materials for Electrochemical Detection and Energy Storage: Supercapacitor, Battery and (Bio)-Sensor. *Recent Pat. Nanotechnol.* **6,** 174–192 (2012).
13. Flink, G. Bidrag till Sveriges mineralogi. *Ark. Kemi Min Geol* **3,** 1–166 (1910).
14. Feitknecht, W. Über die α-Form der Hydroxyde zweiwertiger Metalle. *Helv. Chim. Acta* **21,** 766–784 (1938).
15. Feitknecht, W. Über die Bildung von Doppelhydroxyden zwischen zwei- und dreiwertigen Metallen. *Helv. Chim. Acta* **25,** 555–569 (1942).
16. Feitknecht, W. & Gerber, M. Zur Kenntnis der Doppelhydroxyde und basischen Doppelsalze III. Über Magnesium-Aluminiumdoppelhydroxyd. *Helv. Chim. Acta* **25,** 131–137 (1942).
17. Ingram, L. & Taylor, H. F. W. The crystal structures of sjogrenite and pyroaurite. *Miner. Mag* **36,** 465–479 (1967).
18. La Iglesia, A. & Van Oosterwyck-Gastuche, M. C. To Laboratory and Field Observations. *Clays Clay Miner.* **26,** 397–408 (1978).

19. Allmann, R., Ross, G. & Kodama, H. *Discussion of Ross, GJ.* **53,** (Mineralogical Soc. Amer. 1015 Eighteenth St. Nw Suite 601, Washington, DC 20036, 1968).
20. Caillere, S. & Henin, S. New observation of faratsihite. *Compt Rend* **219,** 256 (1944).
21. Beekman, S. M. Preparation and properties of new gastric antacids I. Aluminum hydroxide-magnesium carbonate dried gels. *J. Am. Pharm. Assoc.* **49,** 191–200 (1960).
22. Soma, I., Wakano, H., Takahashi, H. & Yamaguchi, M. Flame resistant vinyl chloride resin compositions. *Jap Pat.* **50,** 047 (1975).
23. Miyata, S. & Kumura, T. Synthesis of new hydrotalcite-like compounds and their physico-chemical properties. *Chem. Lett.* 843–848 (1973).
24. Bigey, L., Depège, C., de Roy, A. & Besse, J. P. EXAFS and XANES Study of Layered Double Hydroxides. *J. Phys. IV* **7,** 949–950 (1997).
25. Roussel, H., Briois, V., Elkaim, E., de Roy, A. & Besse, J. P. Cationic Order and Structure of [Zn–Cr–Cl] and [Cu–Cr–Cl] Layered Double Hydroxides: A XRD and EXAFS Study. *J. Phys. Chem. B* **104,** 5915–5923 (2000).
26. Bellotto, M. *et al.* A Reexamination of Hydrotalcite Crystal Chemistry. *J. Phys. Chem.* **100,** 8527–8534 (1996).
27. Wang, Q. & O'Hare, D. Recent Advances in the Synthesis and Application of Layered Double Hydroxide (LDH) Nanosheets. *Chem. Rev.* **112,** 4124–4155 (2012).
28. Rives, V. & Angeles Ulibarri, M. Layered double hydroxides (LDH) intercalated with metal coordination compounds and oxometalates. *Coord. Chem. Rev.* **181,** 61–120 (1999).
29. Omwoma, S., Chen, W., Tsunashima, R. & Song, Y.-F. Recent advances on polyoxometalates intercalated layered double hydroxides: From synthetic approaches to functional material applications. *Coord. Chem. Rev.* **258–259,** 58–71 (2014).
30. Sideris, P. J., Nielsen, U. G., Gan, Z. & Grey, C. P. Mg/Al Ordering in Layered Double Hydroxides Revealed by Multinuclear NMR Spectroscopy. *Science* **321,** 113–117 (2008).
31. Cadars, S. *et al.* Identification and Quantification of Defects in the Cation Ordering in Mg/Al Layered Double Hydroxides. *Chem. Mater.* **23,** 2821–2831 (2011).
32. Sideris, P. J., Blanc, F., Gan, Z. & Grey, C. P. Identification of Cation Clustering in Mg–Al Layered Double Hydroxides Using Multinuclear Solid State Nuclear Magnetic Resonance Spectroscopy. *Chem. Mater.* **24,** 2449–2461 (2012).

33. Del Arco, M., Malet, P., Trujillano, R. & Rives, V. Synthesis and Characterization of Hydrotalcites Containing Ni(II) and Fe(III) and Their Calcination Products. *Chem. Mater.* **11,** 624–633 (1999).
34. Solin, S. A., Hines, D., Yun, S. K., Pinnavaia, T. J. & Thorpe, M. F. Layer rigidity in 2D disordered NiAl layer double hydroxides. *J. Non-Cryst. Solids* **182,** 212–220 (1995).
35. Thyveetil, M.-A., Coveney, P. V., Suter, J. L. & Greenwell, H. C. Emergence of Undulations and Determination of Materials Properties in Large-Scale Molecular Dynamics Simulation of Layered Double Hydroxides. *Chem. Mater.* **19,** 5510–5523 (2007).
36. Li, B., He, J. & Evans, D. G. Experimental investigation of sheet flexibility of layered double hydroxides: One-pot morphosynthesis of inorganic intercalates. *Chem. Eng. J.* **144,** 124–137 (2008).
37. Park, T.-R., Park, T. Y., Kim, H. & Min, P. High pressure measurement of the uniaxial stress of host layers on intercalants and staging transformation of intercalation compounds. *J. Phys. Condens. Matter* **14,** 11687–11700 (2002).
38. Miyata, S. Hydrotalcites in relation to composition. *Clays Clay Min.* **28,** 50–56 (1980).
39. Zhao, Y., Li, F., Zhang, R., Evans, D. G. & Duan, X. Preparation of Layered Double-Hydroxide Nanomaterials with a Uniform Crystallite Size Using a New Method Involving Separate Nucleation and Aging Steps. *Chem. Mater.* **14,** 4286–4291 (2002).
40. Millange, F., Walton, R. I. & O'Hare, D. Time-resolved in situ X-ray diffraction study of the liquid-phase reconstruction of Mg–Al–carbonate hydrotalcite-like compounds. *J. Mater. Chem.* **10,** 1713–1720 (2000).
41. Prinetto, F., Ghiotti, G., Graffin, P. & Tichit, D. Synthesis and characterization of sol–gel Mg/Al and Ni/Al layered double hydroxides and comparison with co-precipitated samples. *Microporous Mesoporous Mater.* **39,** 229–247 (2000).
42. Prince, J., Montoya, A., Ferrat, G. & Valente, J. S. Proposed General Sol–Gel Method to Prepare Multimetallic Layered Double Hydroxides: Synthesis, Characterization, and Envisaged Application. *Chem. Mater.* **21,** 5826–5835 (2009).
43. Yamaguchi, N., Ando, D., Tadanaga, K. & Tatsumisago, M. Direct Formation of Mg–Al-Layered Double-Hydroxide Films on Glass Substrate by the Sol–Gel Method With Hot Water Treatment. *J. Am. Ceram. Soc.* **90,** 1940–1942 (2007).
44. Gardner, E., Huntoon, K. M. & Pinnavaia, T. J. Direct Synthesis of Alkoxide-Intercalated Derivatives of Hydrocalcite-like Layered Double Hydroxides: Precursors for the Formation of Colloidal Layered Double Hydroxide Suspensions and Transparent Thin Films. *Adv. Mater.* **13,** 1263–1266 (2001).

45. Costantino, U., Marmottini, F., Nocchetti, M. & Vivani, R. New Synthetic Routes to Hydrotalcite-Like Compounds – Characterisation and Properties of the Obtained Materials. *Eur. J. Inorg. Chem.* **1998,** 1439–1446 (1998).
46. Ogawa, M. & Kaiho, H. Homogeneous Precipitation of Uniform Hydrotalcite Particles. *Langmuir* **18,** 4240–4242 (2002).
47. Adachi-Pagano, M., Forano, C. & Besse, J.-P. Synthesis of Al-rich hydrotalcite-like compounds by using the urea hydrolysis reaction—control of size and morphology. *J. Mater. Chem.* **13,** 1988–1993 (2003).
48. Iyi, N., Matsumoto, T., Kaneko, Y. & Kitamura, K. A Novel Synthetic Route to Layered Double Hydroxides Using Hexamethylenetetramine. *Chem. Lett.* **33,** 1122–1123 (2004).
49. Liu, Z. *et al.* Synthesis, Anion Exchange, and Delamination of Co–Al Layered Double Hydroxide: Assembly of the Exfoliated Nanosheet/Polyanion Composite Films and Magneto-Optical Studies. *J. Am. Chem. Soc.* **128,** 4872–4880 (2006).
50. Kayano, M. & Ogawa, M. Preparation of Large Platy Particles of Co-Al Layered Double Hydroxides. *Clays Clay Miner.* **54,** 382–389 (2006).
51. Okamoto, K., Iyi, N. & Sasaki, T. Factors affecting the crystal size of the MgAl-LDH (layered double hydroxide) prepared by using ammonia-releasing reagents. *Appl. Clay Sci.* **37,** 23–31 (2007).
52. Liang, J. *et al.* Topochemical Synthesis, Anion Exchange, and Exfoliation of Co–Ni Layered Double Hydroxides: A Route to Positively Charged Co–Ni Hydroxide Nanosheets with Tunable Composition. *Chem. Mater.* **22,** 371–378 (2010).
53. Ma, R., Liang, J., Takada, K. & Sasaki, T. Topochemical Synthesis of Co–Fe Layered Double Hydroxides at Varied Fe/Co Ratios: Unique Intercalation of Triiodide and Its Profound Effect. *J. Am. Chem. Soc.* **133,** 613–620 (2011).
54. Ma, R. & Sasaki, T. Nanosheets of Oxides and Hydroxides: Ultimate 2D Charge-Bearing Functional Crystallites. *Adv. Mater.* **22,** 5082–5104 (2010).
55. Miyata, S. Anion exchange capacity of hydrotalcite like compounds. *Clays Clay Min.* **31,** 311–319 (1983).
56. Miyata, S. Properties and adsorption characteristics of hydrotalcites. *Gypsum Lime* **187,** 333–339 (1983).
57. Miyata, S. Anion-exchange properties of hydrotalcite-like compounds. *Clays Clay Min.* **31,** 305–311 (1983).
58. Lei, L., Millange, F., Walton, R. I. & O'Hare, D. Efficient separation of pyridinedicarboxylates by preferential anion exchange intercalation in $[LiAl_2(OH)_6]Cl{\cdot}H_2O$. *J. Mater. Chem.* **10,** 1881–1886 (2000).

59. Ogawa, M. & Hiramine, M. Direct Correlation between Nanostructure and Particle Morphology during Intercalation. *Cryst. Growth Des.* (2014). doi:10.1021/cg401684u
60. Jacobson, A. J. Colloidal Dispersions of Compounds with Layer and Chain Structures. *Mater. Sci. Forum* **152-153,** 1–12 (1994).
61. Sasaki, T., Watanabe, M., Hashizume, H., Yamada, H. & Nakazawa, H. Macromolecule-like Aspects for a Colloidal Suspension of an Exfoliated Titanate. Pairwise Association of Nanosheets and Dynamic Reassembling Process Initiated from It. *J. Am. Chem. Soc.* **118,** 8329–8335 (1996).
62. Sasaki, T. & Watanabe, M. Semiconductor Nanosheet Crystallites of Quasi-TiO2 and Their Optical Properties. *J. Phys. Chem. B* **101,** 10159–10161 (1997).
63. Schaak, R. E. & Mallouk, T. E. Self-assembly of Tiled Perovskite Monolayer and Multilayer Thin Films. *Chem. Mater.* **12,** 2513–2516 (2000).
64. Mas-Ballesté, R., Gómez-Navarro, C., Gómez-Herrero, J. & Zamora, F. 2D materials: to graphene and beyond. *Nanoscale* **3,** 20–30 (2011).
65. Geim, A. K. & Novoselov, K. S. The rise of graphene. *Nat. Mater.* **6,** 183–191 (2007).
66. Wang, Q. H., Kalantar-Zadeh, K., Kis, A., Coleman, J. N. & Strano, M. S. Electronics and optoelectronics of two-dimensional transition metal dichalcogenides. *Nat. Nanotechnol.* **7,** 699–712 (2012).
67. Clearfield, A. Layered Phosphates, Phosphites and Phosphonates of Groups 4 and 14 Metals. *Comments Inorg. Chem.* **10,** 89–128 (1990).
68. Han, Y.-S., Park, I. & Choy, J.-H. Exfoliation of layered perovskite, KCa2Nb3O10, into colloidal nanosheets by a novel chemical process. *J. Mater. Chem.* **11,** 1277–1282 (2001).
69. Clemente-León, M., Coronado, E., Martí-Gastaldo, C. & Romero, F. M. Multifunctionality in hybrid magnetic materials based on bimetallic oxalate complexes. *Chem. Soc. Rev.* **40,** 473–497 (2011).
70. Gómez-Romero, P. & Sanchez, C. Hybrid materials. Functional properties. From Maya Blue to 21st century materials. *New J. Chem.* **29,** 57–58 (2005).
71. Bonnet, S. *et al.* Synthesis of Hybrid Organo–Mineral Materials: Anionic Tetraphenylporphyrins in Layered Double Hydroxides. *Chem. Mater.* **8,** 1962–1968 (1996).
72. Laget, V., Hornick, C., Rabu, P. & Drillon, M. Hybrid organic-inorganic layered compounds prepared by anion exchange reaction: correlation between structure and magnetic properties. *J. Mater. Chem.* **9,** 169–174 (1999).
73. Leroux, F. & Taviot-Guého, C. Fine tuning between organic and inorganic host structure: new trends in layered double hydroxide hybrid assemblies. *J. Mater. Chem.* **15,** 3628–3642 (2005).

74. Rogez, G., Massobrio, C., Rabu, P. & Drillon, M. Layered hydroxide hybrid nanostructures: a route to multifunctionality. *Chem. Soc. Rev.* **40,** 1031–1058 (2011).
75. Sasaki, T. & Watanabe, M. Osmotic Swelling to Exfoliation. Exceptionally High Degrees of Hydration of a Layered Titanate. *J. Am. Chem. Soc.* **120,** 4682–4689 (1998).
76. Malikova, N. *et al.* Diffusion of water in clays – microscopic simulation and neutron scattering. *Chem. Phys.* **317,** 226–235 (2005).
77. Bordallo, H. N. *et al.* Quasi-Elastic Neutron Scattering Studies on Clay Interlayer-Space Highlighting the Effect of the Cation in Confined Water Dynamics. *J. Phys. Chem. C* **112,** 13982–13991 (2008).
78. Ishihara, S. *et al.* Hydrogen-bond-driven 'homogeneous intercalation' for rapid, reversible, and ultra-precise actuation of layered clay nanosheets. *Chem. Commun.* **49,** 3631–3633 (2013).
79. Li, W. *et al.* Recent Advances in Stimuli-Responsive Photofunctional Materials Based on Accommodation of Chromophore into Layered Double Hydroxide Nanogallery. *J. Nanomater.* **2013,** (2013).
80. Costa, F. R., Saphiannikova, M., Wagenknecht, U. & Heinrich, G. in *Wax Cryst. Control · Nanocomposites · Stimuli-Responsive Polym.* 101–168 (Springer Berlin Heidelberg, 2008).
81. Yan, D., Lu, J., Wei, M., Evans, D. G. & Duan, X. Recent advances in photofunctional guest/layered double hydroxide host composite systems and their applications: experimental and theoretical perspectives. *J. Mater. Chem.* **21,** 13128–13139 (2011).
82. Zhao, M.-Q., Zhang, Q., Huang, J.-Q. & Wei, F. Hierarchical Nanocomposites Derived from Nanocarbons and Layered Double Hydroxides - Properties, Synthesis, and Applications. *Adv. Funct. Mater.* **22,** 675–694 (2012).
83. Delgado, J. L., Herranz, M. & Martín, N. The nano-forms of carbon. *J. Mater. Chem.* **18,** 1417–1426 (2008).
84. Hirsch, A. The era of carbon allotropes. *Nat. Mater.* **9,** 868–871 (2010).
85. Tseng, W.-Y. *et al.* Incorporation of C60 in Layered Double Hydroxide. *J. Am. Chem. Soc.* **118,** 4411–4418 (1996).
86. Costache, M. C., Wang, D., Heidecker, M. J., Manias, E. & Wilkie, C. A. The thermal degradation of poly(methyl methacrylate) nanocomposites with montmorillonite, layered double hydroxides and carbon nanotubes. *Polym. Adv. Technol.* **17,** 272–280 (2006).
87. Li, H., Zhu, G., Liu, Z.-H., Yang, Z. & Wang, Z. Fabrication of a hybrid graphene/layered double hydroxide material. *Carbon* **48,** 4391–4396 (2010).

88. Malak-Polaczyk, A., Vix-Guterl, C. & Frackowiak, E. Carbon/Layered Double Hydroxide (LDH) Composites for Supercapacitor Application. *Energy Fuels* **24,** 3346–3351 (2010).
89. Choy, J.-H., Choi, S.-J., Oh, J.-M. & Park, T. Clay minerals and layered double hydroxides for novel biological applications. *Appl. Clay Sci.* **36,** 122–132 (2007).
90. Choi, S.-J. & Choy, J.-H. Layered double hydroxide nanoparticles as target-specific delivery carriers: uptake mechanism and toxicity. *Nanomed.* **6,** 803–814 (2011).
91. Xu, Z. P., Zhang, J., Adebajo, M. O., Zhang, H. & Zhou, C. Catalytic applications of layered double hydroxides and derivatives. *Appl. Clay Sci.* **53,** 139–150 (2011).
92. Selvam, T., Inayat, A. & Schwieger, W. Reactivity and applications of layered silicates and layered double hydroxides. *Dalton Trans.* (2014). doi:10.1039/c4dt00573b
93. He, S., An, Z., Wei, M., Evans, D. G. & Duan, X. Layered double hydroxide-based catalysts: nanostructure design and catalytic performance. *Chem. Commun.* **49,** 5912–5920 (2013).
94. Corma, A., Palomares, A. E. & Rey, F. Optimization of SOx additives of FCC catalysts based on MgO-Al_2O_3 mixed oxides produced from hydrotalcites. *Appl. Catal. B Environ.* **4,** 29–43 (1994).
95. Corma, A., Palomares, A. E., Rey, F. & Márquez, F. Simultaneous Catalytic Removal of SO_x and NO_x with Hydrotalcite-Derived Mixed Oxides Containing Copper, and Their Possibilities to Be Used in FCC Units. *J. Catal.* **170,** 140–149 (1997).
96. Palomares, A. E., López-Nieto, J. M., Lázaro, F. J., López, A. & Corma, A. Reactivity in the removal of SO_2 and NO_x on Co/Mg/Al mixed oxides derived from hydrotalcites. *Appl. Catal. B Environ.* **20,** 257–266 (1999).
97. Palomares, A. E., Uzcátegui, A. & Corma, A. NO_x storage/reduction catalysts based in cobalt/copper hydrotalcites. *Catal. Today* **137,** 261–266 (2008).
98. Choy, J.-H., Kwak, S.-Y., Park, J.-S., Jeong, Y.-J. & Portier, J. Intercalative Nanohybrids of Nucleoside Monophosphates and DNA in Layered Metal Hydroxide. *J. Am. Chem. Soc.* **121,** 1399–1400 (1999).
99. Li, F., Liu, J., Evans, D. G. & Duan, X. Stoichiometric Synthesis of Pure MFe_2O_4 (M = Mg, Co, and Ni) Spinel Ferrites from Tailored Layered Double Hydroxide (Hydrotalcite-Like) Precursors. *Chem. Mater.* **16,** 1597–1602 (2004).
100. Leroux, F. & Besse, J.-P. Polymer Interleaved Layered Double Hydroxide: A New Emerging Class of Nanocomposites. *Chem. Mater.* **13,** 3507–3515 (2001).
101. Wang, X. *et al.* Self-assembly of Ni–Fe layered double hydroxide/graphene hybrids for reducing fire hazard in epoxy composites. *J. Mater. Chem. A* **1,** 4383–4390 (2013).

102. Aricò, A. S., Bruce, P., Scrosati, B., Tarascon, J.-M. & van Schalkwijk, W. Nanostructured materials for advanced energy conversion and storage devices. *Nat. Mater.* **4,** 366–377 (2005).
103. Wang, H. & Dai, H. Strongly coupled inorganic–nano-carbon hybrid materials for energy storage. *Chem. Soc. Rev.* **42,** 3088–3113 (2013).
104. Armand, M. & Tarascon, J.-M. Building better batteries. *Nature* **451,** 652–657 (2008).
105. Li, M. *et al.* Well-dispersed bi-component-active CoO/$CoFe_2O_4$ nanocomposites with tunable performances as anode materials for lithium-ion batteries. *Chem. Commun.* **48,** 410–412 (2012).
106. Latorre-Sanchez, M. *et al.* The synthesis of a hybrid graphene–nickel/manganese mixed oxide and its performance in lithium-ion batteries. *Carbon* **50,** 518–525 (2012).
107. Wang, G., Zhang, L. & Zhang, J. A review of electrode materials for electrochemical supercapacitors. *Chem. Soc. Rev.* **41,** 797–828 (2012).
108. Béguin, F., Presser, V., Balducci, A. & Frackowiak, E. Carbons and Electrolytes for Advanced Supercapacitors. *Adv. Mater.* **26,** 2219–2251 (2014).
109. Hu, Z.-A. *et al.* Synthesis and electrochemical characterization of mesoporous Co_xNi_{1-x} layered double hydroxides as electrode materials for supercapacitors. *Electrochimica Acta* **54,** 2737–2741 (2009).
110. Gao, Z. *et al.* Graphene Nanosheet/Ni^{2+}/Al^{3+} Layered Double-Hydroxide Composite as a Novel Electrode for a Supercapacitor. *Chem. Mater.* **23,** 3509–3516 (2011).
111. Zhang, L. *et al.* Enhanced high-current capacitive behavior of graphene/CoAl-layered double hydroxide composites as electrode material for supercapacitors. *J. Power Sources* **199,** 395–401 (2012).
112. Zhao, J. *et al.* Hierarchical NiMn Layered Double Hydroxide/Carbon Nanotubes Architecture with Superb Energy Density for Flexible Supercapacitors. *Adv. Funct. Mater.* (2014). doi:10.1002/adfm.201303638
113. Liang, Y., Li, Y., Wang, H. & Dai, H. Strongly Coupled Inorganic/Nanocarbon Hybrid Materials for Advanced Electrocatalysis. *J. Am. Chem. Soc.* **135,** 2013–2036 (2013).
114. Wang, H. *et al.* An ultrafast nickel–iron battery from strongly coupled inorganic nanoparticle/nanocarbon hybrid materials. *Nat. Commun.* **3,** 917 (2012).
115. Zou, X., Goswami, A. & Asefa, T. Efficient Noble Metal-Free (Electro)Catalysis of Water and Alcohol Oxidations by Zinc–Cobalt Layered Double Hydroxide. *J. Am. Chem. Soc.* **135,** 17242–17245 (2013).
116. Gong, M. *et al.* An Advanced Ni–Fe Layered Double Hydroxide Electrocatalyst for Water Oxidation. *J. Am. Chem. Soc.* **135,** 8452–8455 (2013).

117. Gong, M. *et al.* Ultrafast High-Capacity NiZn Battery with NiAlCo Layered Double Hydroxide. *Energy Environ. Sci.* (2014). doi:10.1039/C4EE00317A
118. Ballester, G., Coronado, E., Giménez-Saiz, C. & Romero, F. M. Nitroxide Radicals as Templating Agents in the Synthesis of Magnets Based on Three-Dimensional Oxalato-Bridged Heterodimetallic Networks. *Angew. Chem. Int. Ed.* **40,** 792–795 (2001).
119. Coronado, E., Gómez-García, C. J., Nuez, A., Romero, F. M. & Waerenborgh, J. C. Synthesis, Chirality, and Magnetic Properties of Bimetallic Cyanide-Bridged Two-Dimensional Ferromagnets. *Chem. Mater.* **18,** 2670–2681 (2006).
120. Coronado, E., Martí-Gastaldo, C., Navarro-Moratalla, E., Ribera, A. & Galán-Mascarós, J. R. Intercalation of two-dimensional oxalate-bridged molecule-based magnets into layered double hydroxide hosts. *J. Mater. Chem.* **20,** 9476–9483 (2010).
121. Pérez-Ramírez, J., Ribera, A., Kapteijn, F., Coronado, E. & Gómez-García, C. J. Magnetic properties of Co-Al, Ni-Al, and Mg-Al hydrotalcites and the oxides formed upon their thermal decomposition. *J. Mater. Chem.* **12,** 2370–2375 (2002).
122. Coronado, E. *et al.* Spontaneous Magnetization in Ni–Al and Ni–Fe Layered Double Hydroxides. *Inorg. Chem.* **47,** 9103–9110 (2008).
123. Almansa, J. J., Coronado, E., Martí-Gastaldo, C. & Ribera, A. Magnetic Properties of $Ni^{II}Cr^{III}$ Layered Double Hydroxide Materials. *Eur. J. Inorg. Chem.* **2008,** 5642–5648 (2008).
124. Coronado, E. *et al.* Coexistence of superconductivity and magnetism by chemical design. *Nat. Chem.* **2,** 1031–1036 (2010).
125. Kahn, O. *Molecular magnetism.* (VCH Publishers, 1993).
126. Rabu, P. & Drillon, M. Layered Organic–Inorganic Materials: A Way towards Controllable Magnetism. *Adv. Eng. Mater.* **5,** 189–210 (2003).
127. Coey, J. M. D. *Magnetism and Magnetic Materials.* (Cambridge University Press, 2010).
128. Delahaye, É. *et al.* New layered organic-inorganic magnets incorporating azo dyes. *J. Mater. Chem.* **19,** 6106–6115 (2009).
129. Abe, R. *et al.* Preparation of Porous Niobium Oxides by Soft-Chemical Process and Their Photocatalytic Activity. *Chem. Mater.* **9,** 2179–2184 (1997).
130. Sasaki, T. *et al.* Layer-by-Layer Assembly of Titania Nanosheet/Polycation Composite Films. *Chem. Mater.* **13,** 4661–4667 (2001).
131. He, J. X., Kobayashi, K., Takahashi, M., Villemure, G. & Yamagishi, A. Preparation of hybrid films of an anionic Ru(II) cyanide polypyridyl complex with layered double hydroxides by the Langmuir–Blodgett method and their use as electrode modifiers. *Thin Solid Films* **397,** 255–265 (2001).

132. Kaschak, D. M. *et al.* Photoinduced Energy and Electron Transfer Reactions in Lamellar Polyanion/Polycation Thin Films: Toward an Inorganic 'Leaf'. *J. Am. Chem. Soc.* **121,** 3435–3445 (1999).
133. Osada, M. *et al.* High-κ Dielectric Nanofilms Fabricated from Titania Nanosheets. *Adv. Mater.* **18,** 1023–1027 (2006).
134. Li, L., Ma, R., Ebina, Y., Iyi, N. & Sasaki, T. Positively Charged Nanosheets Derived via Total Delamination of Layered Double Hydroxides. *Chem. Mater.* **17,** 4386–4391 (2005).
135. Ma, R., Liu, Z., Li, L., Iyi, N. & Sasaki, T. Exfoliating layered double hydroxides in formamide: a method to obtain positively charged nanosheets. *J. Mater. Chem.* **16,** 3809–3813 (2006).
136. Li, L. *et al.* Layer-by-Layer Assembly and Spontaneous Flocculation of Oppositely Charged Oxide and Hydroxide Nanosheets into Inorganic Sandwich Layered Materials. *J. Am. Chem. Soc.* **129,** 8000–8007 (2007).
137. Ma, R. *et al.* Synthesis and Exfoliation of Co^{2+}–Fe^{3+} Layered Double Hydroxides: An Innovative Topochemical Approach. *J. Am. Chem. Soc.* **129,** 5257–5263 (2007).
138. Han, Y. *et al.* Preparation of Ni^{2+}–Fe^{3+} Layered Double Hydroxide Material with High Crystallinity and Well-Defined Hexagonal Shapes. *Chem. Mater.* **20,** 360–363 (2008).
139. Kagunya, W., Hassan, Z. & Jones, W. Catalytic Properties of Layered Double Hydroxides and Their Calcined Derivatives. *Inorg. Chem.* **35,** 5970–5974 (1996).
140. Refait, P., Abdelmoula, M., Simon, L. & Génin, J.-M. R. Mechanisms of formation and transformation of Ni–Fe layered double hydroxides in and containing aqueous solutions. *J. Phys. Chem. Solids* **66,** 911–917 (2005).
141. Tian, Y., Wang, G., Li, F. & Evans, D. G. Synthesis and thermo-optical stability of o-methyl red-intercalated Ni–Fe layered double hydroxide material. *Mater. Lett.* **61,** 1662–1666 (2007).
142. Nakahira, A., Kubo, T. & Murase, H. Synthesis of LDH-Type Clay Substituted With Fe and Ni Ion for Arsenic Removal and Its Application to Magnetic Separation. *IEEE Trans. Magn.* **43,** 2442–2444 (2007).
143. Iyi, N., Matsumoto, T., Kaneko, Y. & Kitamura, K. Deintercalation of Carbonate Ions from a Hydrotalcite-Like Compound: Enhanced Decarbonation Using Acid–Salt Mixed Solution. *Chem. Mater.* **16,** 2926–2932 (2004).
144. Abellán, G., Coronado, E., Martí-Gastaldo, C., Pinilla-Cienfuegos, E. & Ribera, A. Hexagonal nanosheets from the exfoliation of Ni^{2+}-Fe^{3+} LDHs: a route towards layered multifunctional materials. *J. Mater. Chem.* **20,** 7451–7455 (2010).
145. Cabrera, S. *et al.* Generalised syntheses of ordered mesoporous oxides: the atrane route. *Solid State Sci.* **2,** 405–420 (2000).

146. Bellezza, F., Nocchetti, M., Posati, T., Giovagnoli, S. & Cipiciani, A. Synthesis of colloidal dispersions of NiAl, ZnAl, NiCr, ZnCr, NiFe, and MgFe hydrotalcite-like nanoparticles. *J. Colloid Interface Sci.* **376,** 20–27 (2012).
147. Wu, Q. *et al.* Characterization of exfoliated layered double hydroxide (LDH, Mg/Al = 3) nanosheets at high concentrations in formamide. *J. Mater. Chem.* **17,** 965 (2007).
148. Hu, G., Wang, N., O'Hare, D. & Davis, J. One-step synthesis and AFM imaging of hydrophobic LDH monolayers. *Chem. Commun.* 287–289 (2006).
149. Ida, S., Shiga, D., Koinuma, M. & Matsumoto, Y. Synthesis of Hexagonal Nickel Hydroxide Nanosheets by Exfoliation of Layered Nickel Hydroxide Intercalated with Dodecyl Sulfate Ions. *J. Am. Chem. Soc.* **130,** 14038–14039 (2008).
150. Saiah, F. B. D., Su, B.-L. & Bettahar, N. Nickel–iron layered double hydroxide (LDH): Textural properties upon hydrothermal treatments and application on dye sorption. *J. Hazard. Mater.* **165,** 206–217 (2009).
151. Abellán, G., Carrasco, J. A. & Coronado, E. Room Temperature Magnetism in Layered Double Hydroxides due to Magnetic Nanoparticles. *Inorg. Chem.* **52,** 7828–7830 (2013).
152. Coronado, E., Galán-Mascarós, J. R., Martí-Gastaldo, C. & Ribera, A. Insertion of Magnetic Bimetallic Oxalate Complexes into Layered Double Hydroxides. *Chem. Mater.* **18,** 6112–6114 (2006).
153. Coronado, E., Martí-Gastaldo, C., Navarro-Moratalla, E., Ribera, A. & Tatay, S. Illustrating the Processability of Magnetic Layered Double Hydroxides: Layer-by-Layer Assembly of Magnetic Ultrathin Films. *Inorg. Chem.* **52,** 6214–6222 (2013).
154. Abellán, G., Carrasco, J. A., Coronado, E., Romero, J. & Varela, M. Alkoxide-intercalated CoFe-layered double hydroxides as precursors of colloidal nanosheet suspensions: structural, magnetic and electrochemical properties. *J. Mater. Chem. C* ***2,*** 3723–3731(2014).
155. Horcas, I. *et al.* WSXM: A software for scanning probe microscopy and a tool for nanotechnology. *Rev. Sci. Instrum.* **78,** 013705 (2007).
156. Trujillano, R., Holgado, M. J., Pigazo, F. & Rives, V. Preparation, physicochemical characterisation and magnetic properties of Cu–Al layered double hydroxides with CO_3^{2-} and anionic surfactants with different alkyl chains in the interlayer. *Phys. B Condens. Matter* **373,** 267–273 (2006).
157. Intissar, M., Segni, R., Payen, C., Besse, J.-P. & Leroux, F. Trivalent Cation Substitution Effect into Layered Double Hydroxides $Co_2Fe_yAl_{1-y}(OH)_6Cl{\cdot}nH_2O$: Study of the Local Order: Ionic Conductivity and Magnetic Properties. *J. Solid State Chem.* **167,** 508–516 (2002).

158. Bujoli-Dœuff, M. *et al.* A new two-dimensional approach to molecular-based magnets: Nickel(II)-Chromium(III) double hydroxide systems. *Mater. Res. Bull.* **26,** 577–587 (1991).
159. Morlat-Thérias, S. *et al.* Concomitant Intercalation and Decomplexation of Ferrocene Sulfonates in Layered Double Hydroxides. *J. Solid State Chem.* **144,** 143–151 (1999).
160. Giovannelli, F. *et al.* Magnetic properties of Ni(II)–Mn(III) LDHs. *Mater. Chem. Phys.* **137,** 55–60 (2012).
161. Wang, C. J. *et al.* Reverse Micelle Synthesis of Co–Al LDHs: Control of Particle Size and Magnetic Properties. *Chem. Mater.* **23,** 171–180 (2011).
162. Marvilliers, A. *et al.* Structure, Magnetic Properties and Magnetic Phase Diagram of a Layered, Bimetallic, Cyanide-Bridged Cr^{III}-Ni^{II} Metamagnet. *Eur. J. Inorg. Chem.* **2001,** 1287–1293 (2001).
163. Abellán, G., Coronado, E., Gómez-García, C. J., Martí-Gastaldo, C. & Ribera, A. Intercalation of cobalt(II)-tetraphenylporphine tetrasulfonate complex in magnetic NiFe-layered double hydroxide. *Polyhedron* **52,** 216–221 (2013).
164. Abellán, G., Busolo, F., Coronado, E., Martí-Gastaldo, C. & Ribera, A. Hybrid Magnetic Multilayers by Intercalation of Cu(II) Phthalocyanine in LDH Hosts. *J. Phys. Chem. C* **116,** 15756–15764 (2012).
165. Layrac, G., Tichit, D., Larionova, J., Guari, Y. & Guérin, C. Controlled Growth of Cyano-Bridged Coordination Polymers into Layered Double Hydroxides. *J. Phys. Chem. C* **115,** 3263–3271 (2011).
166. Mydosh, J. A. *Spin glasses: an experimental introduction.* (Taylor & Francis, 1993).
167. Ferreira, T. a. S., Waerenborgh, J. C., Mendonaca, M. H. R. M., Nunes, M. R. & Costa, F. M. Structural and morphological characterization of $FeCo_2O_4$ and $CoFe_2O_4$ spinels prepared by a coprecipitation method. *Solid State Sci.* **5,** 383–392 (2003).
168. Sawatzky, G. A., Van Der Woude, F. & Morrish, A. H. Mössbauer Study of Several Ferrimagnetic Spinels. *Phys. Rev.* **187,** 747–757 (1969).
169. Rodrigues, J. V. *et al.* Synthesis, structure and properties of $[Hpy]_2[\{M(mnt)_2\}_2]$(M = Co or Fe, Hpy = pyridinium, mnt = maleonitriledithiolate). *J. Chem. Soc. Dalton Trans.* 2655–2660 (1994).
170. Miller, J. S. The quest for magnetic polymers – caveat emptor. *Adv. Mater.* **4,** 298–300 (1992).
171. Miller, J. S. The quest for magnetic polymers—caveat emptor. *Adv. Mater.* **4,** 435–438 (1992).
172. Lefebvre, J., Trudel, S., Hill, R. H. & Leznoff, D. B. A Closer Look: Magnetic Behavior of a Three-Dimensional Cyanometalate Coordination Polymer

Dominated by a Trace Amount of Nanoparticle Impurity. *Chem. – Eur. J.* **14,** 7156–7167 (2008).

173. Buckelew, A., Galán-Mascarós, J. r. & Dunbar, K. r. Facile Conversion of the Face-Centered Cubic Prussian-Blue Material $K_2[Mn_2(CN)_6]$ into the Spinel Oxide Mn_3O_4 at the Solid/Water Interface. *Adv. Mater.* **14,** 1646–1648 (2002).
174. Jain, R. *et al.* High-temperature metal–organic magnets. *Nature* **445,** 291–294 (2007).
175. Miller, J. S. & Pokhodnya, K. I. Formation of $Ni[C_4(CN)_8]$ from the reaction of $Ni(COD)_2$ (COD = 1,5-cyclooctadiene) with TCNE in THF. *J. Mater. Chem.* **17,** 3585–3587 (2007).
176. Morpurgo, S., Jacono, M. L. & Porta, P. Copper–Zinc–Cobalt–Aluminium–Chromium Hydroxycarbonates and Mixed Oxides. *J. Solid State Chem.* **122,** 324–332 (1996).
177. Porta, P., Morpurgo, S. & Pettiti, I. Characterization by X-Ray Absorption, X-Ray Powder Diffraction, and Magnetic Susceptibility of Cu–Zn–Co–Al–Containing Hydroxycarbonates, Oxycarbonates, Oxides, and Their Products of Reduction. *J. Solid State Chem.* **121,** 372–378 (1996).
178. Fujita, W. & Awaga, K. Magnetic Properties of $Cu_2(OH)_3$(alkanecarboxylate) Compounds: Drastic Modification with Extension of the Alkyl Chain. *Inorg. Chem.* **35,** 1915–1917 (1996).
179. Abellán, G., Coronado, E., Martí-Gastaldo, C., Waerenborgh, J. & Ribera, A. Interplay between Chemical Composition and Cation Ordering in the Magnetism of Ni/Fe Layered Double Hydroxides. *Inorg. Chem.* **52,** 10147–10157 (2013).
180. Woo, M. A. *et al.* Mixed valence Zn–Co-layered double hydroxides and their exfoliated nanosheets with electrode functionality. *J. Mater. Chem.* **21,** 4286 (2011).
181. Abellán, G. *et al.* Photo-Switching in a Hybrid Material Made of Magnetic Layered Double Hydroxides Intercalated with Azobenzene Molecules. *Adv. Mater.* ***26***, 4156–4162 (2014).
182. Dou, Y., Liu, X., Shao, M., Han, J. & Wei, M. Flexible and transparent free-standing films with enhanced magnetic and luminescent anisotropy. *J. Mater. Chem. A* **1,** 4786–4792 (2013).
183. Shao, M., Wei, M., Evans, D. G. & Duan, X. Magnetic-field-assisted assembly of CoFe layered double hydroxide ultrathin films with enhanced electrochemical behavior and magnetic anisotropy. *Chem. Commun.* **47,** 3171–3173 (2011).
184. Shao, M. *et al.* Magnetic-Field-Assisted Assembly of Layered Double Hydroxide/Metal Porphyrin Ultrathin Films and Their Application for Glucose Sensors. *Langmuir* **27,** 8233–8240 (2011).

185. Manohara, G. V., Prasanna, S. V. & Kamath, P. V. Structure and Composition of the Layered Double Hydroxides of Mg and Fe: Implications for Anion-Exchange Reactions. *Eur. J. Inorg. Chem.* **2011,** 2624–2630 (2011).
186. Baumgartner, J. *et al.* Nucleation and growth of magnetite from solution. *Nat. Mater.* **12,** 310–314 (2013).
187. Arco, M. del, Trujillano, R. & Rives, V. Cobalt–iron hydroxycarbonates and their evolution to mixed oxides with spinel structure. *J. Mater. Chem.* **8,** 761–767 (1998).
188. Gursky, J. A. *et al.* Particle–Particle Interactions between Layered Double Hydroxide Nanoparticles. *J. Am. Chem. Soc.* **128,** 8376–8377 (2006).
189. Park, J. *et al.* One-Nanometer-Scale Size-Controlled Synthesis of Monodisperse Magnetic Iron Oxide Nanoparticles. *Angew. Chem.* **117,** 2932–2937 (2005).
190. Rall, J. D. & Seehra, M. S. The nature of the magnetism in quasi-2D layered α-$Ni(OH)_2$. *J. Phys. Condens. Matter* **24,** 076002 (2012).
191. Pavan, P. C., Gomes, G. de A. & Valim, J. B. Adsorption of sodium dodecyl sulfate on layered double hydroxides. *Microporous Mesoporous Mater.* **21,** 659–665 (1998).
192. You, Y., Zhao, H. & Vance, G. F. Hybrid organic–inorganic derivatives of layered double hydroxides and dodecylbenzenesulfonate: Preparation and adsorption characteristics. *J. Mater. Chem.* **12,** 907–912 (2002).
193. Meyn, M., Beneke, K. & Lagaly, G. Anion-exchange reactions of hydroxy double salts. *Inorg. Chem.* **32,** 1209–1215 (1993).
194. Cervilla, A. *et al.* Intercalation of $[Mo^{VI}O_2(O_2CC(S)Ph_2)_2]^{2-}$ in a Zn(II)-Al(III) Layered Double Hydroxide Host: A Strategy for the Heterogeneous Catalysis of the Air Oxidation of Thiols. *J. Am. Chem. Soc.* **116,** 1595–1596 (1994).
195. Cervilla, A. *et al.* Model Reactions of Molybdo-Reductase. A Novel and Highly Efficient Reduction of Nitrobenzene to Aniline Catalyzed by a Molybdenum-Mediated Oxygen Atom Transfer Reaction. *J. Am. Chem. Soc.* **117,** 6781–6782 (1995).
196. Chibwe, M. & Pinnavaia, T. J. Stabilization of a cobalt(II) phthalocyanine oxidation catalyst by intercalation in a layered double hydroxide host. *J. Chem. Soc. Chem. Commun.* 278–280 (1993).
197. Sels, B. *et al.* Layered double hydroxides exchanged with tungstate as biomimetic catalysts for mild oxidative bromination. *Nature* **400,** 855–857 (1999).
198. Ribera, A., Pérez-Pla, F., Llopis, E., Cervilla, A. & Domenech, A. A kinetic model for the oxidation of benzenethiol catalyzed by the $[Mo^{VI}O_2(O_2CC(S)(C_6H_5)_2)_2]^{2-}$ complex intercalated in a Zn(II)–Al(III) layered double hydroxide host. *J. Mol. Catal. Chem.* **304,** 174–179 (2009).

199. Wei, M. *et al.* Study of the In Situ Postintercalative Polymerization of Metanilic Anions Intercalated in NiAl-Layered Double Hydroxides under a Nitrogen Atmosphere. *Eur. J. Inorg. Chem.* **2006,** 3442–3450 (2006).
200. Coronado, E., Martí-Gastaldo, C., Navarro-Moratalla, E. & Ribera, A. Confined Growth of Cyanide-Based Magnets in Two Dimensions. *Inorg. Chem.* **49,** 1313–1315 (2010).
201. Abellán, G., Coronado, E., Martí-Gastaldo, C., Ribera, A. & Sánchez-Royo, J. F. Layered double hydroxide (LDH)–organic hybrids as precursors for low-temperature chemical synthesis of carbon nanoforms. *Chem. Sci.* **3,** 1481–1485 (2012).
202. Choy, J.-H., Kwak, S.-Y., Jeong, Y.-J. & Park, J.-S. Inorganic Layered Double Hydroxides as Nonviral Vectors. *Angew. Chem. Int. Ed.* **39,** 4041–4045 (2000).
203. Wei, M. *et al.* Intercalation of l-Dopa into Layered Double Hydroxides: Enhancement of Both Chemical and Stereochemical Stabilities of a Drug through Host–Guest Interactions. *Chem. Mater.* **20,** 5169–5180 (2008).
204. Lang, K., Mosinger, J. & Wagnerová, D. M. Photophysical properties of porphyrinoid sensitizers non-covalently bound to host molecules; models for photodynamic therapy. *Coord. Chem. Rev.* **248,** 321–350 (2004).
205. Halma, M. *et al.* Synthesis, characterization, and catalytic activity of anionic iron(III) porphyrins intercalated into layered double hydroxides. *J. Catal.* **257,** 233–243 (2008).
206. Carrado, K. A., Forman, J. E., Botto, R. E. & Winans, R. E. Incorporation of phthalocyanines by cationic and anionic clays via ion exchange and direct synthesis. *Chem. Mater.* **5,** 472–478 (1993).
207. Ukrainczyk, L., Chibwe, M., Pinnavaia, T. J. & Boyd, S. A. ESR Study of Cobalt(II) Tetrakis(N-methyl-4-pyridiniumyl)porphyrin and Cobalt(II) Tetrasulfophthalocyanine Intercalated in Layered Aluminosilicates and a Layered Double Hydroxide. *J. Phys. Chem.* **98,** 2668–2676 (1994).
208. Barbosa, C. A. S., Ferreira, A. M. D. C., Constantino, V. R. L. & Coelho, A. C. V. Preparation and Characterization of Cu(II) Phthalocyanine Tetrasulfonate Intercalated and Supported on Layered Double Hydroxides. *J. Incl. Phenom. Macrocycl. Chem.* **42,** 15–23 (2002).
209. Zhao, H. & Nagy, K. L. Dodecyl sulfate–hydrotalcite nanocomposites for trapping chlorinated organic pollutants in water. *J. Colloid Interface Sci.* **274,** 613–624 (2004).
210. Tong, Z., Shichi, T., Zhang, G. & Takagi, K. The intercalation of metalloporphyrin complex anions into layered double hydroxides. *Res. Chem. Intermed.* **29,** 335–341 (2003).

211. Káfuňková, E. *et al.* Porphyrins Intercalated in Zn/Al and Mg/Al Layered Double Hydroxides: Properties and Structural Arrangement. *Chem. Mater.* **22,** 2481–2490 (2010).
212. Coronado, E., Martí-Gastaldo, C., Navarro-Moratalla, E. & Ribera, A. Intercalation of $[M(ox)_3]^{3-}$ (M = Cr, Rh) complexes into $Ni^{II}Fe^{III}$-LDH. *Appl. Clay Sci.* **48,** 228–234 (2010).
213. Bourzami, R. *et al.* New Metal Phthalocyanines/Metal Simple Hydroxide Multilayers: Experimental Evidence of Dipolar Field-Driven Magnetic Behavior. *Inorg. Chem.* (2014). doi:10.1021/ic4027688
214. Gédéon, A. & Fraissard, J. Use of ESR and ^{129}Xe NMR spectroscopy to characterize CuZSM-5 zeolite synthesized in the presence of a copper–phthalocyanine complex. *Colloids Surf. Physicochem. Eng. Asp.* **158,** 201–206 (1999).
215. Bacci, M. & Cannistraro, S. A vibronic coupling approach for the interpretation of the g-value temperature dependence in type-I copper proteins. *J. Chem. Soc. Faraday Trans. 1 Phys. Chem. Condens. Phases* **83,** 3693–3700 (1987).
216. Demel, J. & Lang, K. Layered Hydroxide–Porphyrin Hybrid Materials: Synthesis, Structure, and Properties. *Eur. J. Inorg. Chem.* **2012,** 5154–5164 (2012).
217. Taviot-Guého, C., Halma, M., Charradi, K., Forano, C. & Mousty, C. Structural and electrochemical characterization of metallo-porphyrins intercalated into ZnCr-layered double hydroxides: some evidence of dimer formation. *New J. Chem.* **35,** 1898–1905 (2011).
218. Shichi, T., Tong, Z., Hirai, S. & Takagi, K. Host-Guest Electron Transfer between Intercalated Co(II)-Tetraphenylporphine Tetrasulfonate and Mg-Fe(III) Layered Double Hydroxides. *Chem. Lett.* **31,** 834–835 (2002).
219. Barbosa, C. A. S., Ferreira, A. M. D. C. & Constantino, V. R. L. Synthesis and Characterization of Magnesium-Aluminum Layered Double Hydroxides Containing (Tetrasulfonated porphyrin)cobalt. *Eur. J. Inorg. Chem.* **2005,** 1577–1584 (2005).
220. Coronado, E. *et al.* Ferromagnetism and Chirality in Two-Dimensional Cyanide-Bridged Bimetallic Compounds. *Inorg. Chem.* **41,** 4615–4617 (2002).
221. Bellouard, F. *et al.* Unusual Magnetic Behavior in the Layered Ferromagnet $[Ni(C_6H_{14}N_2)_2]_3[Fe(CN)_6]_2{\cdot}2H_2O$. *Eur. J. Inorg. Chem.* **2002,** 1603–1606 (2002).
222. Triki, S., Sala-Pala, J., Thétiot, F., Gómez-García, C. J. & Daran, J.-C. New, Multi-Dimensional Cu(tn)-$[M(CN)_6]^{n-}$ Cyano-Bridged, Bimetallic Coordination Materials (M = Fe^{II}, Co^{III}, Cr^{III} and tn = 1,3-Diaminopropane). *Eur. J. Inorg. Chem.* **2006,** 185–199 (2006).

223. Bolfo, J. A. de, Smith, T. D., Boas, J. F. & Pilbrow, J. R. Electron spin resonance study of the oxygenation of cobalt(II) tetraphenylporphyrintetrasulphonate. *J. Chem. Soc. Dalton Trans.* 1495–1500 (1976).
224. Bain, G. A. & Berry, J. F. Diamagnetic Corrections and Pascal's Constants. *J. Chem. Educ.* **85,** 532–536 (2008).
225. Gómez-Romero, P. & Sanchez, C. in *Funct. Hybrid Mater.* (Gómez-Romero, P. & Sanchez, C.) 1–14 (Wiley-VCH Verlag GmbH & Co. KGaA, 2003).
226. Coronado, E., Galán-Mascarós, J. R., Gómez-García, C. J. & Laukhin, V. Coexistence of ferromagnetism and metallic conductivity in a molecule-based layered compound. *Nature* **408,** 447–449 (2000).
227. Coronado, E. & Day, P. Magnetic molecular conductors. *Chem. Rev.* **104,** 5419–5448 (2004).
228. Bénard, S. *et al.* Structure and NLO Properties of Layered Bimetallic Oxalato-Bridged Ferromagnetic Networks Containing Stilbazolium-Shaped Chromophores. *J. Am. Chem. Soc.* **122,** 9444–9454 (2000).
229. Clemente-León, M. *et al.* A hybrid magnet with coexistence of ferromagnetism and photoinduced Fe(III) spin-crossover. *Chem. Sci.* **2,** 1121–1127 (2011).
230. Coronado, E. & Mínguez Espallargas, G. Dynamic magnetic MOFs. *Chem. Soc. Rev.* **42,** 1525–1539 (2013).
231. Si, S., Taubert, A., Mantion, A., Rogez, G. & Rabu, P. Peptide-intercalated layered metal hydroxides: effect of peptide chain length and side chain functionality on structural, optical and magnetic properties. *Chem. Sci.* **3,** 1945–1957 (2012).
232. Sekkat, Z. & Knoll, W. *Photoreactive Organic Thin Films.* (Academic Press, 2002).
233. Bandara, H. M. D. & Burdette, S. C. Photoisomerization in different classes of azobenzene. *Chem. Soc. Rev.* **41,** 1809–1825 (2012).
234. Ogawa, M., Yamamoto, M. & Kuroda, K. Intercalation of an amphiphilic azobenzene derivative into the interlayer space of a layered silicate, magadiite. *Clay Miner.* **36,** 263–266 (2001).
235. Ogawa, M., Ishii, T., Miyamoto, N. & Kuroda, K. Photocontrol of the Basal Spacing of Azobenzene–Magadiite Intercalation Compound. *Adv. Mater.* **13,** 1107–1109 (2001).
236. Iyi, N., Fujita, T., Yelamaggad, C. V. & Lopez Arbeloa, F. Intercalation of cationic azobenzene derivatives in a synthetic mica and their photoresponse. *Appl. Clay Sci.* **19,** 47–58 (2001).
237. Ogawa, M., Ishii, T., Miyamoto, N. & Kuroda, K. Intercalation of a cationic azobenzene into montmorillonite. *Appl. Clay Sci.* **22,** 179–185 (2003).
238. Yamamoto, T., Umemura, Y., Sato, O. & Einaga, Y. Photoswitchable Magnetic Films: Prussian Blue Intercalated in Langmuir–Blodgett Films Consisting of an

Amphiphilic Azobenzene and a Clay Mineral. *Chem. Mater.* **16,** 1195–1201 (2004).

239. Okada, T., Watanabe, Y. & Ogawa, M. Photoregulation of the intercalation behavior of phenol for azobenzene?clay intercalation compounds. *J. Mater. Chem.* **15,** 987–992 (2005).
240. Nabetani, Y. *et al.* An artificial muscle model unit based on inorganic nanosheet sliding by photochemical reaction. *Nanoscale* **5,** 3182–3193 (2013).
241. Heinz, H., Vaia, R. A., Koerner, H. & Farmer, B. L. Photoisomerization of Azobenzene Grafted to Layered Silicates: Simulation and Experimental Challenges. *Chem. Mater.* **20,** 6444–6456 (2008).
242. Abellán, G., García, H., Gómez-García, C. J. & Ribera, A. Photochemical behavior in azobenzene having acidic groups. Preparation of magnetic photoresponsive gels. *J. Photochem. Photobiol. Chem.* **217,** 157–163 (2011).
243. Bauer, J., Behrens, P., Speckbacher, M. & Langhals, H. Composites of Perylene Chromophores and Layered Double Hydroxides: Direct Synthesis, Characterization, and Photo- and Chemical Stability. *Adv. Funct. Mater.* **13,** 241–248 (2003).
244. Marangoni, R., Bouhent, M., Taviot-Guého, C., Wypych, F. & Leroux, F. Zn_2Al layered double hydroxides intercalated and adsorbed with anionic blue dyes: A physico-chemical characterization. *J. Colloid Interface Sci.* **333,** 120–127 (2009).
245. Mandal, S., Tichit, D., Lerner, D. A. & Marcotte, N. Azoic Dye Hosted in Layered Double Hydroxide: Physicochemical Characterization of the Intercalated Materials. *Langmuir* **25,** 10980–10986 (2009).
246. Chakraborty, C., Dana, K. & Malik, S. Intercalation of Perylenediimide Dye into LDH Clays: Enhancement of Photostability. *J. Phys. Chem. C* **115,** 1996–2004 (2011).
247. Han, J. *et al.* Layer-by-Layer Ultrathin Films of Azobenzene-Containing Polymer/Layered Double Hydroxides with Reversible Photoresponsive Behavior. *J. Phys. Chem. B* **114,** 5678–5685 (2010).
248. Raki, L., R., R. D. & Detellier, C. Preparation, characterization, and mossbauer spectroscopy of organic anion intercalated pyroaurite-like layered double hydroxides. *Chem.Mater.* **7,** 221–224 (1995).
249. Zhao, Y. *et al.* Highly Dispersed TiO6 Units in a Layered Double Hydroxide for Water Splitting. *Chem. – Eur. J.* **18,** 11949–11958 (2012).
250. Carja, G., Nakamura, R., Aida, T. & Niiyama, H. Textural properties of layered double hydroxides: effect of magnesium substitution by copper or iron. *Microporous Mesoporous Mater.* **47,** 275–284 (2001).

251. Hutson, N. D., Speakman, S. A. & Payzant, E. A. Structural Effects on the High Temperature Adsorption of CO_2 on a Synthetic Hydrotalcite. *Chem. Mater.* **16,** 4135–4143 (2004).
252. Herrero, M., Benito, P., Labajos, F. M. & Rives, V. Stabilization of Co^{2+} in layered double hydroxides (LDHs) by microwave-assisted ageing. *J. Solid State Chem.* **180,** 873–884 (2007).
253. Alvaro, M., Benitez, M., Das, D., Garcia, H. & Peris, E. Reversible Porosity Changes in Photoresponsive Azobenzene-Containing Periodic Mesoporous Silicas. *Chem. Mater.* **17,** 4958–4964 (2005).
254. Hu, G. & O'Hare, D. Unique Layered Double Hydroxide Morphologies Using Reverse Microemulsion Synthesis. *J. Am. Chem. Soc.* **127,** 17808–17813 (2005).
255. Einaga, Y., Sato, O., Iyoda, T., Fujishima, A. & Hashimoto, K. Photofunctional Vesicles Containing Prussian Blue and Azobenzene. *J. Am. Chem. Soc.* **121,** 3745–3750 (1999).
256. Mikami, R. *et al.* Reversible Photo-Switching of the Magnetization of Iron Oxide Nanoparticles at Room Temperature. *Angew. Chem. Int. Ed.* **43,** 6135–6139 (2004).
257. Bénard, S., Léaustic, A., Rivière, E., Yu, P. & Clément, R. Interplay between Magnetism and Photochromism in Spiropyran–$MnPS_3$ Intercalation Compounds. *Chem. Mater.* **13,** 3709–3716 (2001).
258. Gilbert, A. & Baggott, J. *Essentials of Organic Photochemisry.* (Blackwell: Oxford, 1990).
259. Kumar, G. S. & Neckers, D. C. Photochemistry of azobenzene-containing polymers. *Chem. Rev.* **89,** 1915–1925 (1989).
260. Ichimura, K. Photoalignment of Liquid-Crystal Systems. *Chem. Rev.* **100,** 1847–1874 (2000).
261. Niederberger, M. Nonaqueous Sol–Gel Routes to Metal Oxide Nanoparticles. *Acc. Chem. Res.* **40,** 793–800 (2007).
262. Dunn, N. J., Humphries, W. H., Offenbacher, A. R., King, T. L. & Gray, J. A. pH-Dependent cis → trans Isomerization Rates for Azobenzene Dyes in Aqueous Solution. *J. Phys. Chem. A* **113,** 13144–13151 (2009).
263. Sanchez, A. M., Barra, M. & de Rossi, R. H. On the Mechanism of the Acid/Base-Catalyzed Thermal Cis–Trans Isomerization of Methyl Orange. *J. Org. Chem.* **64,** 1604–1609 (1999).
264. Nabetani, Y. *et al.* A Photoactivated Artificial Muscle Model Unit: Reversible, Photoinduced Sliding of Nanosheets. *J. Am. Chem. Soc.* **133,** 17130–17133 (2011).
265. Wang, X. *et al.* A Thermochromic Thin Film Based on Host–Guest Interactions in a Layered Double Hydroxide. *Langmuir* **26,** 1247–1253 (2010).

266. W, F. & K, A. Reversible Structural Transformation and Drastic Magnetic Change in a Copper Hydroxides Intercalation Compound. *J. Am. Chem. Soc.* **119,** 4563–4564 (1997).
267. Férey, G. & Serre, C. Large breathing effects in three-dimensional porous hybrid matter: facts, analyses, rules and consequences. *Chem. Soc. Rev.* **38,** 1380–1399 (2009).
268. Kreno, L. E. *et al.* Metal–Organic Framework Materials as Chemical Sensors. *Chem. Rev.* **112,** 1105–1125 (2012).
269. Coronado, E., Giménez-Marqués, M., Espallargas, G. M. & Brammer, L. Tuning the magneto-structural properties of non-porous coordination polymers by HCl chemisorption. *Nat. Commun.* **3,** 828 (2012).
270. Horike, S., Shimomura, S. & Kitagawa, S. Soft porous crystals. *Nat. Chem.* **1,** 695–704 (2009).
271. Stuart, M. A. C. *et al.* Emerging applications of stimuli-responsive polymer materials. *Nat. Mater.* **9,** 101–113 (2010).
272. Sakata, Y. *et al.* Shape-Memory Nanopores Induced in Coordination Frameworks by Crystal Downsizing. *Science* **339,** 193–196 (2013).
273. Lewis, N. S. & Nocera, D. G. Powering the planet: Chemical challenges in solar energy utilization. *Proc. Natl. Acad. Sci.* **103,** 15729–15735 (2006).
274. Gray, H. B. Powering the planet with solar fuel. *Nat. Chem.* **1,** 7–7 (2009).
275. Nicolosi, V., Chhowalla, M., Kanatzidis, M. G., Strano, M. S. & Coleman, J. N. Liquid Exfoliation of Layered Materials. *Science* **340,** 1226419 (2013).
276. Walter, M. G. *et al.* Solar water splitting cells. *Chem. Rev.* **110,** 6446–6473 (2010).
277. Suntivich, J., May, K. J., Gasteiger, H. A., Goodenough, J. B. & Shao-Horn, Y. A Perovskite Oxide Optimized for Oxygen Evolution Catalysis from Molecular Orbital Principles. *Science* **334,** 1383–1385 (2011).
278. Hamdani, M., Singh, R. N. & Chartier, P. Co_3O_4 and Co-based spinel oxides bifunctional oxygen electrodes. *Int J Electrochem Sci* **5,** 556–577 (2010).
279. Kanan, M. W. & Nocera, D. G. In Situ Formation of an Oxygen-Evolving Catalyst in Neutral Water Containing Phosphate and Co^{2+}. *Science* **321,** 1072–1075 (2008).
280. Smith, R. D. L. *et al.* Photochemical Route for Accessing Amorphous Metal Oxide Materials for Water Oxidation Catalysis. *Science* **340,** 60–63 (2013).
281. Symes, M. D. & Cronin, L. Decoupling hydrogen and oxygen evolution during electrolytic water splitting using an electron-coupled-proton buffer. *Nat. Chem.* **5,** 403–409 (2013).
282. Toma, F. M. *et al.* Efficient water oxidation at carbon nanotube–polyoxometalate electrocatalytic interfaces. *Nat. Chem.* **2,** 826–831 (2010).
283. Soriano-López, J. *et al.* Cobalt Polyoxometalates as Heterogeneous Water Oxidation Catalysts. *Inorg. Chem.* **52,** 4753–4755 (2013).

284. Pintado, S., Goberna-Ferrón, S., Escudero-Adán, E. C. & Galán-Mascarós, J. R. Fast and Persistent Electrocatalytic Water Oxidation by Co–Fe Prussian Blue Coordination Polymers. *J. Am. Chem. Soc.* **135,** 13270–13273 (2013).
285. Zhang, Y., Cui, B., Zhao, C., Lin, H. & Li, J. Co–Ni layered double hydroxides for water oxidation in neutral electrolyte. *Phys. Chem. Chem. Phys.* **15,** 7363–7369 (2013).
286. Silva, C. G., Bouizi, Y., Fornés, V. & García, H. Layered Double Hydroxides as Highly Efficient Photocatalysts for Visible Light Oxygen Generation from Water. *J. Am. Chem. Soc.* **131,** 13833–13839 (2009).
287. Li, Y. *et al.* Advanced zinc-air batteries based on high-performance hybrid electrocatalysts. *Nat. Commun.* **4,** 1805 (2013).
288. Kamat, P. V. Graphene-Based Nanoassemblies for Energy Conversion. *J. Phys. Chem. Lett.* **2,** 242–251 (2011).
289. Luo, B., Liu, S. & Zhi, L. Chemical Approaches toward Graphene-Based Nanomaterials and their Applications in Energy-Related Areas. *Small* **8,** 630–646 (2012).
290. Wu, X.-L., Wang, L., Chen, C.-L., Xu, A.-W. & Wang, X.-K. Water-dispersible magnetite-graphene-LDH composites for efficient arsenate removal. *J. Mater. Chem.* **21,** 17353–17359 (2011).
291. Wang, L. *et al.* Layered assembly of graphene oxide and Co–Al layered double hydroxide nanosheets as electrode materials for supercapacitors. *Chem. Commun.* **47,** 3556–3558 (2011).
292. Li, B. *et al.* Co_3O_4@graphene Composites as Anode Materials for High-Performance Lithium Ion Batteries. *Inorg. Chem.* **50,** 1628–1632 (2011).
293. Dong, X., Wang, L., Wang, D., Li, C. & Jin, J. Layer-by-Layer Engineered Co–Al Hydroxide Nanosheets/Graphene Multilayer Films as Flexible Electrode for Supercapacitor. *Langmuir* **28,** 293–298 (2012).
294. Werner, S. *et al.* Cationically Charged $Mn^{II}Al^{III}$ LDH Nanosheets by Chemical Exfoliation and Their Use As Building Blocks in Graphene Oxide-Based Materials. *Langmuir* **29,** 9199–9207 (2013).
295. Yang, W. *et al.* Solvothermal One-Step Synthesis of Ni–Al Layered Double Hydroxide/Carbon Nanotube/Reduced Graphene Oxide Sheet Ternary Nanocomposite with Ultrahigh Capacitance for Supercapacitors. *ACS Appl. Mater. Interfaces* **5,** 5443–5454 (2013).
296. Garcia-Gallastegui, A. *et al.* Graphene Oxide as Support for Layered Double Hydroxides: Enhancing the CO_2 Adsorption Capacity. *Chem. Mater.* **24,** 4531–4539 (2012).

297. Abellán, G., Latorre-Sánchez, M., Fornés, V., Ribera, A. & García, H. Graphene as a carbon source effects the nanometallurgy of nickel in Ni,Mn layered double hydroxide–graphene oxide composites. *Chem. Commun.* **48,** 11416–11418 (2012).
298. Tang, D. *et al.* Carbon Quantum Dot/NiFe Layered Double Hydroxide Composite as High Efficient Electrocatalyst for Water Oxidation. *ACS Appl. Mater. Interfaces* (2014). doi:10.1021/am501256x
299. Smith, R. D. L., Prévot, M. S., Fagan, R. D., Trudel, S. & Berlinguette, C. P. Water Oxidation Catalysis: Electrocatalytic Response to Metal Stoichiometry in Amorphous Metal Oxide Films Containing Iron, Cobalt, and Nickel. *J. Am. Chem. Soc.* **135,** 11580–11586 (2013).
300. Zhou, Y., Bao, Q., Tang, L. A. L., Zhong, Y. & Loh, K. P. Hydrothermal Dehydration for the 'Green' Reduction of Exfoliated Graphene Oxide to Graphene and Demonstration of Tunable Optical Limiting Properties. *Chem. Mater.* **21,** 2950–2956 (2009).
301. Bosch-Navarro, C., Coronado, E., Martí-Gastaldo, C., Sánchez-Royo, J. F. & Gómez, M. G. Influence of the pH on the synthesis of reduced graphene oxide under hydrothermal conditions. *Nanoscale* **4,** 3977–3982 (2012).
302. Wang, H.-W. *et al.* Design and synthesis of $NiCo_2O_4$–reduced graphene oxide composites for high performance supercapacitors. *J. Mater. Chem.* **21,** 10504–10511 (2011).
303. Zhang, Y., Zhang, F., Lu, Y., Chen, T. & Yang, L. Preparation and characterization of $NiFe_2O_4$/NiO composite film via a single-source precursor route. *J. Phys. Chem. Solids* **71,** 604–607 (2010).
304. Zhao, X., Xu, S., Wang, L., Duan, X. & Zhang, F. Exchange-biased $NiFe_2O_4$/NiO nanocomposites derived from NiFe-layered double hydroxides as a single precursor. *Nano Res.* **3,** 200–210 (2010).
305. Chen, J.-L. & Yan, X.-P. A dehydration and stabilizer-free approach to production of stable water dispersions of graphene nanosheets. *J. Mater. Chem.* **20,** 4328–4332 (2010).
306. Paredes, J. I., Villar-Rodil, S., Solís-Fernández, P., Martínez-Alonso, A. & Tascón, J. M. D. Atomic Force and Scanning Tunneling Microscopy Imaging of Graphene Nanosheets Derived from Graphite Oxide. *Langmuir* **25,** 5957–5968 (2009).
307. Mironova-Ulmane, N. *et al.* Raman scattering in nanosized nickel oxide NiO. *J. Phys. Conf. Ser.* **93,** 012039 (2007).
308. Jacob, J. & Khadar, M. A. Investigation of mixed spinel structure of nanostructured nickel ferrite. *J. Appl. Phys.* **107,** 114310 (2010).
309. Ahlawat, A. & Sathe, V. G. Raman study of $NiFe_2O_4$ nanoparticles, bulk and films: effect of laser power. *J. Raman Spectrosc.* **42,** 1087–1094 (2011).

310. Stankovich, S. *et al.* Stable aqueous dispersions of graphitic nanoplatelets via the reduction of exfoliated graphite oxide in the presence of poly(sodium 4-styrenesulfonate). *J. Mater. Chem.* **16,** 155–158 (2006).
311. Chen, C.-M. *et al.* Chemically derived graphene–metal oxide hybrids as electrodes for electrochemical energy storage: pre-graphenization or post-graphenization? *J. Mater. Chem.* **22,** 13947–13955 (2012).
312. Nesbitt, H. W., Legrand, D. & Bancroft, G. M. Interpretation of Ni_{2p} XPS spectra of Ni conductors and Ni insulators. *Phys. Chem. Miner.* **27,** 357–366 (2000).
313. Landon, J. *et al.* Spectroscopic Characterization of Mixed Fe–Ni Oxide Electrocatalysts for the Oxygen Evolution Reaction in Alkaline Electrolytes. *ACS Catal.* **2,** 1793–1801 (2012).
314. Kobayashi, Y., Ke, X., Hata, H., Schiffer, P. & Mallouk, T. E. Soft Chemical Conversion of Layered Double Hydroxides to Superparamagnetic Spinel Platelets. *Chem. Mater.* **20,** 2374–2381 (2008).
315. Gunjakar, J. L., Kim, I. Y., Lee, J. M., Lee, N.-S. & Hwang, S.-J. Self-assembly of layered double hydroxide 2D nanoplates with graphene nanosheets: an effective way to improve the photocatalytic activity of 2D nanostructured materials for visible light-induced O2 generation. *Energy Environ. Sci.* **6,** 1008–1017 (2013).
316. Wang, Z., Zhang, X., Li, Y., Liu, Z. & Hao, Z. Synthesis of graphene–$NiFe_2O_4$ nanocomposites and their electrochemical capacitive behavior. *J. Mater. Chem. A* **1,** 6393–6399 (2013).
317. Zhao, B. *et al.* Monolayer graphene/NiO nanosheets with two-dimension structure for supercapacitors. *J. Mater. Chem.* **21,** 18792–18798 (2011).
318. Wimalasiri, Y., Fan, R., Zhao, X. S. & Zou, L. Assembly of Ni-Al layered double hydroxide and graphene electrodes for supercapacitors. *Electrochimica Acta* **134,** 127–135 (2014).
319. Zhang, L. *et al.* 3D porous layered double hydroxides grown on graphene as advanced electrochemical pseudocapacitor materials. *J. Mater. Chem. A* **1,** 9046–9053 (2013).
320. Hao, J. *et al.* Facile Synthesis of 3D Hierarchical Co-Al Layered Double Hydroxides on Graphene as High-Performance Materials for Supercapacitor Electrode. *J. Colloid Interface Sci.* (2014). doi:10.1016/j.jcis.2014.04.003
321. Lu, Z. *et al.* Three-dimensional NiFe layered double hydroxide film for high-efficiency Oxygen Evolution Reaction. *Chem. Commun.* (2014). doi:10.1039/C4CC01625D
322. Trotochaud, L., Young, S. L., Ranney, J. K. & Boettcher, S. W. Nickel–Iron Oxyhydroxide Oxygen-Evolution Electrocatalysts: The Role of Intentional and Incidental Iron Incorporation. *J. Am. Chem. Soc.* **136,** 6744–6753 (2014).

323. Kong, F.-D. *et al.* Electrochemical studies of Pt/Ir–IrO_2 electrocatalyst as a bifunctional oxygen electrode. *Int. J. Hydrog. Energy* **37,** 59–67 (2012).
324. Zhao, Y., Nakamura, R., Kamiya, K., Nakanishi, S. & Hashimoto, K. Nitrogen-doped carbon nanomaterials as non-metal electrocatalysts for water oxidation. *Nat. Commun.* **4,** 2390 (2013).
325. Tian, G.-L. *et al.* Nitrogen-Doped Graphene/Carbon Nanotube Hybrids: In Situ Formation on Bifunctional Catalysts and Their Superior Electrocatalytic Activity for Oxygen Evolution/Reduction Reaction. *Small* (2014). doi:10.1002/smll.201303715
326. Offeman, R. E. & Hummers, W. S. Preparation of graphitic oxide. *J Am Chem Soc* **80,** 1339–1339 (1958).
327. Darder, M., López-Blanco, M., Aranda, P., Leroux, F. & Ruiz-Hitzky, E. Bio-Nanocomposites Based on Layered Double Hydroxides. *Chem. Mater.* **17,** 1969–1977 (2005).
328. Zhao, J. *et al.* Self-assembly of layered double hydroxide nanosheets/Au nanoparticles ultrathin films for enzyme-free electrocatalysis of glucose. *J. Mater. Chem.* **21,** 13926–13933 (2011).
329. Zhang, F. *et al.* Corrosion Resistance of Superhydrophobic Layered Double Hydroxide Films on Aluminum. *Angew. Chem. Int. Ed.* **47,** 2466–2469 (2008).
330. Leroux, F., Raymundo-Piñero, E., Nedelec, J.-M. & Béguin, F. Textural and electrochemical properties of carbon replica obtained from styryl organo-modified layered double hydroxide. *J. Mater. Chem.* **16,** 2074–2081 (2006).
331. Xu, Z. P. & Zeng, H. C. Decomposition Processes of Organic-Anion-Pillared Clays $Co_aMg_bAl(OH)_c(TA)_d{\cdot}nH_2O$. *J. Phys. Chem. B* **104,** 10206–10214 (2000).
332. Xu, Z. P., Xu, R. & Zeng, H. C. Sulfate-Functionalized Carbon/Metal-Oxide Nanocomposites from Hydrotalcite-like Compounds. *Nano Lett.* **1,** 703–706 (2001).
333. Zhao, M.-Q. *et al.* Embedded High Density Metal Nanoparticles with Extraordinary Thermal Stability Derived from Guest–Host Mediated Layered Double Hydroxides. *J. Am. Chem. Soc.* **132,** 14739–14741 (2010).
334. Sun, J. *et al.* Carbon Nanorings and Their Enhanced Lithium Storage Properties. *Adv. Mater.* **25,** 1125–1130 (2013).
335. Stimpfling, T. & Leroux, F. Supercapacitor-Type Behavior of Carbon Composite and Replica Obtained from Hybrid Layered Double Hydroxide Active Container. *Chem. Mater.* **22,** 974–987 (2010).
336. Zhang, L., Li, F., Xiang, X., Wei, M. & Evans, D. G. Ni-based supported catalysts from layered double hydroxides: Tunable microstructure and controlled property for the synthesis of carbon nanotubes. *Chem. Eng. J.* **155,** 474–482 (2009).

337. Prévot, V., Géraud, E., Stimpfling, T., Ghanbaja, J. & Leroux, F. Hierarchically structured carbon replica of hybrid layered double hydroxide. *New J. Chem.* **35,** 169–177 (2011).
338. Simon, P. & Gogotsi, Y. Materials for electrochemical capacitors. *Nat. Mater.* **7,** 845–854 (2008).
339. Jia, J., Yu, J. C., Wang, Y.-X. J. & Chan, K. M. Magnetic Nanochains of $FeNi_3$ Prepared by a Template-Free Microwave-Hydrothermal Method. *ACS Appl. Mater. Interfaces* **2,** 2579–2584 (2010).
340. Lu, X., Liang, G., Sun, Q. & Yang, C. High-frequency magnetic properties of $FeNi_3$–SiO_2 nanocomposite synthesized by a facile chemical method. *J. Alloys Compd.* **509,** 5079–5083 (2011).
341. Liao, Q., Tannenbaum, R. & Wang, Z. L. Synthesis of $FeNi_3$ Alloyed Nanoparticles by Hydrothermal Reduction. *J. Phys. Chem. B* **110,** 14262–14265 (2006).
342. Lu, X., Liang, G. & Zhang, Y. Synthesis and characterization of magnetic $FeNi_3$ particles obtained by hydrazine reduction in aqueous solution. *Mater. Sci. Eng. B* **139,** 124–127 (2007).
343. Liu, X. G. *et al.* (Fe, Ni)/C nanocapsules for electromagnetic-wave-absorber in the whole Ku-band. *Carbon* **47,** 470–474 (2009).
344. Wang, H., Li, J., Kou, X. & Zhang, L. Synthesis and characterizations of size-controlled $FeNi_3$ nanoplatelets. *J. Cryst. Growth* **310,** 3072–3076 (2008).
345. Tang, N. J. *et al.* Complex permeability of $FeNi_3/SiO_2$ core-shell nanoparticles. *Solid State Commun.* **132,** 71–74 (2004).
346. Liu, W. *et al.* Synthesis and magnetic properties of $FeNi_3/Al_2O_3$ core-shell nanocomposites. *Eur. Phys. J. B - Condens. Matter Complex Syst.* **46,** 471–474 (2005).
347. Bozorth, R. M. *Ferromagnetism.* (D. Van Nostrand Company Inc., 1951).
348. Hongxia, G. *et al.* Shape-controlled synthesis of $FeNi_3$ nanoparticles by ambient chemical reduction and their magnetic properties. *J. Mater. Res.* **27,** 1522–1530 (2012).
349. Xu, M. H. *et al.* Highly stable Fe–Ni alloy nanoparticles encapsulated in carbon nanotubes: Synthesis, structure and magnetic properties. *J. Alloys Compd.* **495,** 200–204 (2010).
350. Lu, A.-H., Salabas, E. L. & Schüth, F. Magnetic Nanoparticles: Synthesis, Protection, Functionalization, and Application. *Angew. Chem. Int. Ed.* **46,** 1222–1244 (2007).
351. Lu, A.-H. *et al.* Highly stable carbon-protected cobalt nanoparticles and graphite shells. *Chem. Commun.* 98–100 (2005).
352. Shirley, D. A. High-Resolution X-Ray Photoemission Spectrum of the Valence Bands of Gold. *Phys. Rev. B* **5,** 4709–4714 (1972).

353. Doniach, S. & Sunjic, M. Many-electron singularity in X-ray photoemission and X-ray line spectra from metals. *J. Phys. C Solid State Phys.* **3,** 285 (1970).
354. Li, X. & Zhang, W. Sequestration of Metal Cations with Zerovalent Iron NanoparticlesA Study with High Resolution X-ray Photoelectron Spectroscopy (HR-XPS). *J. Phys. Chem. C* **111,** 6939–6946 (2007).
355. Allen, G. C., Curtis, M. T., Hooper, A. J. & Tucker, P. M. X-Ray photoelectron spectroscopy of iron–oxygen systems. *J. Chem. Soc. Dalton Trans.* 1525–1530 (1974).
356. Joyner, D. J., Johnson, O. & Hercules, D. M. A study of the iron borides. 1. Electron spectroscopy. *J. Am. Chem. Soc.* **102,** 1910–1917 (1980).
357. Grosvenor, A. P., Kobe, B. A., Biesinger, M. C. & McIntyre, N. S. Investigation of multiplet splitting of Fe 2p XPS spectra and bonding in iron compounds. *Surf. Interface Anal.* **36,** 1564–1574 (2004).
358. Karis, O. *et al.* High-kinetic-energy photoemission spectroscopy of Ni at 1s: 6-eV satellite at 4 eV. *Phys. Rev. B* **78,** 233105 (2008).
359. Verma, S. & Pravarthana, D. One-Pot Synthesis of Highly Monodispersed Ferrite Nanocrystals: Surface Characterization and Magnetic Properties. *Langmuir* **27,** 13189–13197 (2011).
360. Teo, B. K., Sun, X. H., Li, C. P., Wong, N. B. & Lee, S. T. Observation of Hybrid Carbon Nanostructures as Intermediates in the Transformation from Hydrocarbon Nanotubes and Nano-onions to Carbon Nanotubes and Nano-onions via Sonolysis on Silicon Nanowires and Nanodots, Respectively. *Chem. Mater.* **22,** 1297–1308 (2010).
361. Sano, N., Wang, H., Chhowalla, M., Alexandrou, I. & Amaratunga, G. a. J. Nanotechnology: Synthesis of carbon 'onions' in water. *Nature* **414,** 506–507 (2001).
362. Rettenbacher, A. S., Elliott, B., Hudson, J. S., Amirkhanian, A. & Echegoyen, L. Preparation and Functionalization of Multilayer Fullerenes (Carbon Nano-Onions). *Chem. – Eur. J.* **12,** 376–387 (2006).
363. By Powders, A. & Solids, P. *Principles, Methodology and Applications, ed. F. Rouquerol, J. Rouquerol and K. Sing.* (Academic Press, New York, 1999).
364. Abellán, G., Carrillo, A. I., Linares, N., Serrano, E. & García-Martínez, J. Hierarchical control of porous silica by pH adjustment: Alkyl polyamines as surfactants for bimodal silica synthesis and its carbon replica. *J. Solid State Chem.* **182,** 2141–2148 (2009).
365. Li, X. & Wei, B. Supercapacitors based on nanostructured carbon. *Nano Energy* **2,** 159–173 (2013).

366. Futaba, D. N. *et al.* Shape-engineerable and highly densely packed single-walled carbon nanotubes and their application as super-capacitor electrodes. *Nat. Mater.* **5,** 987–994 (2006).
367. Largeot, C. *et al.* Relation between the Ion Size and Pore Size for an Electric Double-Layer Capacitor. *J. Am. Chem. Soc.* **130,** 2730–2731 (2008).
368. Wu, Z.-S. *et al.* Three-Dimensional Graphene-Based Macro- and Mesoporous Frameworks for High-Performance Electrochemical Capacitive Energy Storage. *J. Am. Chem. Soc.* **134,** 19532–19535 (2012).
369. Zhong, M. *et al.* Electrochemically Active Nitrogen-Enriched Nanocarbons with Well-Defined Morphology Synthesized by Pyrolysis of Self-Assembled Block Copolymer. *J. Am. Chem. Soc.* **134,** 14846–14857 (2012).
370. Lu, Q. *et al.* Supercapacitor Electrodes with High-Energy and Power Densities Prepared from Monolithic NiO/Ni Nanocomposites. *Angew. Chem. Int. Ed.* **50,** 6847–6850 (2011).
371. Li, B., Cao, H., Shao, J., Qu, M. & Warner, J. H. Superparamagnetic Fe_3O_4 nanocrystals@graphene composites for energy storage devices. *J. Mater. Chem.* **21,** 5069–5075 (2011).
372. Bose, S. *et al.* Carbon-based nanostructured materials and their composites as supercapacitor electrodes. *J. Mater. Chem.* **22,** 767–784 (2011).
373. Zhang, C. *et al.* The efficient synthesis of carbon nano-onions using chemical vapor deposition on an unsupported Ni–Fe alloy catalyst. *Carbon* **49,** 1151–1158 (2011).
374. Zhao, X., Sánchez, B. M., Dobson, P. J. & Grant, P. S. The role of nanomaterials in redox-based supercapacitors for next generation energy storage devices. *Nanoscale* **3,** 839–855 (2011).
375. Simon, P. & Gogotsi, Y. Capacitive Energy Storage in Nanostructured Carbon–Electrolyte Systems. *Acc. Chem. Res.* **46,** 1094–1103 (2013).
376. Liang, Z., Huo, R. H. R., Yin, S., Fazhi, Z. & Xu, S. Eco-efficient synthesis route of carbon-encapsulated transition metal phosphide with improved cyclic stability for lithium-ion batteries. *J. Mater. Chem. A* **2**, 921–925 (2014).
377. Frackowiak, E. & Béguin, F. Carbon materials for the electrochemical storage of energy in capacitors. *Carbon* **39,** 937–950 (2001).
378. Abellán, G., Martinez, J. G., Otero, T. F., Ribera, A. & Coronado, E. A chemical and electrochemical multivalent memory made from $FeNi_3$-graphene nanocomposites. *Electrochem. Commun.* **39**, 15–18 (2014).
379. Banks, C. E., Davies, T. J., Wildgoose, G. G. & Compton, R. G. Electrocatalysis at graphite and carbon nanotube modified electrodes: edge-plane sites and tube ends are the reactive sites. *Chem. Commun.* 829–841 (2005).

380. Prezioso, M. *et al.* A Single-Device Universal Logic Gate Based on a Magnetically Enhanced Memristor. *Adv. Mater.* **25,** 534–538 (2013).
381. Simão, C. *et al.* A robust molecular platform for non-volatile memory devices with optical and magnetic responses. *Nat. Chem.* **3,** 359–364 (2011).
382. Hu, B. & Wu, Y. Tuning magnetoresistance between positive and negative values in organic semiconductors. *Nat. Mater.* **6,** 985–991 (2007).
383. Baibich, M. N. *et al.* Giant Magnetoresistance of (001)Fe/(001)Cr Magnetic Superlattices. *Phys. Rev. Lett.* **61,** 2472–2475 (1988).
384. Xiao, J. Q., Samuel Jiang, J. & Chien, C. L. Giant magnetoresistance in nonmultilayer magnetic systems. *Phys. Rev. Lett.* **68,** 3749–3752
385. Berkowitz, A. E. *et al.* Giant magnetoresistance in heterogeneous Cu-Co alloys. *Phys. Rev. Lett.* **68,** 3745–3748 (1992).
386. Milner, A., Korenblit, I. Y. & Gerber, A. Effect of magnetic impurities on electronic transport of heterogeneous ferromagnets. *Phys. Rev. B* **60,** 14821–14829 (1999).
387. Li, G. *et al.* Spin valve sensors for ultrasensitive detection of superparamagnetic nanoparticles for biological applications. *Sens. Actuators Phys.* **126,** 98–106 (2006).
388. Wang, Z. & Nakamura, Y. Quarternary giant magnetoresistance random access memory. *J. Appl. Phys.* **79,** 6639–6641 (1996).
389. Sareni, B., Krähenbühl, L., Beroual, A. & Brosseau, C. Complex effective permittivity of a lossy composite material. *J. Appl. Phys.* **80,** 4560–4565 (1996).
390. Koerner, H., Price, G., Pearce, N. A., Alexander, M. & Vaia, R. A. Remotely actuated polymer nanocomposites—stress-recovery of carbon-nanotube-filled thermoplastic elastomers. *Nat. Mater.* **3,** 115–120 (2004).
391. Candini, A., Klyatskaya, S., Ruben, M., Wernsdorfer, W. & Affronte, M. Graphene Spintronic Devices with Molecular Nanomagnets. *Nano Lett.* **11,** 2634–2639 (2011).
392. Muñoz-Rojas, F., Fernández-Rossier, J. & Palacios, J. J. Giant Magnetoresistance in Ultrasmall Graphene Based Devices. *Phys. Rev. Lett.* **102,** 136810 (2009).
393. Liao, Z.-M. *et al.* Large Magnetoresistance in Few Layer Graphene Stacks with Current Perpendicular to Plane Geometry. *Adv. Mater.* **24,** 1862–1866 (2012).
394. Jobst, J., Waldmann, D., Gornyi, I. V., Mirlin, A. D. & Weber, H. B. Electron-Electron Interaction in the Magnetoresistance of Graphene. *Phys. Rev. Lett.* **108,** 106601 (2012).
395. Zhao, Y., Cadden-Zimansky, P., Ghahari, F. & Kim, P. Magnetoresistance Measurements of Graphene at the Charge Neutrality Point. *Phys. Rev. Lett.* **108,** 106804 (2012).

396. Gu, H. *et al.* An overview of the magnetoresistance phenomenon in molecular systems. *Chem. Soc. Rev.* **42,** 5907–5943 (2013).
397. Bosch-Navarro, C. *et al.* Influence of the covalent grafting of organic radicals to graphene on its magnetoresistance. *J. Mater. Chem. C* **1,** 4590–4598 (2013).
398. Zhu, J. *et al.* Magnetic graphene nanocomposites: electron conduction, giant magnetoresistance and tunable negative permittivity. *J. Mater. Chem.* **22,** 835–844 (2011).
399. Abellán, G., Coronado, E., Martí-Gastaldo, C., Ribera, A. & Otero, T. F. Magnetic Nanocomposites Formed by $FeNi_3$ Nanoparticles Embedded in Graphene. Application as Supercapacitors. *Part. Part. Syst. Charact.* **30,** 853–863 (2013).
400. Tsang, S. C., Caps, V., Paraskevas, I., Chadwick, D. & Thompsett, D. Magnetically Separable, Carbon-Supported Nanocatalysts for the Manufacture of Fine Chemicals. *Angew. Chem.* **116,** 5763–5767 (2004).
401. Zhou, X.-M. & Wei, X.-W. Single Crystalline $FeNi_3$ Dendrites: Large Scale Synthesis, Formation Mechanism, and Magnetic Properties. *Cryst. Growth Des.* **9,** 7–12 (2009).
402. Love, P. Temperature dependence of electrical conductivity and the probability density function. *J. Phys. C Solid State Phys.* **16,** 5985 (1983).
403. Mott, N. F. & Davis, E. A. *Electronic Processes in Non-Crystalline Materials*. (Oxford University Press, 2012).
404. Long, Y. *et al.* Electronic transport in single polyaniline and polypyrrole microtubes. *Phys. Rev. B* **71,** 165412 (2005).
405. Shklovskii, B. I. & Efros, A. L. Electronic properties of doped semiconductors. *Mosc. Izd. Nauka* **1** (1979).
406. Middleton, A. A. & Wingreen, N. S. Collective transport in arrays of small metallic dots. *Phys. Rev. Lett.* **71,** 3198–3201 (1993).
407. Beecher, P., Quinn, A. J., Shevchenko, E. V., Weller, H. & Redmond, G. Insulator-to-Metal Transition in Nanocrystal Assemblies Driven by in Situ Mild Thermal Annealing. *Nano Lett.* **4,** 1289–1293 (2004).
408. Hwang, E. H. & Das Sarma, S. Dielectric function, screening, and plasmons in two-dimensional graphene. *Phys. Rev. B* **75,** 205418 (2007).
409. Sandow, B., Gloos, K., Rentzsch, R., Ionov, A. N. & Schirmacher, W. Electronic Correlation Effects and the Coulomb Gap at Finite Temperature. *Phys. Rev. Lett.* **86,** 1845–1848 (2001).
410. Zhang, J. & Shklovskii, B. I. Density of states and conductivity of a granular metal or an array of quantum dots. *Phys. Rev. B* **70,** 115317 (2004).
411. Murugaraj, P., Mainwaring, D. & Mora-Huertas, N. Dielectric enhancement in polymer-nanoparticle composites through interphase polarizability. *J. Appl. Phys.* **98,** 054304 (2005).

412. Guo, Z. *et al.* Giant magnetoresistance behavior of an iron/carbonized polyurethane nanocomposite. *Appl. Phys. Lett.* **90,** 053111 (2007).
413. Chauvet, O., Benoit, J. M. & Corraze, B. Electrical, magneto-transport and localization of charge carriers in nanocomposites based on carbon nanotubes. *Carbon* **42,** 949–952 (2004).
414. Guo, Z., Hahn, H. T., Lin, H., Karki, A. B. & Young, D. P. Magnetic and magnetoresistance behaviors of particulate iron/vinyl ester resin nanocomposites. *J. Appl. Phys.* **104,** 014314 (2008).
415. Zhang, D. *et al.* Magnetic and Magnetoresistance Behaviors of Solvent Extracted Particulate Iron/Polyacrylonitrile Nanocomposites. *J. Phys. Chem. C* **114,** 212–219 (2010).
416. Siwach, P. K., Singh, H. K. & Srivastava, O. N. Low field magnetotransport in manganites. *J. Phys. Condens. Matter* **20,** 273201 (2008).
417. Hueso, L. E., Rivas, J., Rivadulla, F. & Lopez-Quintela, M. A. Tuning of colossal magnetoresistance via grain size change in $La_{0.67}Ca_{0.33}MnO_3$. *J. Appl. Phys.* **86,** 3881–3884 (1999).
418. Wang, Y. & Fan, H. J. Low-Field Magnetoresistance Effect in Core–Shell Structured $La_{0.7}Sr_{0.3}CoO_3$ Nanoparticles. *Small* **8,** 1060–1065 (2012).
419. Bai, J. *et al.* Very large magnetoresistance in graphene nanoribbons. *Nat. Nanotechnol.* **5,** 655–659 (2010).
420. Adeyeye, A. O. *et al.* Magnetoresistance behavior of submicron $Ni_{80}Fe_{20}$ wires. *Appl. Phys. Lett.* **70,** 1046–1048 (1997).
421. Park, C., Peng, Y., Zhu, J.-G., Laughlin, D. E. & White, R. M. Magnetoresistance of polycrystalline Fe_3O_4 films prepared by reactive sputtering at room temperature. *J. Appl. Phys.* **97,** 10C303 (2005).
422. Coronado, E., Prieto-Ruiz, J. P. & Prima-Garcia, H. Spin polarization in electrodeposited thin films of the molecule-based magnetic semiconductor $Cr_{5.5}(CN)_{12}{\cdot}11.5H_2O$. *Chem. Commun.* **49,** 10145–10147 (2013).
423. Parker, D. R. *et al.* Crossover from Positive to Negative Magnetoresistance in a Spinel. *J. Am. Chem. Soc.* **126,** 2710–2711 (2004).
424. Zhou, Y.-B., Han, B.-H., Liao, Z.-M., Wu, H.-C. & Yu, D.-P. From positive to negative magnetoresistance in graphene with increasing disorder. *Appl. Phys. Lett.* **98,** 222502 (2011).
425. Bakonyi, I. & Péter, L. Electrodeposited multilayer films with giant magnetoresistance (GMR): Progress and problems. *Prog. Mater. Sci.* **55,** 107–245 (2010).
426. Weiss, R., Mattheis, R. & Reiss, G. Advanced giant magnetoresistance technology for measurement applications. *Meas. Sci. Technol.* **24,** 082001 (2013).

427. Kodama, D. *et al.* Synthesis of submicron sized $Fe_{20}Ni_{80}$ particles and their magnetic properties. *J. Appl. Phys.* **107,** 09A320 (2010).

Publications

Patents

1. **Abellán, G.**, Coronado, E., Ribera, A. "Nanocomposites consisting on graphitized matrix and metallic nanoparticles with supercapacitive and magnetoresistive properties". Patent P201200188 (Spain). WO 2013124503 A1 (International).

2. **Abellán, G.**, Coronado, E., Ribera, A. Zamora, F., Mas-Balleste, R., Rodriguez, D. "Preparation of nanocomposites obtained by the thermal decomposition of materials made of metal coordinated donor atoms located in the cavities of Covalent Organic Frameworks (COFs), and its application as supercapacitors". Patent P201301099 (Spain).

Articles

1. **Abellán, G.**; Coronado, E.; Prima-García, H. "Giant Magnetoresistance with Temperature-dependent Crossover in $FeNi_3$-graphene Nanocomposites" (manuscript in preparation).

2. **Abellán, G.**; Carrasco, J. A.; Coronado, E.; Ribera, A.; Varela, M.; Jaafar, M.; Gómez-Herrero, J.; Zamora, F.; Atienzar, P.; Jordá, J. L.; García, H. "Thermo-Responsive Breathing in Hybrid Magnetic Multilayers Based on LDHs" *submitted.*

3. **Abellán, G.**; Martinez, J. G.; Bosch-Navarro, C.; Romero, J.; Marti-Gastaldo, C.; Otero, T. F.; Coronado, E. "Dual-function Supercapacitive and Water Oxidation Electrocatalysts Based on Graphene/NiFe–LDH Hybrids" *submitted.*

4. **Abellán, G.**; Carrasco, J. A.; Coronado, E.; Prieto-Ruiz, J. P.; Prima-García, H. "In-Situ growth of Ultrathin Films of NiFe-LDHs: Towards a Hierarchical Synthesis of Bamboo-Like Carbon Nanotubes" *Adv. Mater. Int.* **2014**, *in press.*

5. Barrejón, M.; Vizuete, M.; Gómez-Escalonilla, M. J.; Fierro, J. L. G.; Berlanga, I.; Zamora, F.; **Abellán, G.**; Atienzar, P.; Nierengarten, J.-F.; García, H.; Langa, F. "A photoresponsive graphene oxide–C_{60} conjugate" *Chem. Commun.* **2014**. doi:10.1039/c3cc49589b.

6. **Abellán, G.**; Coronado, E.; Martí-Gastaldo, C.; Ribera, A.; Jordá, J. L.; García, H. "Photo-Switching in a Hybrid Material Made of Magnetic Layered Double Hydroxides Intercalated with Azobenzene Molecules" *Adv. Mate*r. **2014**, *26*, 4156.

7. **Abellán, G.**; Carrasco, J. A.; Coronado, E.; Romero, J.; Varela, M. "Alkoxide-intercalated CoFe-layered double hydroxides as precursors of colloidal nanosheet suspensions: structural, magnetic and electrochemical properties" *J. Mater. Chem. C* **2014**, *2*, 3723.

8. **Abellan, G.**; Carrasco, J. A.; Coronado, E.; Prima-García, H. "Synthesis of $FeNi_3$ nanoparticles in benzyl alcohol and their electrical and magnetic properties" *J. Sol-Gel Sci. Technol.* **2014**, *70*, 292.

9. **Abellán, G.**; Martinez, J. G.; Otero, T. F.; Ribera, A.; Coronado, E. "A chemical and electrochemical multivalent memory made from $FeNi_3$-graphene nanocomposites" *Electrochem. Commun.* **2014**, *39*, 15.

10. **Abellán, G.**; Coronado, E.; Martí-Gastaldo, C.; Ribera, A.; Otero, T. F. "Magnetic Nanocomposites Formed by $FeNi_3$ Nanoparticles Embedded in Graphene. Application as Supercapacitors" *Part. Part. Syst. Charact.* **2013**, *30*, 853.

11. **Abellán, G.**; Coronado, E.; Martí-Gastaldo, C.; Waerenborgh, J.; Ribera, A. "Interplay between Chemical Composition and Cation Ordering in the Magnetism of Ni/Fe Layered Double Hydroxides" *Inorg. Chem.* **2013**, *52*, 10147.

12. **Abellán, G.**; Carrasco, J. A.; Coronado, E. "Room Temperature Magnetism in Layered Double Hydroxides due to Magnetic Nanoparticles" *Inorg. Chem.* **2013**, *52*, 7828.

13. **Abellán, G.**; Coronado, E.; Gómez-García, C. J.; Martí-Gastaldo, C.; Ribera, A. "Intercalation of cobalt(II)-tetraphenylporphine tetrasulfonate complex in magnetic NiFe-layered double hydroxide" *Polyhedron* **2013**, *52*, 216.

14. **Abellán, G.**; Latorre-Sánchez, M.; Fornés, V.; Ribera, A.; García, H. "Graphene as a carbon source effects the nanometallurgy of nickel in Ni,Mn layered double hydroxide–graphene oxide composites" *Chem. Commun.* **2012**, *48*, 11416.

15. Palomares, A. E.; Franch, C.; Ribera, A.; **Abellán, G.** "NO_x selective catalytic reduction at high temperatures with mixed oxides derived from layered double hydroxides" *Catal. Today* **2012**, *191*, 47.

16. **Abellán, G.**; Busolo, F.; Coronado, E.; Martí-Gastaldo, C.; Ribera, A. "Hybrid Magnetic Multilayers by Intercalation of Cu(II) Phthalocyanine in LDH Hosts" *J. Phys. Chem. C* **2012**, *116*, 15756.

17. **Abellán, G.**; Coronado, E.; Martí-Gastaldo, C.; Ribera, A.; Sánchez-Royo, J. F. "Layered double hydroxide (LDH)–organic hybrids as precursors for low-temperature chemical synthesis of carbon nanoforms" *Chem. Sci.* **2012**, *3*, 1481.

18. Latorre-Sanchez, M.; Atienzar, P.; **Abellán, G.**; Puche, M.; Fornés, V.; Ribera, A.; García, H. "The synthesis of a hybrid graphene–nickel/manganese mixed oxide and its performance in lithium-ion batteries" *Carbon* **2012**, *50*, 518.

19. **Abellán, G.**; García, H.; Gómez-García, C. J.; Ribera, A. "Photochemical behavior in azobenzene having acidic groups. Preparation of magnetic photoresponsive gels" *J. Photochem. Photobiol. Chem.* **2011**, *217*, 157.

20. **Abellán, G.**; Coronado, E.; Martí-Gastaldo, C.; Pinilla-Cienfuegos, E.; Ribera, A. "Hexagonal nanosheets from the exfoliation of Ni^{2+}-Fe^{3+} LDHs: a route towards layered multifunctional materials" *J. Mater. Chem.* **2010**, *20*, 7451.

21. **Abellán, G.**; Carrillo, A. I.; Linares, N.; Serrano, E.; García-Martínez, J. "Alkyl polyamines as surfactants for bimodal silica synthesis and its carbon replica" *J. Solid State Chem.* **2009**, *182*, 2141.

22. **Abellán, G.**; Carrillo, A. I.; Linares, N.; García-Martínez, J. "Bimodal macro- mesoporous silica network" *NSTI-Nanotech 2008* **2008**, *1*, 552.

Quidquid agis, prudenter agas, et respice finem.

Notes regarding the production of this book

Text was prepared using Microsoft Word from the Microsoft Office Proffessional Plus 2011 Suite by Microsoft with an Apple Macintosh computer (MacBook Pro). Laser-printer output was utilized as a hardcopy manuscript. The author prepared all page layouts with Origin Pro 8.5 from Origin Lab Corporation, Microsoft Power Point from the Microsoft Office Proffessional Plus 2011 Suite by Microsoft, Adobe Photoshop CS6 by Adobe Systems, CrystalMaker 8.7 from CrystalMaker Software and ChemBioOffice Ultra 13 from CambridgeSoft.

Body text was displayed on the screen and reproduced on paper in 11-point Minion Pro with 16-point line spacing, and nearly all the tables and figure captions in 10-point Minion Pro with 14-point line spacing. The sans-serif font used in the titles of this book is Myriad Pro. The width of a standard textblock was 125 mm.